



Review



Pyroelectric nanogenerators (PyNGs) in converting thermal energy into electrical energy: Fundamentals and current status

Satiye Korkmaz^a, İ. Afşin Kariper^{b,c,*}^a Karabük University, Engineering Faculty, Karabük, Turkey^b Erciyes University, Education Faculty, Kayseri, Turkey^c Erciyes Teknopark, Building 1, No. 41, Kayseri, Turkey

ARTICLE INFO

Keywords:

Pyroelectric effect

Pyroelectric nanogenerator (PyNG)

Olsen cycle

ABSTRACT

Nowadays, getting energy from natural resources has become an area of interest for researchers with the increasing demand for renewable energy sources. Like triboelectric (TENG) and piezoelectric nanogenerators (PENG), which generate electrical energy from mechanical energy, pyroelectric nanogenerators (PyNG) can also convert the waste heat in the environment into electrical energy through pyroelectric materials. Especially with the integration of PyNG into wearable electronics, the wasted heat in the environment can easily and effortlessly be made ready for use. Besides, PyNGs can be integrated into masks that have become an indispensable part of our lives with the Covid-19 pandemic, which has become a global health problem today and affected the whole world. Wearable electronics' energy requirement can be met by converting waste heat into electrical energy without any extra effort. In this paper, the theory of the pyroelectric effect, pyroelectric materials, and the structure of PyNGs, and the latest developments in micro/nanoscale devices are presented; efficient materials and future challenges opportunities are discussed.

1. Introduction

Nowadays, it is important to ensure correct energy management to prevent the international crisis caused by global warming and climate change, which are increased with the dependence on oil and coal. This problem can be solved in three ways: finding new energy sources, increasing the efficiency of existing energy sources, and collecting various types of energy that occur in our daily life, in other words, energy harvesting [1]. Here, increasing energy resources' efficiency will not be sufficiently beneficial in the long run; it will only save time. For this reason, the discovery of alternative energy sources and energy harvesting has become one of the most researched topics.

Energy harvesting is carried out by converting the energy scattered around or wasted in our daily life, which is not used but should be used, into electrical energy. It is also called waste energy and can be divided into two categories, mechanical and thermal energy. Energies that come out in daily life from the human body's movements, running machines, etc., can be described as waste mechanical energy [1]. On the other hand, a great extent of the heat energy generated by the human body, vehicle exhausts, convention, and solar radiation is wasted [2–6]. This wasted heat has become an important source of renewable energy. With

the pyroelectric nanogenerator (PyNG), thermal energy can be converted into electrical energy based on the Seebeck effect and pyroelectric effect. Thermoelectric materials and systems used to harvest waste thermal energy generate electrical energy from temperature gradients (dT/dx) via pyroelectric materials. Besides, converting the power coming from temperature fluctuations (dT/dt) of pyroelectric materials and mechanical oscillations (dS/dt) during piezoelectric energy harvesting into electricity has similar properties. All pyroelectric materials also have piezoelectric properties [7].

In the recent period, ZnO, PZT, KNbO₃, and PVDF have been widely used in PyNG production [8–13]. Since PyNGs do not undergo mechanical deformation like piezoelectric nanogenerators (PENG) and triboelectric nanogenerators (TENG), no difficulty was experienced in the devices' operating performance. Especially today, as wearable technology is rapidly developing, nanogenerators have significant potential in terms of powering wearable electronic systems. PyNGs can convert thermal energy into electrical energy via the polarization change between electrodes, using the temperature differences occurring in the human body, especially in winter, and temperature fluctuations around the mouth during breathing [14]. By integrating PyNGs into masks, which have become an indispensable part of our lives with the

* Corresponding author at: Erciyes University, Education Faculty, Kayseri, Turkey.

E-mail address: akariper@erciyes.edu.tr (İ.A. Kariper).<https://doi.org/10.1016/j.nanoen.2021.105888>

Received 2 January 2021; Received in revised form 5 February 2021; Accepted 11 February 2021

Available online 15 February 2021

2211-2855/© 2021 Elsevier Ltd. All rights reserved.

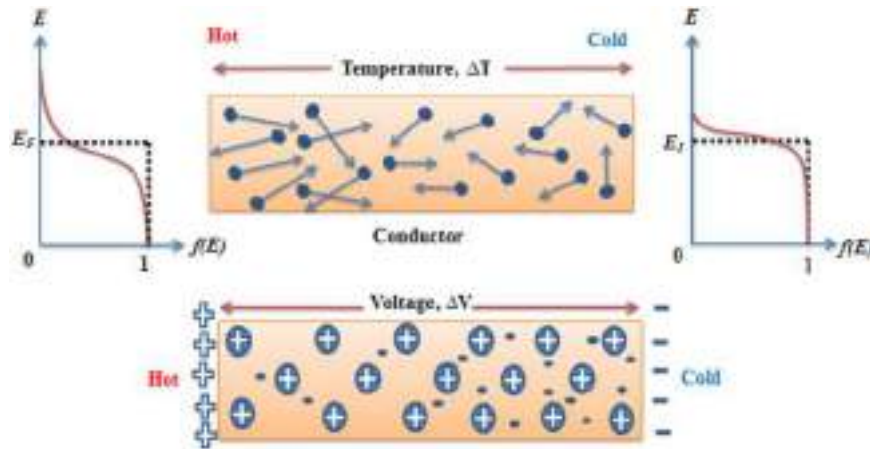


Fig. 1. Seebeck effect.

Covid-19 pandemic that has recently affected the whole world, waste heat can easily be converted into electrical energy without any extra effort. Besides, a large heat loss occurs in the evacuation of hot water from the industrial cooling process. Combustion engines in automobiles also generate large amounts of heat directly dissipated into the environment [15]. It has been reported that half of the energy consumed in the USA in 2009 was wasted as low-temperature waste heat [16,17].

PyNGs consist of three parts: the upper metal layer (upper electrode) designed for the efficient collection of the heat; the middle layer allowing the conversion of thermal energy into electrical energy by changing internal polarization; and the lower metal layer acting as the lower electrode. What is important here is to improve the output performance of PyNG, which has a simple structure, through various approaches such as structural modification, which improves thermal energy absorption. This material modification increases the material's pyroelectric coefficient or improves the polarization by thermal expansion [18]. In this review, the principles that constitute the PyNG development process will be mentioned starting with the Seebeck effect, pyroelectric materials, and working principle; then, recent studies on PyNGs will be discussed.

2. Techniques used for thermal energy harvesting

2.1. Seebeck effect

The temperature difference between two points of a conductor or semiconductor causes a voltage difference; in other words, the temperature gradient in a conductor or semiconductor causes an electric field. This is called the "Seebeck effect (thermoelectric effect)." The effect's magnitude is determined by the Seebeck coefficient, corresponding to the thermoelectric voltage change per unit temperature. The thermocouple principle is based on the Seebeck effect [19].

As shown in Fig. 1, the aluminum rod is heated from one end and cooled from the other end. In this example, the electrons' energy in the warmer zone will be higher, so they will have higher speeds than those in the cold zone. Thus, a clear diffusion occurs in the aluminum rod from the hot end to the cold end. The positive metal ions are left behind in the hot zone, and electrons accumulate in the cold zone. This will continue until the electric field between the positive ions in the hot zone and the excess electrons in the cold zone prevents further electron movement from hot to cold. As a result, a potential difference occurs between the hot and cold ends. The potential difference (ΔV) caused by temperature difference (ΔT) across a metal piece is called the "Seebeck effect." Seebeck coefficient can be expressed as:

$$S = \frac{dV}{dT} \quad (1)$$

The Seebeck coefficient sign will vary depending on the type of carriers conducting the electric current (electrons e^- and holes h^+). If the electric current is transmitted by e^- , the Seebeck coefficient will be negative; if transmitted by h^+ , the Seebeck coefficient's sign will be positive [20]. The Seebeck coefficient, a temperature-dependent material property, has been determined for many materials as a function of temperature ($S = S(T)$). For the given Seebeck coefficient $S(T)$ of a material, the voltage difference between the two points with the temperature T_0 and T is expressed as below [19];

$$\Delta V = \int_{T_0}^T S dT \quad (2)$$

Achieving a constant and large temperature difference is difficult, as the temperature in a real environment tends to be spatially uniform without gradients according to the entropy increase principle. The Seebeck effect has low efficiency in converting thermal energy resulting from time-dependent temperature change with spatial uniformity into electrical energy. Besides, the energy conversion efficiency of existing thermoelectric devices based on the Seebeck effect is still low [21]. For this reason, the pyroelectric effect is used as an alternative approach. Functional layers of most pyroelectric nanogenerators are made of polymers (such as PVDF), which have no Seebeck effect. Therefore, PyNGs, based on the pyroelectric effect, will be discussed as another thermal energy harvesting technique.

2.2. Pyroelectric effect

Pyroelectricity is defined as the effect closely related to the variation of a material's polarization resulting from temperature fluctuations [22, 23]. Aligned electric dipoles in ferroelectric materials create localized charge accumulation at both ends of the sample surface. When the thermal equilibrium state is reached, ferroelectric materials have no net electricity, as an equal number of oppositely charged free charges will retain all localized charges. However, if the temperature is changed, the materials' polarization will change as a response to the temperature change. In this way, the electric fields generated by charging the material surface can be proved by using other charged particles. Depending on the sign of the charges, these particles can be pushed or attracted by pyroelectric materials.

The directions of electric currents in pyroelectric materials differ when the material is heated and cooled. The pyroelectric coefficient representing the pyroelectric efficiency of materials, which is used to characterize the pyroelectric effect of the pyroelectric materials, is an important factor.

$$\Delta P = p \times \Delta T \quad (3)$$

Table 1

Different types of pyroelectric materials with their pyroelectric coefficient p (at an ambient temperature of 25 °C).

Material	Pyroelectric coefficient p ($\mu\text{C m}^{-2} \text{K}^{-1}$) at 25 °C	Reference
Ferroelectric ceramics		
PbZr _{0.5} Ti _{0.5} O ₃ or PZT	-420	[34]
PbZr _{0.3} Ti _{0.7} O ₃	-400	[35,36]
BaTiO ₃	-400	[34]
PbTiO ₃	-250	[37]
Ferroelectric crystals		
Sr _{0.5} Ba _{0.5} Nb ₂ O ₆	-550	[38,39]
Ca _{0.15} (Sr _{0.5} Ba _{0.5}) _{0.85} Nb ₂ O ₆	-360	[40,41]
Triglycerin sulfate or TGS	-350	[26,34]
LiTaO ₃ or lithium tantalate	-200	[34]
Pb ₅ Ge ₃ O ₁₁ or lead germanate	-110	[26,42]
Ca ₁₀ (PO ₄) ₆ (OH) ₂ or Hydroxyapatite	-12	[43]
Ferroelectric semicrystalline polymers		
(CH ₂ CF ₂) _n or PVDF	-27	[26,32]
P(VDF-TrFE) w. 20% TrFE	-31	[26,33,44,45]
P(VDF-TrFE) w. 50% TrFE	-52	[33,46]
P(VDF-TrFE) _{0.5} (PZT) _{0.5}	-45	[46,47]
P(VDF-TrFE) _{0.7} (PZT) _{0.3}	-92	[46-48]
Non-Ferroelectric crystals		
CdSe	-3.5	[26]
CdS	-4.0	[26]
ZnO	-9.4	[26]
Tourmaline	-4.0	[26]

Here p is the pyroelectric coefficient, and its unit is $\text{C m}^{-1} \text{K}^{-1}$. The three nonzero components vector can be expressed as:

$$p_m = \frac{\partial P_m}{\partial T}, \quad m = 1, 2, 3 \quad (4)$$

The pyroelectric coefficient may take different signs. When a pyroelectric crystal is heated, the pyroelectric coefficient is positive when positive charges are present at the positive end, whereas it is negative when negative charges are generated at the positive end. Mechanical boundary conditions should be taken into account in all pyroelectric materials while characterizing the pyroelectric effect, as there may be differences in the polarization of a pyroelectric material when it is subject to deformation caused by the temperature change, which contributes to pyroelectric efficiency. Since cooling or heating is sufficiently homogeneous under mechanical boundary conditions, two types of pyroelectric effects can be observed. When the sample is under constant voltage, only the change in polarization caused by the temperature change contributes to the pyroelectric effect. This is called the primary pyroelectric effect or constant strain pyroelectric effect. The secondary pyroelectric effect includes the contribution resulting from the change in polarization triggered by mechanical action with the material's thermal expansion. If the temperature is evenly distributed throughout the material, this appears as the secondary pyroelectric effect. The pyroelectric coefficient of a pyroelectric material under constant voltage is defined as the sum of pyroelectric coefficients consisting of primary and secondary coefficients [24]. If the pyroelectric materials are heated or cooled inhomogeneously, there will be a stress gradient in the material. This is a peculiar property of piezoelectric materials that are heated/cooled inhomogeneously and is called tertiary pyroelectric effect or false effect. It is important to perform a uniform heating or cooling process during the characterization of pyroelectric materials to minimize or eliminate the tertiary pyroelectric effect [1].

Table 1 shows pyroelectric coefficients of different pyroelectric materials at 25 °C ambient temperature. Besides their pyroelectric properties, all these materials also exhibit some degree of piezoelectric properties. Some pyroelectric materials are ferroelectric, i.e., spontaneous electrical polarization can be reversed by a sufficiently strong external electric field. It means that the material gets paramagnetic when it exceeds the Curie temperature characterized by T_c . These

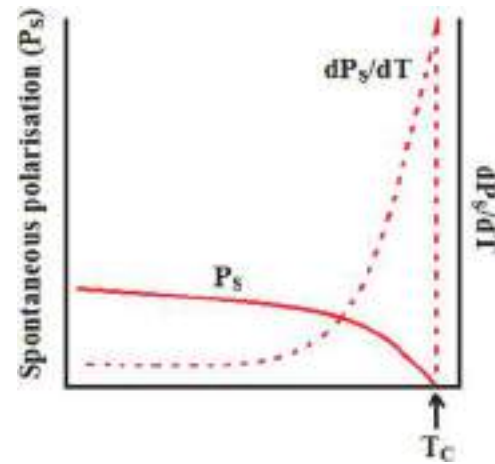


Fig. 2. The dependence of ferroelectric material to pyroelectric coefficient (dP_s/dT) and temperature of spontaneous polarization (P_s) of [49].

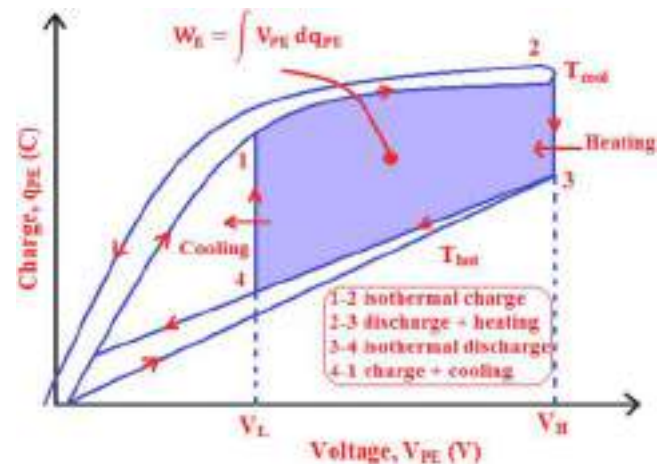


Fig. 3. Typical charge–voltage (C–V) performance of pyroelectric material at two different temperatures. Olsen cycle can be seen in the shaded area formed by the loop 1–2–3–4–1. Reproduced with permission from Nguyen et al. [62]. Pyroelectric energy converter using copolymer P(VDF-TrFE) and Olsen cycle for waste heat energy harvesting [1].

materials are inorganic ceramics such as BaTiO₃ [25] or crystals such as Triglycerin sulfate [26,27] and LiNbO₃ [28], semi-crystalline polymers such as PVDF (Polyvinylidene fluoride) [29–31] and TrFE (Trifluoroethylene) and its copolymer [32,33] or even biological materials such as collagen. Ferroelectric materials generally exhibit larger pyroelectric coefficients than non-ferroelectric ones and therefore attract more attention for applications.

Although ferroelectric materials have higher pyroelectric and piezoelectric coefficients than non-ferroelectric materials, if a ferroelectric material is heated above the Curie temperature (T_c), spontaneous polarization, piezoelectric and pyroelectric properties will disappear with phase transition [7]. In Fig. 2, as the material approaches T_c , the pyroelectric coefficient (dP_s/dT) will increase, and the polarization will begin to disappear rapidly. The phase transition in such materials at Curie temperature is notable for pyroelectric harvesting because of the high potential of releasing electrical energy with the decrease of P_s to zero.

2.2.1. Olsen cycle of the pyroelectric effect

Thermodynamic cycles are used to determine the maximum efficiency in pyroelectric energy harvesting behaviors. The Olsen cycle is the most suitable one to examine the energy conversion behavior of

pyroelectric materials. In the q - V diagram of the pyroelectric effect shown in Fig. 3, the 1–2–3–4–1 cycle shows the Olsen cycle [50–62]. Here the pyroelectric material can be a thin film with two metallic electrodes. Olsen cycle starts by charging the material at low temperature (T_L) (cycle 1–2), and the voltage rises from V_L to V_H . Then the material is heated from T_L to T_H under constant voltage, and T_H gets higher than T_C , the pyroelectric material is discharged (cycle 2–3). As the discharge process continues (cycle 3–4), the voltage decreases towards VL at constant TH temperature. While the pyroelectric material cooled from T_H to T_L is recharged (T_L lower than T_C), V_L remains constant (cycle 4–1). The shaded area gives electrical work output (WE) in Fig. 3, and its unit is $J L^{-1}$.

2.2.2. Theory of nanogenerators from Maxwell's equations

Displacement current was first adopted by Maxwell [63] in 1861 and was introduced considering the consistency between Ampere's magnetic field law and the continuity equation for electric charges. Displacement current is not an electric current of moving free charges but a contribution of a time-varying electric field (vacuum or medium) and dielectric polarization in materials. Recently, researcher Zhong Lin Wang has investigated the relationship between nanogenerators' output and Maxwell's displacement current.

There are two types of currents, namely conduction current, and displacement current. For pyroelectric generators, the current is driven by displacement current within the generator. The polarization is along the z -axis, the displacement field is the polarization vector, $D_z = P_z = \sigma_p(z)$ in the media so that the displacement current is,

$$J_{Dz} = \frac{\partial P_z}{\partial t} = \frac{\partial \sigma_p(z)}{\partial t} \quad (5)$$

Eq. (5) means that the varying velocity of surface polarization charges is the observed output current for a PyNG. The following expression indicates the magnitude of the open-circuit voltage for PyNG,

$$V_{oc} = z\sigma_p(z)/\epsilon \quad (6)$$

where $\sigma_p(z)$ is the density of polarization charges on the surface and ϵ is the dielectrics' permittivity.

Considering the presence of an external load R , the current transport equation for PyNG is,

$$RA \frac{d\sigma}{dt} = z[\sigma_p(z) - \sigma(z)]/\epsilon \quad (7)$$

A is the area of the electrode. When the applied stress is a relatively slow process, z is a function of time t .

A systematic theory has been derived to explain the electromagnetic dynamics of nanogenerators in Maxwell's equations. This general theory's establishment is anticipated to form a theoretical basis for improving nanogenerators' science, technology, and even applications in energy and sensors [64].

2.3. Pyroelectric materials

2.3.1. Triglycine sulfate (TGS)

Triglycine sulfate (TGS), $(NH_2CH_2COOH)_3H_2SO_4$ is the material with the best potential performance among all pyroelectric materials. However, despite its high performance, low Curie temperature ($T_C = 49^\circ C$) has limited the energy harvesting applications of TGS. Therefore, its pyroelectric properties have been improved by modifying TGS while preserving its basic crystal structure. Various new compounds have been synthesized, such as deuterated- triglycine sulfate (DTGS), the substitution of sulfuric with fluoroberyllic acid to obtain triglycine fluoroberyllate (TGFB) with and without deuterated triglycine fluoroberyllate (DTGFB) and the substitution of glycine either with L-alanine or D-alanine (ATGS).

In ATGS, the spontaneous polarization, which becomes stable with

the realization of an electrical tendency in the materials, is attributed to the additional methyl group preventing the rotation of the molecules in the cage [65]. TGSP and ATGSAS derivatives, which have different operating temperatures, can be obtained by doping alanine and phosphoric acid or arsenic acid [66–68]. For example, the operating temperature range of the material can be expanded with the increase of the Curie temperature with the deuteration of TGS. TGS based pyroelectric materials have higher pyroelectric properties than oxide based ferroelectric or polymeric ferroelectric materials, but they are disadvantageous due to high dielectric losses. Besides, they are suitable for most applications with their high pyroelectric voltage-sensitive performances despite their problems, such as water solubility, hygroscopic structure, and brittleness.

2.3.2. Polyvinylidene fluoride (PVDF)

Polymeric ferroelectric polyvinylidene fluoride (PVDF) molecules that exhibit high piezoelectric properties have $-CH_2-CF_2-$, a carbon-hydrogen bond and a polar carbon-fluorine bond (electrically). In the processes performed in solutions cooled at sufficiently slow rates or in acetone solutions, the α phase, a non-piezoelectric phase, is obtained. This molecular structure, which has a trans-gauche-trans-gauche configuration, leads to a non-polar unit cell accumulation. The α phase, which is subjected to voltage or electrical polarization, is transferred to the β phase, where all molecular groups form polar unit cells. In the β phase, PVDF has a pyroelectric effect because of its ferroelectric properties. PVDF, which has a lower pyroelectric coefficient than TGS, also causes high dielectric losses. PVDF has a Curie temperature higher than its melting point of $180^\circ C$. Above $80^\circ C$, PVDF has a limiting effect on the pyroelectric operating temperature, as the polarization starts to decrease. It is very cost-effective compared to other types; it has various derivatives such as trifluoroethylene (VDF-TRFE) and the copolymers of vinylidene fluoride [69–71]. On the other hand, it would be more convenient to produce thin-film-based devices with conventional deposition methods such as spin coating and solution coating [1].

2.3.3. Lithium tantalate (LiTaO₃)

Lithium tantalate (LiTaO₃) is an important pyroelectric material belonging to the oxide family. In the crystal structure of LiTaO₃, the layers of oxygen ions are tightly packed in a hexagonal configuration, and Li⁺ and Ta⁵⁺ ions occupy two of the three octahedral spaces between the layers. LiTaO₃, a polar ferroelectric at room temperature, shows a non-polar paraelectric property at the Curie temperature of $665^\circ C$. Being insoluble in water and having a very high melting temperature, it has a wide operating temperature range. Although LiTaO₃ crystal has a dielectric constant and pyroelectric coefficient corresponding to approximately one-quarter of TGS, it exhibits quite low dielectric losses. On the other hand, its high thermal dissipation appears as a serious disadvantage [1].

2.3.4. Strontium barium niobate (Sr_xBa_{1-x}Nb₂O₆)

Strontium barium niobate, with the chemical formula Sr_xBa_{1-x}Nb₂O₆ ($0.25 \leq x \leq 0.75$), exhibits high pyroelectric properties. When the composition changes between $x = 0.72$ – 0.25 , the Curie temperature drops from $195^\circ C$ to $53^\circ C$. The highest pyroelectric coefficient, the largest dielectric constant, and the lowest dielectric loss are achieved when the composition has equal Sr and Ba fractions. Besides, when the Curie temperature of Sr_xBa_{1-x}Nb₂O₆ is approached to the room temperature by doping with La, the pyroelectric coefficient and dielectric constant can significantly increase [72].

2.3.5. Lead germanate (Pb₅Ge₃O₁₁)

Lead germanate (Pb₅Ge₃O₁₁) has a hexagonal crystal structure and a relatively low Curie temperature of $178^\circ C$ [73–76]. To modify ferroelectricity and improve its pyroelectric properties, barium is used instead of lead, or silicon is used instead of germanium. With these additives, the Curie temperature is lowered to around room

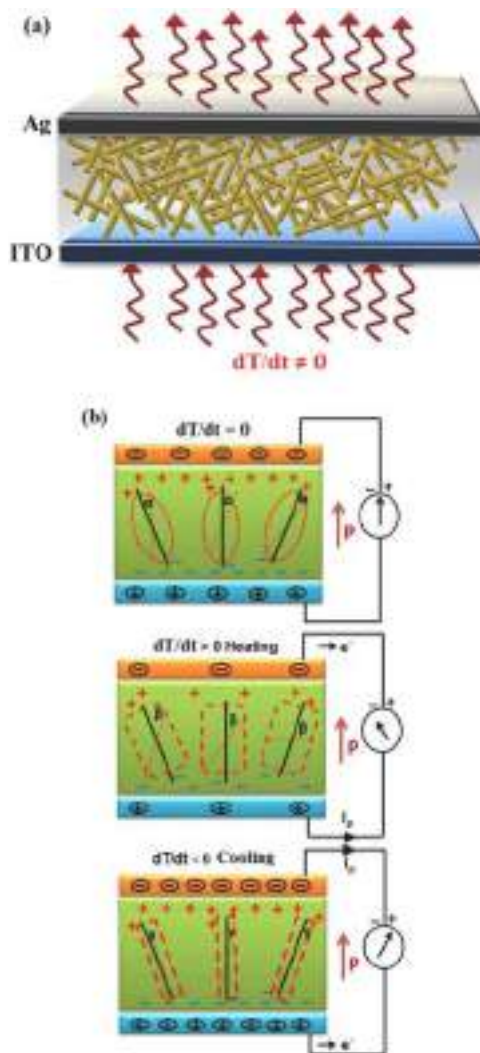


Fig. 4. a) The pyroelectric nanogenerator mechanism based on primary pyroelectric effect; b) Schematic diagrams of the pyroelectric nanogenerator with negative electric dipoles heated and cooled under room temperature [85].

temperature.

2.3.6. Pyroelectric ferroelectrics with perovskite structure

Perovskite structured ferroelectric materials, having ABO_3 chemical formula, are formed through the corner-sharing of the BO_6 octahedra. A and B positions contain various cations and can form different crystal structures such as rhombus, tetragonal and orthorhombic. Almost all features predicted for single crystals can be realized in ceramics; thus, studies have generally focused on ceramics materials. The ceramic process has been reported to provide more flexibility in applying additives without changing the crystal structure. Therefore, compared to their single-crystal counterparts, pyroelectric properties can be developed more easily.

The combination of lead zirconate ($PbZrO_3$, PZ), an antiferroelectric compound, and lead titanate ($PbTiO_3$, PT), a ferroelectric compound, can be used to formulate solid solutions with superior crystallographic phases. It was more suitable for pyroelectric applications because its dielectric constant is lower than other compounds. Pyroelectric properties can be improved by using various additives [77]. Tertiary compounds such as $PbZrO_3$ - $PbTiO_3$ - $PbFe_{1/2}Nb_{1/2}O_3$ have been shown to have very high pyroelectric coefficients in potential applications [78, 79]. The pyroelectric potential, dielectric constants, and dielectric losses of these materials can be improved by adjusting their compositions or

additives. Due to the difficulties of obtaining a large single crystal, most studies have focused on ceramics. Sintered ceramics, which experience intense stress during cooling from the high sintering temperature that exceeds the Curie point, will be broken at room temperature, so pure PT ceramic is almost nonexistent; however, PT-based ceramics can be modified using additives [80]. Compared to PZ-based materials, PT ceramics have relatively lower dielectric constants and dielectric losses. Special sintering techniques, such as hot pressing, can minimize dielectric losses and achieve higher density [81,82]. On the other hand, lead-free ceramics such as $(Ba_{0.84}Ca_{0.15}Sr_{0.01})(Ti_{0.90}Zr_{0.09}Sn_{0.01})O_3$ (BCSTZS) are synthesized by traditional ceramic processing methods, as the interest towards lead-free ferroelectric materials increases to overcome potential environmental pollution concerns. Pyroelectric coefficients, which vary with the temperature, are expected to be further developed in future studies [83].

2.4. Pyroelectric nanogenerator

Pyroelectric nanogenerators convert thermal energy into electrical energy by using the pyroelectric effect. The Seebeck effect, which uses the temperature difference between the two ends of the device to provide diffusion of charge carriers for thermal energy harvesting, which we discussed in detail before, cannot be used for thermal energy harvesting in case of a time-dependent change without temperature gradient. Therefore, the pyroelectric effect should be chosen as a result of temperature fluctuations [84]. Pyroelectric nanogenerators are notable for their potential applications such as temperature monitoring, medical diagnostics, and personal electronics by collecting waste heat energy.

The primary pyroelectric effect, which dominates the pyroelectric response of PZT, BTO, and some other ferroelectric materials, is related to the charge generated in the voltage-free state [86–88]. The mechanism formed by random oscillations of electric dipoles, which increase with increasing temperature, around the equilibrium axis is explained in Fig. 4a, in the schematic illustration of PyNG, in which lead-free $KNbO_3$ -NW/PDMS polymer pyroelectric composite is used. In the structure mainly consisting of three layers, Ag film is used as the upper electrode, NW-composite film in the intermediate layer, and indium tin oxide (ITO) as the lower electrode. The operation mechanism of the device is expressed in Fig. 4b. Accordingly, the electric dipoles in $KNbO_3$ NW result from the Nb^{5+} ion movement in the NbO_6 octahedra, where there are six orientations along the $\langle 001 \rangle$ directions. Electric dipoles will oscillate randomly from the axis of alignment due to thermal fluctuations. In the first case, when the temperature is constant, the total average power of the electric dipoles' spontaneous polarization will be constant, and there will be no electricity output. In the second case, when PyNG reaches a temperature higher than room temperature, the electric dipoles will oscillate in a wider range than the alignment axis, which will cause the overall average polarization to decrease. Thus, by reducing the amount of charge induced on the electrodes, an electron flow will occur. In the last case, when PyNG is started to be cooled, the oscillation angles will decrease due to the decrease in the electric dipoles' thermal activity, and spontaneous polarization will increase. An increase will be observed in the charges induced on the electrodes. Induced electrons will start to flow in the opposite direction.

The secondary pyroelectric effect occurs in ZnO, CdS, and some wurtzite-type materials with decentralized symmetrical structure [8]. The resulting thermal deformation will cause the piezoelectric potential difference allowing the electrons to flow through the external circuit material. Thus, the output performance of PyNG will be related to the piezoelectric coefficient and anisotropic thermal expansion of the material. The structure considered for the secondary pyroelectric effect in Fig. 5a consists of the Ag film as the upper electrode, the ITO as the lower electrode, and the ZnO NW in the intermediate layer. In Fig. 5b, the working mechanism is illustrated; when the temperature of the device is increased from 295 K to 304 K, a pyroelectric potential will occur along

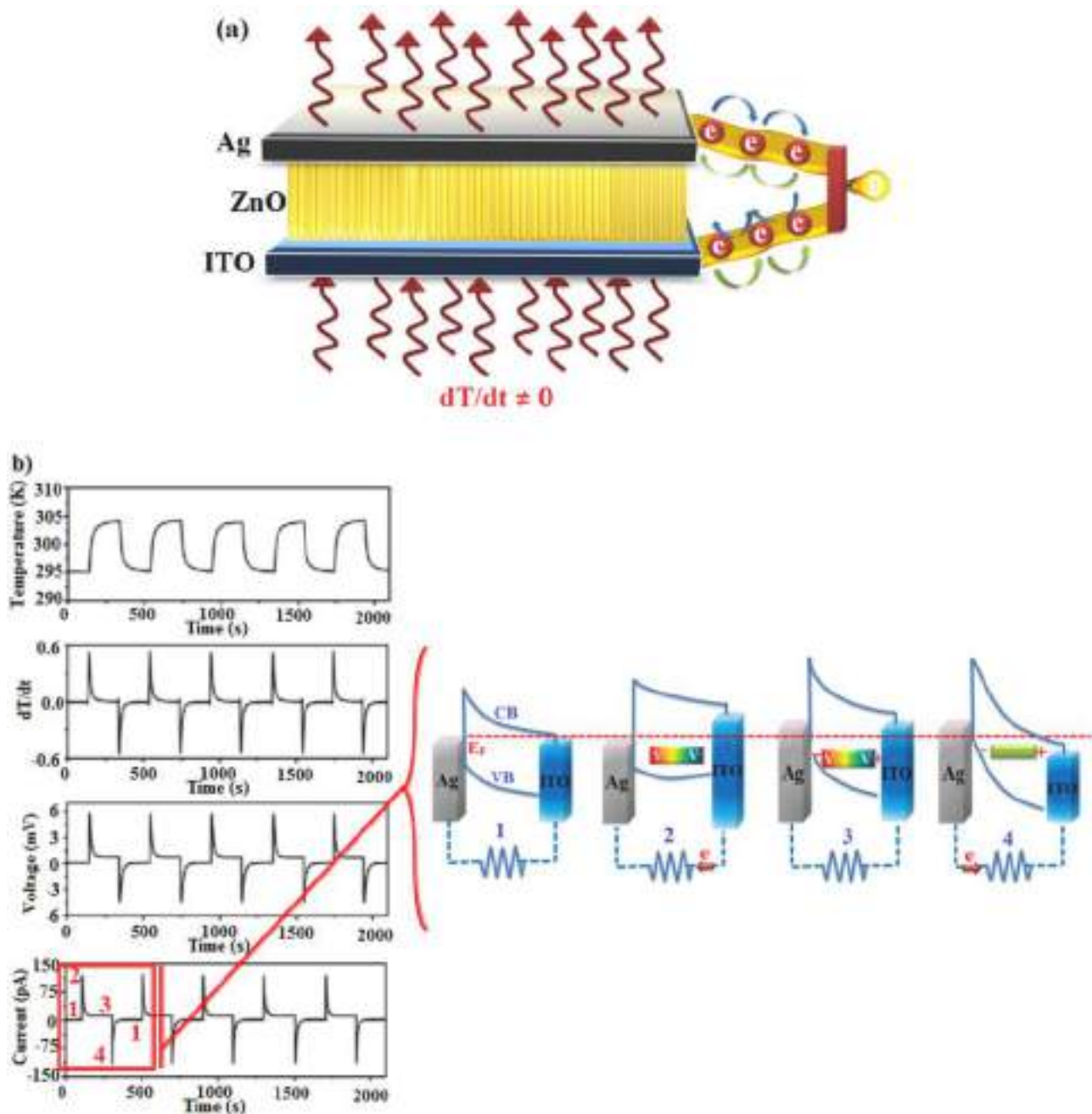


Fig. 5. Mechanism and performance of pyroelectric nanogenerator resulting from the secondary pyroelectric effect. (a) Schematic diagram of ZnO NW pyroelectric nanogenerator structure. (b) The device's output voltage and current under a cyclic temperature change and corresponding energy diagrams of the device in four different stages [85].

the ZnO NW; the negative electric potential will be at the ITO electrode, and the positive electric potential will be at the Ag electrode. Due to the negative electric potential, the conduction band and the Fermi level of the ITO electrode will increase. The electrons will begin to flow from the ITO to the Ag electrode. When the temperature turned to 295 K, the Ag electrode's electrons are released and flow back to the ITO electrode, and the pyroelectric potentials disappear.

3. Circuit applications of pyroelectric devices

The storage of the obtained electrical power is as important as converting thermal energy into electrical energy. Therefore, researchers have performed studies on electronic circuits to achieve this goal. The equivalent thermoelectric circuits of a pyroelectric cell are shown in

Fig. 6. Conversion of thermal power (W) to the temperature change is given in Fig. 6a; the electrical equivalent circuit resulting with an output voltage (V_p) consisted of the pyroelectric current source (I), electrical capacitance (C_p), and resistance (R_p) is given in Fig. 6b. The electrical power obtained by converting thermal energy into electrical energy must be transferred to a storage device such as a resistor or capacitor; the simplest way to do it is a resistance loop directly connected to the device's output. In the temperature cycle, the pyroelectric current (I) passes across the resistance, and the electrical power dissipates into the electrical load. Efficiency is low even if the load resistance matches the output impedance of the pyroelectric device. Since pyroelectric devices are bidirectional, they generate alternating current, and rectification is required for energy harvesting (Fig. 7). The pyroelectric energy source represented by the equivalent circuit in Fig. 6b is connected to the diode

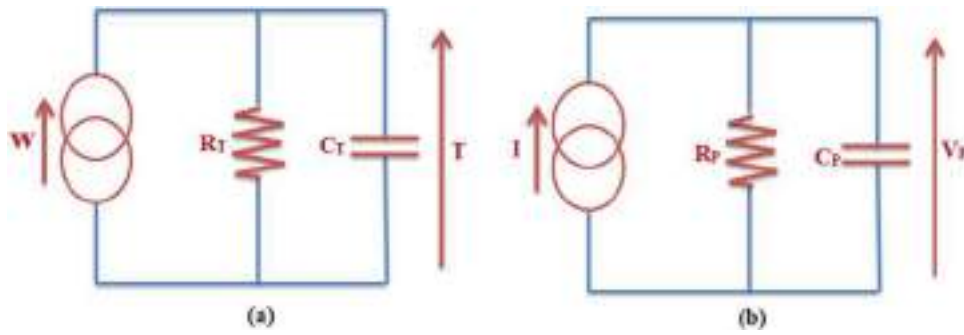


Fig. 6. Thermoelectric equivalent circuits of the pyroelectric cell. (a) Conversion of thermal energy W to the temperature change T (b) Conversion of the current generated by the pyroelectric process to an output voltage V_p [7].

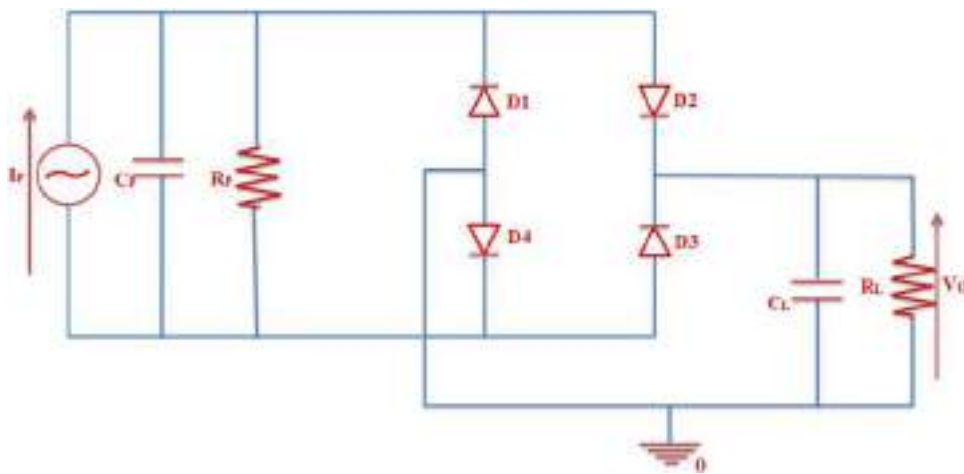


Fig. 7. “Standard” interface circuit [7], consisting of a full-wave bridge rectifier interfacing the charge generated by the pyroelectric source (equivalent circuit in Fig. 6b consisting I_p , C_p , and R_p) C_L and R_L .

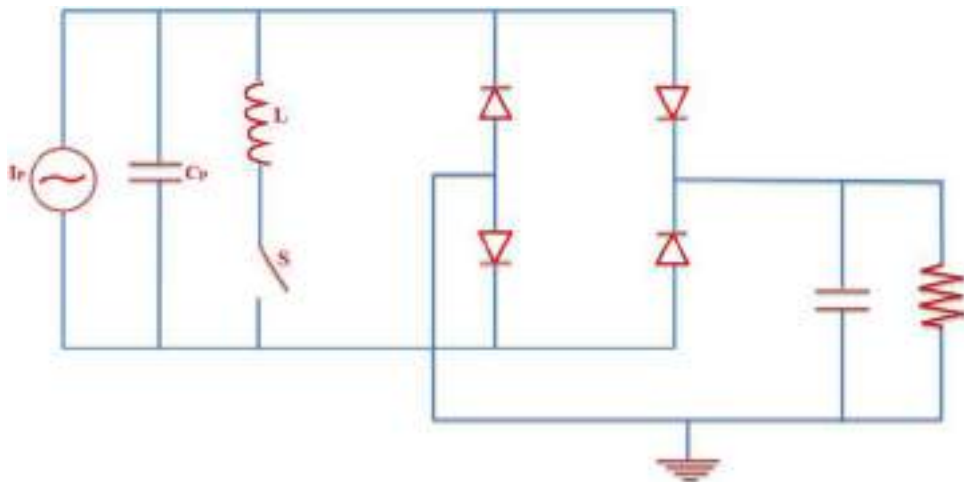


Fig. 8. Parallel synchronous switch harvesting on inductor (SSHI) charge extraction interface circuit [7].

bridge (D1-D4) that provides full-wave output to recover the device’s output voltage. The collected energy is stored in the capacitor C_L and distributed over the resistance R_L to minimize the output voltage fluctuation.

Another method developed to generate pyroelectric energy is a current source (C_p) finished by a resistor and capacitance connected in parallel and increasing the voltage across the load. Amplifiers can increase the existing power, but this method’s application will not be

efficient as the amplifiers require power, and the generated energy is quite low. An approach based on a switched (i.e., non-linear) arrangement in which charge is extracted at maximum and minimum temperature, i.e., when the stored electrical energy is also maximum, is more successful [89–91].

With the arrangement in Fig. 8, where the method is shown when the switch is closed, L_p and C_p form a parallel tuned circuit, driven by I_p to function as a forced oscillator with a resonant frequency $\omega_0 = \frac{1}{\sqrt{L_p C_p}}$.

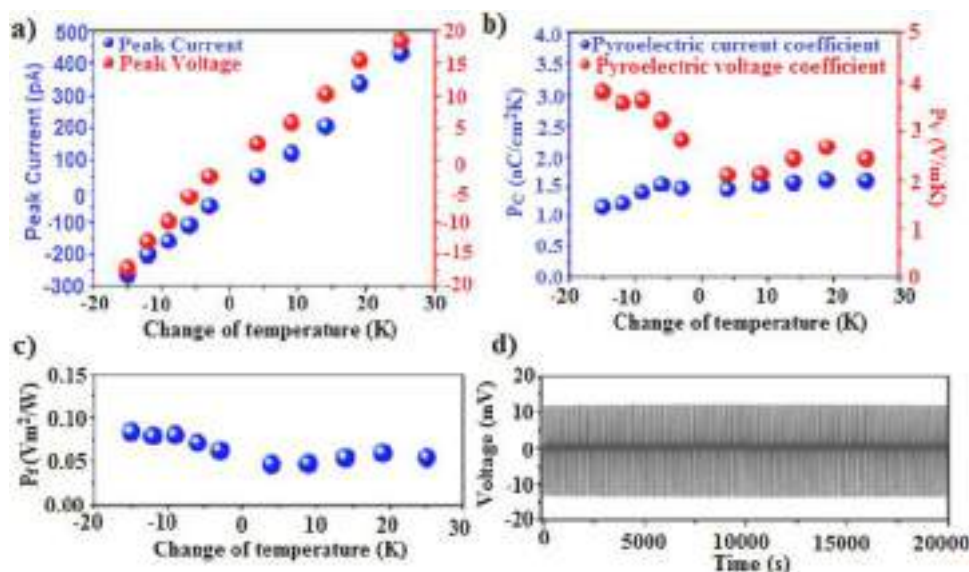


Fig. 9. The output peak voltage/current (a), pyroelectric voltage/current coefficients (b), and energy conversion characteristic value (c), as a function of temperature change. (d) Output stability test of the nanogenerator through cyclic temperature change for over 200 cycles [8].

Suppose S is closed at the temperature cycle's peak, assuming w_0 is much higher than the temperature cycling frequency. In that case, it is possible to capture most of the energy generated by the pyroelectric device. Since the circuit voltage may be much greater than the open-circuit voltage, a significant amount of charge–voltage will be generated. Along with the energy temporarily stored as magnetic energy in L_p , losses may occur due to the switch's and field coils' infinite resistance. Regarding the non-dissipative storage of the energy as a magnetic field by the inductor, significant steps have been taken in terms of efficiency with the buck/boost power converter [92].

4. Recent developments

4.1. ZnO based PyNGs

With their anisotropic physical properties, ZnO nanowires, which provide effective results in TENGs and PENGs (which are used in the conversion of mechanical energy into electrical energy), can generate piezo potentials by voltage or temperature. In 2012, Yang et al. [8] used ZnO nanowires to convert thermal energy into pyroelectric energy for the first time. The combination of pyroelectric and semiconductor properties of ZnO creates a polarization electric field and charge separation across the ZnO nanowire due to the time-dependent temperature change. The higher pyroelectric coefficients of ZnO nanowires compared to bulk/film ZnO may be due to a single-crystal structure with less dislocation density.

The pyroelectric current and voltage coefficients for ZnO nanowires with an average diameter of 200 nm are ~ 1.2 – 1.5 nC/cm² K and ~ 2.5 – 4.0×10^4 V/m K, respectively. NG's energy conversion characteristic coefficient is 0.05–0.08 V m²/W. Fig. 9 shows: Measured voltage/current peaks as a function of temperature change, having an almost linear relationship (Fig. 9a), pyroelectric voltage/current coefficients (Fig. 9b), energy conversion characteristic value (Fig. 9c), and NG's output stability test by cyclic temperature change over 200 cycles (Fig. 9d). The results showed that the output voltage signal is very stable, and no decreasing trend is observed.

As mentioned earlier, when the size and volume of the material are fixed, the primary pyroelectric coefficient is used to describe the charges generated under the temperature change; on the other hand, when the size/volume of the material change with the temperature change, the voltage is induced due to the anisotropic deformation of the material,

resulting with the additional contribution of induced charges. It is generally defined as the secondary pyroelectric effect for wurtzite crystals such as ZnO. The study is important in showing the potential use of pyroelectric nanowires in powering nanodevices, temperature monitoring, radiation detection, X-ray generation, space applications, and most importantly, being the first use of ZnO nanowires in PyNGs.

Near-infrared light (NIR) has a wide range of applications as electromagnetic radiation, from biomedical imaging to environmental monitoring [93,94]. Numerous NIR photodetectors (PDs) have been reported, such as nanocrystal quantum dots, 2D layered materials, and organolead halide perovskite. However, their photoabsorption capacities limit the performance of reported NIR PDs [95–100]. PDs are based on the separation of carriers photogenerated by the electric field created in pn- and/or Schottky junctions. In this process, the photoinduced voltage (PIV) is generated in the resident electric field's opposite direction, reducing the electric field, which weakens the carriers' separation. This limits the photo-response performances of NIR-PDs. For this reason, the performances and application areas of NIR-PDs should be expanded. For non-symmetrical pyroelectric materials, pyroelectric polarization can be induced by time-dependent variation of temperature across the material [8,72]. The change in pyroelectric materials' temperature caused by IR radiation causes pyroelectric polarization potential along polar directions. The time-dependent change of the internal polarization electric field in the ZnO NWs directs electrons' flow through external circuits, thus obtaining a short circuit current. They also form the basis of PyNGs and PENGs [8, 101–103]. Therefore, pn-junction is an important function in both electronics and optoelectronics. Wang et al. [104] developed a self-powered NIR-PD for Si/ZnO NW pn-junction by developing a PyNG triggered by NIR light. ZnO synthesized by the hydrothermal method was produced on the Si layer, as shown in Fig. 10a. Upon the illumination of NIR (1064 nm) from the ZnO side, two optical processes can be induced in the pn-junction device: the instantaneous pyropolarization inside ZnO NWs and the photoexcitation at the local junction caused by the photoabsorption of NIR in 500 μ m-thick Si (Fig. 10b). Since E_b is in the pn-junction depletion region, the holes and electrons are separated and directed towards the p-Si and n-ZnO NW side, as in Fig. 10c. I–V characteristics of p-Si/n-ZnO heterostructure under different power densities resulting from NIR lighting are given in Fig. 10d. The results reveal the high photo-response properties of NIR-PDs. The study presented a different method to achieve active NIR sensing using NIR induced PyNG in applications such as optothermal

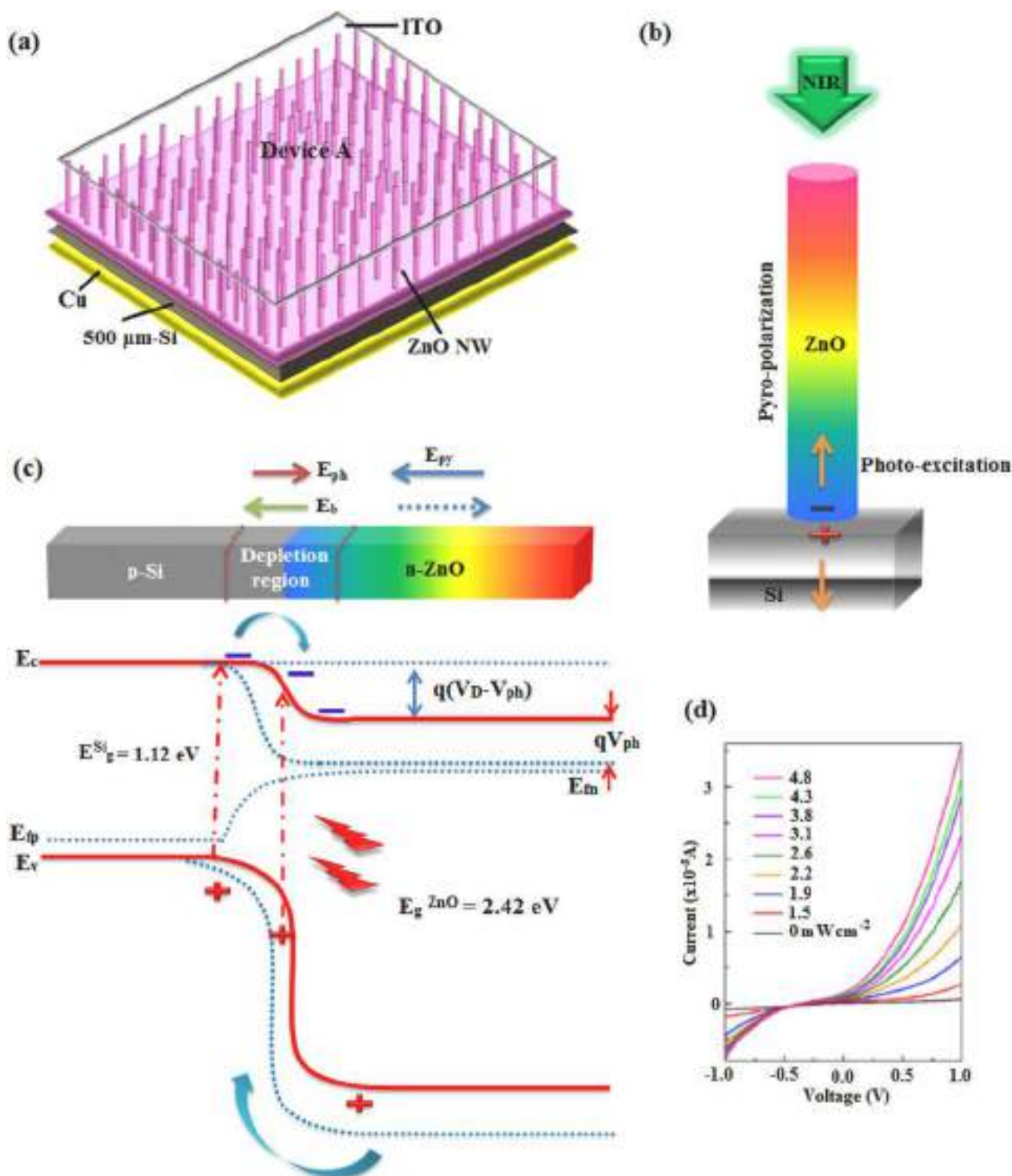


Fig. 10. (a) Schematic illustration of p-Si/n-ZnO NW heterostructure devices, (b) Instant pyro-polarization in ZnO NW upon illumination of 1064 nm light and photoexcitation in local junction, (c) Photogenerated holes and electrons get separated, leading to the formation of E_b , (d) I-V characteristics of p-Si/n-ZnO NIR-PDs under nine different power densities of NIR lighting [104].

detection, biological imaging, and optoelectronic communication.

4.2. PZT based PyNGs

Since 2005, developing self-powered systems that can operate wirelessly without using energy storage systems has become researchers' focus [105–107]. With the nanogenerators, mechanical and

thermal energy can be converted into electrical energy, and the power required, especially for personal electronics, can be generated. Piezoelectric and triboelectric nanogenerators are designed to convert mechanical energy into electrical energy, while pyroelectric nanogenerators are designed to convert thermal energy. The performance of pyroelectric nanogenerators (PyNG) has been tried to be improved for potential applications by using different pyroelectric

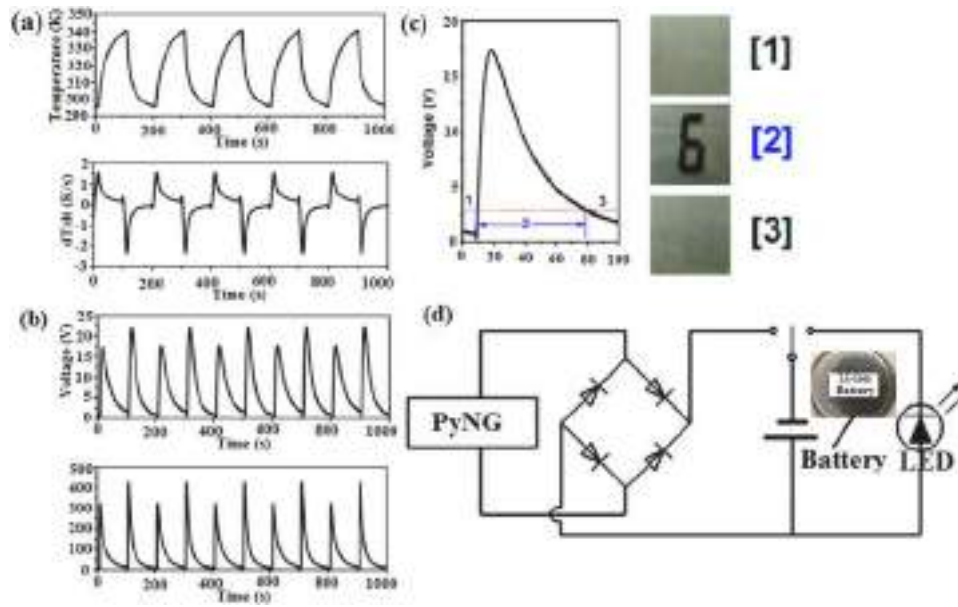


Fig. 11. (a) Cyclic change in the temperature of PyNG and the corresponding differential curve. (b) Measured output voltage and current after rectification with a full-wave bridge circuit. (c) Extended single output voltage peak that can be used to drive an LCD in region "2" (d) Schematic diagram showing the process of charging Li-ion battery and using LED [108].

materials. Yang et al. [108] developed PyNG using lead zirconate titanate (PZT) film. The PyNG design was based on the spontaneous change in the PZT thin film's polarization, resulting from time-dependent temperature fluctuation, allowing electrons to flow in an external circuit. The pyroelectric coefficient of PZT film was $-80 \text{ nC/cm}^2 \text{ K}$; for a temperature change of 45 K at a rate of 0.2 K/s obtained by changing the temperature around the nanogenerator between 295 and 340 K, the output open-circuit voltage of the PENG was found to be 22 V, and the short circuit current density reached 171 nA/cm^2 . The obtained PyNG allowed an LCD operation for more than 60 s with a single output pulse. It has also been reported that the PyNG can charge a Li-ion battery at different frequencies.

Fig. 11a shows the temperature cycle of PyNG from 295 to 340 K and the corresponding temperature change rates. Alternative energy output is adjusted with the full-wave bridge circuit, as shown in Fig. 11b. Fig. 11c, which displays the magnified output voltage peak running an LCD, shows that the LCD operates in the region "2", where the operating time is longer than 60 s. As it is known, the electrical energy generated from temperature fluctuations must be stored to expand the potential applications of PyNG. In the schematic diagram in Fig. 11d, the Li-ion battery, in which TiO_2 nanotube grown on Ti foil is used as the anode, is charged by PyNG and used to power the LED.

The electrical potential distribution across the PZT film was calculated for a temperature change of 45 K using COMSOL software. The film's thickness and the pyroelectric coefficient were determined as 175 nm and $80 \text{ nC/cm}^2 \text{ K}$, respectively. The change of surface charge density can be given as:

$$\Delta\sigma = \Delta P = p \cdot \Delta T \quad (8)$$

Here ΔP is the polarization change, and ΔT is the temperature change. The potential U between the upper and lower electrodes throughout the thickness of the PZT film can be expressed as:

$$U = Ed = \frac{\Delta\sigma \cdot d}{(\epsilon_r - 1)\epsilon_0} \quad (9)$$

E is the electric field, d is the thickness of the PZT film, ϵ_r is the relative dielectric constant of the sample, and ϵ_0 is the free space's permeability [109]. Pyroelectric potential distribution across the PZT film is obtained using Eqs. (8) and (9) of the COMSOL software package.

Using the output voltage and current equations of PyNG, it was found that the increase of the pyroelectric coefficient and the temperature change can increase the output voltage and current. Theoretical calculations show that PyNG performance depends on the materials with high pyroelectric coefficient, temperature change, and film thickness. It is possible to increase the output voltage by increasing the film thickness. The researchers showed that the PyNG obtained in the study can be used for wireless sensors.

Although some temperature sensors have been reported until 2012, very few studies have included PZT micro/nanowire PyNG as a self-powered temperature sensor. In the same year, in a study conducted with Yang et al. [110], PyNG was produced by packaging PZT micro/nanowire placed on a glass substrate with polydimethylsiloxane (PDMS). The schematic illustration of the produced PyNG is given in Fig. 12a.

The diameter of the microwire produced here was specified as $2 \mu\text{m}$ and its length as $10 \mu\text{m}$. For a PyNG to be used as a temperature sensor, the relationship between the output voltage and temperature must be identified accurately. PyNG is attached to a metal body's surface as in Fig. 12b to provide heat dissipation for the sensor measurement process. As in the first case, no output voltage is observed when the sensor is not in contact with the heat source, and a negative voltage pulse (60 mV) was observed when it came into contact with the heat source at 303 K (Fig. 12c). A positive voltage is achieved when the heat source is disconnected from the sensor. Fig. 12d shows the noise signal observed before the voltage peak is related to the sensor's movement in the measurement process. The temperature change rate and the temperature can be sensed when the sensor, fixed on a soft foam plastic substrate preventing it from breaking, is touched with the fingertip, as in Fig. 12e. The negative output voltage of 60 mV turns positive when the finger is moved. The sensor can illuminate an LCD when the heat source's temperature rises to 473 K (with a response time of 0.9 s and a minimum detection limit of temperature change 0.4 K). Such PyNGs can be used in fields such as medical diagnosis, temperature measurement, security monitoring.

Since ferroelectric materials with flexible structure will be insufficient to collect mechanical vibrations and thermal fluctuations from ambient conditions due to their small piezoelectric (-30 pC/N) and pyroelectric coefficients ($2.7 \text{ nC/cm}^2 \text{ K}$) and their inability to resist

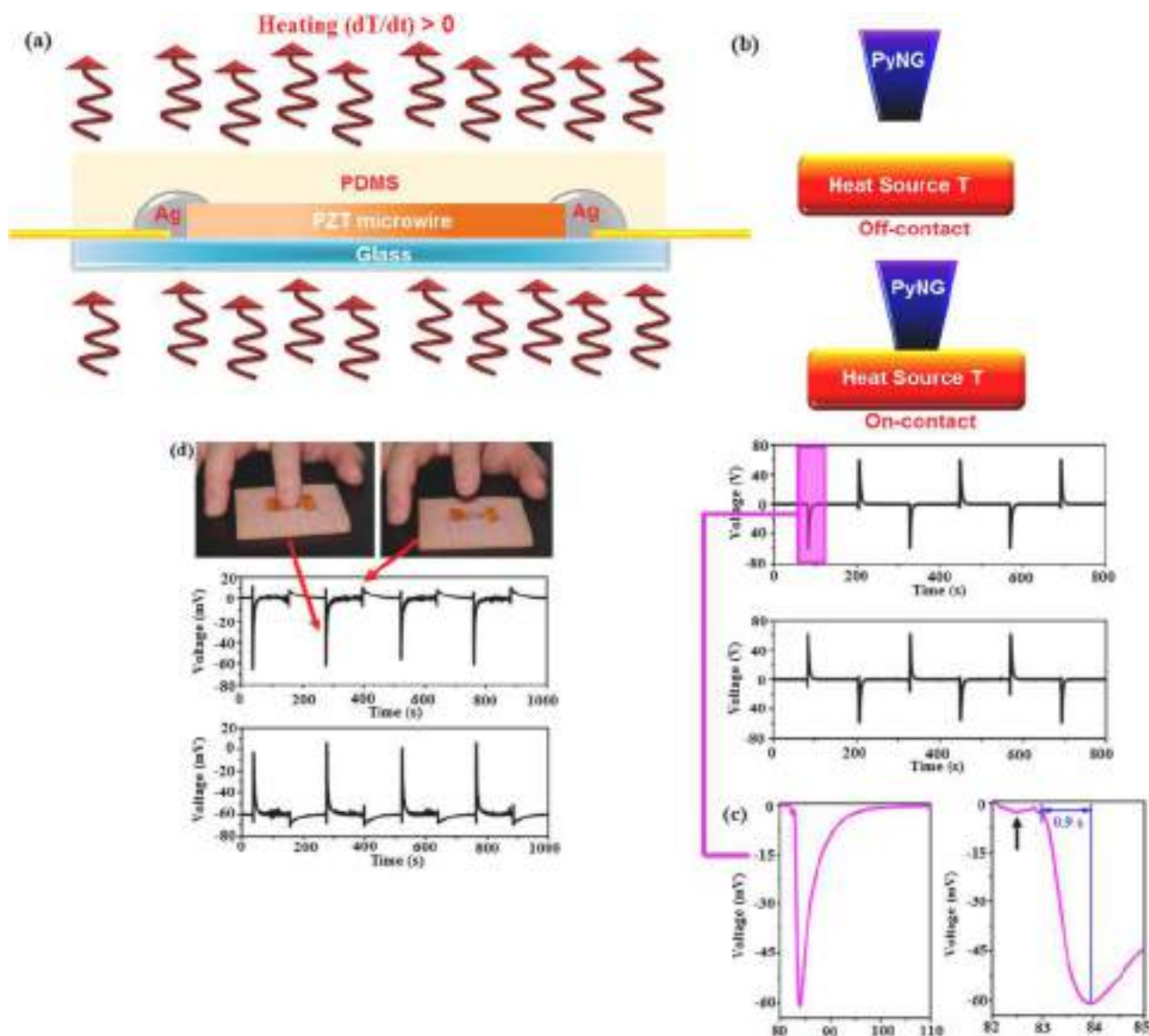


Fig. 12. (a) Schematic diagram showing the structure of PyNG. (b) Schematic diagram of the measurement process of the temperature sensor. (c) Magnified negative output voltage pulse on panel b. (d) V-T curve illustrating four-finger touches to the sensor under forward-back connection [110].

thermal shocks, their use in PyNG is limited [111,112]. However, it is important to develop more durable nanogenerators having higher piezoelectric and pyroelectric coefficients to collect mechanical and thermal vibrations from the environments such as car engines [113, 114]. On the other hand, inorganic ferroelectric oxide films have very high piezoelectric and pyroelectric coefficients and a strong structure against thermal shocks, but their use in energy harvesting applications is limited due to their hardness. Ko et al. [11] developed an inorganic $\text{Pb}(\text{Zr}_{0.52}\text{Ti}_{0.48})\text{O}_3$ (PZT) film-based hybrid piezoelectric-pyroelectric nanogenerator. Fig. 13a shows the schematic illustration of flexible PZT film-based NG. For the enlargement of the PZT film, LaNiO_3 (LNO) sub-electrode with perovskite structure and Ni-Cr metal foil substrate were used. Although flexible PZT film has a perovskite structure, it exhibits lattice vibrations similar to its bulk counterparts (Fig. 13b). The film's ferroelectricity was verified from the hysteresis loop of the applied voltage-dependent electrical polarization, as seen in Fig. 13c. While determining the Curie temperature of the PZT film from Fig. 13d, the film's temperature-dependent dielectric constant (ϵ) is found to be high and has a peak around 400 °C, corresponding to the Curie temperature.

In Fig. 13e, f temperature-dependent piezoelectric (d_{33}) and

pyroelectric coefficients (ρ) are shown. Although piezoelectric and pyroelectric coefficients are temperature dependent, as the temperature increases, the piezoelectric coefficient decreases while the pyroelectric coefficient increases. The piezoelectric coefficient of the flexible PZT film at room temperature is reported as ($d_{33} = 140$ pC/N) and the pyroelectric coefficient as (50 nC/cm² K) [115,116]. In the energy harvesting mechanism of the hybrid NG, the repeated bending/non-bending of the flexible PZT film causes alternating current. On the other hand, thermal cooling causes an increase in the electrical polarization of the PZT film due to reduced thermal fluctuations, whereas the polarization decreases with heating. The successive cooling and heating of the flexible PZT film will also result in alternating current. Thus, when mechanical bending and heating and cooling occur simultaneously, alternating currents coming from PyNGs can be inserted constructively. The car engine's and the radiator's working temperatures are lower than the PZT's Curie temperature; therefore, PZT film-based hybrid NG can be used in the exhaust pipes of cars where hot CO and CO₂ gases are rapidly released into the air. So this study is important in terms of expanding PyNG's potential applications.

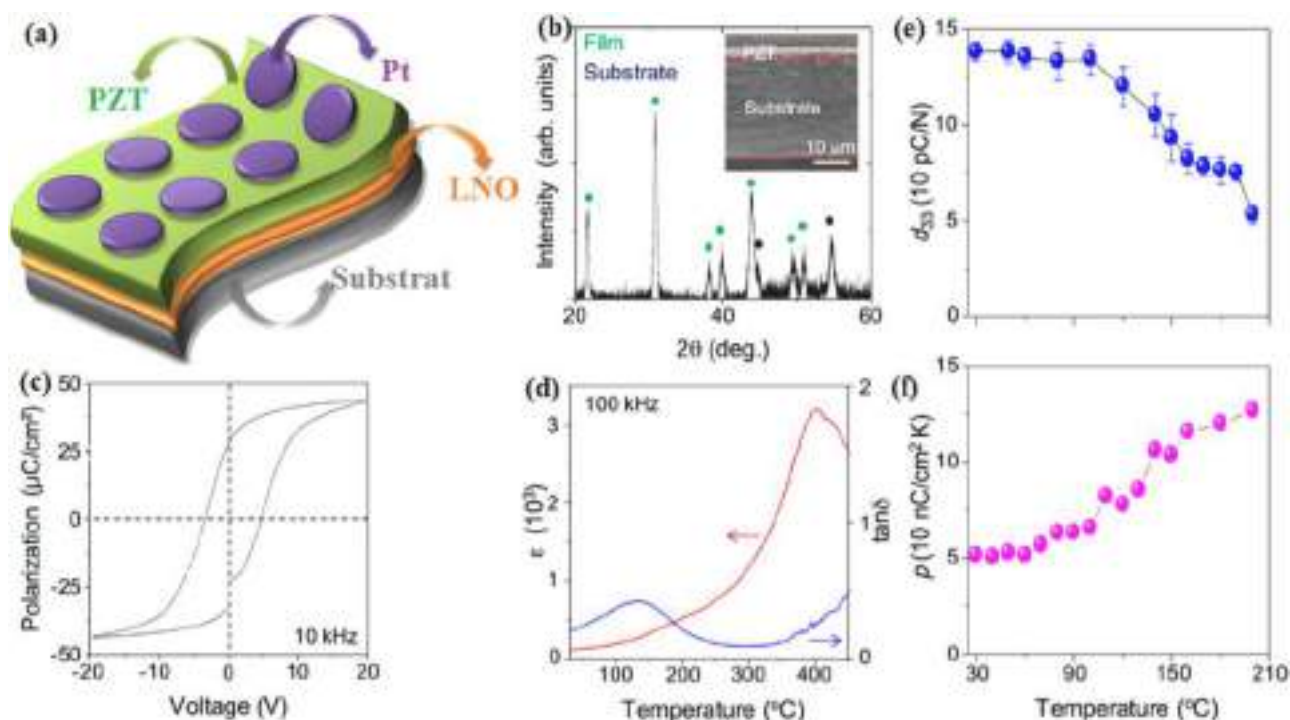


Fig. 13. (a) Schematic illustration of (PZT) film-based hybrid nanogenerator (NG), (b) High-resolution X-ray diffraction pattern of the PZT film (green circles) on the Ni-Cr metal foil substrate (black circles), and (inset) cross-sectional scanning electron microscope (SEM) image. (c) Electrical polarization hysteresis curve measured at 10 kHz, (d) Dielectric constant (e) and dielectric loss ($\tan \delta$) during heating. (e) Temperature dependence of piezoelectric (d_{33}) and (f) pyroelectric (p) coefficients of PZT film [11].

4.3. PVDF based PyNGs

Until 2014, the output voltages and currents obtained from PyNGs, which are based on inorganic pyroelectric materials and pyroelectric cells, were not at the desired level [108]. Later, as the pyroelectric coefficient of organic polyvinylidene fluoride (PVDF) reached up to $\sim 200 \mu\text{C m}^{-2} \text{K}^{-1}$, its use in PyNG has become promising [117–120]. Leng et al. [121] have succeeded in producing PVDF film-based PyNG to collect heat energy from hot/cold geothermal water generated by natural events such as volcano and sunlight and industrial applications such as oil refining, steel, and glass production. The device was put into contact with the hot and cold flow to produce time-dependent temperature changes. After a temperature change of 80°C , the open-circuit voltage was 192 V, the short circuit current was $12 \mu\text{A}$, and the output power density was $14 \mu\text{W}/\text{cm}^2$. Researchers have achieved to illuminate 42 green LEDs or charge a $100 \mu\text{F}$ capacitor up to 3.3 V in 90 s with the produced PyNG.

In Fig. 14a, where the experimental setup is shown, pumps are used to bring cold and hot water to the top. The device, which is moved to the right and left by the oscillator to contact the flows, gives an instant signal when it comes into contact. Besides, together with the output power obtained from PyNG, the photos of the LEDs' reactions to hot and cold flow are shown. Harvesting heat energy from hot water is an important step in developing PyNGs. Fig. 14b shows the output power, current, and voltage of PyNG as a function of load resistance; the output current decreases, and the corresponding open-circuit voltage increases as the load resistance increases. When the temperature rises from 40°C to 80°C , the voltage is observed to be 192.6 V. Besides, as the load resistance increases, the output power first increases and tends to decrease. The maximum output power was found to increase as the hot flow temperature increases; the spontaneous polarization rate also increases under a higher temperature difference, which shows that it generates open-circuit voltage, output current, and output power. Researchers have made important contributions to thermoelectric conversion

technology by efficiently collecting the waste heat from the environment with this study.

As previously reported, flexible and thin PyNGs can be obtained from commercially available ferroelectric polymers such as PVDF and P(VDF-TrFE) because of their high pyroelectric performance [7,9,11,38, 111–116,120–124]. Gao et al. [15] achieved a rapid temperature release mechanism with ambient water vapor and air flows without using an alternating device. Water vapor in the temperature range of about $70\text{--}90^\circ\text{C}$ will condense on the polymeric PyNG surface, and it will increase the temperature of PyNG. The low-velocity airflow passing across PyNG will decrease the temperature with water droplets' evaporation on the surface. In this way, a self-operating temperature oscillation mechanism can be obtained with a low-temperature heat source and wind-like airflow. Fig. 15a shows the PyNG consisting of the hot water vapor and airflow used as an energy source and pyroelectric material. The droplets formed by water vapor on the PyNG surface are used as heat sources for PyNG. Water droplets evaporate with the airflow, absorbing the heat in PyNG and cooling it. The water vapor to be provided by a cup of hot coffee, as in Fig. 15b, will provide the necessary heat to PyNG. PyNG performance has been characterized by measuring peak output voltage, current, and power as a function of loading resistance. As seen in Fig. 15c, the results revealed that the output power first increases and decreases as the load resistance increases.

It has been demonstrated that PVDF based PyNGs achieve higher output current density and power density than P(VDF-TrFE) based ones. For PVDF based PyNG, 145 V open-circuit voltage and $0.12 \mu\text{A}/\text{cm}^2$ short circuit current were achieved. The highest power densities were determined as $1.47 \text{ mW}/\text{cm}^3$ (by volume) and $4.12 \mu\text{W}/\text{cm}^2$ (by area), which is attributed to the high pyroelectric coefficient ($26\text{--}27 \mu\text{C}/\text{m}^2 \text{K}$) of PVDF. Besides, PyNGs based on thinner polymer films exhibit equal or higher performance than thick ones. The alternating current was converted to direct current through the rectifier bridge to give power to electrical devices, and the charge provided was stored in a $2.2 \mu\text{F}$ capacitor (Fig. 15d). With a PVDF-based PyNG and a single hot water

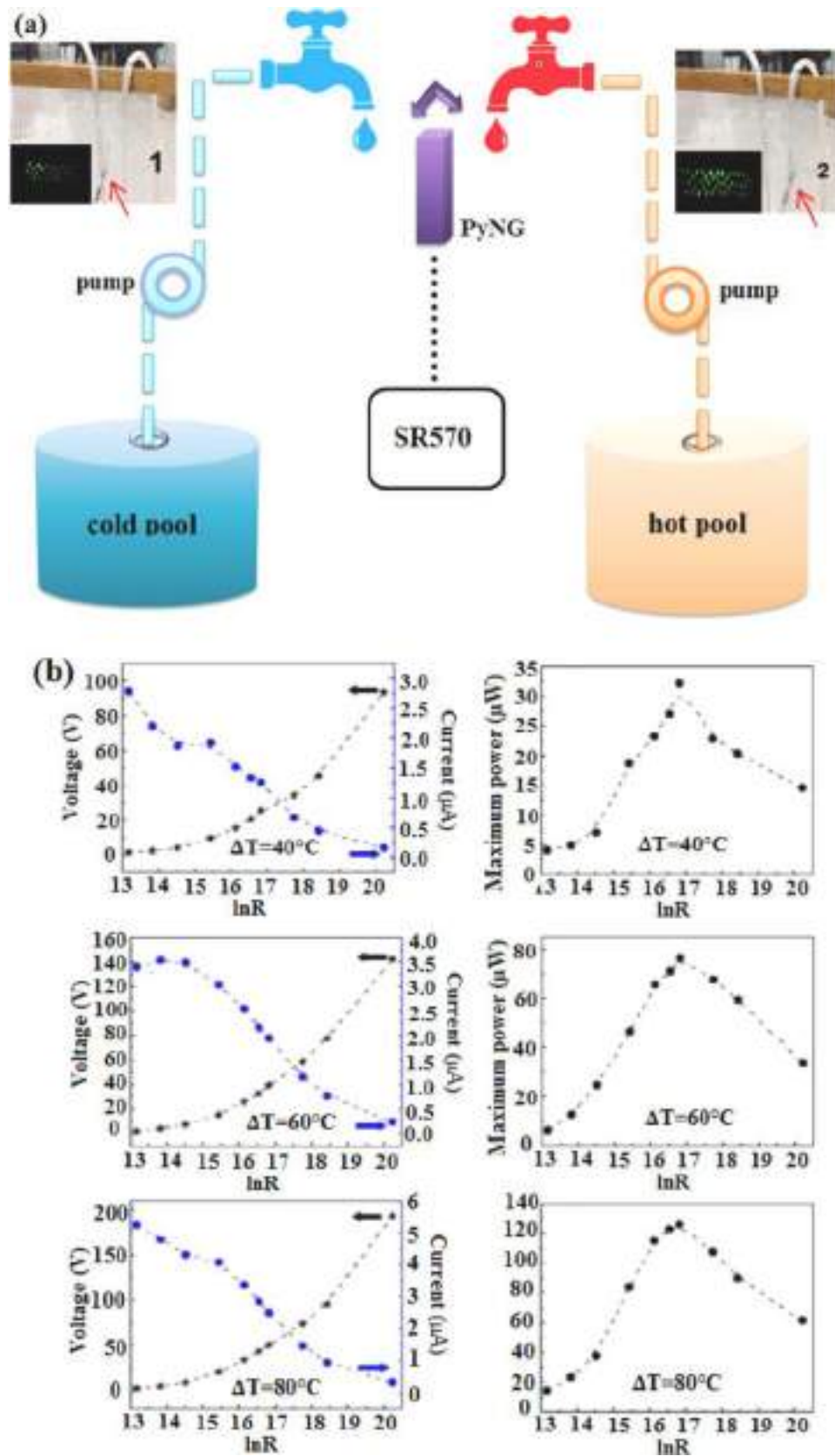


Fig. 14. (a) Experimental setup of PyNG under hot- and cold-water flow. (b) Output current, PEG voltage, and power under 40 °C, 60 °C and 80 °C temperature difference between hot and cold flow [121].

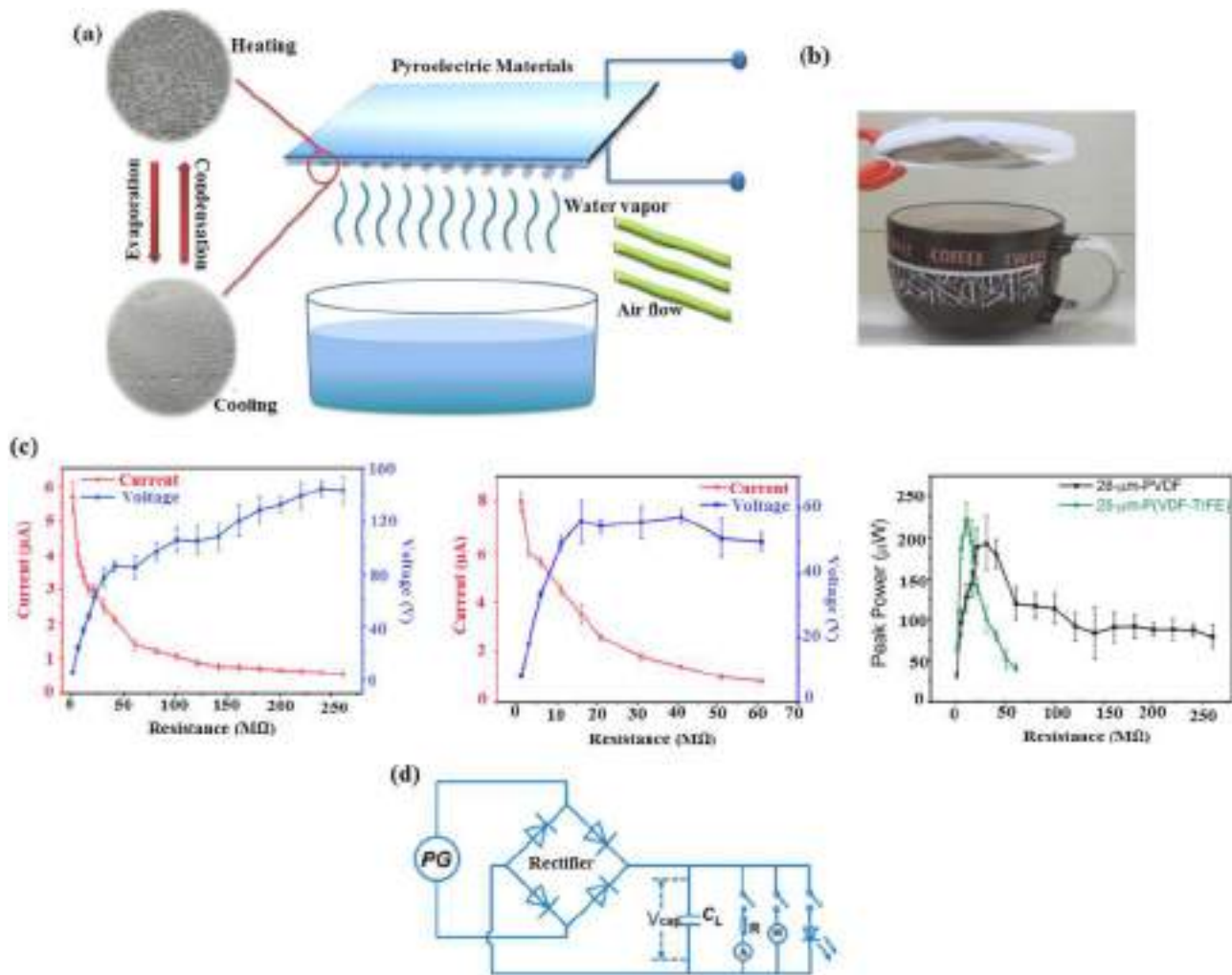


Fig. 15. (a) Schematic illustration of PyNG, (b) The photo of PyNG standing on a cup of hot coffee, (c) Peak output of 28 μm thick PVDF PNG and 25 μm thick P (VDF-TrFE) PNG driven by water vapor, the power of the two PNGs as a function of load resistance, (d) Three-branch equivalent circuit diagram for other studies [15].

source, researchers have achieved performance comparable to the results obtained using hot/cold water [125].

Compared to PENG and TENG, PyNGs do not suffer from mechanical deformation, so they have no reliability problems. On the other hand, the great interest in wearable electronics increases the interest towards self-powered electronics and continues to attract researchers' attention [8,108,126–136]. Especially in winter, due to the high-temperature difference between the human body and the environment, significant temperature fluctuations occur around the mouth during the respiratory process. With a PyNG placed around the mouth, the polarization change created by these temperature fluctuations will generate the potential. This application may be very useful, especially in some countries (such as North China) where one should go outside with a respirator due to air pollution. It has become mandatory to wear a mask almost all over the world in the fight against Covid-19, which has become a pandemic since the past year. Waste heat can be obtained safely by integrating PyNG into breathing devices under these mandatory conditions. Besides, older people's health status and those with serious health problems (such as asthma) can be monitored. Departing for this purpose, Xue et al. [14] produced a PyNG by integrating a PVDF thin film into the N95 respirator. For wearable PyNG, the pyroelectric polymer film covered with electrodes is mounted on the respirator, as shown in Fig. 16a; Al film is preferred as the upper and lower electrode, and PVDF thin film is preferred in the active layer. Especially in winter, the temperature

difference between the human body and the environment can reach 60 °C.

As shown in Fig. 16b, the temperature is recorded during breathing by the PyNG working with the respiration and the temperature sensor fixed on it. High humidity increases the temperature rise of the PVDF but can also prevent the temperature drop. The temperature range on which the pyroelectric effect depends is not significantly affected by humidity. The measurements of output voltage, current, power, and breathing status were performed at 5 °C ambient temperature under different load resistances to evaluate the performance of obtained PyNG. It was found that maximum short circuit current can reach 2.5 μA , and the open-circuit voltage can reach 42 V (Fig. 16c). With increasing load resistance, the current tended to reverse, and the output voltage remained at peaks. The output power reached a maximum of 8.31 μW with 50 $\text{M}\Omega$ load resistance. The results clearly show that sustainable energy harvesting can be achieved by integrating PVDF-based PyNG into the mask.

Zhang et al. produced a flexible generator based on the pyroelectric effect, using PVDF film to collect thermal energy from time-dependent temperature fluctuation [137]. Fig. 17a shows that the pyroelectric generator structure consists of three layers: the upper and lower layers of aluminum (Al) and the PVDF thin film selected as the pyroelectric material. The generator was manufactured in 25 \times 20 mm for ease of operation (Fig. 17b), the size of Al layers was 15 μm , and PVDF film thickness was 120 μm . The flexibility shown in Fig. 17c indicates the

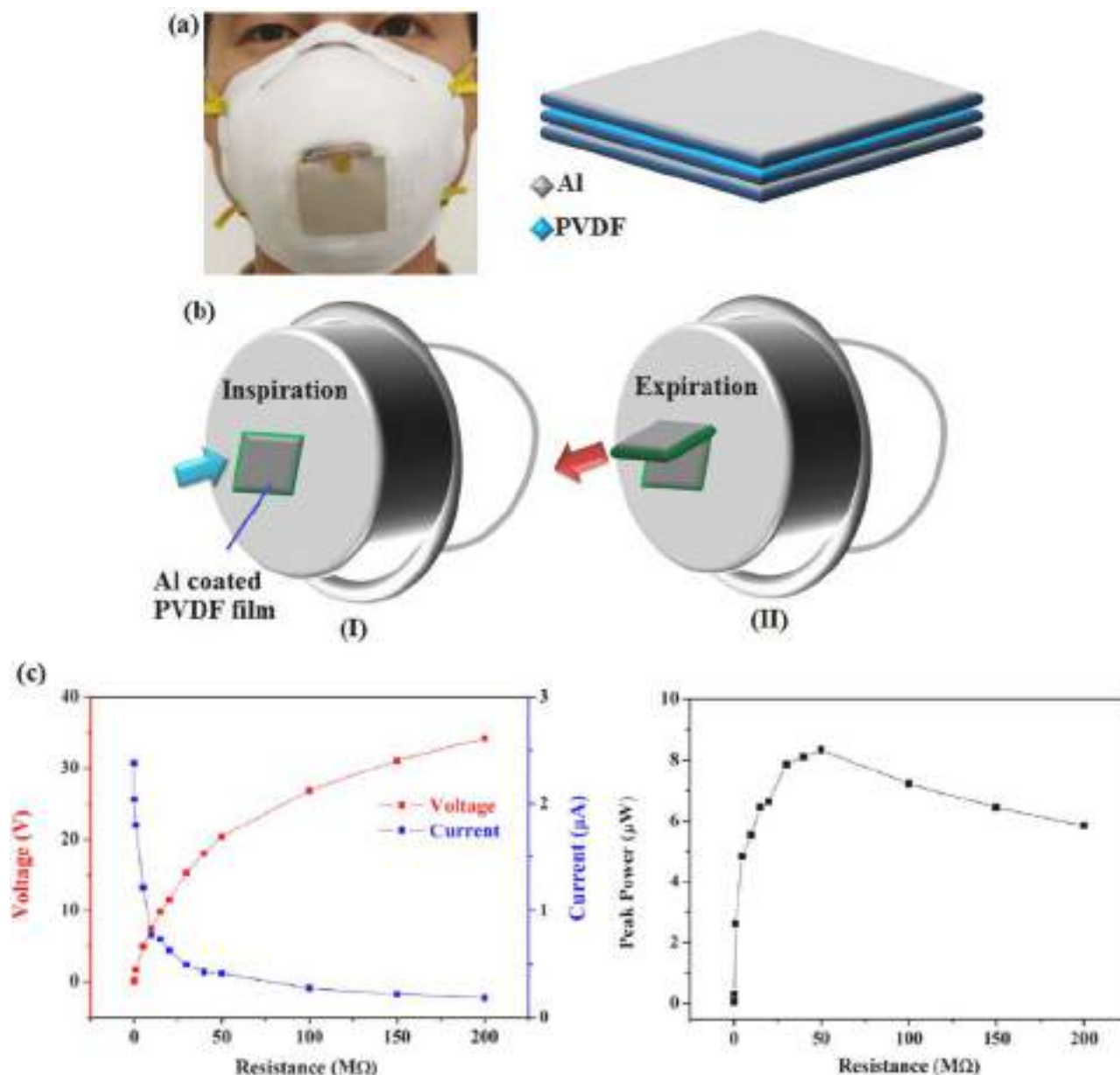


Fig. 16. (a) Photo and diagram of Wearable PyNG. (b) Diagram of a wearable PyNG driven by human breathing (I) Inspiration; (II) Expiration, (c) Peak voltage and current versus load resistance of the pyroelectric nanogenerator (PyNG); peak power of PyNG against load resistance [14].

suitability of the generator for practical applications such as flexible electronics. Moreover, output voltage's dependence on temperature and temperature change is given in Fig. 17d. A clear linear relationship between output voltage temperature and temperature change rate was reported; this relationship will be useful for sensors' practical applications by identifying the real-time temperature and temperature change. The pyroelectric generator can run an LCD and LEDs with 8.2 V open-circuit voltage and 2.2 μW output power at a temperature difference of 50 K; the power can also be stored in the capacitor for later use. Besides, thanks to the linear relationship between output power and temperature change rate, the produced nanogenerator was used as a thermosensor.

In most studies, the produced PENG and PyNG failed to provide uninterrupted power to an electrical device. It will be useful to focus on wind energy, a very good electricity source in this context. The wind nanogenerators developed by some researchers using microturbines will not be useful as they are too large to power microelectronic devices [145–147]. On the other hand, in many studies, PVDF film stands out as

the most preferred piezoelectric material for PENGs used in wind energy harvesting for low power generation. Based on these studies, Raouadi et al. [148] suggested placing the so-called vortex generator in the flow passage to increase the convective heat transfer between the PVDF film and the wind flow [149]. The vortex generator has been used to produce local and continuous turbulence and temperature fluctuation on the PVDF film's surface, exposed to a constant wind flow. Thus, the electrical energy obtained will be uninterrupted and sufficient to provide suitable power to the electronic devices used. Besides, the harvested energy can be stored in the capacitor for high power uses.

PyNG obtained in the study consists of flexible pyroelectric film and vortex generator together with the wind used as an energy source as shown in Fig. 18a. Since the velocity, temperature, and other physical properties will constantly change in every stage of turbulent flow in the system, this will cause continuous irregular fluctuations. Thus, heat conduction proportional to average velocity and average temperature gradients and turbulent stresses resulting from velocity fluctuations heat transfer will provide a continuous pyroelectric flow [150]. In Fig. 18b,

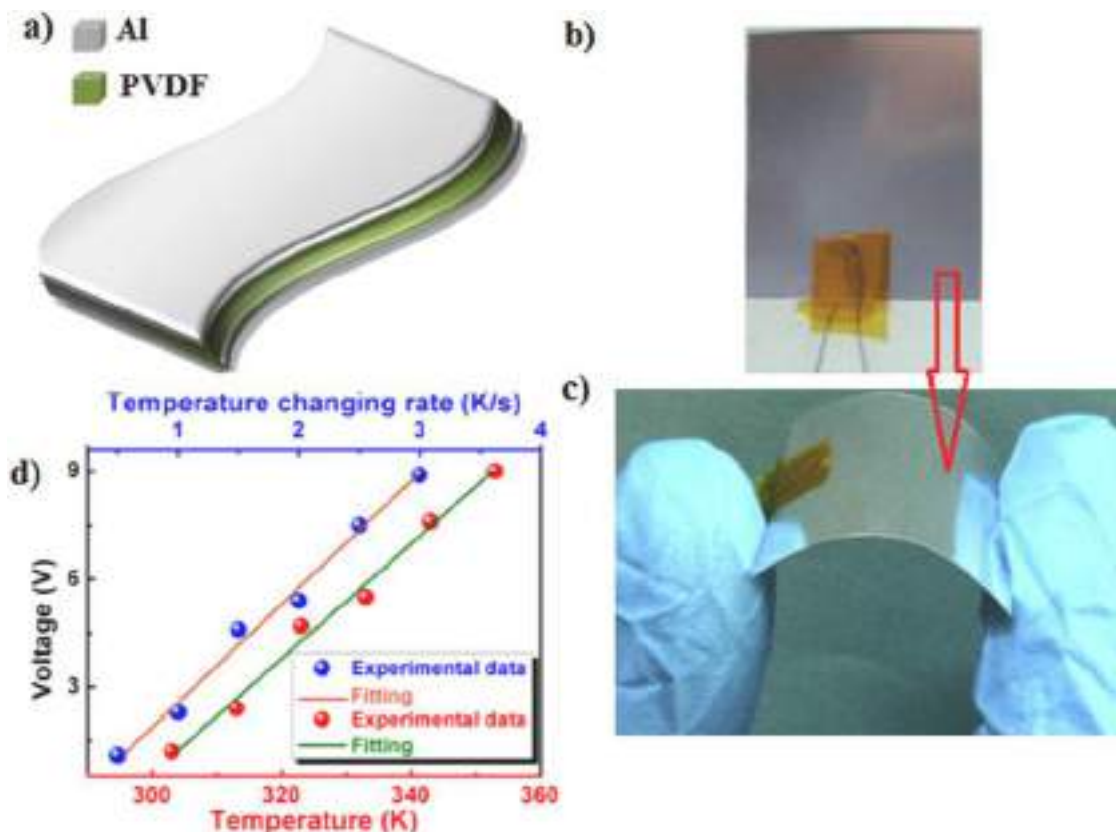


Fig. 17. a) Device structure of the pyroelectric generator, b) Photograph of the constructed pyroelectric generator, c) Image of the bent pyroelectric generator, d) Dependence of the output voltage on the temperature and the temperature changing rate [137].

an oscilloscope and an amplification circuit are used to monitor the PyNG signal. A band-pass filter to amplify current-voltage at the input is built into the amplifier circuit to eliminate electromagnetic noise. The PyNG signal was amplified to be displayed on the PC. The produced PyNG can produce 2.82 W/cm^2 power for 25 m/s wind speed, and this power is expected to increase with increasing wind speed. The results are important for developing cheap and efficient wind-powered PyNG based on flexible PVDF film with strong and uninterrupted energy flow for large-scale electronic applications. On the other hand, much higher output performances can be obtained if PZT film with a greater pyroelectric coefficient than PVDF is used.

4.4. Other types of PyNGs

Studies show that PyNGs' performances are lower than TENGs and PENGs [9,122,123]. For this reason, Lee et al. [124], who were aiming to improve the performance of PyNGs and to expand their usage, produced a stretchable pyroelectric nanogenerator (SPNG) using micropatterned poly (vinylidene fluoride-co-trifluoroethylene) [P(VDF-TrFE)] and micropatterned polydimethylsiloxane (PDMS) to combine piezoelectric and pyroelectric effects. In the study, PDMS, which does not show any piezoelectric or pyroelectric properties, was used as a template applying compression stress to P(VDF-TrFE) with its high thermal expansion. Regarding the schematic illustration in Fig. 19a, the structure is designed by using Piezoelectric and pyroelectric P(VDF-TrFE) [7,12] and PDMS as a template and Ag/Ag nanowires (AgNWs) as electrodes. The pyroelectric potential generated by the exposure of P(VDF-TrFE) to heat drives carriers from the electrodes to the external circuit; the output voltage and output current are measured from the SPNG and the NPNG devices for various temperature change rates ($\sim 0.64 \text{ K} \rightarrow 18.5 \text{ K}$) (Fig. 19b).

The output voltage of the NPNG ranged between $2 \text{ mV} \rightarrow 0.54 \text{ V}$,

whereas the output voltage of the SPNG ranged between $8 \text{ mV} \rightarrow 2.48 \text{ V}$, which is approximately 4–5 times higher than NPNG. The results show that the produced SPNG can be very useful for wearable electronics and e-skin applications with its flexibility and high performance.

Zhang et al. [138] examined the pyroelectric properties of both PZT and PVDF, which stand out with their excellent pyroelectric properties, where PVDF is in the form of film and PZT in the ceramic form. Fig. 20a shows the schematic illustrations of PVDF, a semi-crystalline polymer with a 3-atom primitive cell having CH₂-CH₂ conformation, and PZT with ABO₃ type perovskite structure. Pb²⁺ ions occupy the A positions (corners of the cube), whereas Zr⁴⁺ or Ti⁴⁺ ions occupy the B positions and O²⁻ ions occupy the facial centers [139]. The output currents and Q–V loops of PVDF and PZT based PyNGs were determined under different load resistances to obtain the output power. In Fig. 20b, the total loop load decreases with the increase of Q_C external load resistance; in a short circuit, the transferred load reaches the maximum value (Q_{sc}). Fig. 20c shows the instantaneous power depending on the resistance calculated from the peak current and the output energy per cycle. When PVDF based PyNG was heated from 300 K to 323 K, under 50 GΩ load resistance, maximum power of $0.33 \mu\text{W}$ and output energy of $2.53 \mu\text{J}$ per cycle were obtained. Regarding PZT-based PyNG, when the temperature changed from 300 K to 308 K, maximum power of $8.89 \mu\text{W}$ and output energy of 2.59 mJ were obtained under 1 GΩ load resistance. The research is thought to be useful in estimating the potential value of the electricity generated based on the maximum temperature fluctuation and selecting the appropriate pyroelectric material.

Flexible hybrid nanogenerators produced on piezoelectric and pyroelectric materials, which effectively collect mechanical and thermal energies and convert them into electrical energy, have attracted researchers' attention in recent years. However, the high cost and difficulty of producing these nanogenerators are not suitable for potential applications. The electrospinning method will be a good choice to obtain

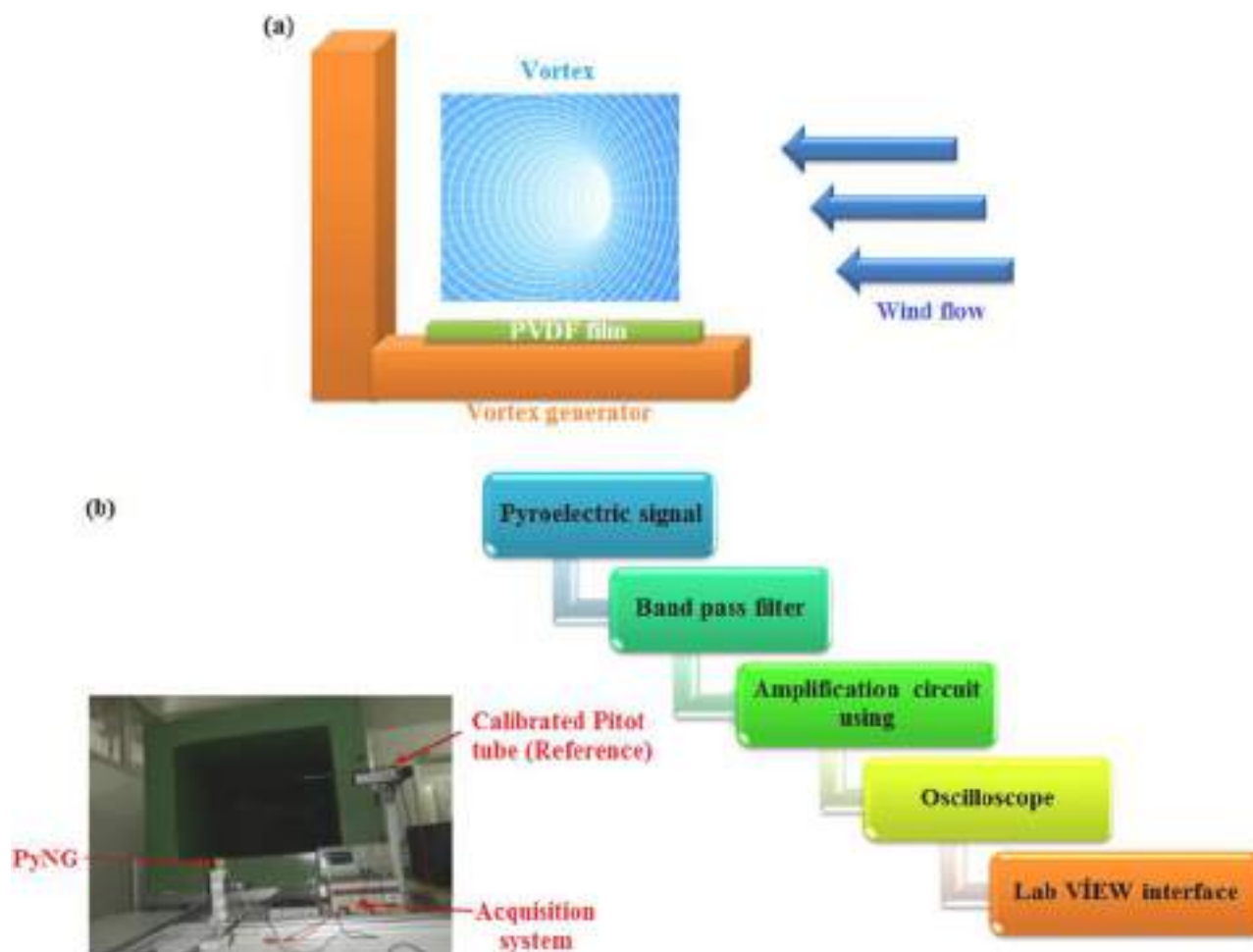


Fig. 18. (a) Mechanism of PyNG, (b) Measurement system of PyNG signal in the open test section of wind tunnel [148].

flexible structures as a simple nanofiber preparation technology. An electrospine is a very suitable way to produce flexible hybrid nanogenerators; PVDF nanofiber membranes (NFMs) are combined with conductive NFMs, without further processing. For this purpose, You et al. [140] used thermoplastic polyurethane (TPU) as substrate, NFM, and electrospun poly(3,4-ethylene dioxathiophene): poly(styrenesulfonate)-polyvinyl pyrrolidone (PEDOT: PSS-PVP) as the upper electrode and TPU NFM-CNT as the lower electrode. A schematic illustration of PyNG is shown in Fig. 21a. It has been reported that a white LED can be illuminated as a result of the electrical output at different frequencies with the mechanical effect applied to PyNG. Besides, piezoelectric and pyroelectric currents were obtained due to simultaneous mechanical and thermal changes (Fig. 21b). The study performed by the researchers shows the potential applications of hybrid piezo-pyroelectric nanogenerators in wearable electronics with the energy harvesting applications from human movements and cold/hot gradients thanks to the flexible structure of PyNG. Fig. 21c shows the output currents measured by mechanical bending at frequencies of 0.25 Hz and 0.5 Hz and endurance test results subjected to bending frequency at 0.5 Hz to confirm the mechanical strength of NG. Moreover, the following values have been reported in Fig. 21d: pyroelectric output current of NG by heating for 3 s and cooling for 5 s; piezoelectric output current at 2.5 Hz frequency; and hybrid piezoelectric/pyroelectric output current while simultaneously heating/cooling NG. Here the total output signal is a combination of piezoelectric and pyroelectric effects.

Sunlight-triggered pyroelectric nanogenerator (S-PyNG) is an energy harvesting method that uses ubiquitous and renewable solar heat as

thermal energy [141]. S-PyNG's low power outputs, which are generally below 5 mW/m^2 , are due to the absence of temperature fluctuations under the sun. The surfaces of these components need to be protected periodically in order to maintain temperature regulation.

For this purpose, Li et al. [142] produced S-PyNG using polyethyleneimine (PEI) reduced graphene oxide (rGO-PEI), which will function as a heat collector from the solar energy, and polarized PVDF film compressed with Ag electrodes to generate electricity (Fig. 22). The crucial step here is to improve the solar thermal properties of GO by reducing it with macromolecular PEI, forming rGO-PEI. The output power of 21.3 mW/m^2 was achieved with the produced S-PyNG under 25 MHz light oscillation frequency; this is approximately 5 times more than previously reported ones. It has been reported that by integrating S-PyNG into a wearable bracelet, electricity can be generated by using hand waving gestures to create temperature fluctuations and by feeding the device directly from sunlight. Researchers attributed the high performance of S-PyNG to the increase in π electrons of rGO-PEI due to the chemical modification of GO with PEI and PVDF as a pyroelectric layer. Using the produced S-PyNG in outdoor sports activities, electrical energy can be obtained from solar energy efficiently.

Zhang et al. produced an integrated, flexible hybrid nanogenerator consisting of a pyroelectric nanogenerator (PyNG), a piezoelectric nanogenerator (PENG), and a triboelectric nanogenerator (TENG) to be used in self-powered cathodic protection (CP) system without using an external power supply [143]. Hybrid NG has been used to produce a self-powered electrochemical corrosion prevention system. The hybrid nanogenerator (NG) shown in Fig. 23a is made of flexible materials; due to pyroelectric and piezoelectric effects' dual characteristics, the upper

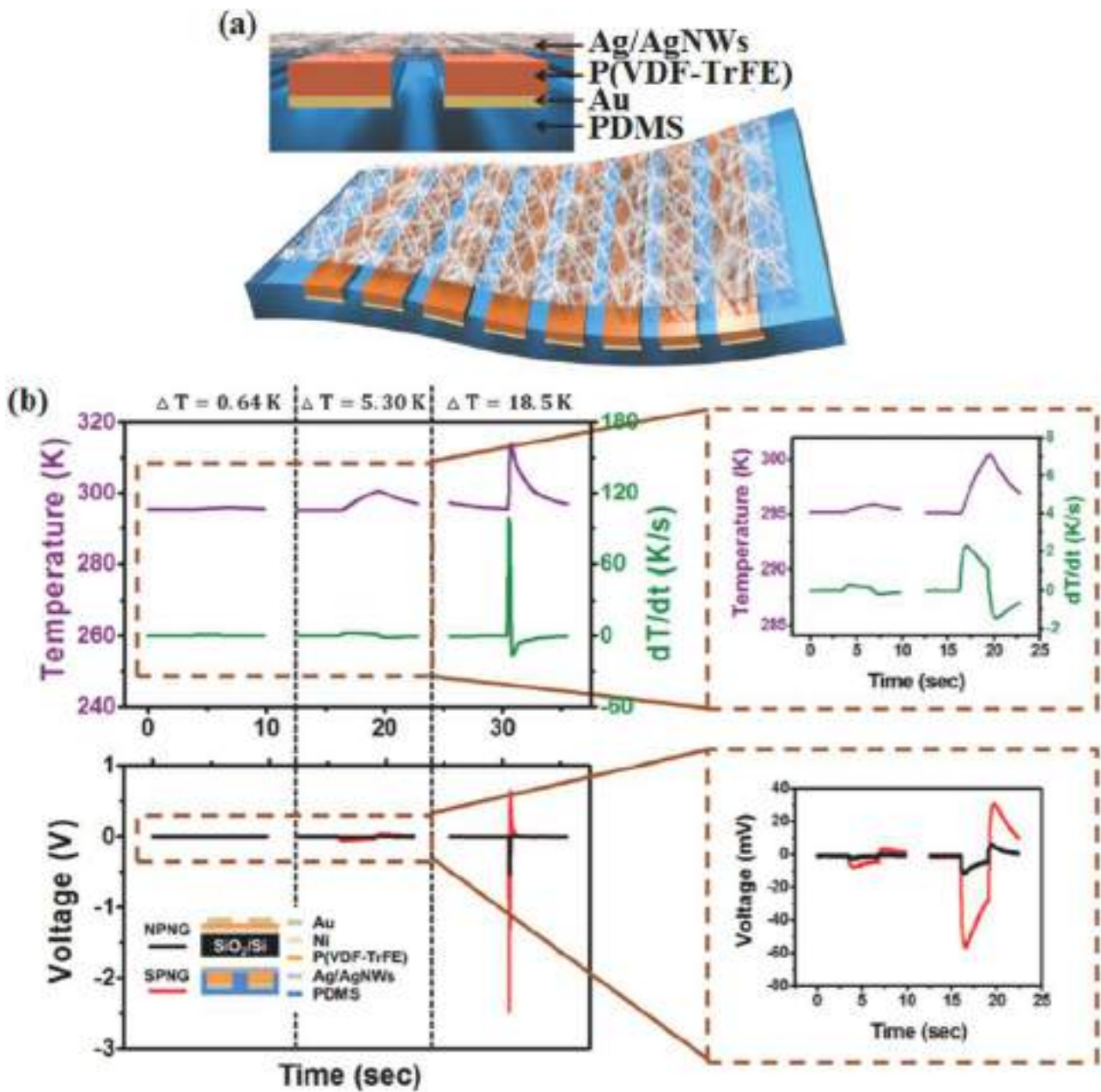


Fig. 19. (a) Schematic illustration of SPNG. (b) Measured output voltages of SPNG and NPNG under differential rates of temperature change [124].

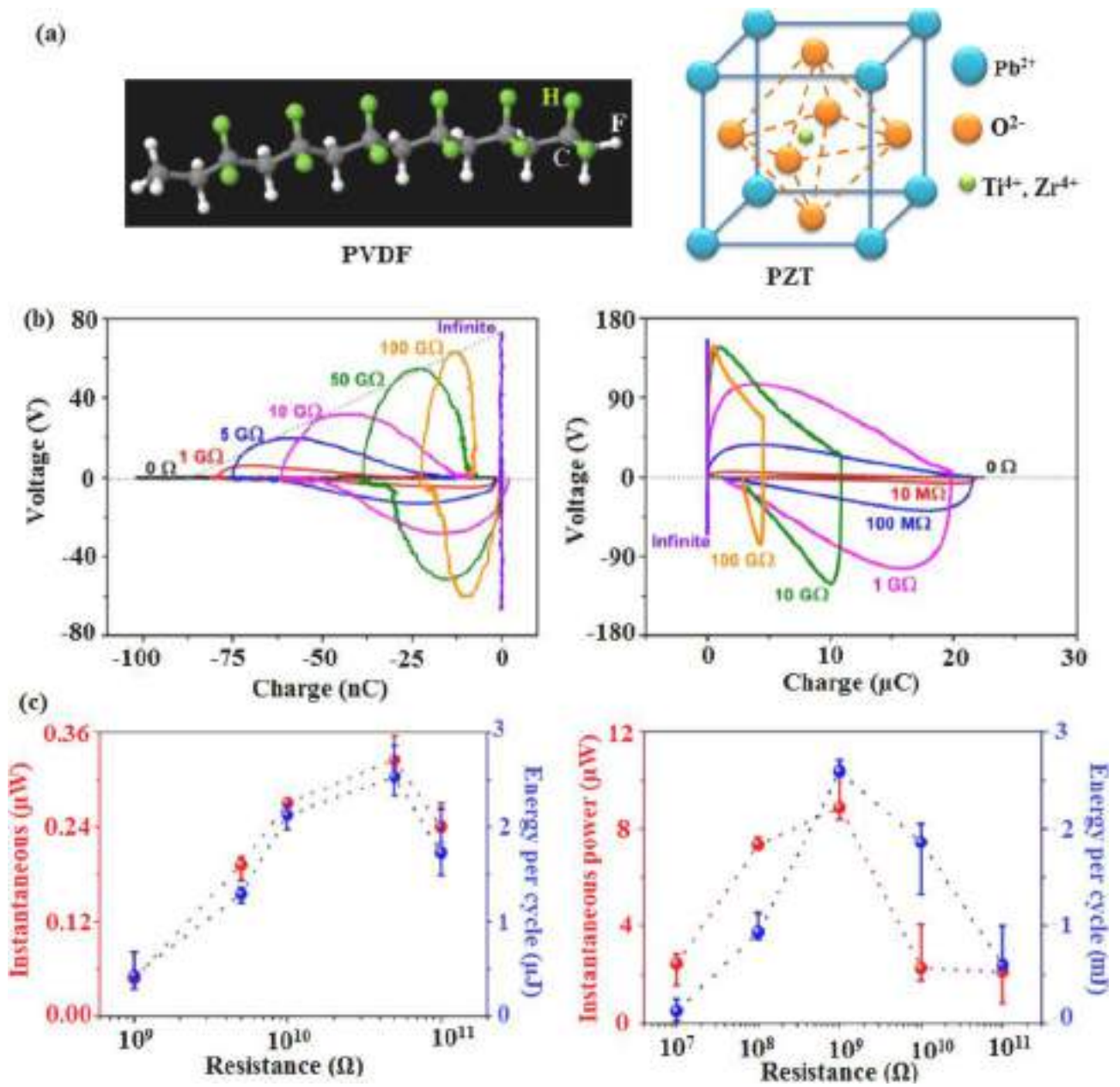


Fig. 20. (a) The 3-atom primitive cell of PVDF and cubic unit cell of PZT, (b) PVDF device and PZT device under various load resistances, (c) Output powers of the PVDF (I) device and the PZT (II) device under various load resistances [138].

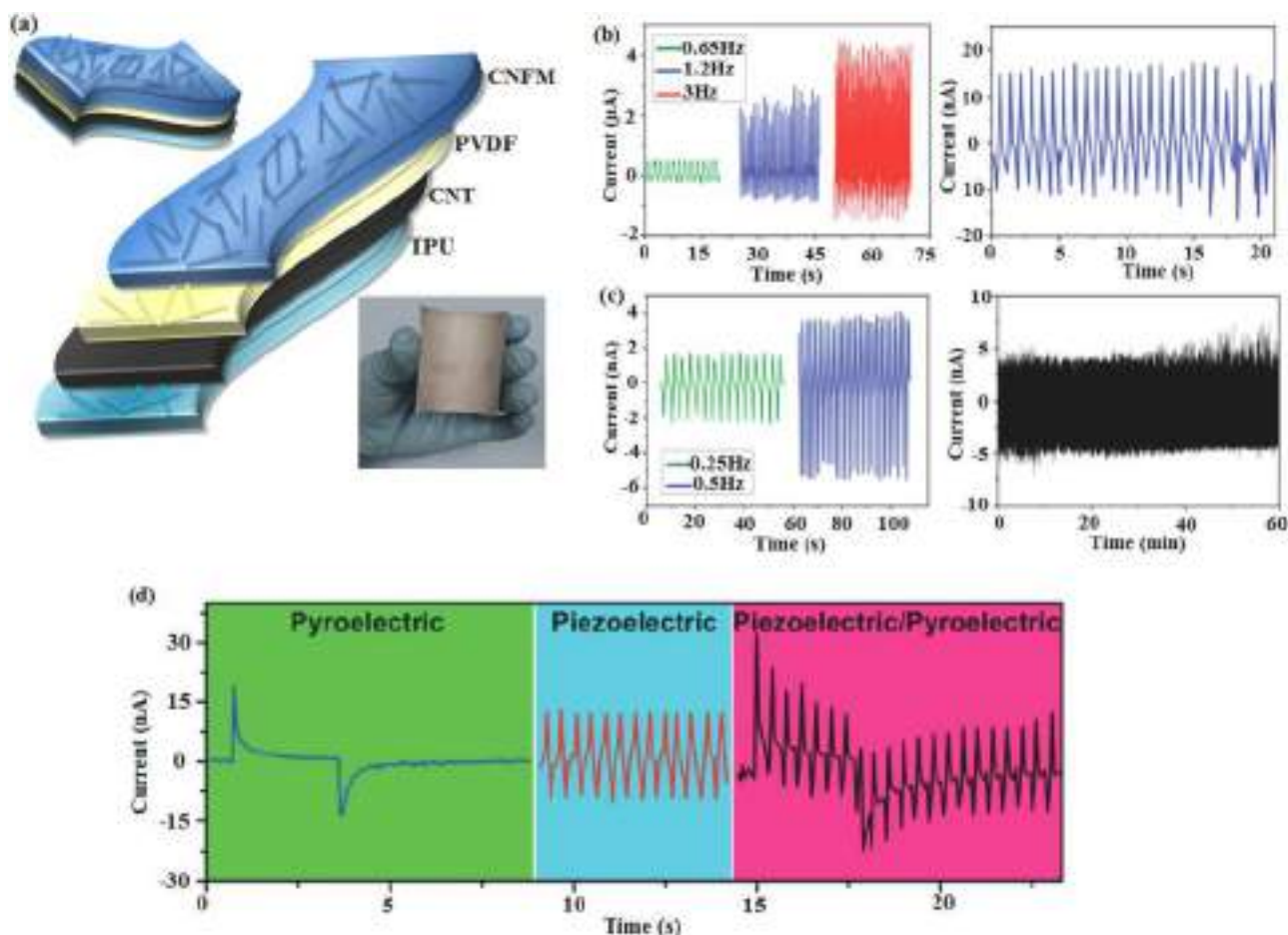


Fig. 21. (a) The nanogenerator consisted of TPU NFM substrate, CNT bottom electrode, PVDF NFM, and CNFM upper electrode; (b) Output current of NG subject to different pulse frequencies; output current of cast PVDF film-based NG under repeated compression pulses at 1.2 Hz; (c) Measured output currents of mechanical bending at 0.25 Hz and 0.5 Hz frequencies and endurance test results of NG subjected to a bending frequency of 0.5 Hz; (d) Pyroelectric output current obtained by heating NG for 3 s and cooling for 5 s. Piezoelectric output current that occurs when NG is affected at a frequency of 2.5 Hz. Hybrid piezoelectric-pyroelectric output current while simultaneously heating/cooling NG [140].

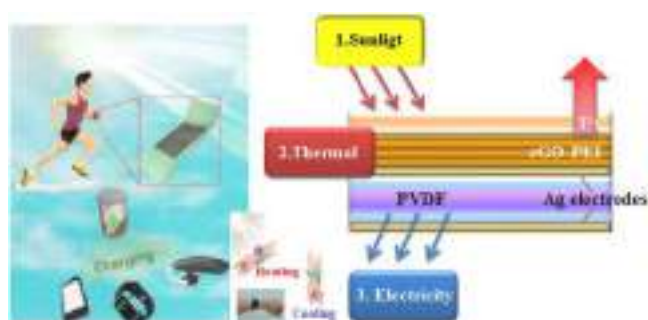


Fig. 22. S-PyNG's application scheme and pyroelectricity generation mechanism as a wearable power generator during outdoor exercises. Heating/cooling is achieved by moving the hand up and down [142].

part is composed of pyroelectric/piezoelectric NG, and the lower one is triboelectric NG. Upper NG was formed by a PVDF film, whose lower and upper surfaces are coated with an Al electrode layer, and triboelectric NG was formed by two Al electrode layers and PTFE film. To obtain a rough surface and a large charge density, thus improving triboelectrification between layers [144], a nanostructure layer was formed on the PTFE film's surface by a typical dry etching using the ICP (inductively coupled plasma) method. The negative voltage/current

pulse was recorded as (3.2 V/0.1 μ A) and positive current/voltage pulse (3.6 V/0.12 μ A) in the forward connection of PVDF film based PyNG. For TENG, an output voltage of 8 V and 0.42 μ A current were reached under forward and backward connection. Fig. 23b shows the schematic diagram of the self-powered electrochemical CP. The CP system powered by hybrid NG is immersed in the electrolyte with a metal cathode and a carbon rod acting as an anode. In Fig. 23c, d, the semi-steady state polarization curves of all samples were recorded after simulated corrosion. The samples' electron transfer resistance with the CP system was much smaller than the samples without CP, and their electron transfer resistance increases as the corrosion increases. As the higher electron transfer resistance corresponds to a larger rust layer, the formation of rust film was observed on the samples' surface without the CP system. The polarization currents decreased with the corrosion time; on the other hand, samples attached to CP supported by hybrid NG had lower polarization potential during corrosion than those without CP. The results show that the CP system powered by the hybrid NG can protect the sample surface from corrosion. The study is important in establishing a CP system with a new approach to clean thermal and mechanical energies in the environment with low cost and high efficiency.

In Fig. 24, there is a summary showing the comparison of studies on PyNG.

In addition to all these, the factors affecting the efficiency of PyNG should also be examined. The factors affecting the efficiency of PyNG can be listed as follows:

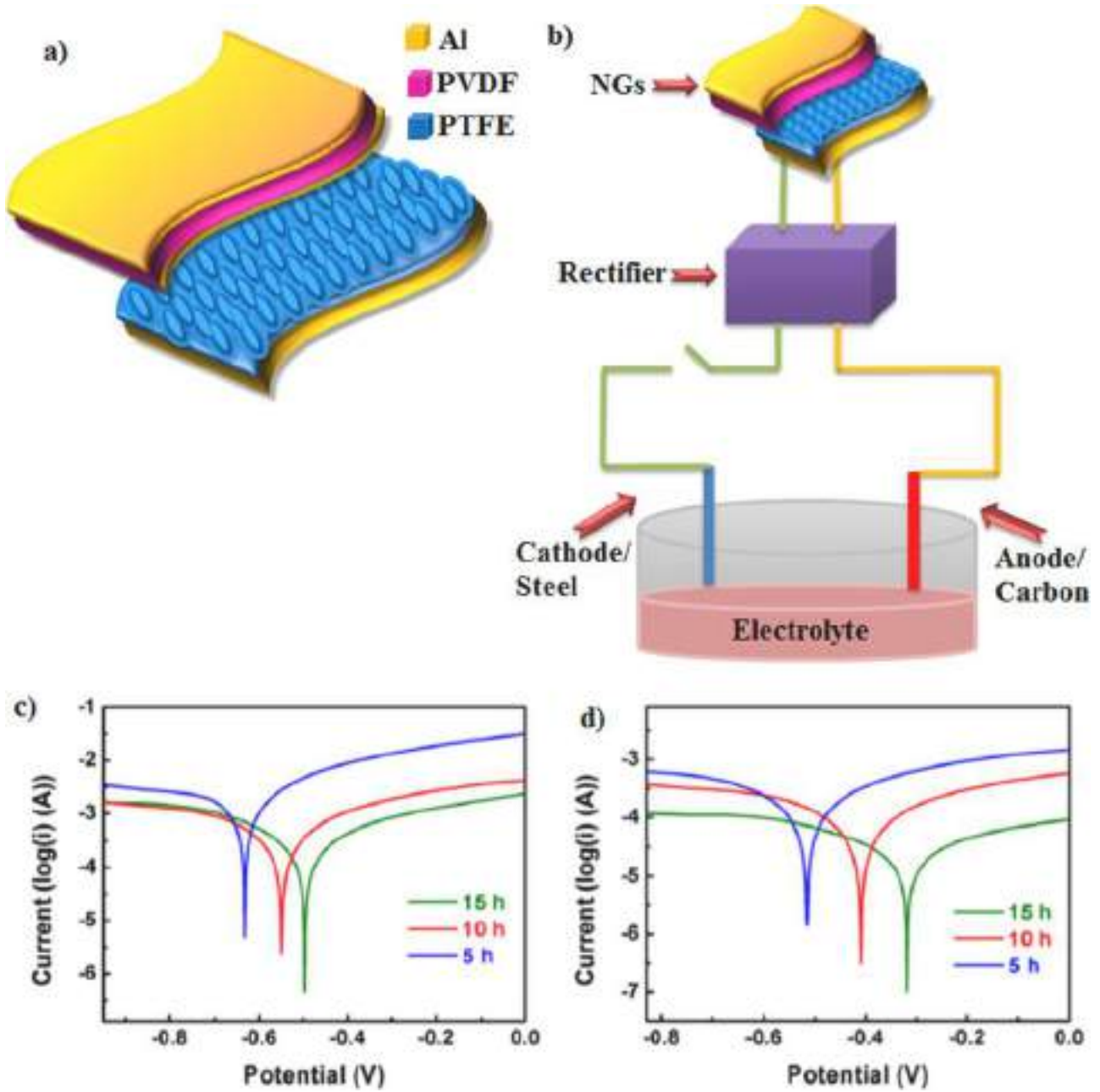


Fig. 23. a) Schematic diagram of the designed flexible hybrid NG, b) Schematic diagram of the self-powered CP system. The following Tafel polarization curves of the carbon steel electrodes after the simulated corrosion c) with and d) without CP system under different durations [143].



Fig. 24. Comparison of studies on PyNGs.

1. Surface area and structure of the electrode
2. Thermal conductivity of the electrode
3. Electrical conductivity of the electrode.

Pyroelectric coefficient P is affected by the factors mentioned above. According to Jolandan et al. [151], it will collect much more electrons on the electrode surface with a large surface area, increasing efficiency. In this context, if the electrode's structure is rough or has a larger surface area, the efficiency is expected to increase. Regarding Eqs. (3) and (4), the temperature gradient is directly proportional to the efficiency of the pyroelectric nanogenerator. Therefore, the thermal conductivity of the electrode becomes important at this point. Electrode conductivity, on the other hand, is of general importance for all electrochemical events. A resistive electrode will lose the electrical energy obtained from the temperature difference due to resistance.

5. Discussion

Unlike thermal energy harvesting, the functioning of PyNGs, which are used to convert waste heat in the environment, is based on temperature gradients. Practical thermal energy harvesting through the Olsen cycle results in the largest energy density. The increase of the energy density of PyNG requires pyroelectric materials to have high dielectric breaking strength; therefore, bulk ceramics and single crystals are disadvantageous due to their low breaking strength. For this reason, the use of thin films and composite materials comes to the fore. Polymer-based PyNGs have a suitable structure for wearable electronics because they are flexible, stretchable, and biocompatible. Ceramic based PyNGs, such as PZT, exhibit higher output power than polymer-based PyNGs with their remarkable high pyroelectric coefficients. Flexibility can be achieved with micropatterned structure, fiber structure, and nanowires. The storage of the generated electrical energy in the energy storage devices such as supercapacitors or batteries may pave the way for another research route in this area. By storing electrical energy converted from waste heat through PyNG and integrating it into flexible

wearable electronics, the daily electrical needs of frequently used devices can be met. The challenges encountered in areas such as the lifespan of PyNGs and the safe use of the devices can be overcome by interdisciplinary research and studies (materials, physics, electronics, etc.). The best way to follow would be to investigate the pyroelectric properties of 2D and 3D structures for researchers because it is not yet concluded whether the efficiency of 2D or 3D ceramic or polymer structures will be higher under thermal effect. Besides, the efficiency of PyNGs is expected to increase significantly by focusing on the subjects, such as doping the substances with high thermal conductivity (such as ZrO_2) to the substrate of lower-upper electrodes. The production of these and similar devices opens the doors of energy harvesting, which does not harm our future environment. One of the best examples is; by integrating PyNGs into masks, which have become an indispensable part of our lives with the Covid-19 pandemic that has affected the whole world, waste heat can be converted into electrical energy easily without any extra effort. It is expected that PyNG, which is worth researching with these aspects, will become widespread soon and become a part of our lives with their usage areas.

Declaration of Competing Interest

The authors declare that they have no known competing financial interests or personal relationships that could have appeared to influence the work reported in this paper.

Data availability

The data of the article is available in public.

References

- [1] V. Ng, L. Kong, W. Que, C. Wang, S. Li, T. Zhang, Pyroelectric materials. *Comprehensive Energy Systems*, 2018, pp. 720–759.

- [2] A.P. Straub, N.Y. Yip, S. Lin, J. Lee, M. Elimelech, Harvesting low-grade heat energy using thermo-osmotic vapour transport through nanoporous membranes, *Nat. Energy* 1 (2016) 16090.
- [3] X.F. Wang, C.F. Tan, K.H. Chan, K. Xu, M. Hong, S.W. Kim, G.W. Ho, Nanophotonic-engineered photothermal harnessing for waste heat management and pyroelectric generation, *ACS Nano* 11 (2017) 10568–10574.
- [4] M. Vaish, M. Sharma, R. Vaish, V.S. Chauhan, Experimental study on waste heat energy harvesting using lead zirconate titanate (PZT-5H) pyroelectric ceramics, *Energy Technol.* 3 (2015) 768–773.
- [5] M.-K. Kim, M.-S. Kim, S. Lee, C. Kim, Y.-J. Kim, Wearable thermoelectric generator for harvesting human body heat energy, *Smart Mater. Struct.* 23 (2014), 105002.
- [6] Y. Yang, K.C. Pradel, Q. Jing, J.M. Wu, F. Zhang, Y. Zhou, Y. Zhang, Z.L. Wang, Thermoelectric nanogenerators based on single Sb-doped ZnO micro/nanobelts, *ACS Nano* 6 (2012) 6984–6989.
- [7] C.R. Bowen, J. Taylor, E. LeBoulbar, D. Zabek, A. Chauhan, R. Vaish, Pyroelectric materials and devices for energy harvesting applications, *Energy Environ. Sci.* 7 (2014) 3836–3856.
- [8] Y. Yang, W. Guo, K.C. Pradel, G. Zhu, Y. Zhou, Y. Zhang, Y. Hu, L. Lin, Z.L. Wang, Pyroelectric nanogenerators for harvesting thermoelectric energy, *Nano Lett.* 12 (2012) 2833–2838.
- [9] Y. Yang, J.H. Jung, B.K. Yun, F. Zhang, K.C. Pradel, W. Guo, Z.L. Wang, Flexible pyroelectric nanogenerators using a composite structure of lead-free KNbO₃ nanowires, *Adv. Mater.* 24 (2012) 5357–5362.
- [10] Y. Zi, L. Lin, J. Wang, S. Wang, J. Chen, X. Fan, P.-K. Yang, F. Yi, Z.L. Wang, Triboelectric–pyroelectric–piezoelectric hybrid cell for high-efficiency energy-harvesting and self-powered sensing, *Adv. Mater.* 27 (2015) 2340–2347.
- [11] Y.J. Ko, D.Y. Kim, S.S. Won, C.W. Ahn, I.W. Kim, A.I. Kingon, S.-H. Kim, J.-H. Ko, J.H. Jung, Flexible Pb(Zr_{0.52}Ti_{0.48})O₃ films for a hybrid piezoelectric-pyroelectric nanogenerator under harsh environments, *ACS Appl. Mater. Interfaces* 8 (2016) 6504–6511.
- [12] J.-H. Lee, K.Y. Lee, M.K. Gupta, T.Y. Kim, D.-Y. Lee, J. Oh, C. Ryu, W.J. Yoo, C.-Y. Kang, S.-J. Yoon, J.-B. Yoo, S.-W. Kim, Highly stretchable piezoelectric-pyroelectric hybrid nanogenerator, *Adv. Mater.* 26 (2014) 765–769.
- [13] T. Park, J. Na, B. Kim, Y. Kim, H. Shin, E. Kim, Photothermally activated pyroelectric polymer films for harvesting of solar heat with a hybrid energy cell structure, *ACS Nano* 9 (2015) 11830–11839.
- [14] H. Xue, Q. Yang, D. Wang, W. Luo, W. Wang, M. Lin, D. Liang, Q. Luo, A wearable pyroelectric nanogenerator and self-powered breathing sensor, *Nano Energy* 38 (2017) 147–154.
- [15] F. Gao, W. Li, X. Wang, X. Fang, M. Ma, A self-sustaining pyroelectric nanogenerator driven by water vapor, *Nano Energy* 22 (2016) 19–26.
- [16] I.M. McKinley, R. Kandilian, L. Pilon, Waste heat energy harvesting using the Olsen cycle on 0:945Pb(Zn_{1/3}Nb_{2/3})O₃-0:055PbTiO₃ single crystals, *Smart Mater. Struct.* 21 (2012), 035015.
- [17] A. Navid, D. Vanderpool, A. Bah, L. Pilon, Towards optimization of a pyroelectric energy converter for harvesting waste heat, *Int. J. Heat Mass Transf.* 53 (2010) 4060–4070.
- [18] H. Ryu, S.W. Kim, Emerging pyroelectric nanogenerators to convert thermal energy into electrical energy, *Small* (2019), 1903469.
- [19] Safa Kasap, *Thermoelectric Effects in Metals: Thermocouples*, Department of Electrical Engineering, University of Saskatchewan, Canada, 2001.
- [20] G. Neeli, D.K. Behara, M.K. Kumar, State of the art review on thermoelectric materials, *Int. J. Sci. Res.* 5 (2016) 1833–1844.
- [21] P.L. Hagelstein, Y. Kucherow, Enhanced figure of merit in thermal to electrical energy conversion using diode structures, *Appl. Phys. Lett.* 81 (2002) 559–561.
- [22] J.C. Joshi, A.L. Dawar, Pyroelectric materials, their properties and applications, *Phys. Status Solidi A Appl. Res.* 70 (1982) 353–369.
- [23] W.L. Zhong, *Physics of Ferroelectricity*, Science Press, Beijing, 1996.
- [24] S.T. Liu, D. Long, Pyroelectric detectors and materials, *Proc. IEEE* 66 (1978) 14–26.
- [25] B. Ertuğ, The overview of the electrical properties of barium titanate, *Am. J. Eng. Res.* 2 (2013) 1.
- [26] S.B. Lang, Pyroelectricity: from ancient curiosity to modern imaging tool, *Phys. Today* 58 (2005) 31.
- [27] M.D. Aggarwal, A.K. Batra, P. Guggilla, M.E. Edwards, B.G. Penn, J.R. Currie, Jr., *Pyroelectric Materials for Uncooled Infrared Detectors: Processing, Properties, and Applications*, 2010. (<https://www2.sti.nasa.gov>).
- [28] S.T. Popescu, A. Petris, V.I. Vlad, Interferometric measurement of the pyroelectric coefficient in lithium niobate, *J. Appl. Phys.* 113 (2013), 043101.
- [29] H. Kawai, The piezoelectricity of poly(vinylidene fluoride), *Jpn. J. Appl. Phys.* 8 (1969) 875.
- [30] J.G. Bergman, J.H. McFee, G.R. Crane, Pyroelectricity and optical second harmonic generation in polyvinylidene fluoride films, *Appl. Phys. Lett.* 18 (1971) 203.
- [31] R.G. Kepler, Piezo electricity, pyroelectricity, and ferroelectricity in organic materials, *Ann. Rev. Phys. Chem.* 29 (1978) 497.
- [32] D.K. Das-Gupta, Pyroelectricity in polymers, *Ferroelectrics* 118 (1991) 165.
- [33] T. Furukawa, Piezoelectricity and pyroelectricity in polymers, *IEEE Trans. Electr. Insul.* 24 (1989) 375.
- [34] H. Meixner, IR-sensor-arrays based on PVDF, *Ferroelectrics* 115 (1991) 279.
- [35] W. Liu, J.S. Ko, W. Zhu, Preparation and properties of multilayer Pb(Zr,Ti)O₃/PbTiO₃ thin films for pyroelectric application, *Thin Solid Films* 371 (2000) 254.
- [36] M.T. Kesim, J. Zhang, S. Trolrier-McKinstry, J.V. Mantese, R.W. Whatmore, S. P. Alpay, Pyroelectric response of lead zirconate titanate thin films on silicon: effect of thermal stresses, *J. Appl. Phys.* 114 (2013), 204101.
- [37] R. Takayama, Y. Tomita, K. Iijima, I. Ueda, Pyroelectric properties and application to infrared sensors of PbTiO₃, PbLaTiO₃ and PbZrTiO₃ ferroelectric thin films, *Ferroelectrics* 118 (1991) 325.
- [38] R.W. Whatmore, Pyroelectric devices and materials, *Rep. Prog. Phys.* 49 (1986) 1335.
- [39] C.S. Dandaneau, T.W. Bodick, R.K. Bordia, F.S. Ohuchi, Thermoelectric properties of reduced polycrystalline Sr_{0.5}Ba_{0.5}Nb₂O₆ fabricated via solution combustion synthesis, *J. Am. Chem. Soc.* 96 (2013) 2230.
- [40] J. Zhang, X. Dong, F. Cao, S. Guo, G. Wang, Enhanced pyroelectric properties of Ca_x(Sr_{0.5}Ba_{0.5})_{1-x}Nb₂O₆ lead-free ceramics, *Appl. Phys. Lett.* 102 (2013), 102908.
- [41] A. Speghini, M. Bettinelli, U. Caldino, M.O. Ramirez, D. Jaque, L.E. Bausa, J. Garcia Sole, Phase transition in Sr_xBa_{1-x}Nb₂O₆ ferroelectric crystals probed by Raman spectroscopy, *J. Phys. D Appl. Phys.* 39 (2006) 4930.
- [42] X. Wu, J. Xu, W. Jin, Thermal properties of lead germanate single crystals grown by the vertical Bridgman method, *J. Cryst. Growth* 282 (2005) 160.
- [43] S.B. Lang, S.A.M. Tofail, A.A. Gandhi, M. Gregor, C. Wolf-Brandstetter, J. Kost, S. Bauer, M. Krause, Pyroelectric, piezoelectric, and photoeffects in hydroxyapatite thin films on silicon, *Appl. Phys. Lett.* 98 (2011), 123703.
- [44] B. Ploss, Pyroelectric and nonlinear dielectric properties of copolymers of PVDF-TrFE, in: H.S. Nalwa (Ed.), *Handbook of Low and High Dielectric Constant Materials and Their Applications*, Academic Press, 1999.
- [45] S.B. Lang, D.K. Das-Gupta, Pyroelectricity: fundamentals and applications, in: H. S. Nalwa (Ed.), *Handbook of Advanced Electronic and Photonic Materials and Devices*, Vol. 4, Academic Press, San Diego, CA, 2001.
- [46] M. Dietze, J. Krause, C.-H. Solterbeck, M. Es-Souni, Thick film polymer-ceramic composites for pyroelectric applications, *J. Appl. Phys.* 101 (2007), 054113.
- [47] M. Dietze, M. Es-Souni, Structural and functional properties of screen-printed PZT–PVDF–TrFE composites, *Sens. Actuators A* 143 (2008) 329.
- [48] C.-G. Wu, G.-Q. Cai, W.-B. Luo, Q.-X. Peng, X.-Y. Sun, W.-L. Zhang, Enhanced pyroelectric properties of PZT/PVDF-TrFE composites using calcined PZT ceramic powders, *J. Adv. Dielectr.* 3 (2013), 1350004.
- [49] S.B. Lang, D.K. Das-Gupta, Pyroelectricity: fundamentals and applications, in: H. S. Nalwa (Ed.), *Handbook of Advanced Electronic and Photonic Materials and Devices*, 4, Academic Press, 2001, pp. 1–54.
- [50] G. Sebald, E. Lefevre, D. Guyomar, Pyroelectric energy conversion: optimization principles, *IEEE Trans. Ultrason. Ferroelectr. Freq. Control* 55 (2008) 538–551.
- [51] R.B. Olsen, D.A. Bruno, J.M. Briscoe, Pyroelectric conversion cycle of vinylidene fluoride trifluoroethylene copolymer, *J. Appl. Phys.* 57 (1985) 5036–5042.
- [52] M. Ikura, Conversion of low-grade heat to electricity using pyroelectric copolymer, *Ferroelectrics* 267 (2002) 403–408.
- [53] L. Kouchachvili, M. Ikura, Improving the efficiency of pyroelectric conversion, *Int. J. Energy Res.* 32 (2008) 328–335.
- [54] L. Kouchachvili, M. Ikura, Pyroelectric conversion – effects of P(VDF-TrFE) preconditioning on power conversion, *J. Electrostat.* 65 (2007) 182–188.
- [55] V. Sencadas, S. Lanceros-Mendez, J.F. Mano, Characterization of poled and non-poled b-PVDF films using thermal analysis techniques, *Thermochim. Acta* 424 (2004) 201–207.
- [56] B.J. Chu, X. Zhou, K.L. Ren, et al., A dielectric polymer with high electric energy density and fast discharge speed, *Science* 313 (2006) 334–336.
- [57] R.B. Olsen, J.M. Briscoe, D.A. Bruno, W.F. Butler, A pyroelectric energy converter which employs regeneration, *Ferroelectrics* 38 (1981) 975–978.
- [58] R.B. Olsen, Ferroelectric conversion of heat to electrical energy – a demonstration, *J. Energy* 6 (1982) 91–95.
- [59] R.B. Olsen, D.D. Brown, High efficiency direct conversion of heat to electrical energy related pyroelectric measurements, *Ferroelectrics* 40 (1982) 17–27.
- [60] R.B. Olsen, D.A. Bruno, J.M. Briscoe, J. Dullea, Cascaded pyroelectric energy converter, *Ferroelectrics* 59 (1984) 4709–4719.
- [61] R.B. Olsen, D.A. Bruno, J.M. Briscoe, Pyroelectric conversion cycles, *J. Appl. Phys.* 58 (1985) 4709–4716.
- [62] H. Nguyen, A. Navid, L. Pilon, Pyroelectric energy converter using co-polymer P(VDF-TrFE) and Olsen cycle for waste heat energy harvesting, *Appl. Therm. Eng.* 30 (2010) 2127–2137.
- [63] J.C. Maxwell, *Philos. Mag. J. Sci., Fourth series, London, Edinburgh and Dublin*, 2009, pp. 161–175.
- [64] Z.L. Wang, On Maxwell's displacement current for energy and sensors: the origin of nanogenerators, *Mater. Today* 20 (2017) 74–82.
- [65] E.T. Keve, K.L. Bye, A.D. Annis, P.W. Whippes, Structural inhibition of ferroelectric switching in triglycine sulfate. 1. Additives, *Ferroelectrics* 3 (1971) 39–48.
- [66] A.S. Balla, C.S. Fang, L.E. Cross, Pyroelectric properties of alanine and deuterium substituted TGSP and TGSAS single-crystals, *Mater. Lett.* 3 (1985) 475–477.
- [67] A.S. Balla, C.S. Fang, Y. Xi, L.E. Cross, Pyroelectric properties of the alanine and arsenic-doped triblycine sulfate single-crystals, *Appl. Phys. Lett.* 43 (1983) 932–934.
- [68] P. Felix, P. Gamot, P. Lacheau, Y. Raverdy, Pyroelectric, dielectric and thermal-properties of TGS, DTGS and TGFB, *Ferroelectrics* 17 (1978) 543–551.
- [69] H. Yamazaki, J. Ohwaki, T. Yamada, T. Kitayama, Temperature-dependence of the pyroelectric response of vinylidene fluoride trifluoroethylene co-polymer and the effect of its poling conditions, *Appl. Phys. Lett.* 39 (1981) 772–773.
- [70] K.T. Chung, B.A. Newman, J.I. Scheinbeim, K.D. Pae, The pressure and temperature-dependence of piezoelectric and pyroelectric response of poled unoriented phase-I poly(vinylidene fluoride), *J. Appl. Phys.* 53 (1982) 6557–6562.
- [71] E. Fukada, T. Furukawa, Piezoelectricity and ferroelectricity in polyvinylidene fluoride, *Ultrasonics* 19 (1981) 31–39.

- [72] S.T. Liu, R.B. Maciulek, Rare-earth-modified Sr_{0.5}Ba_{0.5}Nb₂O₆ ferroelectric crystals and their applications as infrared detectors, *J. Electron. Mater.* 4 (1975) 91–100.
- [73] S.A. Fadnavis, A.G. Katpatal, Nd³⁺ doped lead gadmanate-a good candidate for pyroelectric detector, *Ferroelectrics* 211 (1998) 79–87.
- [74] J.R. Ghulghule, A.G. Katpatal, Pyroelectric behaviour of pure and lanthanum-doped lead germanate single crystal, *J. Phys. Chem. Solids* 60 (1999) 425–428.
- [75] A.V. Wazalwar, A.G. Katpatal, Structural and pyroelectric properties of Nd³⁺+K⁺-doped ferroelectric lead germanate single crystals, *Mater. Lett.* 55 (2002) 221–229.
- [76] X.F. Yue, S. Mendricks, T. Nikolajsen, et al., Transient enhancement of photorefractive gratings in lead germanate by homogeneous pyroelectric fields, *J. Opt. Soc. Am. B Opt. Phys.* 16 (1999) 389–394.
- [77] D. Luff, R. Lane, K.R. Brown, H.J. Marshall, Ferroelectric ceramics with high pyroelectric properties, *Trans. J. Br. Ceram. Soc.* 73 (1974) 251–264.
- [78] R.W. Whatmore, A.J. Bell, Pyroelectric ceramics in the lead zirconate-lead titanate-lead iron niobate system, *Ferroelectrics* 35 (1981) 155–160.
- [79] R.W. Whatmore, High-performance, conducting pyroelectric ceramics, *Ferroelectrics* 49 (1983) 201–210.
- [80] H. Takeuchi, S. Jyomura, Y. Ito, K. Nagatsuma, Rare-earth substituted piezoelectric PbTiO₃ ceramics for acoustic-wave applications, *Ferroelectrics* 51 (1983) 71–80.
- [81] R.W. Whatmore, P.C. Osbond, N.M. Shorrocks, Ferroelectric materials for thermal IR detectors, *Ferroelectrics* 76 (1987) 351–367.
- [82] P.C. Osbond, R.W. Whatmore, Improvements to pyroelectric ceramics via strontium doping of the lead zirconate-lead iron niobate-lead titanate system, *Ferroelectrics* 118 (1991) 93–101.
- [83] X. Liu, D. Wu, Z. Chen, et al., Ferroelectric, dielectric and pyroelectric properties of Sr and Sn codoped BCZT lead free ceramics, *Adv. Appl. Ceram.* 114 (2015) 436–441.
- [84] R.B. Olsen, D. Evans, Pyroelectric energy conversion: hysteresis loss and temperature sensitivity of a ferroelectric material, *J. Appl. Phys.* 54 (1983) 5941.
- [85] Z.L. Wang, G. Zhu, Y. Yang, S. Wang, C. Pan, Progress in nanogenerators for portable electronics, *Mater. Today* 15 (2012) 532–543.
- [86] D. Ehre, E. Lavert, M. Lahav, I. Lubomirsky, Water freezes differently on positively and negatively charged surfaces of pyroelectric materials, *Science* 327 (2010) 672.
- [87] J.D. Zook, S.T. Liu, Pyroelectric effects in thin film, *J. Appl. Phys.* 49 (1978) 4604.
- [88] C.P. Ye, T. Tamagawa, D.L. Polla, Experimental studies on primary and secondary pyroelectric effects in Pb(Zr_xTi_{1-x})O₃, PbTiO₃, and ZnO thin films, *J. Appl. Phys.* 70 (1991) 5538–5543.
- [89] C. Richard, D. Guyomar, D. Audigier, G. Ching, Semi passive damping using continuous switching of a piezoelectric device I, in: *Proceedings of the SPIE Smart Structures and Materials Conference, Passive Damping and Isolation, San Diego, 3672, 1999*, p. 104.
- [90] C. Richard, D. Guyomar, D. Audigier, H. Bassaler, Enhanced semi passive damping using continuous switching of a piezoelectric device on an inductor, in: *Proceedings of the SPIE Smart Structures and Materials Conference, Passive Damping and Isolation, 3989, 2000*, p. 288.
- [91] A. Badel, D. Guyomar, E. Lefeuvre, C. Richard, Efficiency enhancement of a piezoelectric energy harvesting device in pulsed operation by synchronous charge inversion, *J. Intell. Mater. Syst. Struct.* 16 (2005) 889–901.
- [92] D. Guyomar, G. Sebald, E. Lefeuvre, A. Khodayari, Toward heat energy harvesting using pyroelectric material, *J. Intell. Mater. Syst. Struct.* 20 (2009) 265–271.
- [93] S. Kim, Y.T. Lim, E.G. Soltész, A.M. De Grand, J. Lee, A. Nakayama, J.A. Parker, T. Mihajljević, R.G. Laurence, D.M. Dor, L.H. Cohn, M.G. Mounji, G. Bawendi, L. H. Cohn, Near-infrared fluorescent type II quantum dots for sentinel lymph node mapping, *Nat. Biotechnol.* 22 (2004) 93–97.
- [94] C.C. Chen, Y.P. Lin, C.W. Wang, H.C. Tzeng, C.H. Wu, Y.C. Chen, C.P. Chen, L. C. Chen, Y.C. Wu, DNA-gold nanorod conjugates for remote control of localized gene expression by near infrared irradiation, *J. Am. Chem. Soc.* 128 (2006) 3709–3715.
- [95] T. Rauch, M. Böberl, S.F. Tedde, J. Fürst, M.V. Kovalenko, G. Hesser, U. Lemmer, W. Heiss, O. Hayden, Near-infrared imaging with quantum-dot-sensitized organic photodiodes, *Nat. Photonics* 3 (2009) 332–336.
- [96] R. Saran, R.J. Curry, Lead sulphide nanocrystal photodetector technologies, *Nat. Photonics* 10 (2016) 81–92.
- [97] L. Wang, J. Jie, Z. Shao, Q. Zhang, X. Zhang, Y. Wang, Z. Sun, S.T. Lee, MoS₂/Si heterojunction with vertically standing layered structure for ultrafast, high-detectivity, self-driven visible-near infrared photodetectors, *Adv. Funct. Mater.* 25 (2015) 2910–2919.
- [98] F.H.L. Koppens, T. Mueller, P. Avouris, A.C. Ferrari, M.S. Vitiello, M. Polini, Photodetectors based on graphene, other two dimensional materials and hybrid systems, *Nat. Nanotechnol.* 9 (2014) 780–793.
- [99] L. Dou, Y.M. Yang, J. You, Z. Hong, W.H. Chang, G. Li, Y. Yang, Solution-processed hybrid perovskite photodetectors with high detectivity, *Nat. Commun.* 5 (2014) 5404.
- [100] B.R. Sutherland, A.K. Johnston, A.H. Ip, J. Xu, V. Adinolfi, P. Kanjanaboons, E. H. Sargent, Sensitive, fast, and stable perovskite photodetectors exploiting interface engineering, *ACS Photonics* 2 (2015) 1117–1123.
- [101] J.C. Maxwell, The theory of molecular vortices applied to magnetic phenomena, *Philos. Mag. J. Sci., Fourth series, London*, p. 161.
- [102] Z.L. Wang, On Maxwell's displacement current for energy and sensors: the origin of nanogenerators, *Mater. Today* 20 (2017) 74–82.
- [103] J.D. Jackson, *Electrodynamics*, Wiley-VCH Verlag GmbH & Co., KGaA, 1975.
- [104] X. Wang, Y. Dai, R. Liu, X. He, S. Li, Z.L. Wang, Light-triggered pyroelectric nanogenerator based on a pn-junction for self-powered near-infrared photosensing, *ACS Nano* 11 (2017) 8339–8345.
- [105] S. Xu, Y. Qin, C. Xu, Y. Wei, R. Yang, Z.L. Wang, Self-powered nanowire devices, *Nat. Nanotechnol.* 5 (2010) 366–373.
- [106] J. Zhu, C.-M. Hsu, Z. Yu, S. Fan, Y. Cui, Nanodome solar cells with efficient light management and self-cleaning, *Nano Lett.* 10 (2010) 1979–1984.
- [107] M. Lee, J. Bae, J. Lee, C.S. Lee, S. Hong, Z.L. Wang, Self-powered environmental sensor system driven by nanogenerators, *Energy Environ. Sci.* 4 (2011) 3359–3363.
- [108] Y. Yang, S. Wang, Y. Zhang, Z.L. Wang, Pyroelectric nanogenerators for driving wireless sensors, *Nano Lett.* 12 (2012) 6408–6413.
- [109] I.S. Grant, W.R. Phillips, *Electromagnetism*. Manchester Physics, 2nd ed., John Wiley & Sons, New York, 2008.
- [110] Y. Yang, Y. Zhou, J.M. Wu, Z.L. Wang, Single Micro/Nanowire Pyroelectric Nanogenerators as Self-Powered Temperature Sensors, 6, 2012, pp. 8456–8461.
- [111] PVDF Properties and Uses, Precision Acoustics, Ltd., Dorset, 2013. (<http://www.acoustics.co.uk/product/students-datasheet/>).
- [112] R.W. Whatmore, Pyroelectric devices and materials, *Rep. Prog. Phys.* 49 (1986) 1335–1386.
- [113] C.R. Bowen, H.A. Kim, P.M. Weaver, S. Dunn, Piezoelectric and ferroelectric materials and structures for energy harvesting applications, *Energy Environ. Sci.* 7 (2014) 25–44.
- [114] V. Nguyen, R. Zhu, R. Yang, Environmental effects on nanogenerators, *Nano Energy* 14 (2015) 49–61.
- [115] S. Trolier-McKinstry, P. Muralt, Thin film piezoelectrics for MEMS, *J. Electroceram.* 12 (2004) 7–17.
- [116] B. Xiao, V. Avrutin, H. Liu, Ü. Özgür, H. Morkoc, C. Lu, Large pyroelectric effect in undoped epitaxial Pb(Zr,Ti)O₃ thin films on SrTiO₃ substrates, *Appl. Phys. Lett.* 93 (2008), 052913.
- [117] J.G. Bergman, J.H. McFee Jr., G.R. Crane, Pyroelectricity and optical second harmonic generation in polyvinylidene fluoride films, *Appl. Phys. Lett.* 18 (1971) 203–205.
- [118] R.L. Peterson, G.W. Day, P.M. Gruzensky, R.J. Phelan, Analysis of response of pyroelectric optical detectors, *J. Appl. Phys.* 45 (1974) 3296–3303.
- [119] J.H. McFee, J.G. Bergman, G.R. Crane, Pyroelectric and nonlinear optical properties of poled polyvinylidene fluoride films, *Ferroelectrics* 3 (1972) 305–313.
- [120] X. Li, S.-G. Lu, X.-Z. Chen, H. Gu, X.-S. Qian, Q.M. Zhang, Pyroelectric and electrocaloric materials, *J. Mater. Chem. C* 1 (2013) 23.
- [121] Q. Leng, L. Chen, H. Guo, J. Liu, G. Liu, C. Hu, Y. Xi, Harvesting heat energy from hot/cold water by using pyroelectric generator, *J. Mater. Chem. A* (2014) 1–3.
- [122] K.Y. Lee, J. Chun, J.-H. Lee, K.N. Kim, N.-R. Kang, J.-Y. Kim, M.H. Kim, K.-S. Shin, M.K. Gupta, J.M. Baik, S.-W. Kim, Hydrophobic sponge structure-based triboelectric nanogenerator, *Adv. Mater.* 29 (2014) 5037.
- [123] K.Y. Lee, D. Kim, J.-H. Lee, T.Y. Kim, M.K. Gupta, S.-W. Kim, Unidirectional high-power generation via stress-induced dipole alignment from ZnSnO₃ nanocubes/polymer hybrid piezoelectric nanogenerator, *Adv. Funct. Mater.* 24 (2014) 37.
- [124] J.H. Lee, H. Ryu, T.Y. Kim, S.S. Kwak, H.J. Yoon, T.H. Kim, W. Seung, S.W. Kim, Thermally induced strain-coupled highly stretchable and sensitive pyroelectric nanogenerators, *Adv. Energy Mater.* 5 (2015), 1500704.
- [125] Q. Leng, L. Chen, H.Y. Guo, J.L. Liu, G.L. Liu, C.G. Hu, Y. Xi, Harvesting heat energy from hot/cold water with a pyroelectric generator, *J. Mater. Chem. A* 2 (2014) 11940–11947.
- [126] J.C. Maxwell, The theory of molecular vortices applied to magnetic phenomena, *Philos. Mag. J. Sci., Fourth series, London*, p. 161.
- [127] Z.L. Wang, On Maxwell's displacement current for energy and sensors: the origin of nanogenerators, *Mater. Today* 20 (2017) 74–82.
- [128] J.D. Jackson, *Electrodynamics*, Wiley-VCH Verlag GmbH & Co., KGaA, 1975.
- [129] X. Wang, Y. Dai, R. Liu, X. He, S. Li, Z.L. Wang, Light-triggered pyroelectric nanogenerator based on a pn-junction for self-powered near-infrared photosensing, *ACS Nano* 11 (2017) 8339–8345.
- [130] K.N. Kim, J. Chun, J.W. Kim, K.Y. Lee, J.-U. Park, S.-W. Kim, Z.L. Wang, J. M. Baik, Highly stretchable 2D fabrics for wearable triboelectric nanogenerator under harsh environments, *ACS Nano* 9 (2015) 6394–6400.
- [131] J. Wang, S. Li, F. Yi, Y. Zi, J. Lin, X. Wang, Y. Xu, Z.L. Wang, Sustainably powering wearable electronics solely by biomechanical energy, *Nat. Commun.* 7 (2016) 12744.
- [132] W. Wu, S. Bai, M. Yuan, Y. Qin, Z.L. Wang, T. Jing, Lead zirconate titanate nanowire textile nanogenerator for wearable energy-harvesting and self-powered devices, *ACS Nano* 6 (2012) 6231–6235.
- [133] X. Pu, L. Li, M. Liu, C. Jiang, C. Du, Z. Zhao, W. Hu, Z.L. Wang, Wearable selfcharging power textile based on flexible yarn supercapacitors and fabric nanogenerators, *Adv. Mater.* 28 (2016) 98–105.
- [134] M. Lee, C.-Y. Chen, S. Wang, S.N. Cha, Y.J. Park, J.M. Kim, L.-J. Chou, Z.L. Wang, A hybrid piezoelectric structure for wearable nanogenerators, *Adv. Mater.* 24 (2012) 1759–1764.
- [135] S. Li, J. Wang, W. Peng, L. Lin, Y. Zi, S. Wang, G. Zhang, Z.L. Wang, Sustainable energy source for wearable electronics based on multilayer elastomeric triboelectric nanogenerators, *Adv. Energy Mater.* (2017), <https://doi.org/10.1002/aenm.201602832> (In press).
- [136] J. Wang, X. Li, Y. Zi, S. Wang, Z. Li, L. Zheng, F. Yi, S. Li, Z.L. Wang, A flexible fiber-based supercapacitor-triboelectric-nanogenerator power system for wearable electronics, *Adv. Mater.* 27 (2015) 4830–4836.

- [137] H. Zhang, Y. Xie, X. Li, Z. Huang, S. Zhang, Y. Su, B. Wu, L. He, W. Yang, Y. Lin, Flexible pyroelectric generators for scavenging ambient thermal energy and as self-powered thermosensors, *Energy* 101 (2016) 202–210.
- [138] K. Zhang, Y. Wang, Z.L. Wang, Y. Yang, Standard and figure-of-merit for quantifying the performance of pyroelectric nanogenerators, *Nano Energy* 55 (2019) 534–540.
- [139] N. Izyumskaya, Y.I. Alivov, S.J. Cho, H. Morkoç, H. Lee, Y.S. Kang, Processing, structure, properties, and applications of PZT thin films, *Crit. Rev. Solid State* 32 (2007) 111–202.
- [140] M.H. You, X.X. Wang, X. Yan, J. Zhang, W.Z. Song, M. Yu, Z.Y. Fan, S. Ramakrishna, Y.Z. Long, A self-powered flexible hybrid piezoelectric–pyroelectric nanogenerator based on non-woven nanofiber membranes, *J. Mater. Chem. A* 6 (2018) 3500.
- [141] T. Zhao, W. Jiang, H. Liu, D. Niu, X. Li, W. Liu, X. Li, B. Chen, Y. Shi, L. Yin, An infrared-driven flexible pyroelectric generator for non-contact energy harvester, *Nanoscale* 8 (2016) 8111–8117.
- [142] H. Li, C.S.L. Koh, Y.H. Lee, Y. Zhang, G.C. Phan-Quang, C. Zhu, Z. Liu, Z. Chen, H. Y.F. Sim, C.L. Lay, Q. An, X.Y. Ling, A wearable solar-thermal-pyroelectric harvester: achieving high power output using modified rGO-PEI and polarized PVDF, *Nano Energy* 73 (2020), 104723.
- [143] H. Zhang, S. Zhang, G. Yao, Z. Huang, Y. Xie, Y. Su, W. Yang, C. Zheng, Y. Lin, Simultaneously harvesting thermal and mechanical energies based on flexible hybrid nanogenerator for self-powered cathodic protection, *ACS Appl. Mater. Interfaces* 7 (2015) 28142–28147.
- [144] S.H. Wang, L. Lin, Z.L. Wang, Nanoscale triboelectric-effect-enabled energy conversion for sustainably powering portable electronics, *Nano Lett.* 12 (2012) 6339–6346.
- [145] C. Park, P.H. Chou, Ambimax: autonomous energy harvesting platform for multi-supply wireless sensor nodes, in: *Proceedings of the 3rd Annual IEEE Communications Society on Sensor and Ad Hoc Communications and Networks, SECON'06*, IEEE, Reston, 1, 2006, pp. 168–177.
- [146] F.K. Shaikh, S. Zeadally, Energy harvesting in wireless sensor networks: a comprehensive review, *Renew. Sustain. Energy Rev.* 55 (2016) 1041–1054.
- [147] D. Carli, D. Brunelli, D. Bertozzi, L. Benini, A high-efficiency wind-flow energy harvester using micro turbine, in: *Proceedings of the IEEE International Symposium on Power Electronics Electrical Drives Automation and Motion (SPEEDAM)*, Pisa, 2010, pp. 778–783.
- [148] M.H. Raouadi, O. Touayar, Harvesting wind energy with pyroelectric nanogenerator PNG using the vortex generator mechanism, *Sens. Actuators A* 273 (2018) 42–48.
- [149] T. Alam, R.P. Saini, J.S. Saini, Use of turbulators for heat transfer augmentation in an air duct a review, *Renew. Energy* 62 (2014) 689–715.
- [150] B.S. Petukhov. Heat Transfer and Friction in Turbulent Pipe Flow With Variable Physical Properties, High Temperature Institute, Academy of Science of the USSR, Moscow, USSR, 1970.
- [151] D. Lingam, A.R. Parikh, J. Huang, A. Jain, M. Minary-Jolandan, Nano/microscale pyroelectric energy harvesting: challenges and opportunities, *Int. J. Smart Nano Mater.* 4 (4) (2013) 229–245.



PHYTOCHEMICAL ANALYSIS AND ANTIBACTERIAL ACTIVITIES OF FRANKINCENSE OF *BOSWELLIA SERRATA*

Fatimah I. Sultan

Technical Agricultural College, Plant Production Techniques Dept. Northern Technical University, Mosul, Iraq.

Abstract

This research was interested in studying the anti-bacterial activity by the natural products separated from the crude frankincense resin of *Boswellia serrata*, as a number of fatty acids have been separated (Myristate, Palmatic, Oleic, Linolic, Arachidate, Arachidatenate and Lignocerate) were separated by the GLC device from chloroformic extract. The following phenolic compounds were also separated in their free form Kaempferol, Quercetine, Epigene, Gallic acid, Catechin by HPLC device from methanol extract. Four different concentrations of separated active compounds were prepared (100, 75, 50, 25 mg/ml) and then tested their anti-bacterial efficacy for two types of bacteria that gram positive *Bacillus subtilis*, *Streptococcus pneumoniae* and a one type of gram negative *Proteus vulgaris*. The inhibition zoon was measured in comparison with the ciprofloxacin antibiotic as positive control and at a concentration (5µg/ml). The test results showed a different inhibitory efficacy of the phenols and fatty acids separated from the plant against the bacteria used in the study and by using the Disc Diffusion Method and the result Show that for phenols had a higher inhibitory effect than the fatty acids against the bacteria used and compared with the standard antibiotic.

Key words: *Boswellia serrata*, Natural Products, GLC and HPLC analysis, Antibacterial Activity, Ciprofloxacin.

Introduction

Medicinal plants contain active compounds that are natural products of the metabolism process within the plant and are of medical importance for treating many diseases that affect humans, especially infections caused by bacterial infections. (Dalirsani, *et al.*, 2011 and Al-Dulayymi, 2014). Plant antimicrobials are an important factor in eliminating pathogenic bacterial infections (Gibbons, 2008). Many researchers stressed the need to support the chemical treatment system with active substances separated from plants to treat diseases (Archana and Abraham, 2011). Researchers continued their efforts to interest in separating and diagnosing active compounds from medicinal plants and studying their antibacterial activities (Stavri, *et al.*, 2007; Mahalingam, *et al.*, 2011 and Ismail, *et al.*, 2014). Frankincense resin is extracted from the *Boswellia serrata* tree scattered in the Arabian Peninsula, northern Somalia, Ethiopia and Iraq and is used as an incense due to its sweet aroma (Banno, 2006).

Frankincense resin is extracted from the tree by making a wound or an incision in its bark that appears

***Author for correspondence** : E-mail : drfatimah@ntu.edu.iq

like milk or resin and which dries out and appears in a brown olibanum (Ismail, *et al.*, 2014). *Boswellia serrata* tree gum and resin extract is used to treat many bacterial and fungal infections (Weckesser, 2007). It is also used to treat cancerous diseases, as many studies have proven its effectiveness against human leukemia (Ernst, 2008 and Mohammed Aman, *et al.*, 2010).

Frankincense resin is used in the treatment of many diseases as it strengthens the heart and brain and treats forgetfulness and blood diarrhea as it treats arthritis and other infections due to its work to regulate the production of immune cytokines and also contains cortisone inhibiting inflammation, which does not have side effects such as that caused by the industrial cortisone (Banno, 2006; Langmead, 2006 and Chevrier, 2005).

Several research studies have confirmed that the *Boswellia serrata* tree resin contains fatty acids, especially what has been separated in this current study, Such as Myristate, Palmatic, Oleic, Linolic, Arachidate, Arachidatenate, and Lignocerate. It was diagnosed with GLC-MAS device and which has proven its anti-bacterial effectiveness (Ahmed, *et al.*, 2015 and Yuan, *et al.*, 2006). And also demonstrated that *Boswellia serrata*

tree resin contains phenolic compounds such as Thujene, Camphene, β -Pinene, Myrcene, Limonene, M-cymene and cis-verbenol and that has proven its effective antibacterial and this was confirmed by researchers (Ayub, *et al.*, 2018).

Materials and Methods

The Preparation of Plant Extracts Using Continuous Soxhlet Apparatus

Using the Soxhlet system, the chloroform and methanol extract were prepared and extracted according to the boiling point of each solvent as 100g of frankincense resin was weighed and placed in the device at a rate of 20 hours extraction until the solvent became colorless and then the second solvent was applied in the same way and then concentrated extracted with a rotary evaporator at 45°C. Samples are then kept in the refrigerator in dark conditions until use (Harbone, 1984 and Al-Dulayymi, 2014).

Saponification

In the saponification process, the fatty acids are separated and in basic media (Arthur, 1972), as 5g of chloroform extract to frankincense resin was added and 50 ml of KOH was added and left for 90 min by refluxed and at a temperature not exceeding 100°C. After cooling, add distilled water by 50ml and then separate the solution aqueous about fat from non-adhesion by adding 25ml ether by suppurating funnel. Then we took the extract that contains the fatty acids and added concentrated sulfuric acid to reach PH = 2. Then we get the free fatty acids with the ethereal, The product is then esterified from fatty acids to decrease the polarity and increase its volatility in the GLC diagnostic apparatus (Loury, 1967 and Sultan, *et al.*, 2020a).

Acid hydrolysis

The free phenols were separated from the crud methanol extract and by the acid hydrolysis process, as 50 ml of HCL was added to 10g of the methanol extract of the frankincense resin and by refluxed the phenols were obtained and after the solution cooled, the ethyl acetate was used in suppurating funnel to isolate the organic layer from the layer Aqueous, then the ethyl acetate is evaporated with a rotary evaporator to obtain free phenols, and then kept in a cooled dark condition until diagnosis (Harborne 1998 and Sultan, *et al.*, 2020a).

Diagnosis of fatty acids

Gas Liquid Chromatography (GLC) was diagnosed with fatty acids and by comparing Retention time (Rt) of the extract sample with standard fatty acids, the measurement was performed at the Ministry of Science

and Technology in Baghdad, with a device of Japanese origin. This technique was used to diagnose fatty acids based on the retention time (Rt) values for the extracted samples compared to the standard retention time.

High Performance Liquid Chromatography (HPLC)

Use the HPLC device to diagnose free separated phenols with purified by filters with a diameter of 0.1 Micrometer and the column used C18-ODS wavelength of 360 nm, measured at the Ministry of Science and Technology in Baghdad.

Antimicrobial activity

Isolates were taken from the bacterial bank at the University of Mosul, as bacterial pathogens were selected that were pathogenic to humans, gram positive such as *Bacillus subtilis*, *Streptococcus pneumoniae*, and one gram negative such as *Proteus vulgaris*, the bacterial isolates were kept at 4°C in the center of the nutrient broth.

Determination of antimicrobial activity

The bacterial suspension was prepared under sterile conditions and to obtain young and newly developed colonies and incubated at 37°C for 24 hours, then the bacterial suspension was diluted by normal slain and compared with McFarland solution 108 cells/cm³, spread the bacterial suspension uniformly with a sterile (L) penis in the Hinton agar medium and while the spread the bacterial is impregnated in the medium, filter disc saturated with active compounds separated from crude gum are prepared as the filter paper disc are of 6 mm diameter and Watmann No. 1 as four concentrations of separated active compounds were prepared, Which 25, 50, 75, 100 mg/cm³, the filter paper disc were saturated at a rate of 0.1 cm³ (Miladinovic, 2000 and Sultan, 2018).

The experiment was carried out with three replications for each extract and each bacterium, as the saturated disc were installed in the medium and under complete sterilization conditions and incubated for 16 hours at a temperature of 37°C. The damping inhibition zoon measured by millimeters and by means of a titration instrument. DMSO solution was used without using the extract as a negative control sample. (Djipa, *et al.*, 2000; Nascimento, *et al.*, 2000 and Sultan, *et al.*, 2020b).

Inhibition results were compared with the ciprofloxacin (5µg/ml) antibiotic as a control sample. The data were analyzed statistically using the Duncan test with a p≤0.01 level and by applying the SAS program between the averages and knowledge of the differences between them.

Results and Discussion

Diagnosis of some fatty acids by Gas-liquid chromatography GLC

The fatty acids of the frankincense resin extract were diagnosed with GLC technique. GLC-chromatograms and extractor retention time were obtained within the apparatus and compared with standard compounds. The concentration of each fatty acid inside the extract was also known.

The following fatty acids were diagnosed: (Myristate, Palmatic, Oleic, Linolic, Arachidate, Arachidatenate, Lignocerate), as table 1 and Fig. 1 indicated the rotation time of each of them.

As shown in table 1 and Fig. 2 the ratios of the fatty acids diagnosed with the GLC device separated from the chloroformic extract after its saponification are from the highest concentration to the lowest concentration (Palmatic 0.129, Myristate 0.119, Lignocerate 0.114, Lenolic 0.026, Arachidatenate 0.008, Oleic 0.007). It also showed the retention time and concentration of each fatty acid separated from Olibanum.

Table 1: The Ret. time of standard and extract fatty acid by GLC analysis.

Standard	Fatty acid													
	Myristate		Palmatic		Oleic		Lenolic		Arachidate		Arachidatenate		Lignocerate	
	R _t min	Conc.	R _t min	Conc.	R _t min	Conc.	R _t min	Conc.	R _t min	Conc.	R _t min	Conc.	R _t min	Conc.
	15.578		17.785		20.731		21.959		23.755		24.407		29.456	
Extract	15.566	0.119	17.655	0.129	20.759	0.007	21.921	0.026	23.772	0.107	24.330	0.008	29.430	0.114

Table 2: The Ret. time of standard and extract phenolic compounds by HPLC analysis.

Standard	Phenolic									
	Gallic acid		Catechin		Epigene		Quercetin		Kaempferol	
	R _t min	Conc.	R _t min	Conc.	R _t min	Conc.	R _t min	Conc.	R _t min	Conc.
	4.79		6.04		8.07		11.90		13.75	
Extract	4.736	41.2	6.044	5.2	8.080	11.3	11.996	4.7	13.772	8.6

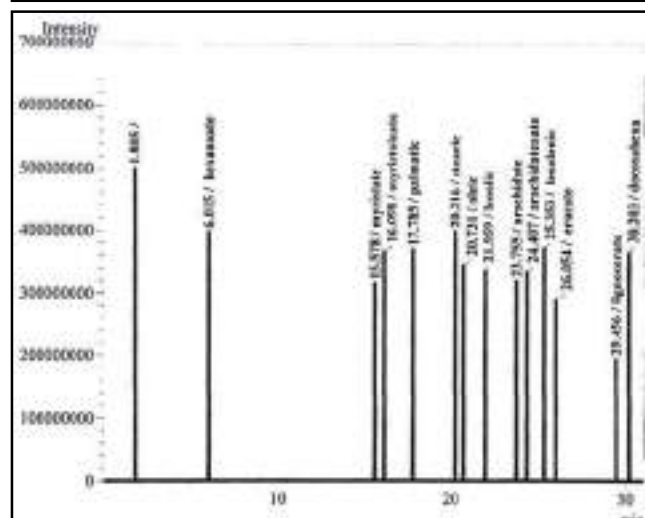


Fig. 1: GLC analyses of standard fatty acid.

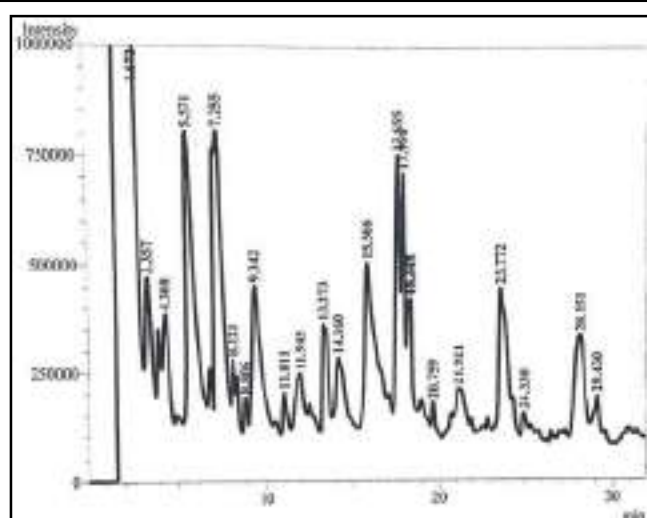


Fig. 2: GLC analyses of extract fatty acid.

The results of the current study showed that Olic acid is present with the lowest percentage of 0.007 and that Palmatic acid is present with the highest percentage of 0.129 and then the rest of the separated fatty acids follow (Yuan, *et al.*, 2006).

Several researchers have confirmed that the *Boswellia serrata* plant contains fatty acids, among which Oleic acid, Linoleic acid, Arachidic acid, Arachidonic acid, Palmitic acid and Lauric acid (Ahmed, *et al.*, 2015; Ayub, *et al.*, 2018 and Yuan, *et al.*, 2006).

Chloroforme extract also contained Omega of type 6 and 9, which has a role in antibacterial activity. It also has a high effectiveness in strengthening the immune system, reducing cholesterol and repairing body tissues (Ikuyma, *et al.*, 2007 and Sultan, *et al.*, 2020a).

Diagnosis of some free phenols with high performance liquid chromatography HPLC

The acid hydrolysis process was performed on the methanol extract of frankincense resin and some free phenols were separated and diagnosed with HPLC, which showed a difference in the content of methanol

extract of phenols, with concentrations, retention time and sub-curve space different from each other, as follows: (Gallic acid 4.736, Epigene 8.080, Kaempferol 13.772, Catechin 6.044, Quercetin 4.7) as shown in table 2 and Fig. from 3 and 4.

The results of the current study agreed with the results of the researcher Ayub, *et al.*, 2018 in the frankincense resin *Boswellia serrata* plant containing free phenols

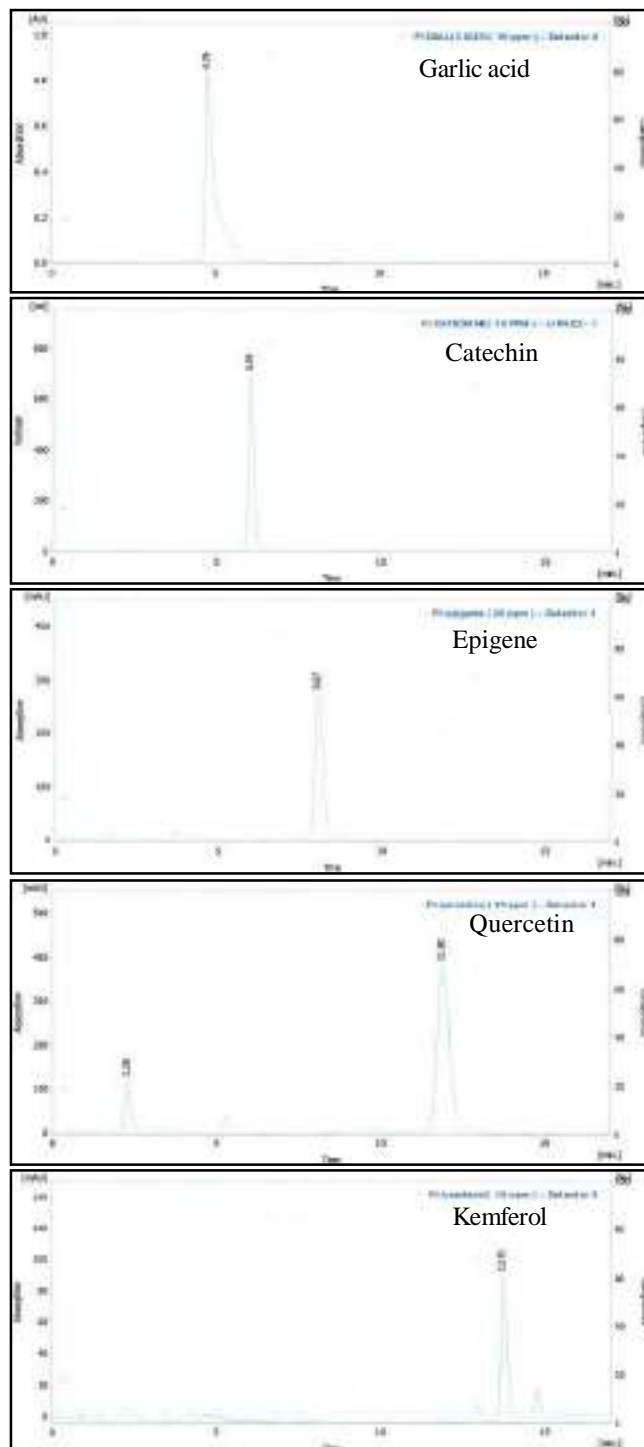


Fig. 3: HPLC analyses of standard phenolic compounds.

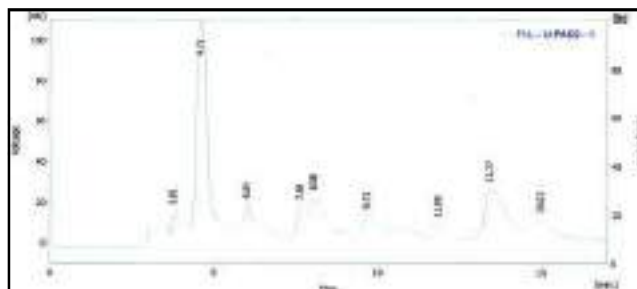


Fig. 4: HPLC analyses of extract phenolic compounds.

used in the treatment of many diseases that affect humans, especially alleviating the symptoms of arthritis, and this is due to its anti-inflammatory properties. The researcher Ismail, *et al.*, 2014 also confirmed that the *Boswellia serrata* plant contributes to treating asthma, fighting cancerous diseases and improving bowel function (Sultan, *et al.*, 2020b and Sultan, 2018).

The effect of the chemical compounds separated from frankincense resin on some pathogenic bacteria and by using an sensitivity test (disc diffusion).

Use the sensitivity test (disc diffusion) to find out the effect of the effective chemical compounds against some positive and negative germs, as the extract contained free phenols and different concentrations with somewhat higher effect than the fatty acid extract against the pathogen bacteria used in the study and compared with the antibiotic ciprofloxacin as shown in table 3 and Pictures (1 + 2).

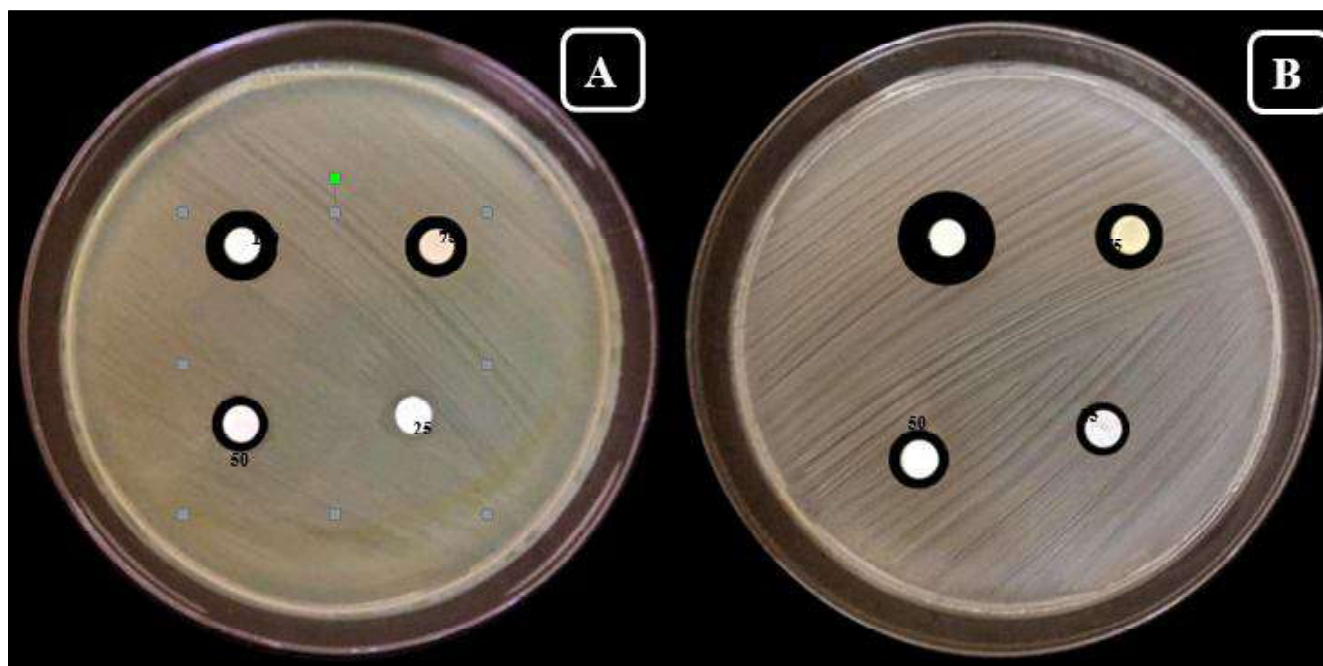
It was the highest effect of fatty acids against a bacterium *Bacillus subtilis* with a diameter of 18 mm inhibition, the effect was higher than the standard antibiotic, the highest effect of free phenols was 22 mm against *Streptococcus pneumoniae*.

It is also the highest effect of the antibiotic under study, the inhibitory effect is due to the separated chemical compounds as many researchers the role of fatty acids in getting rid of microorganisms and the resulting infection

Table 3: Antimicrobial efficacy of chemical composition of *Boswellia serrata* extract (mm).

Microorganism	Chemical Composition	Concentration (mg/c ³) / Zone inhibition in (mm)				
		100	75	50	25	Ciprofloxacin (5µg/ml)
<i>Bacillus subtilis</i>	F	18	15	10	8	15
<i>Bacillus subtilis</i>	ph	20	16	13	10	
<i>Streptococcus pneumoniae</i>	F	22	12	8	-	18
<i>Streptococcus pneumoniae</i>	ph	14	11	9	-	
<i>Proteus vulgaris</i>	F	12	8	-	-	10
<i>Proteus vulgaris</i>	ph	14	12	9	-	

F = Fatty acid, PH = Phenolic Compound.



Photos (1+2): Antibacterial effect of A. fatty acids agents *Bacillus subtilis*.
B. Phenolic compounds agents *Proteus vulgaris*.

from (Ali, *et al.*, 2008 and Ahmed, *et al.*, 2015).

Fatty acids also affect the energy complex by changing the oxygen pathway and thus cell destruction. The bacterium, in addition to the inhibition of a large number of vital components of the bacterial cell and this was confirmed by researchers (Yuan, *et al.*, 2006 and Abd Emaged, *et al.*, 2009).

The results of the study are consistent with the findings of the researchers, Ahmed, *et al.*, 2015 in the ability of phenolic compounds to treat bacterial infections and the resulting diseases. By inhibiting metabolic reactions by affecting the enzymes of these reactions, they interfere with proteins and lead to denaturation of protein that stops the biological activities of the bacterium and its death (Williams and Lewis, 2011).

References

- Abd El-Mageid, M.M., N.A. Salma, M.A.M. Saleh and H.M. Abo Taleb (2009). Antioxidant and Antimicrobial characteristics of red and brown Algae extracts. Conference or recent technologies in Agriculture.
- Ahmed, H.H., A.A. Abd-Rabou1, A.Z. Hassan and S.E. Kotob (2015). Phytochemical Analysis and Anti-cancer Investigation of *Boswellia serrata* Bioactive Constituents *In Vitro*. *Asian Pacific Journal of Cancer Prevention*, **16**.
- Al-Dulayymi, F.I. (2014). "Separation and Identification of Many Natural Products from Some Flowers of Medicinal Plants and Their Biological and Synergistic effects with Isolated Phenazine from *Pseudomonas aeruginosa* Against Some Pathogenic Microorganism". Ph.D. Thesis, College of Education for Pure Science, University of Mosul, 51-56.
- Ali, N.A.A.W., M. Wurster, N. Arnold, A. Teichert, J. Schmidt, U. Lindequist and L. Wessjohann (2008). Chemical Composition and Biological Activities of Essential Oils from the Oleogum Resins of Three Endemic Soqotraen *Boswellia* Species. *Rec. Nat. Prod.*, **2(1)**: 6-12.
- Archana, S. and J. Abraham (2011). Comparative analysis of antimicrobial activity of leaf extracts from fresh green tea, commercial green tea and black tea on pathogens. *J. Appl. Pharma Sci.*, **1(8)**: 149-152.
- Arthur, I. Vogel (1972). "Practical organic chemistry including qualitative organic analysis, 3rd edition, 445.
- Ayub, M.A., M.A. Hanif, R.A. Sarfraz and M. Shahid (2018). Biological activity of *Boswellia serrata* Roxb. Oleo gum resin essential oil: effects of extraction by supercritical carbon dioxide and traditional methods. *International Journal of Food Properties*, **21(1)**: 808-820.
- Banno, N., T. Akihisa, K. Yasukawa, H. Tokuda, K. Tabata, Y. Nakamura, R. Nishimura, Y. Kimura and T. Suzuki (2006). Anti-inflammatory activities of the triterpene acids from the resin of *Boswellia carterii*. *J. Ethnopharmacol.*, **107**: 249-253.
- Chevrier, M.R., A.E. Ryan, D.Y. Lee, M. Zhongze, Z. Wu-Yan and C.S. Vi (2005). *Boswellia carterii* extract inhibits TH1 cytokines and promotes TH2 cytokines *in vitro*. *Clin Diag Lab Immunol.*, **12**: 575-580.
- Dalirsani, Z., M. Adibpour, M. Aghazadeh, M. Amirchaghmaghi, F. Falaki, P.M. Mozafari and F.M. Hamzei (2011). *In vitro* Comparison of inhibitory activity of 10 plant extracts against *Candida albicans*. *Aust. J. Basic. Appl. Sci.*, **5(5)**: 930-

- 935.
- Djipa, C.D., M. Delmee and J. Quetinleclerca (2000). Antimicrobial activity of bark extracts of *Syzygium jambos* L. Alston (Myrtaceae). *J. Ethnopharmacology*, **71**: 307-313.
- Ernst, E. (2008). Frankincense: systematic review. *BMJ*, **337**: a2813.
- Gibbons, S. (2008). Phytochemicals for bacterial resistance- Strengths, weaknesses and opportunities. *Planta Medica*, **74**: 594-602.
- Harborne, J.B. (1984). *Phytochemical Methods*. 2nd ed., Chapman & Hall.
- Harborne, J.B. (1998). *Phytochemical Methods*. 3rd ed., Chapman & Hall.
- Ismail, Sh.M., S. Aluru, K.R.S. Sambasivarao and B. Matcha (2014). Antimicrobial activity of frankincense of *Boswellia serrata*. *Int. J. Curr. Microbiol. App. Sci.*, **3(10)**: 1095-1101.
- Langmead, L. and D.S. Rampton (2006). Complementary and alternative therapies for inflammatory bowel disease. *Aliment Pharmacol Ther.*, **23**: 341-349.
- Loury, M. (1967). A general method for rapid conversion of fats to methyl esters. *Rev. France. Corps. Gras.*, **14**: 383-9.
- Mahalingam, R., V. Ambikapathy and A. Pauneerselvam (2011). Studies on antifungal activities of some medicinal plants against *Ceratocystis paradoxa* causing pineapple disease work. *J. Sci. Tech.*, **1(7)**: 10-13.
- Mohammed Aman, Ravishankar Rai, V. Pradeepa and V. Samaga (2010). Antimicrobial and Phytochemical Screening of *Boswellia serrata* Roxb., *Rhus mysorensis* Heyne, *Strychnos potatorum* Linn. F. and *Schefflera stellata* Gaertn. *Medicinal and Aromatic Plant Science and Biotechnology*, **4(1)**: 69-72.
- Nascimento, C.F., J. Locatelli, P.C. Freitas and G.L. Silva (2000). Antibacterial activity of plant extracts and phytochemicals on antibiotic resistance bacteria. *J. Microbiol.*, **31**: 247-256.
- Okuyama, H., I. Yuko, S. Yueji, H. Tomohito and E.M. William (2007). "Fatty acids effectively prevent coronary heart disease and other late-onset diseases: the excessive linoleic acid syndrome. World review of Nutritional dietetics 96 (prevention of coronary heart disease). 83-103 Karger doi 10.11591000097809.
- Patel, B. and K.C. Patel (2014). Antibacterial activity of *Boswellia serrata* roxb. ex colebr. ethanomedicinal plant against gram negative UTI pathogens life sciences leaflets free download issn 2277-4297 (print) 0976-1098 (online).
- Stavri, M., L.J.V. Piddock and S. Gibbon (2007). Bacterial efflux pump inhibitors from natural sources. *J. Antimicrob. Chemother.*, **59**: 1247-1260.
- Sultan, F.I. (2018). Chromatographic Separation and Identification of Many Fatty acids and Phenolic Compounds from Flowers of *Celosia cristata* L. and Its Inhibitory Effect on Some Pathogenic Bacteria. *Australian Journal of Basic and Applied Sciences*, **12(7)**: 25-31.
- Sultan, F.I., A.A. Al-Farha and Shaaban Ibtisam (2020a). Separation and identification of some fatty acids and phenolic compounds from *Portulaca oleracea* L. and study their biological effect on two types of pathogenic bacteria. *AJAB* 2020-02-119 was accepted May 2020.
- Sultan, F.I., A.Ch. Khorsheed and A.M.S. Khalel (2020b). Separation of four fatty acids and two phenolic compounds from *Camellia sinensis* using chromatographic techniques and evaluated their antibacterial activity. *Eurasia J. Bio. Sci.*, **14(1)**: e-ISSN1307-9867).
- Weckesser, S., K. Engel, B. Simon-Haarhaus, A. Wittmer, K. Pelz and C.M. Schempp (2007). Screening of plant extracts for antimicrobial activity against bacteria and yeasts with dermatological relevance. *Phytomedicine*, **14**: 508-516.
- Williams, D. and M. Lewis (2011). Pathogenesis and treatment of oral Candidiasis. *J. Oral Microbiol.*, **3**: 5771-5782.
- Yuan, G., M.L. Wahlqvist, H. Guoqing, M. Yang and D. Li (2006). Natural products and anti-inflammatory activity Asia Pac. *J. Clin. Nutr.*, **15(2)**: 143-152.

Mechanical Characterization of the Green Coconut Fiber for Application in the Footwear Industry

Célia Regina da Costa

School of Arts, Sciences and Humanities of University of Sao Paulo (EACH-USP)
03828-000 Brazil (55)11 44882043 celiareginadacosta2012@gmail.com

Regina Aparecida Sanches

School of Arts, Sciences and Humanities of University of Sao Paulo (EACH-USP)
03828-000 Brazil (55) 11 3091-8803 regina.sanches@usp.br

Júlia Baruque Ramos

School of Arts, Sciences and Humanities of University of Sao Paulo (EACH-USP)
03828-000 Brazil jbaruque@usp.br (55)11 3091-8116

Jorge Boueri

School of Arts, Sciences and Humanities of University of Sao Paulo (EACH-USP)
03828-000 Brazil jjboueri@usp.br (55)11 3091-1024

Bárbara Maria Gama Guimarães

School of Arts, Sciences and Humanities of University of Sao Paulo (EACH-USP)
03828-000 Brazil barbara.guimaraes@usp.br

*Corresponding author e-mail: celiareginadacosta2012@gmail.com

Abstract

In the tropical countries, the green coconut water consumption generates a great problem with the fruit final destination. To minimize this problem, it is necessary to find applicability to the residues. In this sense, this study had as its objective to investigate the characteristics of the green coconut fiber, from the fruit disposed in the city of Francisco Morato – Sao Paulo, and to compare them to the characteristics from other natural fibers, to check the viability of application of these fibers in the manufacturing of shoe parts. It was made a biological maceration on the fibers and traction and microscopy tests were run. The results showed that the green coconut fibers have potential related to other natural fibers studied in literature, to be used as reinforcement in the manufacturing of shoe parts and other design products.

Keywords: *Cocus nucifera L.*, characterization of the green coconut fiber, footwear, traction test, microscopy optical, fiber extraction.

Introduction

The needs required by the modern man led to a rampant consumption of the non-renewable resources which manifests in damage to the environment, such as accumulation of non-biodegradable trash on soil and issue of pollutant gas on the atmosphere (Leite *et al.*, 2010).

The synthetic fibers were initially developed with the objective of improving the characteristics of the natural fibers properties and cooperating when it comes to the vulnerability of the textile industries towards problems in the agricultural production of fibers (Barbosa, 2002). Nowadays, the synthetic fibers derivative from oil had an increasing index in its applications. However, due to the raise of environmental problems emerged from the processing or discard of its products, there was the need to look for biodegradable and renewable raw materials.

In the footwear industry, the components used in the manufacturing are pollutant, essentially when it is about the leather tanning with chromium salts. In this phase there is a great amount of solid and gaseous waste thrown in the effluents (Ganem, 2007); and also when it comes to the manufacturing of other parts of the shoe, such as the sole. The polyurethane (PU), which is a synthetic polymer with a high performance used in the manufacturing of insoles and soles, also generates pollution during its processes, and issue toxic substances in the environment (Fernandes, 2008).

There is a pursuit for new materials that ease these environmental problems, thus there is an interest in research for the development of compounds that use natural fibers as alternatives to replace products that damage the environment (Visconte, 2006). Natural fibers have been used by men for millennia to produce fabric and techniques for textile production, and are present among the world cultures (Duarte *et al.*, 2012).

The use of natural fibers is associated to the factor that they are biodegradable, less abrasive and have a low cost related to the synthetic fibers (Leite, 2010). The green coconut fibers come from renewable sources, originating from the food industry waste in the tropical countries, where the green coconut water is consumed, and its use also collaborates in the reduction of solid waste that is issued in the environment (Visconde, 2006).

The mature coconut fiber is already applied in the industry and agriculture, yet the fiber of the green coconut bark does not have much applicability due to the high moisture of the barks (85%), and the fibers characteristics disfavor certain applications that are often employed with the dry coconut fibers. Its use by the fibers finishing industries is not high because of the lack of knowledge on its properties (Rosa *et al.*, 2001).

The coconut fibers are lignocellulosic materials collected from the coconut mesocarp, the coconut palm fruit (*Cocos nucifera L.*) mainly grown in the tropics. The fibers have hardness and mechanical resistance due to the high lignin, which also serves as a protection for the tissue against the action of microorganisms (Leite *et al.*, 2010).

These characteristics of the green coconut fibers increase its possibilities of use in some shoe parts, for the

rigidity provided by the lignin gives a good resistance. Another important element found in these fibers is the preservation against the bacteria attacks, for the lignin has a high natural preservation towards other natural fibers already studied in literature. Table 1 shows percentages of total lignin found on natural fibers:

According to Corrandini *et. al.* (2009), there is still few studies aiming to the use of green coconut fibers despite of their characteristics comparing to other natural fibers.

Embrapa (Brazilian Agricultural Research Corporation), together with a metallurgy industry, developed an equipment to separate the dust and the fiber from the green coconut shell. This equipment made feasible the agricultural use of the fiber, and also provides substrate to the insole manufacturing for the footwear industry (Silveira, 2008).

The main stages for the fiber extraction are (Silveira, 2008):

- **Trituration:** the residue is cut by a roll of fixed knives, which shave the barks, and then goes through fixed hammers that are responsible for the product crushing;
- **Squeezing:** withdrawal of moisture and toxic salts used along the plant cultivation;
- **Fiber selection and dust:** the fibers are separated from the dust with a machine that has a roll of fixed knives and a perforated sheet. The material is whirled along the machine axis, and by a density difference the dust comes out through the sheet holes, and the fiber comes out at the end of the course;
- **Fiber sieving:** the fiber impurities are separated with a thick sieve;
- **Dust thermal treatment:** to eliminate the microorganisms it is undergone a rotative heater at 80°C for 20 minutes;
- **Pressing:** the dust and fiber, which are little dense, are compacted with a hydraulic press to reduce the transportation costs.

The use of green coconut fibers can generate the production of low-cost materials, and also reduce the solid waste resulting from the increasing coconut consumption (Santos, 2002). The knowledge on the chemical, mechanical and other characteristics of the green coconut is substantial to understand its use potential (Corrandini, 2009).

In Brazil, coconut fiber was used in the manufacture of seats car, but was replaced by polyurethane after 1990s. Currently, the sector that has been highlighted is gardening, due the ecological factors in the protection against the extinction of the tree fern (*Dicksonia sellowiana Hook*). The fiber of coconut can be applied in sectors of design objects for home, furniture, composites, geotextiles and others.

The objective of this study was to investigate some mechanical characteristics of the coconut fiber for a possible applicability on the footwear industry, in order to contribute to its potential in the

manufacturing of certain parts of the shoe, replacing the ones already made in a very environment-pollutant way (MARTINS *et al.*, 2013).

1. Materials and methods

The fruit were collected in disposal areas of the coconut water businesses, in the city of Francisco Morato, greater São Paulo region.

1.1 Chemical characterization

Literatures that relate the lignin with the possibility of green coconut fiber use in the manufacturing of shoe parts that need rigidity were researched.

1.2 Treatment and characterization of the coconut fibers

First, the green coconut fibers were separated from the external part of the bark, then they were subjected to a biological maceration process, in which the coconut barks remained immersed in water for 4 weeks so that the spontaneous anaerobic fermentation of the vegetable matter could happen and help in the woody bundles liberation (Castilhos, 2011). After this stage, the fibers were left in water for 24h more for removal of water-soluble extractives and impurities originary from the maceration process, and air-dried for 24h.

1.3 Samples acclimatization

The fibers were previously acclimatized for a period of 7 days at 20°C and 65% relative humidity. The samples were conditioned in conditioning tool for textiles or conditioner brand Mesdan (Climatest model M250-RH, Italy).

1.4 Optical microscopy

Analyses were analyzed usind an stereo-microscope (Leica, model MS5, Germany)

coupled to video camera to capture digital images (Vista Protos IV, model VPC

122/CH, 1/2" CCD, Britain). The images were captured and processed by the system code 2000 Video Analyser 250 (Mesdan, Italy).

1.5 Mechanical characterization – tension tests

Assays for determining the tensile properties and elongation were performed on a dynamometer ("tester machine") Instron (model 5569, Norwood, USA). The load cell used for testing was a maximum of 10 N (1 kgf or approximately). Were employed rubberized grip jaws with dimensions of 2.5 x 2.5 cm. The distance between the grips was 25 mm and the displacement speed during testing was 50 mm / min. 20 fibers were tested. Were determined averages, standard deviations and coefficients of variation of breaking load (N), tenacity at break (cN / tex), elongation at breaking load (mm), percentage elongation at break (%) and Young's modulus (N / tex).

2. Results and Discussion

2.1 Chemical composition

According to the researched literatures on the total lignin present in the green coconut fibers, approximately 44%, gives the fiber a good resistance and a protection against microorganism attacks, crucial aspects for the use in the footwear industry (Razera, 2006). The high lignin favors the fibers flexibility (Corrandini, 2009; Pannirselvam *et al.*, 2005).

2.2 Optical microscopy

The optical microscopy consisted in analyzing the fiber surface, providing an image produced by the interaction between light and fiber, with a wide field of observation. Figure 1 shows the optical microscopy done on the surface of the green coconut fibers, with a magnification of 20 times, and Figure 2 shows the same fiber with a magnification of 32 times. The superficial aspect is shaped like a “twisted shoelace”, which gives the fiber a better rigidity.

2.3 Mechanical properties – tension tests

The mean values of linear density, tenacity and tensile strain of the green coconut fibers were determined; the experimental values are on Table 2.

The tenacity values of the green coconut fibers are lower when compared to the ones found in literature on jute and sisal. The tensile strain, on the other hand, is higher than the other natural fibers found in literature (Table 3).

The green coconut fibers can be divided in fine, medium and thick. The experimental results showed that the most resistant fibers are those with higher linear density.

The experimental results indicate that the mechanical properties of the green coconut fibers present a good resistance and demonstrate that these fibers can be applied in shoes. The high lignin provides a good flexibility quality to the fiber.

These results show that the green coconut fiber can be used in parts of shoe manufacturing, for they have good mechanical characteristics, easy production, availability among other advantages.

3. Conclusion

Nowadays we can see a variety of materials used in the shoes manufacturing, such as the polyurethane (PU), used in soles and midsoles due to its resistance to abrasion and good adherence to the ground; the polystyrene, used in heels due to its resistance to impact; the ABS (acrylonitrile butadiene styrene), which has an excellent resistance to break. However, the most used material in the footwear industry is the leather, due to its ideal characteristics like good flexibility and wear. Nevertheless, these materials processes are highly pollutant and come from non- renewable raw materials. There is a trend in using natural materials in the footwear industry because of the scarcity and the environmental problems created during

the manufacturing processes. In this sense, the green coconut fiber is being studied for the use in the footwear industry.

From the obtained results, we can conclude that the high lignin in the green coconut fibers provides a good flexibility and a natural protection against microorganism attacks. The tenacity is close to the one found in literature, although it is higher than the values found for other natural fibers, such as: sisal fiber (1,5%) and jute (0,7%). Ergo, the green coconut fibers have potential, compared to other natural fibers researched in literature, to be used as reinforcements in shoe parts manufacturing.

The pursuit for sustainable materials is important to application in sectors that need renewable raw materials and need to reduce their environmental pollution, as the footwear industries and home decoration objects.

References

ASTM (American Society for Testing and Materials) ASTM D 3822. 2001. *Standard Test Method for Tensile Properties of Single Textile Fibers*. Pennsylvania: C ASTM International.

ABNT NBR ISO 139 (Associação Brasileira de Normas Técnicas). 2008. *Têxteis – Atmosferas - padrão para condicionamento e ensaio*.

Barbosa, M. Z. (2002). Perspectivas para a demanda de algodão e de fibras sintéticas (pp. 55-56). *BNDS Relato Setorial*.

Castilhos, L. F. F. (2011). Aproveitamento da fibra de coco. Instituto de Tecnologia do Paraná: TECPAR.

Corrandini, E., Rosa, M. F., Macedo, B.P., Paladin, P. D., & Mattoso, L. H. C. (2009). Composição química, propriedades mecânicas e térmicas da fibra de frutos de cultivares de coco verde (pp. 837-846). Jaboticabal: Revista Brasileira de Fruticultura 3.

Correa, C. A. (2000). Caracterização Mecânica: tração e impacto. São Carlos: Associação Brasileira de polímeros - ABPol.

Duarte S. A. Y., Queiroz, R. S., Sanches, R. A., Vicentini, C. R. G., & Dedini, F. G. (2012). Ethnobotany of Natural Fibres - *Bactris setosa* (tucum) in a Traditional Rural Community (pp. 18-20). Poland: *Fibres & Textiles in Eastern Europe* 2.

Fernandes, I.P.M.F. (2008). Dispersões aquosas de poliuretano e poliuretano-ureia. Concepção do produto e metodologias de caracterização. Dissertação de Mestrado- Escola Superior de Tecnologia e de Gestão de Engenharia Química.

Ganem, R. S., (2007), Curtumes: aspectos ambientais. Biblioteca Digital Câmara dos Deputados.

[Online]

Available:

http://bd.camara.gov.br/bd/bitstream/handle/bdcamara/1281/curtumes_aspectos_sena.pdf?sequence=1 (December 7, 2012).

- Leite, M. C. A. M., Furtado, C.R. G., Couto, L. O., Oliveira, F. L. B. O., & Marabezi, T. R. C. (2010). Avaliação da biodegradação de compósitos de poli (ϵ - caprolactona)/fibra de coco verde (pp. 339-344). São Carlos: Polímeros. 20.
- MARTINS, A. P., WATANABE, T., SILVA, P. L. R., BORELLI, C., MARCICANO, J. P. P., & SANCHES, R. A. (2013). Aproveitamento de fibra de coco verde para aplicabilidade têxtil. Use of young nut coir fiber for textile applicability. Rio de Janeiro: Redige v.4, n.2.
- Pannirselvam, P. V., Lima, F. A. M., Dantas, B. S., Santiago, B. H. S., Ladchumanadasivam, & Fernandes, M. R. P.(2005). Desenvolvimento de projeto para produção de fibra de coco com inovação de tecnologia limpa e geração de energia (pp.56-61). Brasília: Revista Analytica 15.
- Razera, I. A. T. (2006). Fibras lignocelulósicas como agente de reforço de compósitos de matriz fenólica e lignofenólica. Tese de Doutorado, Universidade de São Paulo, São Carlos.
- Romero, L. L., Vieira, J. O. W. M, Martins, R. F, & Medeiros, L. A. R.(1995). Fibras artificiais e sintéticas. Brasília: BNDS. Relatório setorial.
- Rosa, M. de F., Abreu, F. A. P., Furtado, A. A. L., Brigido, A. K. L., & Norões, E. R. V. (2001). Processo agroindustrial: obtenção de pó de casca de coco verde. Fortaleza: Embrapa Agroindústria Tropical.
- Santos, M. S. (2002). Propriedades térmicas e mecânicas de materiais à base de PET pós- consumo e cargas de coco. Dissertação de Mestrado, Universidade Federal do Rio de Janeiro.
- Saville, B. P. (2007). Physical testing of textiles. Cambridge: The Textile Institute Woodhead Publishing Limited.
- Silveira, M. S. (2008). Aproveitamento das cascas de coco verde para produção de briquete em Salvador-BA. Dissertação Pós-graduação em Gerenciamento e Tecnologias Ambientais no Processo Produtivo – Ênfase em Produção Limpa, Escola Politécnica da Universidade Federal da Bahia.
- Visconte, L.L.Y., Ishizaki, M. H., Furtado, C. R. G., Leite, M. C. A. M., & Leblanc, J. L. (2006). Caracterização mecânica e morfológica de compósitos de polipropileno e fibras de coco verde: influência do teor de fibra e das condições de mistura (182-186). Polímeros: Ciência e Tecnologia 16.

Table 1. Lignin in natural fibers

Natural fiber	Total lignin (%)
Mature coconut	48,3±1,9
Green coconut	44±1,0
Banana tree	16,8±1,0
Jute	15,9±0,5
Sisal	12

Font: Razera 2006

Table 2. Mean values of the linear density, tenacity and tensile strain of the *Cocus nucifera*.

Specimen	Linear density (tex)	Tenacity at Break (cN/tex)	Tensile strain at Break (%)
Mean	20.7	12.91	22.38

Font: Author 2012

Table 3. Tenacity and tensile strain of some fibers

Fiber	Tenacity (cN/tex)	Tensile strain (%)
Jute	26,5	0,7
Sisal	35,3	1,5
Green coconut	12,91	22,38

Font: Razera 2006 and Saville 2007

Figure 1- Green coconut fiber (magnification 20x)

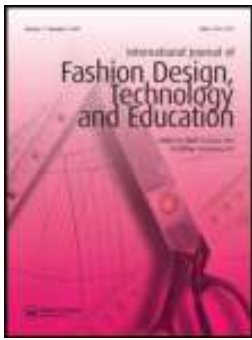


Font: Author 2012

Figure 2 – Green coconut fiber (magnification 32x)



Font: Author 2012



Development and evaluation of apparel and footwear made from renewable bio-based materials

Huantian Cao, Richard P. Wool, Paula Bonanno, Quan Dan, Jillian Kramer & Stacey Lipschitz

To cite this article: Huantian Cao, Richard P. Wool, Paula Bonanno, Quan Dan, Jillian Kramer & Stacey Lipschitz (2014) Development and evaluation of apparel and footwear made from renewable bio-based materials, International Journal of Fashion Design, Technology and Education, 7:1, 21-30, DOI: [10.1080/17543266.2013.859744](https://doi.org/10.1080/17543266.2013.859744)

To link to this article: <https://doi.org/10.1080/17543266.2013.859744>



Published online: 22 Nov 2013.



Submit your article to this journal [↗](#)



Article views: 1003



View related articles [↗](#)



View Crossmark data [↗](#)



Citing articles: 5 View citing articles [↗](#)

Development and evaluation of apparel and footwear made from renewable bio-based materials

Huantian Cao^{a*}, Richard P. Wool^b, Paula Bonanno^a, Quan Dan^b, Jillian Kramer^a and Stacey Lipschitz^a

^aDepartment of Fashion and Apparel Studies, University of Delaware, Newark, DE 19716, USA; ^bDepartment of Chemical and Biomolecular Engineering, University of Delaware, Newark, DE 19716, USA

(Received 30 April 2013; final version received 16 October 2013)

The production of textiles, apparel, and footwear causes resource depletion, environmental pollution, and human health problems. This research developed materials, i.e. water-resistant but breathable composites as leather substitutes (eco-leather), a thermosetting resin, and a hard composite, from bio-based sources such as plant oils, natural fibre cloth, and chicken feather fibres. These materials, together with commercially available environmentally friendly natural textiles, were used to develop shoes and a coat. Wear tests and questionnaire surveys were conducted with female college students to evaluate the users' acceptance of materials and prototypes. It was found that the environmentally friendly materials used in the shoes and coat were comfortable. The participants thought the renewable bio-based materials developed from plant oils and natural fibres were wearable, versatile, and practical. If the design and style met their requirements, the participants expressed they would like to buy apparel and footwear products made from these environmentally friendly materials.

Keywords: bio-based; eco-leather; resin; composite; sustainability

1. Introduction

Consumers have purchased an increasing amount of textile, apparel, and footwear products over the past few decades. According to the American Apparel and Footwear Association (AAFA, 2009) the total US consumption was 19.5 billion garments and 2.2 billion pairs of shoes in 2008, compared with 14.1 billion garments and 1.7 billion pairs of shoes in 1999. This indicates an increase of approximately 38% in apparel and 29.4% in footwear consumption in a nine-year period. Textile fibres are the beginning materials for fabrics, as well as apparel and footwear products. Thus, increasing apparel and footwear consumption has resulted in higher demand for textile fibres.

There are two categories of textile fibres, natural fibres from plants (e.g. cotton) or animals (e.g. wool) and manufactured fibres. The production of natural fibres is restricted by agricultural factors such as land, water availability, and weather. A University of Cambridge study (Allwood, Laursen, de Rodriguez, & Bocken, 2006) reported that the demand for manufactured fibres nearly doubled from about 20 million tonnes in 1990 to about 40 million tonnes in 2004, while the demand for natural fibres remained constant in the same period. The raw materials for manufactured fibres can come from renewable resources such as wood pulp for rayon or lyocell fibres. However, the significant increase in manufactured fibre demand was mainly driven by polyester (Allwood et al., 2006), which currently uses petroleum, a non-renewable resource, as the raw material.

In addition to the resource depletion problem associated with petroleum-based fibres, the production of materials for apparel and footwear products causes many other environmental problems. Among the 2.2 billion pairs of shoes the US consumers purchased in 2008, about one-third were categorised as leather products and one-third as plastic/vinyl products (AAFA, 2009). The chemical processes to convert raw animal hides to leather, especially tanning (the process to treat animal skins and hides to make them more pliable as well as water and rot resistant), cause environmental pollution and human health problems. Chromium salts are used in about 90% of global tanning production (Nair, Hansdah, Dhal, Mehta, & Pandey, 2012). The oxidising product of tanning agent chromium (III) is chromium (VI), a known toxin and carcinogen. In chrome tanning, a considerable portion of the chromium is neither bound nor incorporated in the hide tissue and as a result passes into the effluent (Tariq, Shah, & Shaheen, 2009). Vinyl (polyvinyl chloride or PVC), which is used as a leather substitute, causes severe environmental problems and human health hazards through manufacture, use, and disposal. Dioxins, the most important by-products of the PVC lifecycle (Thornton, 2002), are persistent and bioaccumulative endocrine disruptive chemicals (EDCs), which represent a global threat to the health of human beings and wildlife (Bergman, Heindel, Jobling, Kidd, & Zoeller, 2013). Large quantities of phthalates (may be up to 60% by weight) are added to PVC as plasticisers to reduce the glass transition temperature and make the

*Corresponding author. Email: hcao@udel.edu

plastics more flexible (Thornton, 2002). A few phthalates are EDCs. Due to these problems, many nations, industries, and companies are working on the elimination of PVC as a synthetic leather substitute (Thornton, 2002).

To design chemical products and processes that minimise the use and generation of hazardous substances, Anastas and Warner (1998) developed 12 principles of green chemistry. Anastas and Zimmerman (2003) further developed 12 principles of green engineering to provide a framework for scientists and engineers in designing materials, products, processes, and systems that are benign to human health and the environment. Between the green chemistry (Anastas & Warner, 1998, p. 30) and green engineering (Anastas & Zimmerman, 2003) principles, there are a few overlaps, including waste prevention (principle 1 in green chemistry and principle 2 in green engineering), less hazardous chemical syntheses and processes (principle 3 in green chemistry and principle 1 in green engineering), and the use of renewable feedstocks or recourses (principle 7 in green chemistry and principle 12 in green engineering).

Due to the environmental impacts of the textile and apparel industry, sustainable apparel design, development, production, retailing, and consumption are becoming more important in both academic research (Armstrong & LeHew, 2011; Gam, Cao, Farr, & Heine, 2009) and industrial practices (Golden, Subramanian, & Zimmerman, 2011). In 2011, a group of leading apparel companies (brands and retailers), suppliers, and non-profit organisations founded the Sustainable Apparel Coalition (SAC) (Golden et al., 2011), intending to develop solutions for the environmental and human health impacts and make the apparel and footwear industry sustainable. In 2012, the SAC (www.apparelcoalition.org) released an assessment tool, Higg Index 1.0, which enables companies to evaluate the environmental impacts of materials, products, facilities, and processes. To reduce the chemical impacts of apparel and footwear products, the application of green chemistry in materials and production is incorporated in the Higg Index 1.0. However, the Higg Index 1.0, which is currently being pilot tested for improvements, has few examples or details on how green chemistry can be applied in the apparel and footwear industry. The SAC is seeking guidance and contributions towards applications of green chemistry in the industry, and members of the SAC are recognising the need for more environmentally benign sources for chemicals and materials.

The shortage of depleting resources such as coal, oil, and gas; the greenhouse effect, growth of the world population, and the pursuit of sustainable development have resulted in an accelerating shift towards chemical products derived from renewable biological feedstocks (Behr & Johnen, 2009). Renewable resources include carbohydrates (such as cellulose and starch), lignin, fats and oils, proteins, and vegetable secretions and extracts (such as wax, natural rubber, and herbal dyes). Among fats and oils, soya bean oil, a by-product of soya bean flour production,

and palm oil are the most important fatty raw materials worldwide (Behr & Johnen, 2009). The main component in plant oils is triglycerides, which are composed of three fatty acids connected by a glycerol centre (Khot et al., 2001). The unsaturated (C=C) sites on the fatty acids in triglycerides can be chemically modified and used for polymerisation (La Scala & Wool, 2005). La Scala and Wool (2005) synthesised rigid and stiff thermosetting resins with an excellent tensile strength using plant oils (triglycerides) as the starting chemicals. Adding nano-filler as the additive to triglyceride-based thermosetting resins could further toughen the material (Lu & Wool, 2008). Using nanoclay as the filler, an elastic nano-composite was generated from bio-based elastomer synthesised from soya bean oil (Zhu & Wool, 2006). Campanella, Bonnailie, and Wool (2009) used soya bean oil as the starting material to produce polyol, which is further synthesised to produce polyurethane foams. Chicken feathers are wastes from the poultry industry and expensive to dispose of. The poultry industry in the US produces about 2.3 billion pounds of feathers per year, and composting is the most effective reuse of feathers (McGovern, 2000). To reduce waste and find valuable applications, researchers (Barone & Schmidt, 2005; Cheng et al., 2009; Huda & Yang, 2009; Zhan, Wool, & Xiao, 2011) investigated the development of composites using chicken feather fibres. Hong and Wool (2005) used soya bean oil and chicken feather fibres to develop a bio-based composite material suitable for electronic, automotive, and aeronautical applications.

The purpose of this research was to use renewable bio-based materials to develop apparel and footwear products. This research was an interdisciplinary collaboration between researchers in Chemical and Biomolecular Engineering (CBE) and Fashion and Apparel (FA). CBE researchers used renewable bio-based materials to develop water-resistant but breathable composites as leather substitutes (eco-leather), a thermosetting resin, and a hard composite. FA researchers used these materials, together with carefully selected environmentally friendly textiles, to design and develop prototype shoes and a coat. Using these new bio-based materials in apparel and footwear products could reduce the industry's dependence on non-renewable petroleum-derived materials and solve the environmental problems associated with traditional materials, such as leather and PVC. Female college students were chosen as the target users for the products. Human subject wear tests and questionnaire surveys were conducted with female college students to evaluate the users' acceptance of the prototype shoes and the coat.

2. Materials and processes

2.1. Starting materials

A liquid moulding resin, normally viscous and insoluble in water, is a compound which can be hardened after treatment. The starting chemicals for the bio-based resins

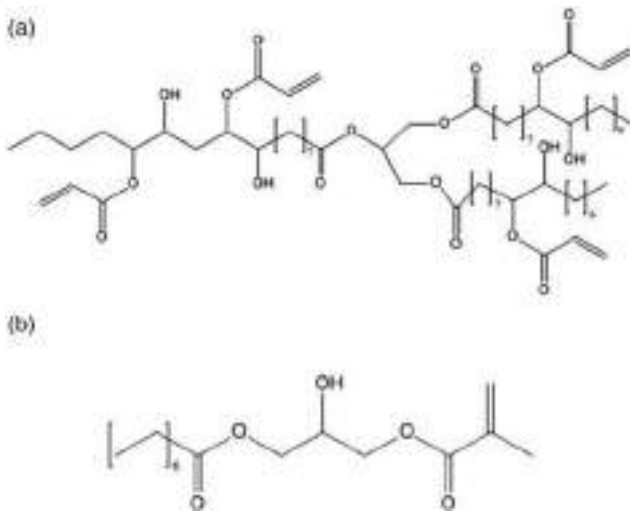


Figure 1. The chemical structures of AESO and MLAU: (a) AESO and (b) MLAU.

were acrylated epoxidized soya bean oil (AESO), methacrylated lauric acid (MLAU), and linseed and soya bean oil with 30% styrene (CB4-30). AESO, derived from soya bean oil, was synthesised through a reaction of acrylic acid and epoxidized soya bean oil. MLAU was derived from palm seed oil and CB4-30 was from linseed and soya bean oil. The chemical structures of AESO and MLAU are in Figure 1.

Chicken feather fibres were obtained from Featherfiber Corp. (Nixa, MO). Other textile materials used in this research included 100% organic cotton fabrics and 100% wool fabric. The three types of plain weave greige-goods organic cotton fabrics (153, 237, and 339 g/m², respectively) were purchased from Organic Cotton Plus (Ridgefield, CT). The sateen organic cotton fabric (142 g/m²) was purchased from NearSea Natural, Inc. (Rowe, NM). The 100% wool flannel fabric (388 g/m²), purchased from Pendleton Woolen Mills (Portland, OR), was Cradle to CradleSM environmentally certified biological nutrients by McDonough and Braungart Design Chemistry (MBDC).

2.2. Procedure

Radical polymerisation with the addition of an initiator and catalyst was used in this research. Depending upon the conditions of curing, either benzoyl peroxide or trigonox (tert-butyl peroxybenzoate) was used as the initiator. Under the conditions for room temperature curing, a catalyst cobalt naphthenate (CoNap) was added. Due to the fact that oxygen acted as an inhibitor to the polymerisation process, the solution was placed into a vacuum and degassed.

2.3. Eco-leather

The eco-leather is a composite made from natural fibre cloth (greige-goods organic cotton fabrics) and an AESO/MLAU

(50/50 composition) resin. Peel ply films were used to provide a layer between the reusable mould and the composite. The sheets of peel ply film were sprayed with an air dry releasing agent to ensure the composite and film would be easily separated after curing. After degassing, a peel ply film was laid on the mould and half of the resin was evenly spread on the film. Then, the cotton fabric was placed on top of the resin and the other half of the resin was spread evenly on top. A second peel ply was placed on top and the mould was covered with a lid. The mould was placed in the hot press and cured at room temperature with pressure for 24 h. After that, the mould was placed in an oven at 120°C for an additional 2 h of post curing. These composites made from renewable bio-based sources are water-resistant but permeable to air, and can be used as environmentally friendly materials to replace leather and pleather in apparel and footwear applications. After evaluating the three composites, the researchers decided that eco-leather samples made from the two greige-goods organic cotton fabrics (237 and 339 g/m²) and resin composites were appropriate for shoe applications.

2.4. Thermosetting resin

Before scaling up, small bar resin samples were developed and used to compare compositions and characteristics for the shoe outsole. Several different compositions of AESO/MLAU and CB4-30 were tested. After comparison, a 50/50 composition of AESO/MLAU was selected because of its sturdy yet flexible property. High temperature curing was utilised to achieve the desired properties. Similar to the development of eco-leather, peel ply films were used, and the sheets of peel ply film were sprayed with an air dry releasing agent to ensure the resin and film would be easily separated after curing. In a mould, the degassed resin was evenly spread across a peel ply film, and then a second peel ply film was laid on top of the resin. The mould was placed in an oven to cure at 90°C for 2 h, and then post cured at 120°C for 2 h. After cooling, the samples were removed from the mould, and separated from the peel ply film.

2.5. Hard composite

The material was made from a chicken feather fibre and CB4-30 composite. The combination provided a hard composite which is desired for the heel. Similar to the development of eco-leather and shoe sole resin, mould, peel ply films, and air dry releasing agent were used. After degassing, the chicken feather fibres and CB4-30 resin were mixed together. The chicken feather fibres and resin mixture were applied to the peel ply film in a mould. Then, a second peel ply film and a lid were applied on top. The mould was placed in a hot press, in which the sample was cured at 90°C with high pressure for 2 h. Then, it was post cured in the hot press at 120°C for 2 h. After cooling, the sample was separated from the peel ply film.

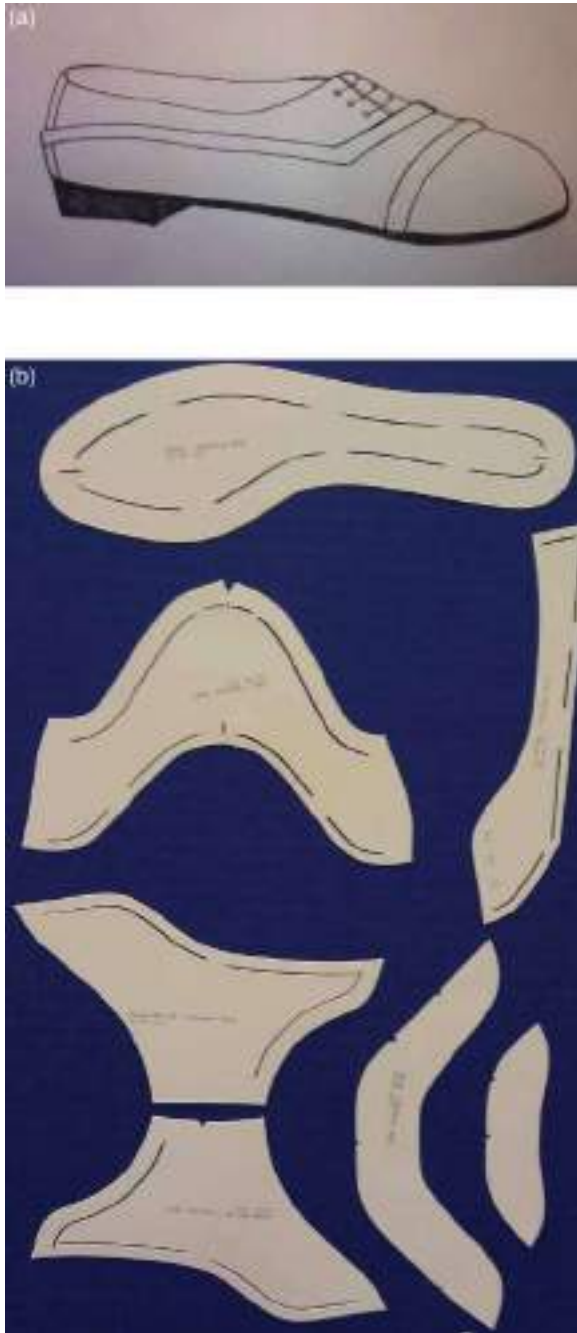


Figure 2. Shoe design sketch and pattern: (a) design sketch and (b) pattern.

3. Design and development of one pair of shoes and one coat

3.1. Design and development of the shoe prototype

After assessing the eco-leather, resin, and hard composite materials, a sketch of the oxford shoe design was developed as shown in Figure 2(a). The Product Creation Technologies Team of a shoe manufacturing company assisted the research team in pattern making and prototype development. With the industrial assistance, the research team

was able to use the pattern making computer software for footwear design and industrial machines for shoe making. The sketch of the shoe design was adapted into a 3D pattern as in Figure 2(b). During the prototype development, it was found that the eco-leather did not have the same stretchy property as the upper material commonly used by the shoe manufacturing company. Adjustments were made by adding additional length to the pattern in certain areas, and the prototype shoes were developed as in Figure 3. The summary of the materials used in the prototype is in Table 1.

3.2. Design and development for the coat

The pattern for the coat was based on general jacket block slopers. The researchers adapted the general form into a kimono-styled jacket, so there were minimal seams in the coat and the production would be quicker and less expensive. No shoulder pads were used with this design. The front closure was a wrap style so the centre front seam was extended in both directions. A belt can be tied on the outside of the coat to keep it closed, eliminating the need for buttons.

The Cradle to CradleSM environmentally certified wool fabric was used as the coat outer shell. The Cradle to CradleSM certification ensures the fabric production processes, including chemicals used, have been rigorously tested and is environmentally friendly and safe for human health. The fabric came in a variety of colour choices, but only one type (flannel) and fabric weight. After assessing the fabrics and reviewing literature (Gam, Cao, Bennett, Helm Kemp, & Farr, 2011), the researchers decided that these fabrics were suitable for coat outer shell, but lining was needed. To improve warmth comfort of the coat, and to convert waste into valuable resources, chicken feather fibres were used as the fibrefill for the coat. It was found that chicken feather fibres were short and could move and make fibrefill uneven. The researchers decided to use chicken feather fibrefill quilted with sateen organic cotton fabric as lining. Figure 4 shows the coat, and summary of the materials used in the coat is in Table 1.

4. Evaluation of the prototypes

Human subject wear tests and questionnaire surveys were designed to evaluate the user's acceptance and comfort of the prototype shoes and the coat. The two testing protocols have been approved by the university's Institutional Research Board prior to the testing.

4.1. Wear tests

The coat was made in 'Medium' size, and the shoes were made in size 7. Ten female college students who wear 'Medium' size coat and size 7 shoes were recruited to participate in the wear tests. The students were asked to wear a shirt and socks when they came to participate in the tests.



Figure 3. The prototype shoes.

Table 1. Materials used in the shoes and coat.

Product	Part	Materials
Shoes	Upper	Eco-leather composites
	Lining	Sateen organic cotton fabric
	Insole	Chicken feather quilted with sateen organic cotton fabric
	Outsole	Thermosetting resin
	Heel	Thermosetting resin and hard composite
Coat	Outer shell	Cradle to Cradle SM certified wool fabric
	Quilted lining	Chicken feather fibrefill quilted with sateen organic cotton fabric

For each wear test session, only one student was present and participating. The researchers briefly explained the background and purpose of the research, and then presented the shoes and coat to the participant.

In the shoes testing, the participant first viewed the shoes, then put the shoes on sock-covered feet while remaining seated. After that, the participant stood up, walked 10 regular steps away from the desk and walked 10 regular steps back on a hard floor. Then, the participant walked outside of the room and walked on a combination of hard floor, carpet, and stairs. Following each section of viewing, putting on and seated, walking on hard floor, and walking on a combination of hard floor, carpet, and stairs, the participant answered questions related to fit and comfort.

In the coat testing, the participant first viewed the coat, and then donned the coat over a shirt, tied the belt of the coat around the waist, and remained standing. After that, the participant was prompted to perform a series of movements:



Figure 4. The prototype coat.

stretching arms out to either side, making a 'T' shape; raising both arms above head for 5 s; crossing the arms in front of chest to 'hug yourself'; and walking 10 steps forward and walking 10 steps back. Following each section of viewing, donning and standing, and movements, the participant answered questions related to fit and comfort.

In the last section, the researchers provided the participant with knowledge about sustainability and environmentally friendly materials used in the shoes and coat, the participant then answered a few more ‘follow-up’ questions. The questions in the wear tests included 5-point Likert scales with 5 as ‘being the most/best’ or ‘strongly agree’ and open-ended questions for comments.

4.2. Survey

The questionnaire surveys were conducted with 40 female college students. The participants were randomly separated into two groups, with 20 students in each group. The participants in the first group were educated about the advances of renewable bio-based materials, the positive effects on the environment, and the purpose of the project. Then, they were presented the shoes and coat and asked to complete the questionnaire. The participants in the second group did not have the ‘sustainability education’ part. The researchers presented the shoes and coat to the participants, and then they were asked to complete the same questionnaire. The questions in the survey included 7-point Likert scales with 7 as ‘extremely good’ or ‘strongly agree’, and open-ended questions for comments.

5. Evaluation results and discussion

5.1. Wear tests

The results of wear testing scales for the shoes are in Table 2. After viewing the shoes, half (5 out of 10) of the participants rated scale ‘2’ on the question ‘How “fashionable” do the

shoes appear’ (mean = 2.6), and half (5 out of 10) of the participants rated scale ‘1’ on the question ‘Would you buy these shoes’ (mean = 2.2). The design of the shoes was considered not ‘fashionable’ by female college students, and this was one of the reasons that they did not want to buy. For the question ‘Would you buy shoes with different design or style with these materials’, half (5 out of 10) of the participants rated scale ‘4’ (mean = 4.1), indicating a significant increase in willingness to buy the shoes (paired samples *t*-test comparing Q5 and Q6 in Table 2 *p*-value <0.01) if the style met their requirements. The participants liked the materials but did not like the shoe style. Half (5 out of 10) of the participants rated scale ‘5’ on the question ‘How suitable is the sole material’ (mean = 3.8). However, the mean for the question ‘How suitable is the upper material’ was 2.8. Five participants commented that they did not like the colour of the eco-leather as the upper material.

Table 3 summarises the analysis of variance (ANOVA) results comparing fit and comfort in different wearing situations, i.e. seated, walking on hard floor in a room, and walking on a combination of hard floor, carpet, and stairs outside of a room. All of the *p*-values for the homogeneity of variance Levene’s tests were above 0.05, indicating equal population variances (homogeneity). All ANOVA *p*-values were above 0.05. Therefore, the participants did not feel significant difference in fit, overall comfort, upper material comfort, and sole material comfort when they were seated or walked. The means of the scales from questions 7–18 in Table 2 were 3.9 or higher, indicating that the shoes fit well for the participants and were comfortable to wear in different situations. The upper material of eco-leather was

Table 2. Shoes wear test results (5-point Likert scale).

Section	Questions	Mean	σ
Appearance (just viewing)	1. How ‘fashionable’ do the shoes appear?	2.6	1.17
	2. How comfortable do the shoes appear?	3.1	1.29
	3. How suitable is the upper material?	2.8	1.23
	4. How suitable is sole material?	3.8	1.55
	5. Would you buy these shoes?	2.2	1.40
	6. Would you buy shoes with different designs or styles with these materials?	4.1	1.23
Wear (seated)	7. How well do the shoes fit?	4.2	1.23
	8. How comfortable are the shoes overall?	4.3	0.67
	9. How comfortable is the upper material?	4.4	0.70
	10. How comfortable is the sole?	4.1	1.20
Wear (walk 10 steps in a room: hard floor)	11. How well do the shoes fit?	3.9	0.88
	12. How comfortable are the shoes overall?	3.9	0.74
	13. How comfortable is the upper material?	4.4	0.52
	14. How comfortable is the sole?	4.0	0.94
Wear (walk on a combination of hard floor, carpet, and stairs)	15. How well do the shoes fit?	4.0	0.94
	16. How comfortable are the shoes overall?	4.3	0.48
	17. How comfortable is the upper material?	4.4	0.70
	18. How comfortable is the sole?	4.3	0.82
	19. Would you buy the shoes?	3.1	1.20
	20. Would you buy shoes with different designs or styles with these materials?	4.1	0.99

Table 3. ANOVA test results comparing fit and comfort in different wearing situations.

	Homogeneity of variance (Levene statistic) <i>p</i> -value	ANOVA <i>p</i> -value
Fit (comparing Q7, Q11, and Q15 in Table 2)	.598	0.803
Overall comfort (comparing Q8, Q12, and Q16 in Table 2)	.629	0.290
Upper material comfort (comparing Q9, Q13, and Q17 in Table 2)	.598	1.0
Sole material comfort (comparing Q10, Q14, and Q18 in Table 2)	.704	0.793

considered very comfortable with the mean of 4.4 in all wearing situations (questions 9, 13, and 17 in Table 2). The sole was also considered comfortable with the means 4.0 or higher in the three wearing situations (questions 10, 14, and 18 in Table 2). Most of the following comments were positive. The participants commented that the materials were comfortable, wearable, versatile, and practical. After wearing, the participants' willingness to buy the prototype shoes significantly increased (paired samples *t*-test comparing Q5 and Q19 in Table 2 *p*-value = 0.02). Two participants commented that they felt comfortable when wearing them and were more inclined to buy.

There were a few negative comments after wearing the shoes. Three participants commented that the bottom was slippery or needed more traction. Two participants

Table 5. Paired samples *t*-test results comparing fit and comfort in different wearing situations.

	Paired samples <i>t</i> -test <i>p</i> -value
Fit (comparing Q7 and Q11 in Table 4)	.17
Overall comfort (comparing Q8 and Q12 in Table 4)	.34
Warm (comparing Q10 and Q15 in Table 4)	.08
Skin comfort (comparing Q9 and Q17 in Table 4)	.44

mentioned that the outsole lacked flexibility, and two participants mentioned that insole was slippery or not comfortable. It was also noted that the outsole resin crackled when one participant walked outside of the building in a cold temperature (below 10°C). The possible reason was the relatively high glass transition temperature (T_g) of the resin.

The results of wear testing scales for the coat are in Table 4. Questions 14 and 16 in Table 4 were reverse ordering that the lower rating was considered as more positive. After viewing the coat, the participants considered the design 'fashionable' (mean = 4.2), the coat comfortable (mean = 3.8), and the outer and quilted lining materials suitable (mean = 4.2 for outer material and mean = 4.3 for quilted lining).

The participants' feedbacks on the wearing experience were mostly positive (better than the neutral scale of 3). The only negative means were questions 16 (reverse ordering question, mean = 3.6 indicating participants felt the coat too heavy) and 19 (mean = 2.9). Table 5 summarises the

Table 4. Coat wear test results (5-point Likert scale).

Section	Questions	Mean	σ
Appearance (just viewing)	1. How 'fashionable' does the coat appear?	4.2	0.79
	2. How comfortable does the coat appear?	3.8	1.14
	3. How suitable does the outer material seem?	4.2	1.23
	4. How suitable does the quilted lining seem?	4.3	1.06
	5. Would you buy this coat?	3.4	1.17
	6. Would you buy coats with different designs or styles with these materials?	4.5	0.71
Wear (donning and standing)	7. How well does the coat fit?	4.1	0.88
	8. How comfortable is the coat overall?	3.6	1.07
	9. How comfortable is the coat on skin?	3.1	0.99
Wear (after a series of movements)	10. How warm is the coat?	3.9	0.88
	11. How well does the coat fit?	3.7	0.82
	12. How comfortable is the coat overall?	3.4	1.07
	13. How flexible is the coat?	3.0	1.25
	14. How much limit your range of motion?	2.6	1.17
	15. How warm is the coat?	4.2	0.79
	16. How heavy is the coat?	3.6	0.70
	17. How comfortable is the coat on skin?	3.3	1.42
	19. Would you buy the coat?	2.9	1.10
	20. Would you buy coats with different designs or styles with these materials?	3.8	1.55

paired samples *t*-test results comparing fit and comfort in different wearing situations, i.e. standing still and after different arm movements and walking. All of the *p*-values for the *t*-tests were above 0.05, indicating that there were no significant differences in fit and comfort between standing still and body movements. The coat could easily adjust for body movements, and the participants' feelings on warmth and comfort were consistent. After wearing the coat, the participants' willingness to buy the prototype coat or coats with different styles but same materials did not significantly change (paired samples *t*-test: comparing Q5 and Q19 in Table 4 *p*-value = 0.24; comparing Q6 and Q20 in Table 4 *p*-value = 0.21).

In the last section of wear tests, after learning the environmental problems related to textile and apparel materials, and the environmentally friendly materials used in the prototype shoes and the coat, the participants rated favourably on the statement 'I would be more likely to buy the prototypes knowing that they are made from sustainable materials' (mean = 4.2, $\sigma = 1.03$ for the shoes; and mean = 3.8, $\sigma = 1.48$ for the coat), and the statement 'I would view the prototypes of these same materials favourably if made in another design or style' (mean = 4.2, $\sigma = 1.03$ for the shoes; and mean = 4.4, $\sigma = 0.97$ for the coat). The participants were interested in the apparel and footwear made from sustainable materials. For the eco-leather material, six (out of ten) participants considered it a possible substitute for leather, and another three participants commented that it could replace leather in some applications. Seven participants thought eco-leather could be used on bags, purses, and totes. Among them, one commented eco-leather might only be used in small bags or wallets. Using renewable bio-based plant oils and natural fibres as starting materials, eco-leather could possibly be an environmentally friendly substitute for leather and PVC pleather in apparel, footwear, and accessories applications.

5.2. Survey

The survey results for the prototype shoes are in Table 6. The first six questions were related to the materials and design of the shoes. The participants positively rated the quality of the materials, feel/hand, overall appearance, and comfort of the shoes. The shoe style was not similar to the shoes the participants owned. This result was consistent to the wear test finding that female college students did not consider it 'fashionable,' and did not like the style. The last five questions were related to the participants' attitudes towards sustainable materials and products. The participants were interested in and willing to buy sustainable products, however, their answers to 'willing to pay more for sustainable products' (question 9 in Table 6) were close to a neutral scale of 4. Comparing the two groups of participants who were given the materials sustainability education and who were not, the *t*-tests showed that the group with sustainability education had significantly different rating on quality of materials (question 1 in Table 6, *p*-value = 0.03), and more apt to buy sustainable products (question 8 in Table 6, *p*-value = 0.03). These shoe materials, i.e. eco-leather upper, bio-based resin sole, bio-based composite heel, were new to these college students. They considered these sustainability characteristics as part of material quality and rated higher (mean = 5.20, compared with mean = 4.42 for the 'without education' group). Learning the sustainability characteristics of these new materials also made them more apt to buy sustainable products (mean = 5.30, compared with mean = 4.45 for the 'without education' group).

The survey results for the coat are in Table 7. The first seven questions were related to the materials and design of the coat. All means for the first 7 questions were above the neutral scale of 4 for both groups. The participants positively rated the quality of the outer fabric and quilted lining materials, feel/hand, overall appearance and comfort of the coat. The coat style was similar to the coats the

Table 6. Survey results for the shoes (7-point Likert scale).

Question	With education		W/o education		<i>t</i> -Test <i>p</i> -value
	Mean	σ	Mean	σ	
1. Rate the quality of materials	5.20	1.06	4.42	1.07	0.03
2. Rate feel/hand of the shoes	5.00	1.03	4.40	1.19	0.10
3. Rate overall appearance of the shoes	4.35	1.46	4.35	1.39	1.00
4. Rate the comfort level of the shoes	4.25	0.97	4.50	0.79	0.39
5. Rate the similarity of style as your shoes	3.15	1.90	2.90	1.63	0.66
6. Rate the reflection of current shoe styles	4.50	1.88	4.55	1.76	0.93
7. I am interested in buying sustainable fashion	5.60	1.47	5.85	0.99	0.53
8. I am more apt to buy sustainable products	5.30	1.03	4.45	1.39	0.03
9. I am willing to pay more money for sustainable products	3.80	1.61	4.10	1.62	0.56
10. I am interested in learning more about sustainable products	5.65	1.57	5.40	1.14	0.57
11. I would be more likely to buy the sample shoe if it was made from sustainable materials	4.30	1.87	4.60	1.60	0.59

Table 7. Survey results for the coat (7-point Likert scale).

Question	With education		W/o education		<i>t</i> -Test <i>p</i> -value
	Mean	σ	Mean	σ	
1. Rate the quality of outer fabric	4.90	1.68	5.65	0.88	0.09
2. Rate the quality of quilted lining	5.50	1.00	5.70	0.92	0.52
3. Rate the feel/hand of coat	5.10	1.02	5.58	0.96	0.14
4. Rate the overall appearance of coat	4.85	1.23	5.25	0.97	0.26
5. Rate the comfort level of the coat	4.90	1.33	5.42	0.84	0.16
6. Rate the similarity of style as your coats	4.25	1.48	4.20	1.74	0.92
7. Rate the reflection of current coat style	4.80	1.28	5.15	1.39	0.41
8. I am interested in buying sustainable fashion	5.65	1.09	5.35	1.39	0.45
9. I am more apt to buy sustainable products	4.75	1.65	4.30	1.53	0.38
10. I am willing to pay more money for sustainable products	3.85	1.60	4.00	1.49	0.76
11. I am interested in learning more about sustainable products	5.50	1.57	5.05	1.28	0.33
12. I would be more likely to buy the sample coat if it was made from sustainable materials	4.50	1.50	4.15	1.06	0.48

participants owned and they considered the coat reflected the current style. The last five questions were related to the participants' attitudes towards sustainable materials and products. Similar to the survey results for the shoes, the participants were interested in and willing to buy sustainable products, however, their answers to 'willing to pay more for sustainable products' (question 10 in Table 7) were close to a neutral scale of 4. Comparing the two groups of participants who were given the materials sustainability education and who were not, the *t*-tests showed that there were no significant differences between these two groups in all questions (all *p*-values > .05). Unlike the shoes, where most of the materials (eco-leather upper, bio-based resin sole, and bio-based composite heel) were developed by the research group and never seen by the participants, most of coat materials were purchased from the market. This may be the reason that the materials sustainability education did not have a significant effect on the participants' opinion on material quality and apt to buy sustainable products.

6. Conclusion

This research developed new materials for the apparel and footwear industry, i.e. water-resistant but breathable composites as leather substitutes (eco-leather), a thermosetting resin, and a hard composite, from renewable bio-based sources, such as plant oils, natural fibre cloth, and chicken feather fibres. These materials, together with commercially available environmentally friendly textiles from renewable sources, such as organic cotton and Cradle to CradleSM certified wool fabrics, were used to develop shoes and a coat. Green chemistry (Anastas & Warner, 1998) and green engineering (Anastas & Zimmerman, 2003) principles were applied in the development of materials and products. The green chemistry and engineering principles of less hazardous chemical syntheses and processes, and waste prevention were applied by using environmentally friendly textiles and development of eco-leather to replace

leather or PVC pleather. Furthermore, the green chemistry and engineering principles of using renewable feedstocks or recourses were applied by using bio-based renewable plant oils and natural fibre cloth as starting materials for material syntheses. This research identifies the feasibility of applying the principles of green chemistry and engineering to materials development for the apparel and footwear industry.

Wear tests and surveys were conducted to evaluate the users' acceptance of materials and prototypes. The wear tests concluded the shoe upper (eco-leather) and sole materials, and the environmentally friendly textile materials used in the coat, were found to be comfortable. The participants thought the renewable bio-based materials developed by CBE researchers were wearable, versatile, and practical. If the design and style met their requirements, the participants were willing to buy the apparel and footwear products made from these environmentally friendly materials. They considered sustainability as part of material quality, especially for the shoe materials developed by the CBE researchers in this project. Though the participants expressed general interest in buying sustainable apparel and footwear products, their willingness to pay more for sustainable products was not high (close to a neutral scale).

The wear tests and survey also found areas of future improvements for the bio-based materials and product design. Future improvements for outsole thermosetting resin will be in reducing T_g and adding traction. Reducing T_g could prevent crackling in cold weather and make the material more flexible. Possible methods to reduce T_g include modifying the composition of AESO/MLAU or adding environmentally friendly plasticisers. Adding traction can be accomplished by using a different mould. Future improvements for eco-leather upper material will be focused on adding colours. The colour of the eco-leather was due to the off-white colour of the greige-goods organic cotton fabrics. Coloured eco-leather could be produced in two ways: adding dyes or pigments in the eco-leather

production; or using coloured fabrics in the eco-leather development. Female college students participated in this study considered the design of the shoes not 'fashionable.' Future improvements for shoe development will be focused on designing new styles for young wearers.

The limitations in this research included that only one apparel prototype and one footwear prototype were made and tested; all of the participants in the wear tests and survey were from a university on the eastern coast of the USA; and the numbers of participants in wear and survey tests were relatively low. The target users of the prototypes are female college students. Human subject tests with female students in other universities and regions and different styles of apparel and footwear prototypes will help better understand user acceptance of apparel and footwear products made from renewable bio-based materials. It will also help disseminate the renewable bio-based apparel and footwear materials to a larger population.

Acknowledgements

This research was supported by U.S. Environmental Protection Agency (USEPA) grant No. SU834707. Its contents are solely the responsibility of the grantee and do not necessarily represent the official views of the USEPA. Further, USEPA does not endorse the purchase of any commercial products or services mentioned in the publication. The authors thank Reebok International Ltd., Canton, MA, for the assistance in making the prototype shoes.

References

- Allwood, J. M., Laursen, S. E., de Rodriguez, C. M., & Bocken, N. M. P. (2006). *Well dressed? The present and future sustainability of clothing and textiles in the United Kingdom*. Cambridge: University of Cambridge, Institute of Manufacturing (ISBN 1-9024526-52-0).
- American Apparel and Footwear Association (2009). *Trends: An annual statistical analysis of U.S. apparel and footwear industries (annual 2008 edition)*. Retrieved March 31, 2013, from <https://www.wewear.org/assets/1/7/Trends2008.pdf>
- Anastas, P. T., & Warner, J. C. (1998). *Green chemistry: Theory and practice*. New York, NY: Oxford University Press.
- Anastas, P. T., & Zimmerman, J. B. (2003). Design through the 12 principles of green engineering. *Environmental Science and Technology*, 37, 94A–101A.
- Armstrong, C. M., & LeHew, M. L. A. (2011). Sustainable apparel product development: In Search of a new dominant social paradigm for the field using sustainable approaches. *Fashion Practice: The Journal of Design, Creative Processes, and the Fashion*, 3, 29–62.
- Barone, J. R., & Schmidt, W. F. (2005). Polyethylene reinforced with keratin fibers obtained from chicken feathers. *Composites Science and Technology*, 65, 173–181.
- Behr, A., & Johnen, L. (2009). Alternative feedstocks for synthesis. In P. T. Anastas (Ed.), *Handbook of green chemistry – green processes*, Chap 3, pp. 69–92. In C.-J. Li (Ed.), *Green Synthesis*, Vol. 7. Weinheim, Germany: Wiley-VCH.
- Bergman, Å., Heindel, J. J., Jobling, S., Kidd, K. A., & Zoeller, R. T. (2013). *State of the science of endocrine disrupting chemicals – 2012*. World Health Organization and United Nations Environmental Programme (ISBN 9789241505031 (WHO) and 978-92-807-3274-0 (UNEP)), Geneva, Switzerland. Retrieved March 31, 2013, from <http://www.unep.org/hazardoussubstances/UNEPsWork/StateoftheScience/tabid/105913/Default.aspx>
- Campanella, A., Bonnaillie, L. M., & Wool, R. P. (2009). Polyurethane foams from soyoil-based polyols. *Journal of Applied Polymer Science*, 112, 2567–2578.
- Cheng, S., Lau, K., Liu, T., Zhao, Y., Lam, P.-M., & Yin, Y. (2009). Mechanical and thermal properties of chicken feather fiber/PLA green composites. *Composites Part B: Engineering*, 40, 650–654.
- Gam, H. J., Cao, H., Bennett, J., Helmkemp, C., & Farr, C. (2011). Application of design for disassembly in men's jacket: A study on sustainable apparel design. *International Journal of Clothing Science and Technology*, 23, 83–94.
- Gam, H. J., Cao, H., Farr, C., & Heine, L. (2009). C2CAD: A sustainable apparel design production model. *International Journal of Clothing Science and Technology*, 21, 166–179.
- Golden, J. S., Subramanian, V., & Zimmerman, J. B. (2011). Sustainability and commerce trends. *Journal of Industrial Ecology*, 15, 821–824.
- Hong, C. K., & Wool, R. P. (2005). Development of a bio-based composite material from soybean oil and keratin fibers. *Journal of Applied Polymer Science*, 95, 1524–1538.
- Huda, S., & Yang, Y. (2009). Feather fiber reinforced lightweight composites with good acoustic properties. *Journal of Polymers and the Environment*, 17, 131–142.
- Khot, S. N., Lascala, J. J., Can, E., Morye, S. S., Williams, G. I., Palmese, G. R., ... Wool, R. P. (2001). Development and application of triglyceride based polymers and composites. *Journal of Applied Polymer Science*, 82, 703–723.
- La Scala, J., & Wool, R. P. (2005). Property analysis of triglyceride-based thermosets. *Polymer*, 46, 61–69.
- Lu, J., & Wool, R. P. (2008). Additive toughening effects on new bio-based thermosetting resins from plant oils. *Composites Science and Technology*, 68, 1025–1033.
- McGovern. (2000). Recycling poultry feathers: More bang for the cluck. *Environmental Health Perspectives*, 108(8), A366–A369.
- Nair, A. D. G., Hansdah, K., Dhal, B., Mehta, K. D., & Pandey, B. D. (2012). Bioremoval of Chromium (Iii) from model tanning effluent by novel microbial isolate. *International Journal of Metallurgical Engineering*, 1(2), 12–16.
- Tariq, S. R., Shah, M. H., & Shaheen, N. (2009). Comparative statistical analysis of chrome and vegetable tanning effluents and their effects on related soil. *Journal of Hazardous Materials*, 169, 285–290.
- Thornton, J. (2002). *Environmental impact of polyvinyl chloride building materials*. Healthy Building Network (ISBN 0-9724632-0-8). Retrieved March 31, 2013 from http://www.healthybuilding.net/pvc/Thornton_Enviro_Impacts_of_PVC.pdf
- Zhan, M., Wool, R. P., & Xiao, J. Q. (2011). Electrical properties of chicken feather fiber reinforced epoxy composites. *Composites Part A: Applied Science and Manufacturing*, 42, 229–233.
- Zhu, L., & Wool, R. P. (2006). Nanoclay reinforced bio-based elastomers: Synthesis and characterization. *Polymer*, 47, 8106–8115.



Article

Application of Bacterial Cellulose in the Textile and Shoe Industry: Development of Biocomposites

Marta Fernandes ¹, António Pedro Souto ¹, Fernando Dourado ² and Miguel Gama ^{2,*}

- ¹ 2C2T-Centre for Textile Science and Technology, Campus de Azurém, University of Minho, 4800-058 Guimarães, Portugal; marta.fernandes@det.uminho.pt (M.F.); souto@det.uminho.pt (A.P.S.)
- ² CEB-Centre of Biological Engineering, Campus de Gualtar, University of Minho, 4710-057 Braga, Portugal; fdourado@deb.uminho.pt
- * Correspondence: fmgama@deb.uminho.pt; Tel.: +351-253-604-418

Abstract: Several studies report the potential of bacterial cellulose (BC) in the fashion and leather industries. This work aimed at the development of BC-based composites containing emulsified acrylated epoxidized soybean oil (AESO) that are polymerized with the redox initiator system hydrogen peroxide (H₂O₂) and L-ascorbic acid and ferrous sulfate as a catalyst. BC was fermented under static culture. The polymerization of the emulsified organic droplets was tested before and after their incorporation into BC by exhaustion. The composites were then finished with an antimicrobial agent (benzalkonium chloride) and dyed. The obtained composites were characterized in terms of wettability, water vapor permeability (WVP), mechanical, thermal and antimicrobial properties. When AESO emulsion was polymerized prior to the exhaustion process, the obtained composites showed higher WVP, tensile strength and thermal stability. Meanwhile, post-exhaustion polymerized AESO conferred the composite higher hydrophobicity and elongation. The composites finished with the antimicrobial agent showed activity against *S. aureus*. Finally, intense colors were obtained more uniformly when they were incorporated simultaneously with the emulsified AESO with all the dyes tested.

Keywords: bacterial cellulose; acrylated epoxidized soybean oil; biocomposite; emulsion polymerization; leather; textile

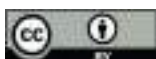


Citation: Fernandes, M.; Souto, A.P.; Dourado, F.; Gama, M. Application of Bacterial Cellulose in the Textile and Shoe Industry: Development of Biocomposites. *Polysaccharides* **2021**, *2*, 566–581. <https://doi.org/10.3390/polysaccharides2030034>

Academic Editors: Alessandra Braga Ribeiro, Ricardo J. B. Pinto and Cédric Delattre

Received: 11 May 2021
Accepted: 28 June 2021
Published: 2 July 2021

Publisher's Note: MDPI stays neutral with regard to jurisdictional claims in published maps and institutional affiliations.



Copyright: © 2021 by the authors. Licensee MDPI, Basel, Switzerland. This article is an open access article distributed under the terms and conditions of the Creative Commons Attribution (CC BY) license (<https://creativecommons.org/licenses/by/4.0/>).

1. Introduction

An emerging trend within the fashion fabric industry concerns the eco-friendliness and sustainability of the production of fabrics in using bio-based materials or products derived from renewable resources with properties interesting enough to warrant commercial viability. The groundbreaking concept of self-grown fabrics from natural renewable resources such as bacterial cellulose, seaweed, algae, kelp, fungi and mycelium, has increased collaborative efforts between designers and scientists to explore the use of these natural green materials in textiles. A case in point is bacterial cellulose (BC), a highly pure biopolymer produced by fermentation of bacteria such as those of the genus *Komagataeibacter*. Under static conditions, BC is produced in the form of a gelatinous three-dimensional nano-fibrous network [1,2]. Compared to vegetable cellulose, BC presents unique properties including high crystallinity [3], high specific surface area [4], high water absorption [5] and high mechanical strength [6]. The unique structure and impressive physico-mechanical properties of BC have supported the development of several applications in different areas, such as food packaging [7,8], biomedical [9,10], cosmetics [11], filtration [12,13] and electronic devices [14,15]. BC is also emerging as a potential alternative to conventional woven/leather materials. The German start-up ScobyTec developed a vegan alternative to leather made of BC produced from kombucha, which was used to make various products such as gloves, children's shoes and business handbags. The material, called ScobyTec BNC, possesses high mechanical strength and is non-flammable [16]. In the project SOYA

C(O)U(L)TURE, settled by the Indonesian collective XXlab, BC is produced using the liquid waste from tofu production. The cellulose sheets are further pressed, dried, colored and coated [17]. The company Malai Design & Materials from India is also using coconut wastewater for the fermentation of BC. The obtained BC sheets are processed and can be reinforced with natural fibers, resins and gum to create a leather-like material [18]. The growing attention given to BC as an alternative to leather and cotton-based products is due to its leather-like appearance. Furthermore, the moldability of BC and the possibility of growing it in any shape are advantageous for the development of fashion products and an example includes the following: Fermenting BC under static culture which results in planar sheets or in pre-defined 3D forms. The formed BC could also be recultivated by resubmerging the sheets or 3D prototypes into fresh broth to produce complex structures and with textural characteristics. Alternatively, the formed planar BC could be dried in 3D molds (e.g., wooden mannequin) [19]. BC-based 3D art integrating SMD-LED (surface-mounted device-light-emitting diode) through conductive threads was developed by molding BC [20]. BC produced with a desired shape represents a peculiar approach to producing clothing with zero-waste. Each part of the garment was fermented to the required size and shape and then dyed and finished with animal oil or wax [21]. The moldability of BC was also studied by placing wet BC produced with a natural dye extract in a preform followed by drying [22].

In the following subsections, we review the scientific work carried out within the scope of the application of BC in the textile and fashion industry. Within this application scope, results from the development of novel bacterial cellulose (BC)-based composites containing emulsified AESO polymerized with a new redox initiator system are presented. This system, which is composed of hydrogen peroxide and L-ascorbic acid and ferrous sulfate as a catalyst, is biodegradable and can be used in the polymerization of AESO at amenable temperatures (30 °C). The composites were surface-treated with biocide to confer antimicrobial properties. Finally, these composites were also dyed.

1.1. BC Coated on Fibers, Yarns, Fabrics

An approach to the use of BC in the textile industry, consists of coating fibers, yarns, or fabrics with BC nanofibers, increasing the surface area and the mechanical properties of the obtained composites. The interfacial adhesion of natural fibers, such as hemp and sisal fibers, with biopolymers significantly increased by adding those fibers to the BC culture medium before fermentation [23]. In order to develop wearable electronics, cotton yarns were first soaked in BC nanofiber suspension under sonication to increase the surface area before the deposition of pyrrole [24]. Hybrid fabrics (wool/BC, silk/BC, cotton/BC, cellulose acetate/BC, nylon/BC, polyester/BC, Kevlar[®]/BC, viscose rayon/BC and Bemlise[®]/BC) were developed by producing BC with different fabrics added to the culture medium. In order to obtain double-sided coating, the fabrics were inverted during the experiments. Although BC was produced at the surface of all fabrics, it showed no affinity for the non-cellulosic material and easily peeled off during the NaOH washing step [25]. A similar procedure was used to develop cotton, polyester and rayon hybrid fabrics where the BC coating increased the thickness and bursting strength and decreased the penetration of water through the composite fabrics and the water vapor permeability [26]. A method to produce BC/ENM (regenerated cellulose electrospun nanofibrous membrane) hybrid fabrics with targeted dimensions was developed through in situ self-assembly, by adding a polypropylene mesh template to the fermentation medium. The growth of BC nanofibers into the empty voids of the mesh improved the fabric performance by decreasing the surface hydrophobicity and water uptake, while increasing the tensile strength of the composite [27].

1.2. Regenerated BC Fibers

Regenerated cellulose fibers have been used in the textile industry since the early twentieth century and currently possess a market share of about 6.4% of the total fiber

production. These fibers are traditionally produced from wood pulp or cotton linters, requiring a large plantation area. BC is a sustainable alternative to traditional cellulose sources which can be produced anywhere without the use of forest or land resources [28]. Despite some attempts to harvest cellulosic filament during the cultivation stage [29–31], dissolution seems to be the most promising method for the development of BC continuous filaments. Solutions of BC dissolved in dimethylacetamide/lithium chloride (DMAc/LiCl) and 1-allyl-3-methyl-imidazolium chloride (AMIMCl) were used to prepare BC/multi-walled carbon nanotubes composite fibers by wet-spinning [32] and by electrospinning [33], respectively. Regenerated fibers were also prepared by wet-spinning BC dissolved in *N*-methylmorpholine-*N*-oxide monohydrate (NMMO·H₂O) [34] and in zinc chloride aqueous solution (ZnCl₂·3H₂O) [35]. Other authors prepared regenerated BC blend fibers by wet-spinning, such as BC/alginate using lithium hydroxide/urea/thiourea (LiOH/urea/thiourea) aqueous solvent system [36] or BC/hydroxypropyl chitosan using the solvent NMMO·H₂O [37]. More recently, regenerated BC fibers were produced by dry-jet wet-spinning using NMMO·H₂O as solvent [38].

1.3. Development of BC Macrofibers

The production of macrofibers from oriented BC nanofibers, with promising potential applications such as smart textiles and for structural reinforcement, can also be developed. Macrofibers obtained in a continuous process based on aligned BC nanofibers by wet-spinning were developed in a process where the cellulose suspensions were first prepared by TEMPO oxidation. Then, the suspensions were spun into an acetone coagulation bath and dried. Subsequently, the filaments with a controlled humidity were stretched to align the BC nanofibers. These macrofiber filaments were subjected to cross-linking by multivalent ions, to prevent the decrease of the mechanical properties due to the weakening of the interfacial linkage between the nanofibers in a high moisture environment [39]. BC macrofibers with improved mechanical properties were also prepared by wet-drawn stripes of BC membranes by using a tensile testing machine, to improve the filament alignment. Then the wet-drawn samples were twisted into macrofibers with nine turns per inch and then dried at 90 °C under tension to reduce the voids and to induce a strong interfilament hydrogen bonding. These macrofibers can be shaped and dyed, possessing interesting potential for application in the textile industry [40]. In another work, the alignment of BC nanofibers was achieved via a simple one-step solvent-assisted drawing process. Films of BC were first soaked in *N*-methyl-2-pyrrolidinone solvent, then wet-drawn and followed by hot-press drying at 60 °C. To obtain ultrathin films with high tensile strength and high toughness, layers of the BC film were removed using tape (mechanical exfoliation). These films were then soaked in water and twisted, resulting in strong fibers. The production of multifunctional fibers, namely dyed fibers, CNT (carbon nanotubes)/BC fibers and CoFe₂O₄/BC magnetic fibers, was also demonstrated by soaking aligned BC ultrathin films in the respective solutions followed by sonicating and then twisting and drying [41]. Hierarchical helical nanocomposite macrofibers were developed using a wet-spinning method by extruding mixtures of BC nanofibers dispersions and alginate through a capillary needle into a CaCl₂ coagulation bath, forming filaments with aligned BC nanofibers. Then, two single BC/alginate gel filaments were twisted together into a hierarchical helical BC/Alginate macrofiber, with certain twist levels according to a multilevel wet-twisting process. The alignment of BC contributed to the ultimate mechanical properties of the composite, whereas the alginate matrix contributed to the stress transfer between BC nanofibers, resulting in a simultaneous improvement of the tensile strength, elongation and toughness [42].

1.4. BC Purification, Bleaching and Dyeing

The possibility of coloring materials is a fundamental feature in the textile and footwear sectors. Several studies have been conducted for the color modification of BC, including bleaching, dyeing with natural and artificial dyes and in situ and ex situ dyeing

processes. After cultivation, BC presents a yellowish-brown color derived from the culture medium. Washing of BC with 3% NaOH solution results in the effective removal of bacteria and the remnants of the culture medium that does not affect the BC nanoscale 3D network structure. In order to ensure the subsequent uniform dyeing and bright colors, bleaching with 5% H₂O₂ solution for 60 min at 90 °C removed the brown-yellow color of BC (white index of 73.15), without deforming the cellulose structure [43,44].

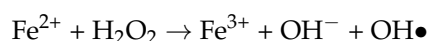
Dyeing of BC was carried out by producing BC in the presence of a direct acid or basic dye in the culture media. Optical microscopy observation showed that the direct and basic dyestuffs stained the BC, but the acid one did not. Analysis of wide angle X-ray diffraction (WAXD) data indicated that direct dyestuffs inhibited the crystallization of BC above 0.05 wt% dyestuff concentration in the culture medium, but basic dyestuff had almost no influence on the BC's crystallization [45]. In another work, in order to produce colored BC nonwovens, different natural and artificial dyes were added to the culture medium. Colors were successfully incorporated into the BC when natural dyes and the blue artificial dye were used, while other artificial dyes inhibited BC growth [46]. The dyeability of BC produced under static culture using in situ and ex situ methods was also studied using direct acid and reactive dyestuffs. Although only the lower half of the BC was colored during the cultivation (in situ method), after drying it showed uniform color on both sides and presented clearer colors when compared with the dried BC colored by the ex situ method [47]. An environmentally friendly process was developed for the bio-coloration of BC via phenolic oxidation by laccase immobilized onto BC. Specifically, flavonoids were successfully polymerized by the immobilized laccase, which gave rise to yellow, orange and dark brown oligomers that colored the BC. Best results were obtained with the flavonoids catechol and catechin [48]. BC films were also dyed by immersion of BC into plant-based natural dye (*Clitoria ternatea* L. and *Hibiscus rosa-sinensis*) solutions, while retaining the crystallinity, thermal and mechanical properties of BC [49].

1.5. Improvement of BC Flexibility, Hydrophobicity and Mechanical Properties

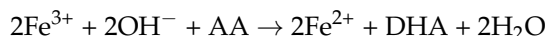
Despite its excellent properties, the hydrophilic nature of BC and the loss of flexibility and porosity upon drying (due to the collapsing of the 3D network) have limited its application in the textile and footwear industry. In order to improve the mechanical properties of BC and to reduce the water regain, PLA and PU-based biopolymers were embedded into BC by dip-coating and electrospinning. Although some improvement was observed in the tensile strength when BC was coated with PU-based biopolymer by electrospinning, further work is needed to, namely, reduce the moisture regain [50,51]. The hydrophobicity and flexibility of BC from kombucha were improved by immersing dried BC sheets in a textile softener solution followed by immersion in a hydrophobic finishing agent solution. BC was then dried at 120 °C for 1 min. From about 60° (native BC) the obtained hydrophobic composite had a water contact angle of 114° [52]. Laccase-assisted reactions allowed the functionalization of BC with poly(fluorophenol) and lauryl gallate oligomers, improving its hydrophobicity and durability (in terms of its dimensional stability and tensile strength). For the functionalization with poly(fluorophenol), laccase was first entrapped onto the surface of the BC fibers and then used to in situ polymerize the fluorophenol. For the lauryl gallate oligomers functionalization, wet BC was submerged in lauryl gallate oligomers that were previously synthesized by laccase. The resulting materials also presented hydrophobic surfaces and durability [53,54]. The flexibility and mechanical properties of BC were also improved by immersion in glycerol and coating the BC fibers with stearic acid [55]. In a recent work, the durability of BC was improved by physically entrapping plant-based proteins (from soy and mushroom) and glycerol to improve their processability. The reinforced BC also presented higher contact angle, tensile strength, improved flexibility, crease recovery and dimensional stability [56]. Two recently published reviews analyzed the methods of producing BC and their application in the fashion sector [57,58].

In our previous works, BC was used as a structuring material for the development of a new leather analogue from alternative biological products, specifically modified vegetable oils and other hydrophobic polymers. BC was submitted to an exhaustion process, allowing the bulk impregnation of hydrophobic polymers such as commercial nano/microparticles, Persoftal MS Con.01 (polydimethylsiloxane (PDMS)-based) and Baygard EFN (perfluorocarbon (PFC)-based) and acrylated epoxidized soybean oil (AESO) [59–61]. In our first approach, BC-based nanocomposites were developed by impregnating BC membranes with PDMS-based or PFC-based products, either separately or combined in a sequential process. The obtained composites were hydrophobic (maximum contact angle (CA) of 135°), breathable (maximum water vapor permeability of 373 g·m⁻²·24 h⁻¹) and possess satisfactory performance regarding the mechanical properties (maximum tensile strength of 48.4 MPa) [61]. Then, aiming at increasing the bio-based content of the composite, BC membranes were impregnated with acrylated epoxidized soybean oil (AESO) in a mixture also containing the PDMS-based polymer and polyethylene glycol (PEG) 400 as a plasticizer, yielding a product with greater elasticity and improved BC-polymers interfacial adhesion. The hydrophobic BC composites owned distinct performances, which were manipulated by varying the percentage of the polymer [59]. Using another approach, AESO resin was emulsified prior to the exhaustion process to allow its better diffusion into the bulk of the BC 3D network, being used in mixtures containing PEG 400, PDMS-based and PFC-based products. The resulting composites were hydrophobic (maximum CA of 138°) and thermally stable (up to 200 °C) and, overall, endowed with suitable mechanical properties for the proposed application (maximum tensile strength of 36 MPa) [60].

Despite the successful preparation of these composites based on BC and emulsified AESO [60], the catalysts used were highly toxic to the environment. In this work, we demonstrate the AESO polymerization with a less aggressive redox initiator system: hydrogen peroxide (H₂O₂) (oxidant), L-ascorbic acid (AA) (reductant) and ferrous sulfate (FeSO₄) as the catalyst; and under lower temperature (30 °C). The mechanism of redox reaction involves the transfer of a one-electron from the ferrous ion (Fe²⁺) to hydrogen peroxide, dissociating peroxide's oxygen–oxygen bond and generating one hydroxyl radical and one hydroxyl ion described as follows.



The reducing agent (AA) is transformed into dehydroascorbic acid (DHA) during the regeneration of Fe²⁺ to Fe³⁺, allowing the generation of new radicals, which is described as follows [62].



The biodegradability of vegetable oils, which is advantageous from an ecological and environmental point of view, implies their susceptibility to an enzymatic attack by microbial lipases. The scientific literature describes the enzymatic degradation of epoxidized, acryloylated and cross-linked vegetable oils [63]. Using biocides could be a simple strategy to delay this biodegradability during the useful life cycle of the materials. In order to minimize the chances of a rapid degradability of the composites, the surface functionalization of the BC composites with antimicrobial properties was studied.

The dyeing of cellulosic fibers is commonly achieved using reactive, direct or vat dyes. They are applied by different processes, according to the conditions required to achieve a good diffusion and fixation rate, uniformity and adequate fastness. Exhaustion processes are carried out in aqueous solutions of dyes in the presence of suitable auxiliaries capable of promoting affinity between the dye and the fiber at the appropriate temperature and time to complete the diffusion of the dye, its adsorption and fixation onto the surface of the fiber [64]. Although the general mechanisms involved in the BC-based composites dyeing can be generally drawn from the dyeing process of textile cellulosic fibers, adding polymeric mixtures in the production of the composites may change the dyeing process. Thus, in

this work, the dyeing of composites with different dyes was tested by applying the dye (i) simultaneously with the production of the composites and (ii) in the obtained composites.

2. Materials and Methods

2.1. Materials

BC membranes were offered by Satisfibre S.A. (Braga, Portugal). Soybean oil, epoxidized acrylate (Sigma-Aldrich, Steinheim, Germany), lauryl methacrylate (97%) (Acros Organics, Geel, Belgium), 1,6-hexanediol diacrylate (80%) (Sigma-Aldrich, Steinheim, Germany), tri(propylene glycol) diacrylate (Sigma-Aldrich, Steinheim, Germany), Triton X-100 (Sigma-Aldrich, Steinheim, Germany), isobutanol (Merck Millipore, Darmstadt, Germany), hydrogen peroxide (30%) (Sigma-Aldrich, Steinheim, Germany), L-ascorbic acid (Sigma-Aldrich, Steinheim, Germany), ferrous sulfate (Merck Millipore, Darmstadt, Germany) and polyethylene glycol 400 (Merck Millipore, Darmstadt, Germany) were used as received. Persoftal MS Conc.01 and Baygard EFN (Tanatex Chemicals, Ede, The Netherlands) were offered by the ADI Center (Santo Tirso, Portugal). The antimicrobial finishing chemicals and the dyes were kindly supplied by Smart Inovation (Barcelos, Portugal) and DyStar (Porto, Portugal), respectively.

2.2. Development of Composites with AESO Emulsion Polymerized before and after Exhaustion

2.2.1. Emulsion Polymerization and Development of the Composites

For the production of BC-based composites by the incorporation of a mixture of Persoftal MS Conc.01 (polydimethylsiloxane (PDMS)), polyethyleneglycol (PEG) 400 and acrylated epoxidized soybean oil (AESO), different mixtures were prepared as presented in Table 1.

Table 1. Proportions of each component in the mixtures used in the production of BC composites.

AESO Mixture (%)		AESO Emulsion (%)		Polymers Mixture (Exhaustion) (%)	
AESO	50	AESO mixture	20	AESO emulsion	75
Lauryl methacrylate	40	Triton-X-100/Butanol (2/1)	2	Persoftal MS Con.01	20
1,6-hexanediol diacrylate	5	Water	78	PEG 400	5
Tri(propylene glycol diacrylate	5				

First, a mixture was prepared by adding different reactive monomers to AESO to improve its processability and enhance crosslinking. This mixture was composed of AESO (50% m/m); lauryl methacrylate (40% m/m)-a fatty acid-based reactive diluent to reduce the viscosity of the mixture [65]; 1,6-hexanediol diacrylate (5% m/m) and tri(propylene glycol diacrylate (5% m/m) used as crosslinking enhancers [66]. Then, a mixture with a mass ratio of 20:2:78 (AESO mixture/surfactant (Triton-X-100/Butanol 2/1)/water) was emulsified using a homogenizer (Unidrive X 1000 D, CAT, Staufen, Germany) at a speed of 25,000 rpm for 12 min.

The polymerization of the AESO emulsion was first tested using a redox initiator system, hydrogen peroxide (H₂O₂) (oxidant), L-ascorbic acid (AA) (reductant) and with ferrous sulfate (FeSO₄) as the catalyst. A flask containing the AESO mixture emulsion was placed in an ultrasound bath to avoid agglomeration and, per 100 g of the emulsion, 0.003 g of FeSO₄ were added followed by 1.5 g of H₂O₂ (30%) (previously dissolved in water); after 20 min, 0.9 g of AA (previously dissolved in water) were added to the mixture in five portions and in intervals of 20 min each. The polymerization was carried out for 3 h more at 25 °C.

For the production of the composites, 8 BC membranes with about 3.5 cm in thickness, a size of 13.0 × 24.0 cm and weighting 900 g (wet mass) were first mechanically pressed to remove the excess of water to a final wet mass of 200 g, corresponding to 5.5% dry mass in BC and a thickness of around 0.5 cm. The compressed membranes were then treated by exhaustion with 1200 mL of a mixture containing 75% of the emulsified AESO mixture, 20%

Persoftal MS Con.01 and 5% PEG 400 (Table 1): four of which with the emulsified AESO mixture previously polymerized as described above (Composite A) and another four with the non-polymerized emulsified AESO mixture (Composite B).

The exhaustion process was carried out in an Ibelus machine equipped with an infrared heating system using a container with a capacity of approximately 2200 cm³, with a rotation of 50 rpm for 40 cycles. Starting from room temperature, the desired temperature (30 °C) was achieved using a gradient of 2 °C·min⁻¹. The treatment lasted for 7 days at 30 °C, after which the samples were oven dried (WTC binder oven) at 40 °C until constant mass. For the Composite B (samples produced with the non-polymerized AESO emulsion), after exhaustion and before drying, the membranes were treated again by exhaustion with a new solution containing the redox initiators and the catalyst for 3 days at 30 °C to polymerize the impregnated emulsion.

2.2.2. Characterization of the Composites

The obtained composites were evaluated according to their wettability, water vapor permeability (WVP) and mechanical and thermal properties.

The wettability of the samples was characterized via static contact angle measurements using a Dataphysics instrument and OCA20 software (version 1.5, Dataphysics, Filderstadt, Germany) with a video system for the capture of images in static mode using the sessile drop method. At least five measurements at different places were taken for each sample by positioning a drop of 5 µL of distilled water on the composite's surface with a microliter syringe.

The samples' WVP was determined following the Standard BS 7209:1990 [67]. Briefly, a sample is sealed over the top of a test dish containing 46 mL of distilled water. The assembly is transferred to a rotating turntable for 1 h, under isothermal conditions, to equilibrate the water vapor pressure gradient across the sample. The assembly is then weighted and rotated for 24 h and then weighted once more.

The WVP is represented by the following Equation (1) and expressed in g·m⁻²·24 h⁻¹:

$$\text{WVP} = \frac{24W}{At} \quad (1)$$

where W is the mass (g) of water vapor lost in t hours, A is the area of the sample exposed to vapor (m²) and t is the time between the various weightings (h).

For the tensile strength measurements, the full width of the sample (25 mm) was fixed. A length that allows an initial distance between the clamps of the strength tester equipment (Hounsfield HSK100, Salfords, UK) of 100 mm was set out between grips; the samples were then submitted to tensile. Four samples of each material were tested at a constant speed of 100 mm·min⁻¹.

Thermogravimetric analysis (TGA) was done using a Hitachi STA7200 (Tokyo, Japan). For this, samples weighing 7–9 mg (the exact mass was recorded before each assay) were placed in platinum pans. The temperature range was from 25 to 600 °C, using a heating rate of 10 °C·min⁻¹, with nitrogen flushed at flow rate of 200 mL·min⁻¹.

The dynamic mechanical properties of the BC composites were measured on a Hitachi DMA7100 (Tokyo, Japan) equipment in tension mode. The storage modulus (E') was recorded from 25 to 250 °C, at a frequency of 1 Hz and heating rate of 2 °C·min⁻¹. The dimensions of the samples were 10 mm × 10 mm (tested area).

2.3. Finishing and Dyeing

2.3.1. Antimicrobial Finishing

The humidity and warm temperatures developed in footwear are favorable to the growth of bacteria, fungi and molds, some of which contain lipases that may accelerate the biodegradation of the materials and release undesirable malodors. In order to evaluate the antimicrobial action of the finishing treatments of BC composites with commercially available biocides, the Si BAC (Smart Innovation, Barcelos, Portugal) product was selected

for which the active ingredient is benzalkonium chloride. Solutions containing the biocide with different concentrations and the fixative (Smart Fix, Smart Innovation, Barcelos, Portugal) were prepared and applied to dried BC composites by exhausting at 40 °C in a bath ratio of 1:20 (*m/v*) (Table 2).

Table 2. Conditions used in the antimicrobial finishing of BC composites.

Sample	Si BAC (%) (<i>w/w</i>)	Smart Fix (%) (<i>w/w</i>)	Time (min)
Control	-	-	30
1 BAC	2	0.4	30
2 BAC	2	0.4	60
3 BAC	4	0.4	60

After drying until constant mass, the antimicrobial activity of the composites was evaluated using the agar diffusion plate test, ISO 20645:2006 [68]. This method allows the qualitative determination of a surface antibacterial activity by detecting the presence of a halo around the edges of the sample (zone of inhibition) and the bacterial growth underneath. Suspensions of Gram positive *Staphylococcus aureus* (*S. aureus*) and Gram negative *Escherichia coli* (*E. coli*) were prepared in trypticase soy broth and left to grow overnight at 37 °C and 120 rpm. Then, their concentration was adjusted to 1×10^7 CFUs/mL and added to tryptic soy agar. The agar was then poured into 55 mm diameter sterilized Petri dishes and, after solidification, squared-sized BC composites of 1×1 cm were placed above them, guaranteeing maximum contact and incubated for 24 h at 37 °C.

2.3.2. Dyeing of the Composites

Dyeing is an essential process in the development of textile and footwear products. In order to ascertain the dyeability of BC-based composites, different classes of dyes (direct, reactive, dispersed and acid) were used. Their application was tested at the beginning of the exhaustion process during the production of the composites and in the dried composites.

Simultaneous dyeing and production of the BC-based composites were carried out as follows:

- (a) Sirius Scarlet K-CF direct dye (0.1 g/100 g) was added to the mixture containing the AESO emulsion, PDMS and PEG 400 polymers, followed by the polymerization of the emulsion. The BC composites were then produced by the exhaustion process;
- (b) Same process used in (a) but with Procion Red H-E3N reactive dye;
- (c) Same process used in (a) but with Dianix Scarlet CC disperse dye;
- (d) Procion Red H-E3N reactive dye (0.1 g/100 g) was added to the mixture containing the AESO emulsion previously polymerized and the other polymers. The BC composites were then produced by the exhaustion process;
- (e) Procion Red H-E3N reactive dye (0.1 g/100 g) was added to the mixture containing the AESO emulsion and the other polymers. Then, the membranes were exhausted and finally polymerized;
- (f) Same process used in (e) but with Dianix Scarlet CC disperse dye.

For the dyeing of dry composites, the following tests were performed:

- (g) Dyeing with the reactive dye Procion Red H-E3N (0.1 g/100 g) aqueous solution for 1.5 h at 30 °C;
- (h) Dyeing with the acid dye Solvaderm Black (0.1 g/100 g) aqueous solution for 1.5 h at 30 °C; and
- (i) Dyeing with the disperse dye Dianix Blue S-BG (0.1 g/100 g) aqueous dispersion for 1.5 h at different temperatures: 60, 80, 100 and 120 °C.

3. Results and Discussion

3.1. Properties of the Composites

The obtained composites were characterized with respect to their wettability, water vapor permeability (WVP), mechanical and thermal properties (Table 3, Figures 1 and 2).

Table 3. Properties of the BC and BC composites.

Sample	Thickness (mm)	WCA (°)	WVP ($\text{g}\cdot\text{m}^{-2}\cdot 24\text{ h}^{-1}$)	Tensile Strength (MPa)	Elongation (%)
BC	0.48 ± 0.01	63.1 ± 4.7	289.6	37.5 ± 0.8	3.6 ± 0.6
Composite A (pre-polymerization)	1.27 ± 0.01	93.1 ± 5.7	65.1 ± 1.3	12.1 ± 1.8	15.5 ± 0.9
Composite B (post-polymerization)	1.22 ± 0.01	103.6 ± 3.2	28.8 ± 2.7	8.3 ± 0.4	19.1 ± 4.5

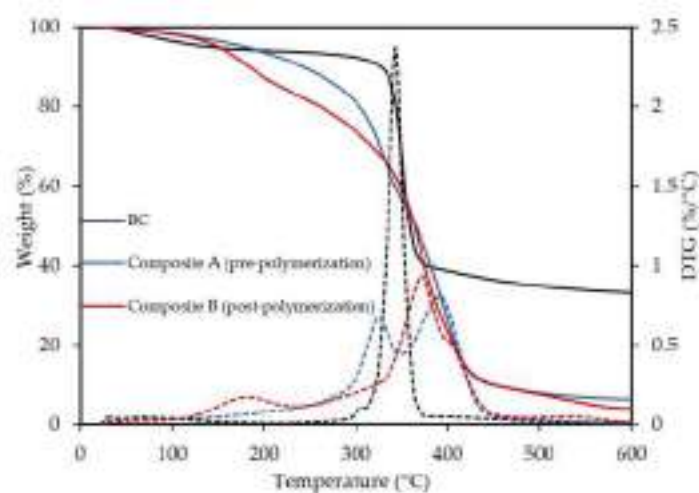


Figure 1. TGA curves (solid lines) and respective derivative (dashed lines) of BC and BC composites.

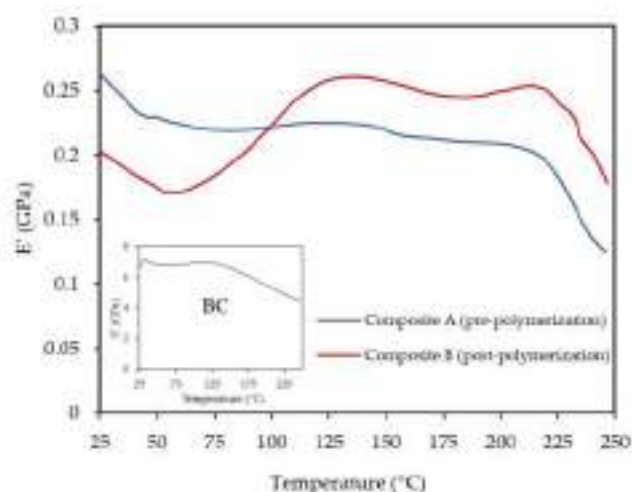


Figure 2. Evolution of the storage modulus (E') versus temperature at 1 Hz for BC (inserted graph) and BC composites as obtained by dynamic mechanical analysis.

As observed by the considerable increase in thickness (Table 3), the AESO emulsion mixture (Table 1) penetrated well into the BC membranes. The water contact angles values further confirmed the impregnation of the BC by changing its surface wettability ($\text{WCA} > 90^\circ$), which is slightly higher in the sample with the AESO polymerized after the

exhaustion process (Composite B). As observed in our previous work [60], the incorporation of PDMS-based polymer into BC significantly increased the WCA of the composites. The low surface tension of PDMS, which is $19.5\text{--}23.6\text{ mN}\cdot\text{m}^{-1}$ [69,70], contributes to the decrease in the free energy and the surface wettability of the composite. Furthermore, AESO resin contains hydrophobic long-chain non-polar fatty acid chains [71], which improve the hydrophobicity of the composites.

Regarding the water vapor permeability, although the BC porosity was not completely obstructed by the incorporation of the polymer's mixture, the WVP values were much lower than those of pristine BC which can also be explained by the higher thickness of the composites and their hydrophobic character. As shown in our previous work [60,61], the increased thickness and water resistance of the composites affected the adsorption process of the water vapor permeation mechanism.

Concerning the mechanical properties, as compared to BC, the tensile strength of the composites was lower but the elongation was much higher. These results can be explained by the extensive surface coating of the surface hydroxyl groups of the cellulose nanofibers which prevents their contribution to the mechanical strength through hydrogen bonding [72–74]. Hence, the mechanical strength and elongation of the composites become dependent on the intermolecular bonding of the matrix polymers. The added polymers also had a plasticizing effect, which increased the free volume and allowed greater mobility between the different layers of the BC membrane [75–77]. Composite B showed lower tensile strength value owing to the lower degree of polymerization of the crosslinked AESO, as will be discussed below.

Thermogravimetric analysis (TGA) was used to evaluate the thermal properties and kinetics of degradation of the composites. The TGA and the derivative thermograms (DTG) are shown in Figure 1.

The DTG curve of BC shows a single and narrow weight loss at $351.0\text{ }^{\circ}\text{C}$, indicating a fast degradation involving dehydration, depolymerization of the main polymer network and the decomposition of glucosyl units followed by the formation of a charred residue [78,79]. In the case of the composites, each of the samples presented two distinct peaks. Composite B (post-polymerization) shows one first event at $182.4\text{ }^{\circ}\text{C}$ before the main degradation. This degradation stage can be assigned to the evaporation and decomposition of unreacted monomers, catalysts or other low molecular weight components in the composites [80–83]. On the other hand, Composite A (pre-polymerization) had the first degradation peak only at $328.3\text{ }^{\circ}\text{C}$ and, hence, it can be inferred that the pre-polymerization using the redox initiator system hydrogen peroxide/L-ascorbic acid was more effective when compared to the post-polymerization approach. This can also explain the lower WVP and tensile strength, higher contact angle and the higher elongation values of Composite B. The lower polymerization of AESO may have resulted in the aggregation or coalescence of the emulsified AESO particles, reducing the porosity of the composite, but allowing higher mobility between the different layers of the BC membrane due to the plasticizing effect of the added polymers [60]. The main mass loss step of both composites corresponding to the highest percentage of mass loss occurred at higher temperatures as compared to BC, respectively, at $392.6\text{ }^{\circ}\text{C}$ and $373.1\text{ }^{\circ}\text{C}$ for Composites A and B. This can be attributed to the decomposition of PDMS-based polymer and crosslinked AESO. The temperature corresponding to the maximum rate of weight-loss of the polymers was around $420\text{ }^{\circ}\text{C}$ [84,85].

The storage modulus (E') obtained by dynamic mechanical analysis (DMA) of pure BC and the composites over a temperature range of $25\text{ }^{\circ}\text{C}$ to $250\text{ }^{\circ}\text{C}$ at a frequency of 1 Hz is presented in Figure 2.

The obtained data show that BC has high stiffness with a storage modulus at room temperature of 6.5 GPa due to the strong hydrogen bonds between the nanofibers. However, a considerably lower storage modulus was observed for the BC composites, which can be ascribed to the plasticizing effect of the impregnated polymers resulting in the segmental mobilization of the nanocellulose chains. Among the composites, Composite A showed a

higher storage modulus for temperatures up to approximately 100 °C. These results are in good agreement with the tensile strength measurements, which were plausibly associated with a higher crosslinking density. In addition, it was also possible to observe that the storage modulus of Composite B decreased when the temperature rose to 55 °C and then increased when it rose to 130 °C. This could be due to the loss of unreacted material, as was observed in the TGA results, which consequently gave rise to densification of the composite structure during heating, allowing an improved stress transfer behavior at higher temperatures.

Comparing the results of these composites, by using the redox initiator system hydrogen peroxide and L-ascorbic acid with the ones from our previous work [60] a substantial improvement in the elongation at break (pre-polymerization and post-polymerization) and in the tensile strength (pre-polymerization) was achieved. Overall, the polymerization of the AESO emulsion using biodegradable catalysts was validated and since the polymerization occurred before the exhaustion process, this method was more effective in the preparation of the composites.

3.2. Antimicrobial Activity

The antibacterial activity of the BC composites finished (surface-functionalized) with different concentrations and time of exhaustion of the biocide benzalkonium chloride (BAC) against *S. aureus* and *E. coli* was determined using the zone of inhibition method. *S. aureus* and *E. coli* are among the most prevalent species of Gram positive and Gram negative bacteria, respectively. As shown in Figure 3, all samples with the biocide compound produced a zone of inhibition (halo) against the *S. aureus* (Gram positive) and this area increased with concentration and with the time of treatment.

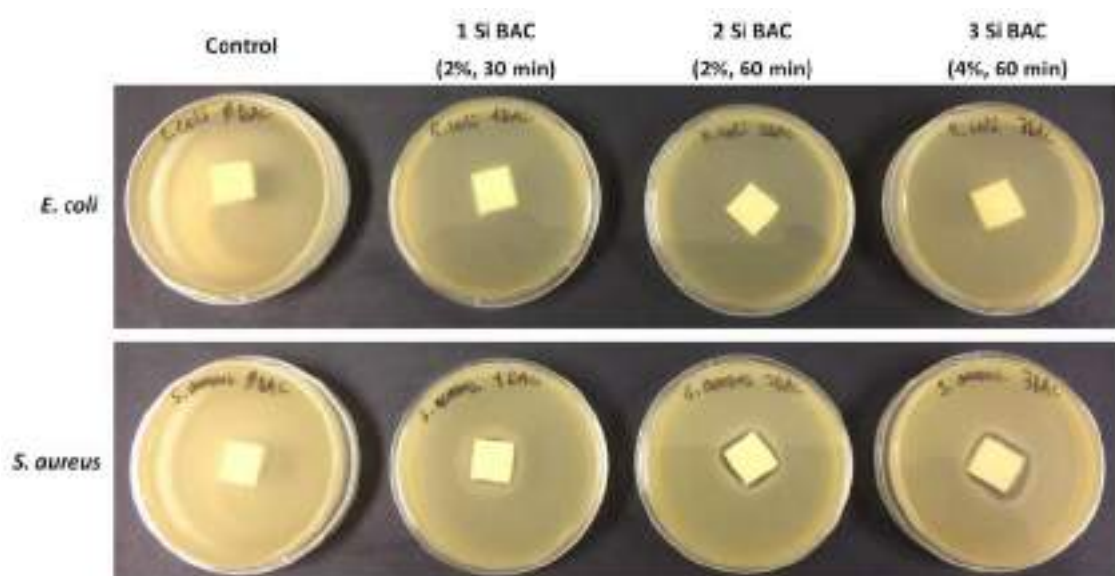


Figure 3. Antibacterial activity of the BC composites surface functionalized with benzalkonium chloride-based product against *Escherichia coli* and *Staphylococcus aureus*.

No inhibition was observed against *E. coli*, possibly due to the poor antimicrobial capacity of the benzalkonium chloride (cationic) against Gram negative bacteria [86].

3.3. Dyeing

Figure 4 shows sample photos of the dyed composites. All samples showed intense colors and were very flexible and hydrophobic (inserted photo in Figure 4e as an example). For samples dyed during the exhaustion with the AESO mixture as shown in Figure 4a–f, the dye diffused well into the bulk of BC and resulted in more uniform colors. However, in samples dyed after the production of the composites as shown in Figure 4g,h, the dye only

remained in the outer layers (inserted photo in Figure 3g) and the color was less uniform. It was also possible to observe that by increasing the temperature during dyeing with the dispersed dye as shown in Figure 4i, more intense colors were obtained and, despite the greater shrinkage, this change contributed to obtaining a material with a texture more similar to that of leather.

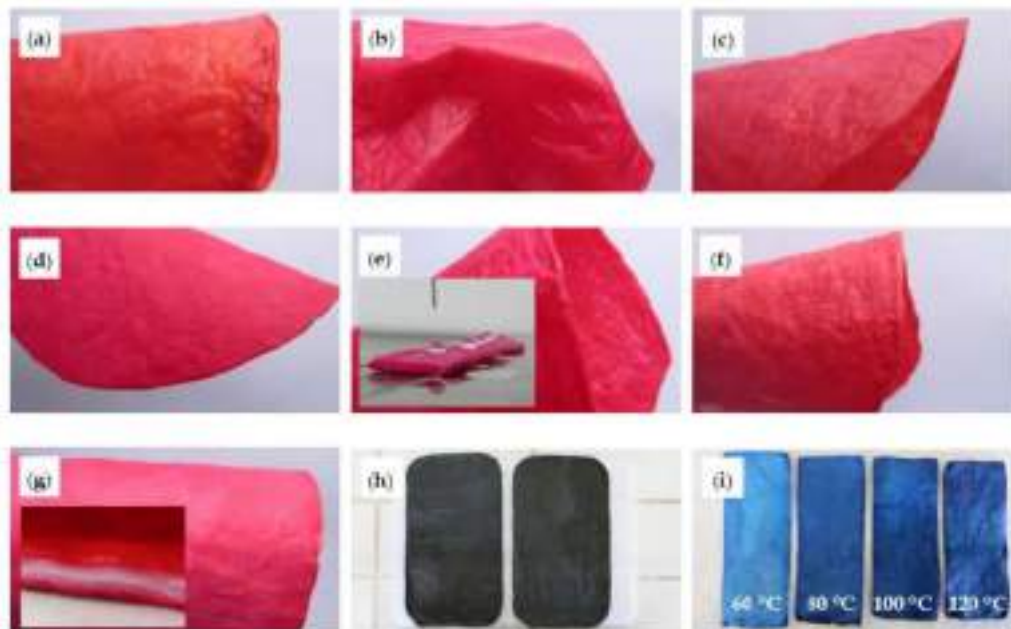


Figure 4. Photos of the dyed BC composites. Letters (a–i) correspond to the experimental conditions described in Section 2.3.2. Simultaneous dyeing and production of the BC-based composites (a–f) and dyeing of dry composites (g–i).

From the above, incorporating the dye simultaneously with the AESO mixture is a more efficient approach towards dyeing BC composites. These results also permitted a simple and potentially low-cost strategy for this process, albeit it will be necessary to carry out color washing and rubbing fastness tests, as well as to optimize the process conditions by considering the variables of pH, bath ratio, temperature, dye concentration, auxiliary products and the duration of the process.

4. Conclusions

Coupled with the increase in the population growth rate and resource consumption, environmental awareness and social concern regarding the environmental impact of the textile industry is emerging, which highlights the increasing need for the development of green and sustainable approaches throughout this industry's supply chain. Self-grown fabrics from renewable resources has streamlined the textile and fashion industries, with BC as an exemplary model of a product that could match the growing needs for sustainability. Several approaches have been taken, from semi-empirical to more systematic ones, towards improving the properties of BC for use in the textile and leather industries, which were reviewed here.

The possibility of producing BC, AESO, PDMS and PEG 400 composites through the exhaustion process using biodegradable catalysts was validated here. The polymerization of the AESO emulsion before the exhaustion process proved to be more effective in terms of WVP, tensile strength and thermal stability. However, more work is required to optimize the process. Composites finished with biocides showed antimicrobial activity against *S. aureus* and incorporating the dye simultaneously with the AESO mixture was the most efficient approach towards composites with intense colors.

Author Contributions: Conceptualization, A.P.S., M.G. and F.D.; methodology, M.F.; writing—original draft preparation, M.F.; writing—review and editing, M.F., M.G. and F.D.; supervision, A.P.S., M.G. and F.D.; project administration, M.G. All authors have read and agreed to the published version of the manuscript.

Funding: This research was funded by the FEDER funds through the Operational Competitiveness Program—COMPETE and by National Funds through Fundação para a Ciência e Tecnologia (FCT) under the project POCI-01-0145-FEDER-007136 and UID/CTM/00264/2019 and by the Portuguese Foundation for Science and Technology (FCT) under the scope of the strategic funding of UIDB/04469/2020 unit.

Institutional Review Board Statement: Not applicable.

Informed Consent Statement: Not applicable.

Data Availability Statement: All findings discussed are based on the data contained within the present study.

Acknowledgments: The authors thank Satisfibre, S.A. (Portugal), for the supply of bacterial cellulose.

Conflicts of Interest: The authors declare no conflict of interest.

References

1. Gorgieva, S.; Trček, J. Bacterial Cellulose: Production, Modification and Perspectives in Biomedical Applications. *Nanomaterials* **2019**, *9*, 1352. [CrossRef] [PubMed]
2. Lin, D.; Liu, Z.; Shen, R.; Chen, S.; Yang, X. Bacterial Cellulose in Food Industry: Current Research and Future Prospects. *Int. J. Biol. Macromol.* **2020**, *158*, 1007–1019. [CrossRef] [PubMed]
3. Klemm, D.; Heublein, B.; Fink, H.P.; Bohn, A. Cellulose: Fascinating Biopolymer and Sustainable Raw Material. *Angew. Chem. Int. Ed.* **2005**, *44*, 3358–3393. [CrossRef] [PubMed]
4. Kim, D.Y.; Nishiyama, Y.; Kuga, S. Surface Acetylation of Bacterial Cellulose. *Cellulose* **2002**, *9*, 361–367. [CrossRef]
5. Potivara, K.; Phisalaphong, M. Development and Characterization of Bacterial Cellulose Reinforced with Natural Rubber. *Materials* **2019**, *12*, 2323. [CrossRef]
6. Cazón, P.; Velázquez, G.; Vázquez, M. Characterization of Bacterial Cellulose Films Combined with Chitosan and Polyvinyl Alcohol: Evaluation of Mechanical and Barrier Properties. *Carbohydr. Polym.* **2019**, *216*, 72–85. [CrossRef]
7. Cazón, P.; Vázquez, M. Bacterial Cellulose as a Biodegradable Food Packaging Material: A Review. *Food Hydrocoll.* **2021**, *113*. [CrossRef]
8. Silva, F.A.G.S.; Dourado, F.; Gama, M.; Poças, F. Nanocellulose Bio-Based Composites for Food Packaging. *Nanomaterials* **2020**, *10*, 2041. [CrossRef]
9. Liu, W.; Du, H.; Zhang, M.; Liu, K.; Liu, H.; Xie, H.; Zhang, X.; Si, C. Bacterial Cellulose-Based Composite Scaffolds for Biomedical Applications: A Review. *ACS Sustain. Chem. Eng.* **2020**, *8*, 7536–7562. [CrossRef]
10. Islam, S.U.; Ul-Islam, M.; Ahsan, H.; Ahmed, M.B.; Shehzad, A.; Fatima, A.; Sonn, J.K.; Lee, Y.S. Potential Applications of Bacterial Cellulose and Its Composites for Cancer Treatment. *Int. J. Biol. Macromol.* **2021**, *168*, 301–309. [CrossRef]
11. Martins, D.; Rocha, C.; Dourado, F.; Gama, M. Bacterial Cellulose-Carboxymethyl Cellulose (BC:CMC) Dry Formulation as Stabilizer and Texturizing Agent for Surfactant-Free Cosmetic Formulations. *Colloids Surf. A Physicochem. Eng. Asp.* **2021**, *617*, 126380. [CrossRef]
12. Alves, A.A.; Silva, W.E.; Belian, M.F.; Lins, L.S.G.; Galembeck, A. Bacterial Cellulose Membranes for Environmental Water Remediation and Industrial Wastewater Treatment. *Int. J. Environ. Sci. Technol.* **2020**, *17*, 3997–4008. [CrossRef]
13. Wahid, F.; Zhao, X.J.; Duan, Y.X.; Zhao, X.Q.; Jia, S.R.; Zhong, C. Designing of Bacterial Cellulose-Based Superhydrophilic/Underwater Superoleophobic Membrane for Oil/Water Separation. *Carbohydr. Polym.* **2021**, *257*. [CrossRef]
14. Poddar, M.K.; Dikshit, P.K. Recent Development in Bacterial Cellulose Production and Synthesis of Cellulose Based Conductive Polymer Nanocomposites. *Nano Sel.* **2021**, 1–24. [CrossRef]
15. Ma, L.; Bi, Z.; Xue, Y.; Zhang, W.; Huang, Q.; Zhang, L.; Huang, Y. Bacterial Cellulose: An Encouraging Eco-Friendly Nano-Candidate for Energy Storage and Energy Conversion. *J. Mater. Chem. A* **2020**, *8*, 5812–5842. [CrossRef]
16. Material District. Leather-Free Handbag Made of Bacterial Cellulose. Available online: <https://materialdistrict.com/article/handbag-bacterial-cellulose/> (accessed on 25 August 2020).
17. Sick-Leitner, M. SOYA C(O)U(L)TURE—Useful Things Arise out of Waste. Available online: <https://ars.electronica.art/aeblog/en/2015/09/30/soya-coulture/> (accessed on 14 September 2020).
18. Raut, A. Malai: A Sustainable, Vegan Alternative to Leather. Available online: <https://www.architecturaldigest.in/content/malai-a-sustainable-vegan-alternative-to-leather/> (accessed on 2 September 2020).
19. Ng, F.M.C.; Wang, P.W. Natural Self-Grown Fashion from Bacterial Cellulose: A Paradigm Shift Design Approach in Fashion Creation. *Des. J.* **2016**, *19*, 837–855. [CrossRef]

20. Ng, A. Grown Microbial 3D Fiber Art, Ava: Fusion of Traditional Art with Technology. In Proceedings of the International Symposium on Wearable Computers (ISWC), Maui, HI, USA, 5–8 May 2017; pp. 209–214.
21. Chan, C.K.; Shin, J.; Jiang, S.X.K. Development of Tailor-Shaped Bacterial Cellulose Textile Cultivation Techniques for Zero-Waste Design. *Cloth. Text. Res. J.* **2018**, *36*, 33–44. [[CrossRef](#)]
22. Tyurin, I.; Getmantseva, V.; Andreeva, E.; Kashcheev, O. The Study of the Molding Capabilities of Bacterial Cellulose. In Proceedings of the 19th World Textile Conference on Textiles at the Crossroads (AUTEX 2019), Ghent, Belgium, 20–25 April 2019.
23. Pommet, M.; Juntaro, J.; Heng, J.Y.Y.; Mantalaris, A.; Lee, A.F.; Wilson, K.; Kalinka, G.; Shaffer, M.S.P.; Bismarck, A. Surface Modification of Natural Fibers Using Bacteria: Depositing Bacterial Cellulose onto Natural Fibers to Create Hierarchical Fiber Reinforced Nanocomposites. *Biomacromolecules* **2008**, *9*, 1643–1651. [[CrossRef](#)]
24. Xu, Q.; Fan, L.; Yuan, Y.; Wei, C.; Bai, Z.; Xu, J. All-Solid-State Yarn Supercapacitors Based on Hierarchically Structured Bacterial Cellulose Nanofiber-Coated Cotton Yarns. *Cellulose* **2016**, *23*, 3987–3997. [[CrossRef](#)]
25. Mizuno, M.; Kamiya, Y.; Katsuta, T.; Oshima, N.; Nozaki, K.; Amano, Y. Creation of Bacterial Cellulose-Fabric Complexed Material. *SEN I GAKKAISHI* **2012**, *68*, 42–47. [[CrossRef](#)]
26. Kamal, A.S.M.; Misnon, M.I.; Zakaria, M.N.; Kadir, M.I.A.; Ahmad, M.R. Characteristics of Cotton, Polyester and Rayon Fabrics Coated with *Acetobacter Xylinum*. *Int. J. Eng. Technol.* **2018**, *7*, 181–184.
27. Naeem, M.A.; Alfred, M.; Saba, H.; Siddiqui, Q.; Naveed, T.; Shahbaz, U. A Preliminary Study on the Preparation of Seamless Tubular Bacterial Nanocomposite Fabrics. *J. Compos. Mater.* **2019**, *53*. [[CrossRef](#)]
28. Felgueiras, C.; Azoia, N.G.; Gonçalves, C.; Gama, M.; Dourado, F. Trends on the Cellulose-Based Textiles: Raw Materials and Technologies. *Front. Bioeng. Biotechnol.* **2021**, *9*, 1–20. [[CrossRef](#)] [[PubMed](#)]
29. Tokura, S.; Tamura, H.; Takai, M.; Higuchi, T.; Asano, H. Continuous Harvest of Cellulosic Filament during Cultivation of *Acetobacter Xylinum*. In Proceedings of the Cellulosic Pulps, Fibres and Materials Conference—Cellucon '98, Bryan, TX, USA, 1–5 July 1998; pp. 3–12.
30. Sakairi, N.; Asano, H.; Ogawa, M.; Nishi, N.; Tokura, S. A Method for Direct Harvest of Bacterial Cellulose Filaments during Continuous Cultivation of *Acetobacter Xylinum*. *Carbohydr. Polym.* **1998**, *35*, 233–237. [[CrossRef](#)]
31. Tokura, S.; Asano, H.; Sakairi, N.; Nishi, N. Direct Filature of Bacterial Cellulose from Culture Medium. *Macromol. Symp.* **1998**, *127*, 23–30. [[CrossRef](#)]
32. Chen, P.; Kim, H.S.; Kwon, S.M.; Yun, Y.S.; Jin, H.J. Regenerated Bacterial Cellulose/Multi-Walled Carbon Nanotubes Composite Fibers Prepared by Wet-Spinning. *Curr. Appl. Phys.* **2009**, *9*, e96–e99. [[CrossRef](#)]
33. Chen, P.; Yun, Y.S.; Bak, H.; Cho, S.Y.; Jin, H.J. Multiwalled Carbon Nanotubes-Embedded Electrospun Bacterial Cellulose Nanofibers. *Mol. Cryst. Liq. Cryst.* **2010**, *519*, 169–178. [[CrossRef](#)]
34. Gao, Q.; Shen, X.; Lu, X. Regenerated Bacterial Cellulose Fibers Prepared by the $NmMo \cdot H_2O$ Process. *Carbohydr. Polym.* **2011**, *83*, 1253–1256. [[CrossRef](#)]
35. Lu, X.; Shen, X. Solubility of Bacteria Cellulose in Zinc Chloride Aqueous Solutions. *Carbohydr. Polym.* **2011**, *86*, 239–244. [[CrossRef](#)]
36. Zhang, S.; Luo, J. Preparation and Properties of Bacterial Cellulose/Alginate Blend Bio-Fibers. *J. Eng. Fiber. Fabr.* **2011**, *6*, 69–72. [[CrossRef](#)]
37. Lu, X.; Tang, S.; Huang, B.; Shen, X.; Hong, F. Preparation and Characterization of Bacterial Cellulose/Hydroxypropyl Chitosan Blend as-Spun Fibers. *Fibers Polym.* **2013**, *14*, 935–940. [[CrossRef](#)]
38. Makarov, I.S.; Golova, L.K.; Vinogradov, M.I.; Levin, I.S.; Gromovkykh, T.I.; Arkharova, N.A.; Kulichikhin, V.G. Cellulose Fibers from Solutions of Bacterial Cellulose in N-Methylmorpholine N-Oxide. *Fibre Chem.* **2019**, *51*, 175–181. [[CrossRef](#)]
39. Yao, J.; Chen, S.; Chen, Y.; Wang, B.; Pei, Q.; Wang, H. Macrofibers with High Mechanical Performance Based on Aligned Bacterial Cellulose Nanofibers. *ACS Appl. Mater. Interfaces* **2017**, *9*, 20330–20339. [[CrossRef](#)]
40. Wang, S.; Jiang, F.; Xu, X.; Kuang, Y.; Fu, K.; Hitz, E.; Hu, L. Super-Strong, Super-Stiff Macrofibers with Aligned, Long Bacterial Cellulose Nanofibers. *Adv. Mater.* **2017**, *29*, 1–8. [[CrossRef](#)]
41. Wu, Z.; Chen, S.; Wu, R.; Sheng, N.; Zhang, M.; Ji, P.; Wang, H. Top-down Peeling Bacterial Cellulose to High Strength Ultrathin Films and Multifunctional Fibers. *Chem. Eng. J.* **2020**, *391*, 123527. [[CrossRef](#)]
42. Gao, H.L.; Zhao, R.; Cui, C.; Zhu, Y.B.; Chen, S.M.; Pan, Z.; Meng, Y.F.; Wen, S.M.; Liu, C.; Wu, H.A.; et al. Bioinspired Hierarchical Helical Nanocomposite Macrofibers Based on Bacterial Cellulose Nanofibers. *Natl. Sci. Rev.* **2020**, *7*, 73–83. [[CrossRef](#)]
43. Han, J.; Shim, E.; Kim, H.R. Effects of Cultivation, Washing, and Bleaching Conditions on Bacterial Cellulose Fabric Production. *Text. Res. J.* **2019**, *89*, 1094–1104. [[CrossRef](#)]
44. Kamal, A.S.M.; Misnon, M.I.; Fadil, F. The Effect of Sodium Hydroxide Concentration on Yield and Properties of Bacterial Cellulose Membranes. In Proceedings of the IOP Conference Series: Materials Science and Engineering, Pattaya, Thailand, 13–15 March 2020; Volume 732, pp. 1–7.
45. Miyamoto, H.; Tsuduki, M.; Ago, M.; Yamane, C.; Ueda, M.; Okajima, K. Influence of Dye-stuffs on the Crystallinity of a Bacterial Cellulose and a Regenerated Cellulose. *Text. Res. J.* **2014**, *84*, 1147–1158. [[CrossRef](#)]
46. Wood, D.; Hang, L.; Salusso, C.J. Production and Characterization of Bacterial Cellulose Fabrics. In Proceedings of the International Textile and Apparel Association (ITAA) Annual Conference Proceedings, Santa Fe, Mexico, 18–22 December 2015; pp. 11–13.
47. Shim, E.; Kim, H.R. Coloration of Bacterial Cellulose Using in Situ and Ex Situ Methods. *Text. Res. J.* **2019**, *89*, 1297–1310. [[CrossRef](#)]

48. Song, J.E.; Su, J.; Noro, J.; Cavaco-Paulo, A.; Silva, C.; Kim, H.R. Bio-Coloration of Bacterial Cellulose Assisted by Immobilized Laccase. *AMB Express* **2018**, *8*. [[CrossRef](#)]
49. de Costa, A.F.S.; de Amorim, J.D.P.; Almeida, F.C.G.; de Lima, I.D.; de Paiva, S.C.; Rocha, M.A.V.; Vinhas, G.M.; Sarubbo, L.A. Dyeing of Bacterial Cellulose Films Using Plant-Based Natural Dyes. *Int. J. Biol. Macromol.* **2019**, *121*, 580–587. [[CrossRef](#)]
50. Lee, Y.-A.; Xiang, C.; Ghalachyan, A.; Ramasubramanian, G.; Li, R.; Madbouly, S.; Farr, C. Exploring Optimal Solutions for Sustainable Product Development Using Renewable Bacteria Cellulose Fiber and Biopolymer Composites. In Proceedings of the 71st Annual Conference of the International Textile and Apparel Association 2014 (ITAA #71), Charlotte, NC, USA, 12–16 November 2014; pp. 8–9.
51. Lee, Y.A. Case study of renewable bacteria cellulose fiber and biopolymer composites in sustainable design practices. In *Sustainable Fibres for Fashion Industry*; Muthu, S.S., Gardetti, M.A., Eds.; Springer: Singapore, 2016; Volume 1, ISBN 978-981-10-0520-6.
52. Araújo, S.; da Silva, F.M.; Gouveia, I.C. The Role of Technology towards a New Bacterial-Cellulose-Based Material for Fashion Design. *J. Ind. Intell. Inf.* **2015**, *3*, 168–172. [[CrossRef](#)]
53. Song, J.E.; Cavaco-Paulo, A.; Silva, C.; Kim, H.R. Improvement of Bacterial Cellulose Nonwoven Fabrics by Physical Entrapment of Lauryl Gallate Oligomers. *Text. Res. J.* **2020**, *90*, 166–178. [[CrossRef](#)]
54. Song, J.E.; Silva, C.; Cavaco-Paulo, A.M.; Kim, H.R. Functionalization of Bacterial Cellulose Nonwoven by Poly(Fluorophenol) to Improve Its Hydrophobicity and Durability. *Front. Bioeng. Biotechnol.* **2019**, *7*, 1–10. [[CrossRef](#)]
55. Kamiński, K.; Jarosz, M.; Grudzień, J.; Pawlik, J.; Zastawnik, F.; Pandyra, P.; Kołodziejczyk, A.M. Hydrogel Bacterial Cellulose: A Path to Improved Materials for New Eco-Friendly Textiles. *Cellulose* **2020**, *27*, 5353–5365. [[CrossRef](#)]
56. Kim, H.; Song, J.E.; Kim, H.R. Comparative Study on the Physical Entrapment of Soy and Mushroom Proteins on the Durability of Bacterial Cellulose Bio-Leather. *Cellulose* **2021**, *28*, 3183–3200. [[CrossRef](#)]
57. da Silva, C.J.G.; de Medeiros, A.D.M.; de Amorim, J.D.P.; do Nascimento, H.A.; Converti, A.; Costa, A.F.S.; Sarubbo, L.A. Bacterial Cellulose Biotextiles for the Future of Sustainable Fashion: A Review. *Environ. Chem. Lett.* **2021**. [[CrossRef](#)]
58. Rathinamoorthy, R.; Kiruba, T. Bacterial Cellulose-A Potential Material for Sustainable Eco-Friendly Fashion Products. *J. Nat. Fibers* **2020**, 1–13. [[CrossRef](#)]
59. da Silva, F.A.G.S.; Fernandes, M.; Souto, A.P.; Ferreira, E.C.; Dourado, F.; Gama, M. Optimization of Bacterial Nanocellulose Fermentation Using Recycled Paper Sludge and Development of Novel Composites. *Appl. Microbiol. Biotechnol.* **2019**, *103*, 9143–9154. [[CrossRef](#)]
60. Fernandes, M.; Souto, A.P.; Gama, M.; Dourado, F. Bacterial Cellulose and Emulsified AESO Biocomposites as an Ecological Alternative to Leather. *Nanomaterials* **2019**, *9*, 1710. [[CrossRef](#)]
61. Fernandes, M.; Gama, M.; Dourado, F.; Souto, A.P. Development of Novel Bacterial Cellulose Composites for the Textile and Shoe Industry. *Microb. Biotechnol.* **2019**, *12*, 650–661. [[CrossRef](#)] [[PubMed](#)]
62. Wang, S. Redox-Initiated Adiabatic Emulsion Polymerization. Theses and Dissertations. Ph.D. Thesis, Paper 1294. Lehigh University, Bethlehem, PA, USA, 2013.
63. Kiatsimkul, P.P.; Sutterlin, W.R.; Suppes, G.J. Selective Hydrolysis of Epoxidized Soybean Oil by Commercially Available Lipases: Effects of Epoxy Group on the Enzymatic Hydrolysis. *J. Mol. Catal. B Enzym.* **2006**, *41*, 55–60. [[CrossRef](#)]
64. Burkinshaw, S.M. *Physico-Chemical Aspects of Textile Coloration*; Society of Dyers and Colorists, Ed.; John Wiley & Sons, Inc.: West Sussex, UK, 2016; ISBN 978-1-118-72569-6.
65. Cousinet, S.; Ghadban, A.; Fleury, E.; Lortie, F.; Pascault, J.P.; Portinha, D. Toward Replacement of Styrene by Bio-Based Methacrylates in Unsaturated Polyester Resins. *Eur. Polym. J.* **2015**, *67*, 539–550. [[CrossRef](#)]
66. Wei, G.; Xu, H.; Chen, L.; Li, Z.; Liu, R. Isosorbide-Based High Performance UV-Curable Reactive Diluents. *Prog. Org. Coatings* **2019**, *126*, 162–167. [[CrossRef](#)]
67. BS 7209:1990. *Specification for Water Vapour Permeable Apparel Fabrics*; British Standards Institute: London, UK, 1990.
68. ISO. *ISO 20645:2006 Textile Fabrics—Determination of Antibacterial Activity—Agar Diffusion Plate Test*; International Organization for Standardization: Geneva, Switzerland, 2006.
69. Xu, X.; Jagota, A.; Paretkar, D.; Hui, C. Surface Tension Measurement from the Indentation of Clamped Thin Films. *Soft Matter* **2016**, *12*, 5121–5126. [[CrossRef](#)]
70. Tian, Y.; Ina, M.; Cao, Z.; Sheiko, S.S.; Dobrynin, A.V. How to Measure Work of Adhesion and Surface Tension of Soft Polymeric Materials. *Macromolecules* **2018**, *51*, 4059–4067. [[CrossRef](#)]
71. Li, C.; Xiao, H.; Wang, X.; Zhao, T. Development of Green Waterborne UV-Curable Vegetable Oil-Based Urethane Acrylate Pigment Prints Adhesive: Preparation and Application. *J. Clean. Prod.* **2018**, *180*, 272–279. [[CrossRef](#)]
72. Soykeabkaew, N.; Sian, C.; Gea, S.; Nishino, T.; Peijs, T. All-Cellulose Nanocomposites by Surface Selective Dissolution of Bacterial Cellulose. *Cellulose* **2009**, *16*, 435–444. [[CrossRef](#)]
73. Asgher, M.; Ahmad, Z.; Iqbal, H.M.N. Bacterial Cellulose-Assisted de-Lignified Wheat Straw-PVA Based Bio-Composites with Novel Characteristics. *Carbohydr. Polym.* **2017**, *161*, 244–252. [[CrossRef](#)]
74. Gea, S.; Bilotti, E.; Reynolds, C.T.; Soykeabkaew, N.; Peijs, T. Bacterial Cellulose-Poly(Vinyl Alcohol) Nanocomposites Prepared by an in-Situ Process. *Mater. Lett.* **2010**, *64*, 901–904. [[CrossRef](#)]
75. Salarbashi, D.; Bazeli, J.; Tafaghodi, M. Environment-Friendly Green Composites Based on Soluble Soybean Polysaccharide: A Review. *Int. J. Biol. Macromol.* **2019**, *122*, 216–223. [[CrossRef](#)]

76. Boon, D.; Lim, K.; Gong, H. Highly Stretchable and Transparent Films Based on Cellulose. *Carbohydr. Polym.* **2018**, *201*, 446–453. [[CrossRef](#)]
77. Sun, Y.; Meng, C.; Zheng, Y.; Wang, Y.; Qiao, K.; Yue, L.; Xie, Y.; He, W. The Effects of Two Biocompatible Plasticizers on the Performance of Dry Bacterial Cellulose Membrane: A Comparative Study. *Cellulose* **2018**, *25*, 5893–5908. [[CrossRef](#)]
78. Frone, A.N.; Panaitescu, D.M.; Chiulan, I.; Nicolae, C.A.; Casarica, A.; Gabor, A.R.; Trusca, R.; Damian, C.M.; Purcar, V.; Alexandrescu, E.; et al. Surface Treatment of Bacterial Cellulose in Mild, Eco-Friendly Conditions. *Coatings* **2018**, *8*, 221. [[CrossRef](#)]
79. Hu, Y.; Sheng, J.; Yan, Z.; Ke, Q. Completely Amorphous Cellulose Biosynthesized in Agitated Culture at Low Temperature. *Int. J. Biol. Macromol.* **2018**, *117*, 967–973. [[CrossRef](#)]
80. Liu, C.; Liu, Z.; Tisserat, B.H.; Wang, R.; Schuman, T.P.; Zhou, Y.; Hu, L. Microwave-Assisted Maleation of Tung Oil for Bio-Based Products with Versatile Applications. *Ind. Crop. Prod.* **2015**, *71*, 185–196. [[CrossRef](#)]
81. Liu, K.; Madbouly, S.A.; Kessler, M.R. Biorenewable Thermosetting Copolymer Based on Soybean Oil and Eugenol. *Eur. Polym. J.* **2015**, *69*, 16–28. [[CrossRef](#)]
82. Liu, F.; Miao, L.; Wang, Y.; Xue, X.; Yang, H. Progress in Organic Coatings Green Fabrication of Ultraviolet Curable Epoxy Acrylate-Silica Hybrid Coatings. *Prog. Org. Coatings* **2017**, *109*, 38–44. [[CrossRef](#)]
83. Zhang, C.; Yan, M.; Cochran, E.W.; Kessler, M.R. Biorenewable Polymers Based on Acrylated Epoxidized Soybean Oil and Methacrylated Vanillin. *Mater. Today Commun.* **2015**, *5*, 18–22. [[CrossRef](#)]
84. Sousa, A.F.; Ferreira, S.; Lopez, A.; Borges, I.; Pinto, R.J.B.; Silvestre, A.J.D.; Freire, C.S.R. Thermosetting AESO-Bacterial Cellulose Nanocomposite Foams with Tailored Mechanical Properties Obtained by Pickering Emulsion Templating. *Polymer* **2017**, *118*, 127–134. [[CrossRef](#)]
85. Radhakrishnan, T.S. Thermal Degradation of Poly(Dimethylsilylene) and Poly(Tetramethyldisilylene-Co-Styrene). *J. Appl. Polym. Sci.* **2005**, *99*, 2679–2686. [[CrossRef](#)]
86. Wei, B.; Yang, G.; Hong, F. Preparation and Evaluation of a Kind of Bacterial Cellulose Dry Films with Antibacterial Properties. *Carbohydr. Polym.* **2011**, *84*, 533–538. [[CrossRef](#)]

Emerging Pyroelectric Nanogenerators to Convert Thermal Energy into Electrical Energy

Hanjun Ryu and Sang-Woo Kim*

Pyroelectric energy harvesting systems have recently received substantial attention for their potential applications as power generators. In particular, the pyroelectric effect, which converts thermal energy into electrical energy, has been utilized as an infrared (IR) sensor, but upcoming sensor technology that requires a miniscule amount of power is able to utilize pyroelectric nanogenerators (PyNGs) as a power source. Herein, an overview of the progress in the development of PyNGs for an energy harvesting system that uses environmental or artificial energies such as the sun, body heat, and heaters, is provided. It begins with a brief introduction of the pyroelectric effect, and various polymer and ceramic materials based PyNGs are reviewed in detail. Various approaches for developing polymer-based PyNGs and various ceramic materials-based PyNGs are summarized in particular. Finally, challenges and perspectives regarding the PyNGs are described.

1. Introduction

The conversion of environmental energy into electrical energy has recently become a research topic of interest on the self-powering internet of things systems (IoTs).^[1–6] However, due to energy limitations, IoTs require astronomical budgets for constant maintenance, such as battery replacement and power construction.^[7,8] If a temporary power source is used, it will require periodic replacement of the battery, which causes an enormous waste of resources.^[9–11] In addition, it is difficult to directly connect power cables with tremendous sensors, so a wireless energy transfer function or a self-powering function is necessary for the sustainable operation of IoTs.^[12] Though ultralow power consumption technology can extend the operation time of IoTs, it is still not a permanent solution for persistent operation.^[13] Therefore, converting wasted environmental energy into valuable electricity is one of the important technologies for a self-powering IoTs.^[14–18]

Among the various energy harvesting systems,^[19–23] converting thermal energy into electric energy is a recently emerging technology.^[24–31] Unlike other energy converting systems, the pyroelectric effect, which converts thermal energy into electric

energy, has been used as a sensor due to its sensitive responsiveness to temperature fluctuations. However, increasing output performance of the pyroelectric nanogenerators (PyNGs) and decreasing power consumption of IoTs have begun a paradigm shift of pyroelectric devices from sensors to power sources. In addition, the PyNGs are easily hybridized with other energy harvesting systems, such as piezoelectric and triboelectric NGs (TENGs) which are recently developed energy harvesters^[32–39] to enhance the output performance.^[40] Piezoelectric and triboelectric NG convert external mechanical energy into electrical energy using piezoelectric effect and triboelectric effect, respectively. Thus, thermal energy which is generated by nature, mechanical friction, and machines, can be


effectively converted into electric energy through the pyroelectric effect, and it can be utilized as new type power sources of IoTs.

As shown in **Figure 1a**, pyroelectric applications such as heat sensors, infra-red (IR) sensors, thermal imaging, fire alarms, gas analyzers, and pollution monitors have been continuously developed and utilized since the pyroelectric effect was introduced.^[41–44] Recently, pyroelectric energy harvesting systems have emerged as new applications of the pyroelectric effect, and research on PyNGs has gradually increased. Typical PyNGs comprise three layers: the patterned top metal layer is designed to receive heat energy efficiently, and also acts as a top electrode; the middle pyroelectric layer converts thermal energy into electric energy through changing its internal polarization; and the bottom metal layer acts as a bottom electrode (Figure 1b). Due to the simple structures of the PyNGs, pyroelectric material design and structure design are key factors for enhancing the output performance. For example, there are several approaches to enhance the output performance of the PyNGs, such as increasing thermal energy absorption by structure modification, increasing the pyroelectric coefficient by material modification, or enhancing internal polarization change by thermal expansion. Therefore, in this review paper, we will discuss the working principle of the PyNGs as well as detailed overview of polymer-based PyNGs and ceramic based-PyNGs.

2. The Pyroelectric Effect

Pyroelectric materials have internal spontaneous polarization (P_s) in the absence of an electric field and pyroelectric effect is temporary change of P_s by the temporal temperature change

Dr. H. Ryu, Prof. S.-W. Kim
School of Advanced Materials Science and Engineering
Sungkyunkwan University (SKKU)
Suwon 16419, Republic of Korea
E-mail: kimsw1@skku.edu

 The ORCID identification number(s) for the author(s) of this article can be found under <https://doi.org/10.1002/smll.201903469>.

DOI: 10.1002/smll.201903469

of pyroelectric materials.^[42] When the temperature increases, decreasing P_s by thermal vibration leads to a decrease of surface charges bound to the surface.^[42] If the pyroelectric material is under open circuit condition, electrical potential is generated across the material.^[45] If the pyroelectric material is under short circuit condition, electrical current flows through external circuit. Theoretical short circuit output current is defined as follows in Equation (1)

$$i = \frac{dQ}{dt} = pA \frac{dT}{dt} \quad (1)$$

where i is generated current, Q is pyroelectric charge, p is the pyroelectric coefficient, A is surface area of pyroelectric material, and t is time. The unclamped material's pyroelectric coefficient under constant stress and electric field is expressed by following Equation (2)

$$p^{\sigma, E} = \left(\frac{dP_s}{dT} \right)_{\sigma, E} \quad (2)$$

where subscripts σ and E correspond to constant stress and electric field, respectively. Though the pyroelectric coefficient is vector quantity, the measured pyroelectric coefficient is often treated as a scalar quantity.^[46] In order to precise quantification of pyroelectric coefficient, several methods are introduced

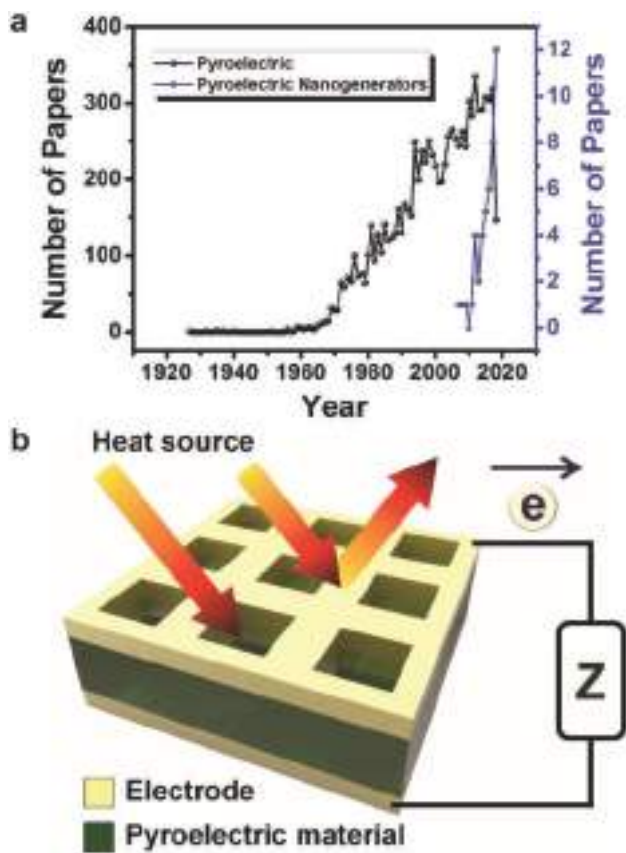


Figure 1. a) Time sequence of relevant articles on pyroelectrics and pyroelectric nanogenerators in Scopus. b) Schematic illustration of energy harvesting system based on pyroelectric effect.



Hanjun Ryu received his Ph.D. degree under the supervision of Prof. Sang-Woo Kim at the School of Advanced Materials Science and Engineering, Sungkyunkwan University (SKKU), Korea, in 2019. His research interests are fabrication and characterization of pyroelectric, piezoelectric, and triboelectric nanogenerators for energy harvesting, and portable self-powered devices.



Sang-Woo Kim is an SKKU distinguished professor (SKKU fellow) at Sungkyunkwan University (SKKU). His recent research interest is focused on piezoelectric/triboelectric nanogenerators, photovoltaics, and 2D materials including graphene, MoS₂ etc. Now he is a director of SAMSUNG-SKKU

Graphene/2D Research Center and is leading the National Research Laboratory for Next Generation Hybrid Energy Harvesters. He was the Conference Chair of the fourth Nanogenerator Piezotronics (NGPT) in 2018.

under static and dynamic conditions.^[46] Static condition methods are 1) charge compensation method, 2) hysteresis measurement method, 3) direct electrocaloric measurement, 4) flat band-voltage shift, 5) X-ray photoelectron spectroscopy (XPS) method, and 6) X-ray diffraction (XRD) and density functional theory. Dynamic condition methods are 1) temperature ramping methods, 2) optical methods, 3) periodic pulse technique, 4) laser intensity modulation methods, and 5) harmonic waveform techniques. Although these are very precise analysis methods to evaluate pyroelectric materials, complicated device structures and input environmental conditions interfere their pyroelectric output performance. Thus, reflecting output current and physical parameters of PyNG is more useful for evaluating practical pyroelectric coefficient of PyNG, whose pyroelectric coefficient is calculated by followed Equation (3)

$$p = \frac{i}{A \cdot dT/dt} \quad (3)$$

As shown in **Figure 2a–c**, schematic images show the working principle of the PyNG based on temperature change induced P_s change.^[47] For example, crystalline polymers with aligned molecular chains can have P_s due to the alignment of polarized covalent bonds and ionically bonded ceramic

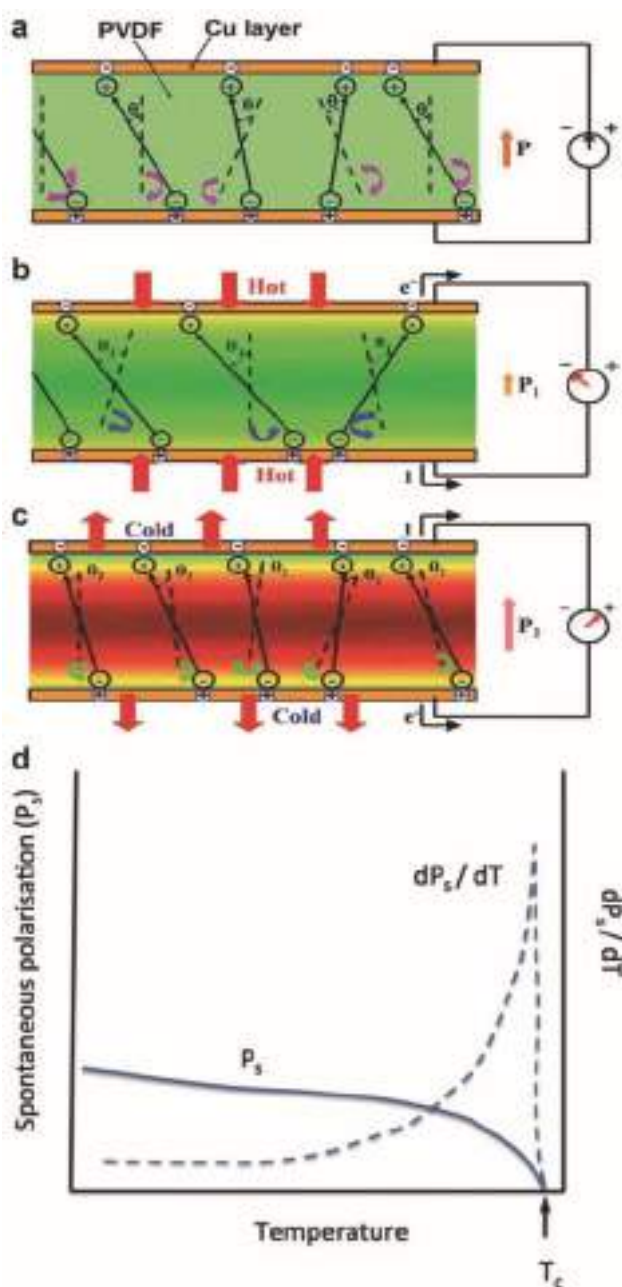


Figure 2. Schematic working principle images of the PyNG under a) constant temperature, b) heated, and c) cooled conditions. Reproduced with permission.^[47] Copyright 2014, The Royal Society of Chemistry. d) Temperature dependence of internal spontaneous polarization and pyroelectric coefficient of pyroelectric material. Reproduced with permission.^[30] Copyright 2014, The Royal Society of Chemistry.

materials can also have P_s due to the polarization of crystal structure.^[41] Ideally, all internal dipoles formed by P_s would align along one direction, but wiggling atoms disturb the perfect dipole alignment. Under invariable temperature condition, P_s and wiggling angle (θ) are constant, and there is no current flow through external circuit (Figure 2a). When the temperature increases ($dT/dt > 0$), thermal energy change dipole alignment, which wiggle around their respective pole axes

(Figure 2b). Thus, diverse polarizations have larger wiggling angles ($\theta_1 > \theta$) at higher temperatures, significantly decreasing the intensity of P_s . Thus, induced surface charges on pyroelectric material are reduced and released surface charges flow through the external circuit. When the temperature recovers to its original status, the dipole alignment of pyroelectric material is recovered, so increasing surface charges induce reverse current flows through the external circuit. Conversely, when the temperature decreases ($dT/dt < 0$), internal dipoles have smaller angles ($\theta_2 < \theta$) due to reduced thermal energy, which significantly increases the intensity of P_s (Figure 2c). Thus, induced surface charges on pyroelectric material are increased and induced surface charges flow through the external circuit. When the temperature recovers to its original status, the dipole alignment of pyroelectric material is recovered, so decreasing surface charges induce reverse current flows through external circuit. Therefore, temperature change induced internal polarization change generates electrical energy based on the pyroelectric effect.

The P_s change of pyroelectric materials dependent on temperature is shown in Figure 2d.^[30] The P_s decreases with different polarization change rate while increasing the temperature of material. When the pyroelectric material reaches the Curie temperature (T_C), the P_s rapidly decreases to zero, but the pyroelectric coefficient rises significantly. Though pyroelectric material loses its pyroelectric property above the T_C , strong polarization change beneath the T_C of the material will be effective for pyroelectric energy harvesting. Working temperature condition controls will increase the pyroelectric coefficient of the materials, which is able to dramatically increase output current of PyNGs.

3. Polymer Based Pyroelectric Nanogenerators

3.1. PyNGs Driven by Various Environmental Conditions

Ferroelectric materials such as lead zirconate titanate (PZT), barium titanate (BTO), polyvinylidene fluoride (PVDF), and poly(vinylidene fluoride-co-trifluoroethylene) [P(VDF-TrFE)] that maintain spontaneous polarization has both pyroelectric and piezoelectric property and has utilized for IR sensor, actuator, and energy harvester. Polymer-based pyroelectric nanogenerators mainly utilize ferroelectric polymers, which are PVDF and P(VDF-TrFE). Despite the low pyroelectric coefficient of PVDF, PVDF has high mechanical flexibility and biocompatibility, which applicable to wearable devices.^[45] Leng et al. reported a high performance PVDF based PyNG with simple Cu/PVDF/Cu structure using hot and cold water as a thermal energy source (Figure 3a).^[47] In order to prevent oxidation and conductivity by water, 30 μm thick polyvinyl chloride (PVC) thin film covered the device. The device was evaluated by alternating contact with the hot flow (40, 60, 80 $^\circ\text{C}$) and cold flow (0 $^\circ\text{C}$). As the hot flow temperature increased, the output performance of the PyNG increased from 6 to 11 μA . In addition, they mechanically deformed the PyNG to enhance the internal polarization change at varying temperature. The output performance of the thermal expanding/shrinking induced mechanically deformed PyNG was dramatically enhanced, which were around 100 to 190 V

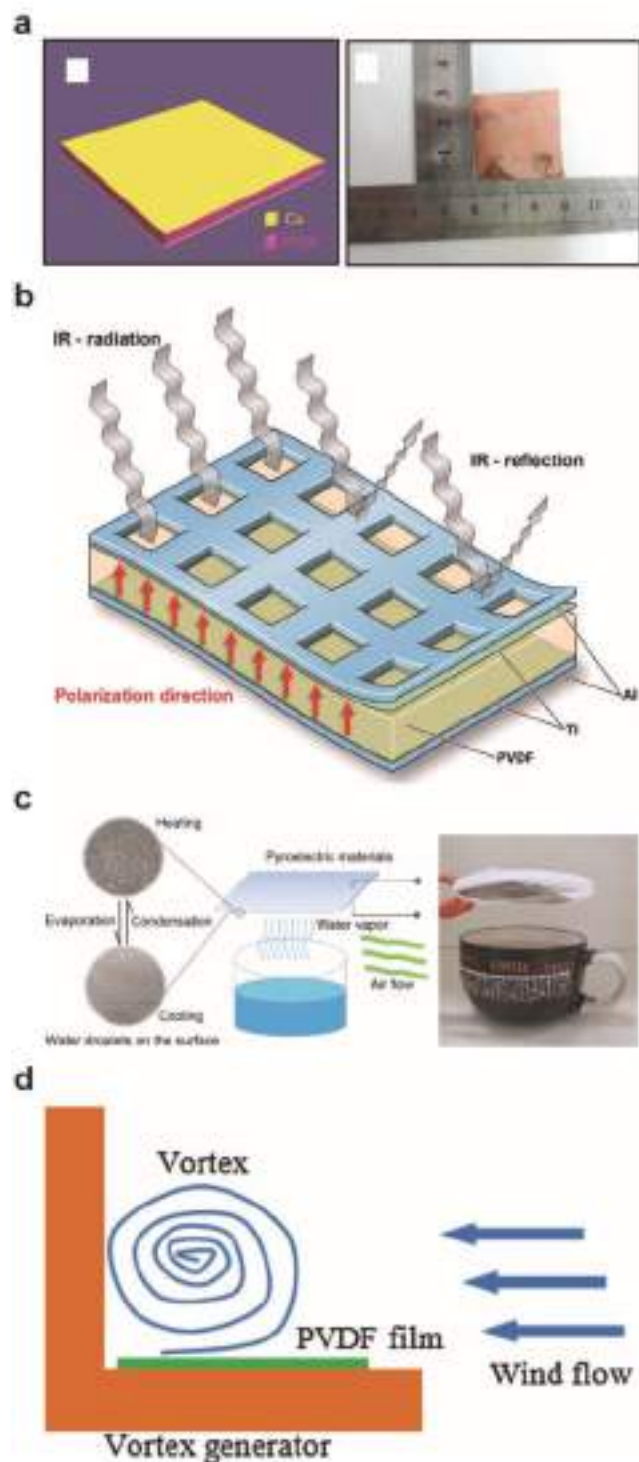


Figure 3. Thin film polymer based PyNGs. a) Schematic and real photo images of PVDF thin film-based PyNG. Reproduced with permission.^[47] Copyright 2014, The Royal Society of Chemistry. b) Schematic image of IR radiation reacted PyNG. Reproduced with permission.^[48] Copyright 2015, WILEY-VCH Verlag GmbH & Co. KGaA, Weinheim. c) Schematic and real photo images of a water vapor-driven PyNG. Reproduced with permission.^[50] Copyright 2016, Elsevier Ltd. d) Schematic image of wind flow driven PVDF-based PyNG. Reproduced with permission.^[51] Copyright 2016, Elsevier Ltd.

while hot water temperature changed from 40 to 80 °C. At the optimum external load resistance, the maximum output power reached 126 μW . To understand high output voltage of the PyNG, finite element method (FEM) simulation was performed using COMSOL Multiphysics software. The pyroelectric coefficient of PVDF film was 2.7 $\text{nC cm}^{-2} \text{K}^{-1}$.^[41] The simulated electrical potential distribution of cross-sectional PVDF film was maximum 774 V, which was higher than the experiment results due to partial contact with the flows and heat loss from the PVC thin film. For the actual usage of the PyNG, they operated 42 light emitting diodes (LEDs) and charged a 100 μF capacitor.

Zabek et al. demonstrated a PVDF based flexible PyNG with micropatterned top electrode layer in order to enhance heat transfer and to achieve larger temperature fluctuations (Figure 3b).^[48] Partially covered micropatterned top electrode was exposed to an IR radiation as a heat source, which was largely absorbed wavelength of PVDF.^[49] The partially covered aluminium (Al) electrodes with $10 \times 10 \mu\text{m}^2$ square array on flexible PVDF film. In order to evaluate PyNGs, a 175 W IR light bulb placed on 15 cm upper than the samples and heated the samples up from room temperature. The PVDF based PyNGs showed different temperature profiles depending on the electrode coverage (100%, 88%, 70%, 53%, 45%, 28%, and 19%), which resulted in 45% and 53% coverage devices showing about 30% larger temperature change than the others. This large temperature changes led faster rates of change in temperature and led to 400% higher voltage and current output performance. Therefore, balanced design between current collector and exposed PVDF area was able to maximize their energy conversion efficiency without complicate development.

Gao et al. reported P(VDF-TrFE) base high performance PyNGs driven by hot water vapor to utilize fast temperature oscillation (Figure 3c).^[50] Water is a perfect heat transfer medium due to its ability to absorb and release a large amount of heat through evaporation and vapor condensation on a surface. A large flexible thin film PyNG was fabricated by polyimide (PI) tape sealed PVDF and P(VDF-TrFE). Water vapor was supplied by continuous evaporation from hot water and the PyNG evaluated at room temperature with less than 50% relative humidity (RH) condition. In order to create an oscillating airflow like environment, a mini-fan was used to produce a 1–2 m s^{-1} oscillating flow. Hot water vapor condensed to form microscale water droplets on the surface of PyNG, and released heat to the PyNG. When the PyNG was exposed to airflow, the local humidity near the PyNG was decreased and microscale water droplets were quickly evaporated with absorbing heat of the PyNG. The IR camera measured the PyNG and hot source temperature, which the PyNG heated up around 65 °C by hot water vapor and quickly cooled down to 40 °C by air flow. This observation demonstrated that water vapor was able to efficiently heat up and cool down, and the PyNG harvested peak voltage of 160 V and peak current of 5.5 μA using the thermal energy of water vapor. The maximum power output of the PyNG was 220 μW at optimum resistance, and it successfully demonstrated charging of a 2.2 μF capacitor, operating a digital watch, and turning on blue LEDs.

Raouadi and Touayar described pyroelectric effect base wind energy harvesting using wind turbulence and vortex generator

(Figure 3d).^[51] They inserted a vortex generator in the flow passage to enhance the convective heat transfer between a PyNG and wind, and they designed wind tunnel for accurate measurement of a PVDF based PyNG. When air flow passed through the vortex generator, turbulences were created with changing temperatures and physical properties of flow. Viscous stresses which were proportional to the gradient of the velocity and heat fluxes were proportional to the temperature gradient. Additionally, heat transfer was occurred by turbulence heat fluxes. Thus, the PyNG was able to generate energy without interruption. A number of output signals were strongly related with flow velocity, and peak output voltage of the PyNG also increased with increasing flow velocity. The maximum power of the wind driven PyNG was $2.8 \mu\text{W cm}^{-2}$ at optimum load resistance, and it was able to operate a white LED and sound buzzer.

3.2. Development of Pyroelectric Materials

Polymer based flexible and thin PyNGs have been used to harvest thermal energy at various environmental conditions with a variety of structures. However, due to the limitation of pyroelectric coefficient, output performance of PyNGs is not dramatically enhanced. In order to overcome the low pyroelectric coefficient, several approaches have been reported such as crystallinity control for enhancing the pyroelectric coefficient, strain coupling effect, and polymer modification. Kim et al. reported that high dipole moment solvents controlled the crystallinity of P(VDF-TrFE) to enhance the pyroelectric coefficient (Figure 4a).^[52] Dipole moment of tetrahydrofuran (THF), methylethyl ketone (MEK), dimethylformamide (DMF), and dimethylsulfoxide (DMSO) is 1.75, 2.7, 3.8, and 4.1 D, respectively. Dissolved P(VDF-TrFE) in four different solvents were examined their crystallinity by XRD and differential scanning calorimetry (DSC) measurements. Gel permeation chromatography (GPC) measurements were performed to measure the relative chain length of P(VDF-TrFE). A high dipole moment solvent based P(VDF-TrFE) thin film had small full width at half maximum (FWHM) value of β ferroelectric phase^[53] and DSC result showed that high dipole moment solvent-based P(VDF-TrFE) had the highest crystallinity than other samples. High crystallinity

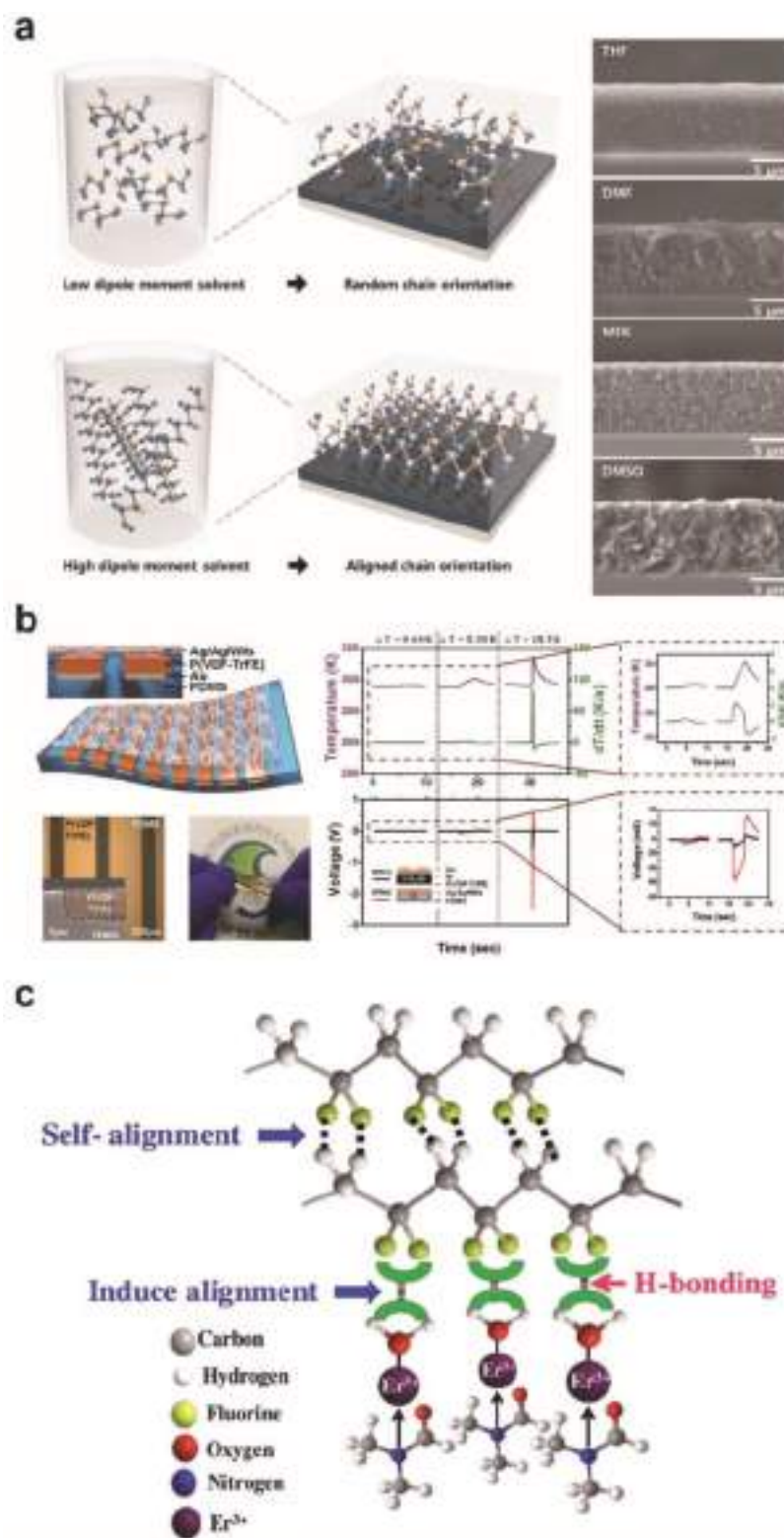


Figure 4. The strategy of enhancing output power of PyNGs. a) Schematic images of low and high crystalline P(VDF-TrFE). Reproduced with permission.^[52] Copyright 2017, WILEY-VCH Verlag GmbH & Co. KGaA, Weinheim. b) Schematic illustrations of the stretchable PyNG and output performance. Reproduced with permission.^[55] Copyright 2015, WILEY-VCH Verlag GmbH & Co. KGaA, Weinheim. c) Schematic image of the β -phase nucleation process Er-PVDF film. Reproduced with permission.^[60] Copyright 2017, Springer Nature.

of P(VDF-TrFE) was mainly due to long end-to-end chain length of P(VDF-TrFE).^[54] GPC measurement also confirmed high dipole moment solvent-based P(VDF-TrFE) had a high molecular weight. High crystalline P(VDF-TrFE) had a higher degree of dipole alignment and pyroelectric coefficient than low crystalline P(VDF-TrFE) which result in 1.4 times higher output peak voltage and current. Therefore, higher dipole moment solvent offered promising strategy to increase pyroelectric coefficient of P(VDF-TrFE) and power performance of P(VDF-TrFE) based PyNGs.

Lee et al. introduced stretchable PyNGs and thermally induced stain coupling effect in order to enhance output performance of PyNG using P(VDF-TrFE) and polydimethylsiloxane (PDMS) (Figure 4b).^[55] Micropatterned PDMS was able to be utilized as stretchable substrate for PyNG and its high thermal expansion coefficient than P(VDF-TrFE) was able to induce compress force to P(VDF-TrFE) while heating.^[56] They confirmed the β ferroelectric phase of patterned P(VDF-TrFE) by Fourier transform infrared (FT-IR) and XRD spectroscopy.^[57,58] Different thermal expansion coefficient of neighboring two materials built thermal expansion induced strain, so specially designed PDMS provided additional strain to P(VDF-TrFE) during heat. Internal polarity of the P(VDF-TrFE) was changed by heat and strain, which result in five times enhanced pyroelectric output performance by same temperature changing condition. In addition, the low thermal conductivity of PDMS remained higher heat in P(VDF-TrFE) than the high thermal conductivity substrate device.^[59] Thus, large thermal expansion of PDMS induced huge compressive strain into P(VDF-TrFE), which generated a larger negative potential by coupling negative piezoelectric and negative pyroelectric potential. They also demonstrated that the PDMS based PyNG was able to stretch over 15% without output degradation and operated red, yellow, and green LEDs and black liquid crystal display (LCD). Micropatterned substrate based the stretchable and strain coupled PyNG offered efficient strategy to enhance output performance and stretchability of polymer based PyNG.

Ghosh et al. reported Er³⁺ modified PVDF (Er-PVDF) film based enhanced pyroelectric property through the formation of a self-polarized ferroelectric β phase and porous structure (Figure 4c).^[60] Similar additives such as Ce³⁺, Eu³⁺ and Yb³⁺ also have a self-polarized ferroelectric β phase and have been explored to enhance the piezoelectric properties of PVDF,^[61–63] but integrated PVDF and Er³⁺ design enhances thermal sensitivity under an IR irradiation due to superior optical activity of Er³⁺.^[60] When Er-salt was mixed with PVDF-DMF solution, Er³⁺ was presented in Er-PVDF that was confirmed by XPS.^[64–68] The strong O–H bond of water and F–C bond of PVDF drove the –CH₂–CF₂ dipoles so Er-PVDF dipole was self-polarized ferroelectric β phase with high thermal stability than bare PVDF. Er-salt created porous structure of PVDF with a flower like surface morphology due to fast crystallization, so it was highly flexible compared to thin PVDF film. Due to Er³⁺, Er-PVDF film was a good IR absorber. Thus, small-scale energy was efficiently converted into electric energy by pyroelectric effect. When temperature change rate was less than 1 K s^{–1}, peak current of output was 13 nA. Using the PyNG, it was successfully charged a 4.7 μ F capacitor to operate the low power consumer electronics. Therefore, in order to enhance the PVDF property, IR sensitive Er³⁺ modification was one of the promising methods.

3.3. Wearable Pyroelectric Nanogenerators

Human is one of the abundant thermal energy sources, so PyNGs are able to use power source of wearable electronics. To utilize PyNGs as wearable device, flexibility, stretchability, or fiber type materials are required. Xue et al. reported integrated a N95 respirator and a PVDF thin film PyNG for harvesting energy of human respiration (Figure 5a).^[69] They demonstrated self-powered breathing sensor using a flexible PVDF film installed on a common respirator for sustainable energy harvesting and self-powered breathing monitoring. The size of 3.5 cm \times 3.5 cm PVDF thin film with thickness of 30 μ m was exposed by the body exhaled gas that had the same temperature of body. The temperature-changing rate of the PyNG by human exhaled gas was 13 C s^{–1} and the corresponding peak output current and voltage of the PyNG was 2.5 μ A and 42 V, respectively. The maximum output performance of the PyNG was 8.31 μ W at the load resistance of 50 M Ω , and the PyNG showed stable output performance after ten days without power degradation. The water vapor accompanied from exhaled gas was able to condense on the PyNG, which resulted in an increasing temperature quickly, but decreasing temperature slowly. In order to demonstrate a sustainable capacitor charging by exhale gas, a simple circuit using a 10 μ F capacitor and a rectifier was designed for energy harvester. The PyNG successfully charged a capacitor to 1 V in 18 s and turned LEDs and LCD on.

Although PVDF thin film is able to be used as a wearable device, fiber type PVDF is required to overcome the limitation of the flexibility and stretchability of thin film PVDF. Mokhtari et al. introduced an electrospinning method to make PVDF nanofibers (Figure 5b).^[70] Electrospinning at low temperature of chamber or quick evaporation of solvent formed the β ferroelectric phase of PVDF without post treatment, but the mechanical force by rotating was not effective in forming the β ferroelectric phase. A high voltage was applied in order to eject the PVDF solution at a controlled flow rate. An electrostatic force from a high voltage overcame the surface tension of the PVDF solution at the needle of electrospinning equipment. The charged fluid jet was collected on ground due to electric field between the PVDF solution and ground. The whipping motion of the PVDF jet allowed the solvent evaporation, so the β ferroelectric phase PVDF nanofibers were collected on the collection plate. The distance between the tip and the collection plate was one of the key factors to control the diameter of PVDF nanofiber. In order to analyze PVDF nanofibers, FT-IR, XRD, and DSC analysis were performed and proved the β ferroelectric phase. Therefore, the electrospinning method is able to make the β phase PVDF nanofibers and fabric without additional poling process for wearable energy harvesters.

3.4. Wearable Pyroelectric Nanogenerators

In order to realize the stretchable hybrid PyNGs for wearable electronic devices, Lee et al. reported patterned PDMS-carbon nanotubes (CNTs) composite and graphene nanosheets based highly stretchable PyNGs (Figure 6).^[71] Graphene, which had high thermal conductivity and flexibility was used as top electrode instead of metal electrode.^[72,73] To fabricate the stretchable hybrid PyNG, patterned PDMS-CNT composite for stretchable

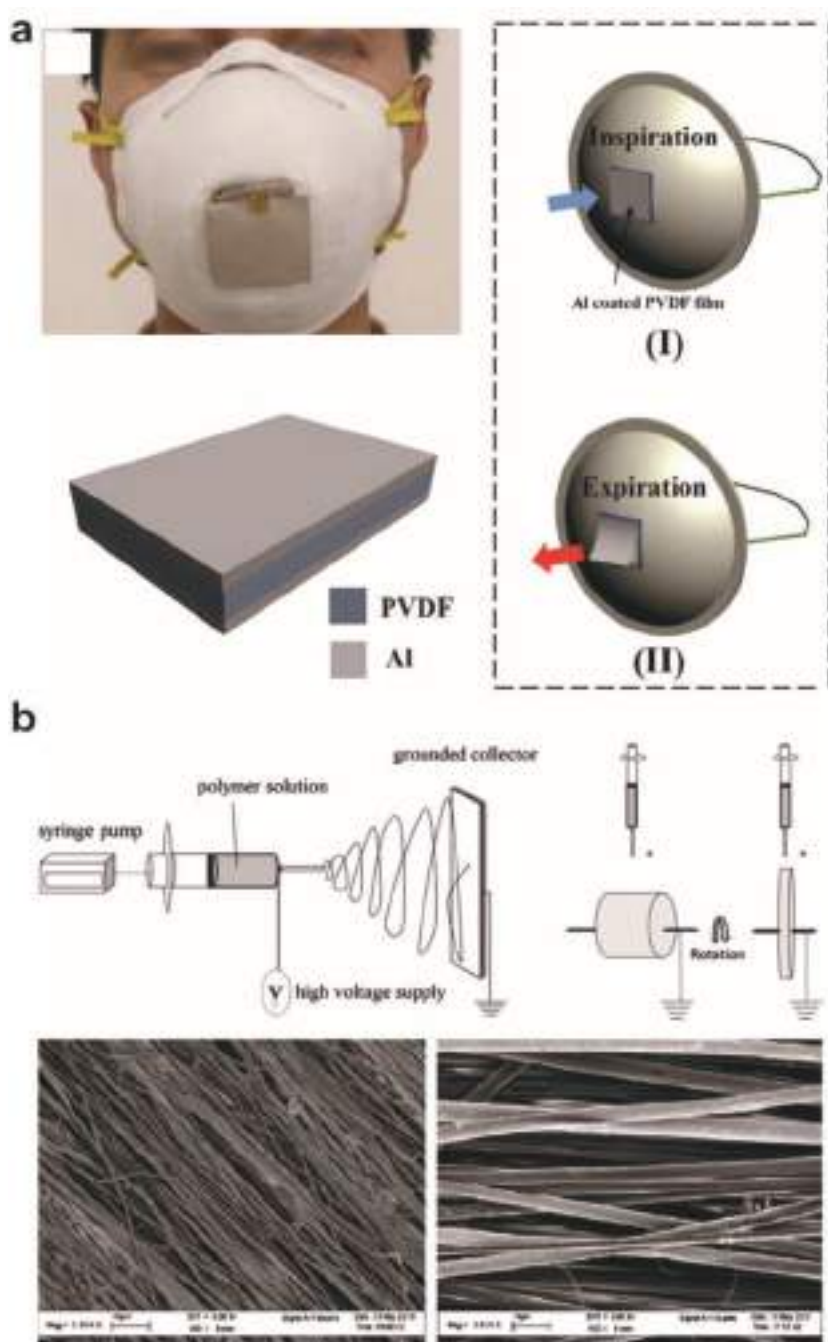


Figure 5. Wearable PyNGs using polymer material. a) Real photo and schematic images of the wearable PyNG. Reproduced with permission.^[69] Copyright 2017, Elsevier Ltd. b) Schematic image of electrospinning process and SEM images of fibrous PVDF. Reproduced with permission.^[70] Copyright Taylor & Francis.

substrate was obtained using silicon (Si) master mold. P(VDF-TrFE) was spin coated on the micropatterned PDMS-CNT directly, and annealed at 140 °C for 2 h. XRD and FT-IR analysis were confirmed the β ferroelectric phase of P(VDF-TrFE). Lastly, multilayer graphene was transferred on the P(VDF-TrFE). Due to patterned CNT-PDMS, P(VDF-TrFE) and graphene followed the pattern of CNT-PDMS, which result in increasing stretchability of P(VDF-TrFE) and graphene electrode than

flat P(VDF-TrFE) and graphene. Human body was able to apply mechanical deformation and temperature change on the hybrid PyNG. Thus, both piezoelectric and pyroelectric effect occurred in P(VDF-TrFE), which resulted in both piezoelectric and pyroelectric output being generated.

Piezoelectric and pyroelectric effects both changed internal polarization of P(VDF-TrFE) by external force and temperature change, respectively. Stretching and releasing of P(VDF-TrFE) made opposite internal polarization change, and heating and cooling also made opposite internal polarization change. Thus, mechanical change and temperature change were able to reinforce internal polarization change with proper environment change. For example, releasing and heating the device enhanced internal polarization change in P(VDF-TrFE), or compress and heating the device enhanced internal polarization change in P(VDF-TrFE). Piezoelectric peak output voltage of the hybrid PyNG was 1 V, and pyroelectric peak output voltage of the Hybrid PyNG was 0.4 V. The hybrid PyNG output peak voltage was increased up to 1.4 V under mechanical deformation and temperature change, which was similar with summation of each piezoelectric and pyroelectric output voltage. They demonstrated that the stable output performance of the hybrid PyNG depends on the stretch rate and mechanical durability after 30% stretching. Thus, patterned substrate is able to provide stretchability to nonstretchable P(VDF-TrFE) and graphene for wearable application.

3.5. Hybrid Pyroelectric Nanogenerators

Hybridization of the various energy harvesting systems is an effective strategy for enhancing the energy conversion efficiency, thus hybrid pyroelectric, piezoelectric, triboelectric, and photovoltaic energy harvesters are used for high performance energy harvesting systems. In order to hybridize different energy harvesting systems, impedance of each energy harvesting system is matched, or energy harvesters with different impedance use temporary energy storage such as capacitor, battery to coordinate different energy harvesters in one device. Thus, similar impedance-based hybrid nanogenerators are not required special electrical connection, but different impedance-based hybrid nanogenerators are required for power management circuit or impedance matching. You et al. demonstrated PVDF based piezoelectric and pyroelectric hybrid nanogenerator (PPNG) (Figure 7).^[74] They reported a lightweight and flexible hybrid nanogenerator using PVDF nanofiber

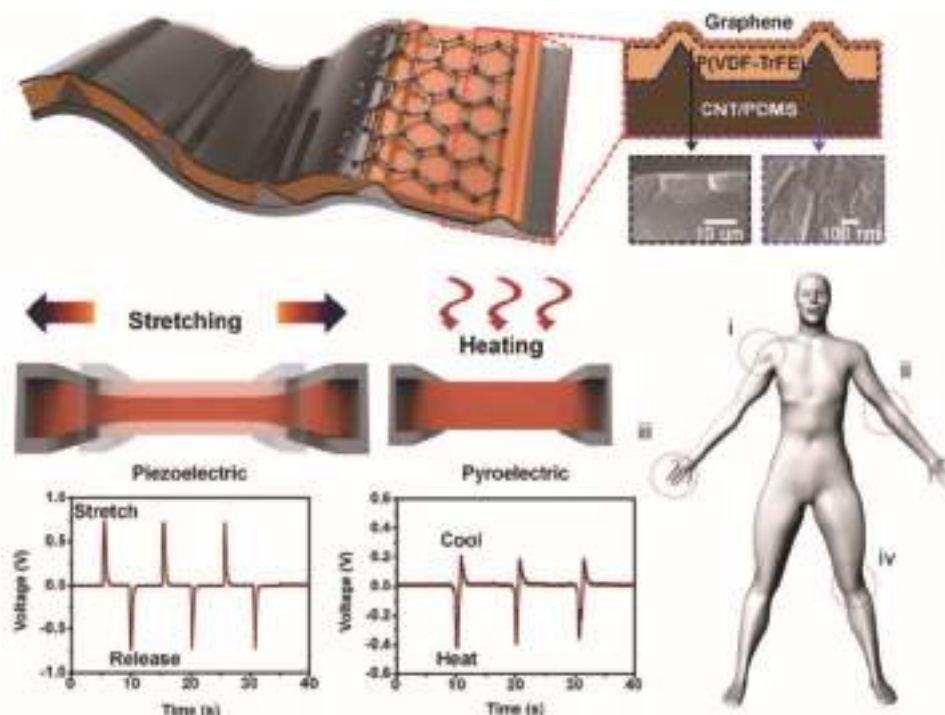


Figure 6. Schematic images of highly stretchable hybrid PyNG. Reproduced with permission.^[71] Copyright 2013, WILEY-VCH Verlag GmbH & Co. KGaA, Weinheim.

membrane (NFM) without post poling treatment. A thermoplastic polyurethane (TPU), carbon nanotube slurry (CNTs), PVDF, and PEDOT:PSS-polyvinyl pyrrolidone (PVP) conductive NFM (CNFM) were sequentially deposited by electrospinning process. The morphologies of the NFMs were characterized using a scanning electron microscope (SEM) and XRD. The conductivity of CNTs layer was about $4.4 \times 10^{-3} \text{ S cm}^{-1}$, and the conductivity of CNFM was about $1.27 \times 10^{-4} \text{ S cm}^{-1}$. Due to the electrospinning process, both electrodes showed outstanding flexibility, thus, they were suitable for wearable applications. The hybrid NG that the effective size was $4 \text{ cm} \times 4 \text{ cm}$ generated $2.85 \mu\text{J}$ at 3 Hz impact-release cycle. Due to the time-dependent piezoelectric output performance, output performance of the hybrid NG was increasing with increasing impact force and speed. Pyroelectric output performance of the hybrid NG was about 20 nA small temperature change condition, and piezo-pyroelectric output performance of the hybrid NG was successfully summation due to enhanced spontaneous polarization change. They demonstrated a walking-based energy harvesting system and arm bending based energy harvesting system for wearable applications. When the device was under mechanical deformation and temperature change, both piezoelectric output and pyroelectric output were successfully integrated to generate a hybrid output.

Integrated with another energy harvesting system is a practical approach for increasing the power performance of an energy harvester. In particular, TENGs have simple structures for generating displacement current to convert mechanical energy into electric energy. Sun et al. reported one structure flexible and biocompatible tribo/piezo/pyroelectric hybrid NG with transparent electrodes (Figure 8a).^[75] The hybrid NG consisted of PDMS, PVDF and silver (Ag) nanowires which were

favorable in terms of mass production and the hybrid NG had 82% transmission due to high transparency of each component. Replicated leaf-venation (LV) pattern mould was utilized to enhance conductivity with high transparency of electrodes. To harvest mechanical energy, finger pressing the PDMS generated surface triboelectric charge on PDMS and internal polarization change of PVDF. Induced current flows between top and bottom transparent electrodes by triboelectric charge and internal dipole change generated 55 V and pyroelectric effect induced current flows generated 86 V. They demonstrated potential flexible smart wearable sensors using the hybrid NGs. Wrist, throat, and neck attached the hybrid NG successfully demonstrated heartbeat, swallowing, neck tilting and coughing sensors. They inserted LCD film between electrode and PDMS to demonstrate temperature gradient of human finger, so the color of LCD changed from black to red, green, and blue depend on the temperature change rates by finger touch. They also demonstrated breath sensor that was able to distinguish weak, normal, and deep breath depend on the pyroelectric output performance driven change of LCD color display.

Another reported tribo/piezo/pyroelectric hybrid NG by Zhang et al. was used as both a thermal and mechanical energy harvester, and for electromagnetic shielding purposes using PVDF, Ag, and rubber (Figure 8b).^[76] Decreasing electromagnetic radiation is important for preventing potential threats to human health,^[77,78] thus they presented a new type wearable hybrid NG included wide electromagnetic shielding range. The developed stretchable and wearable electromagnetic shielding hybrid NG (ES-HNG) was composed of a stretchable TENG and several piezo/pyro hybrid NGs. The TENG was composed of a layer of conductive anti-electromagnetic radiation fabric and rubber. Owing to the island structure of the ES-HNG, it had

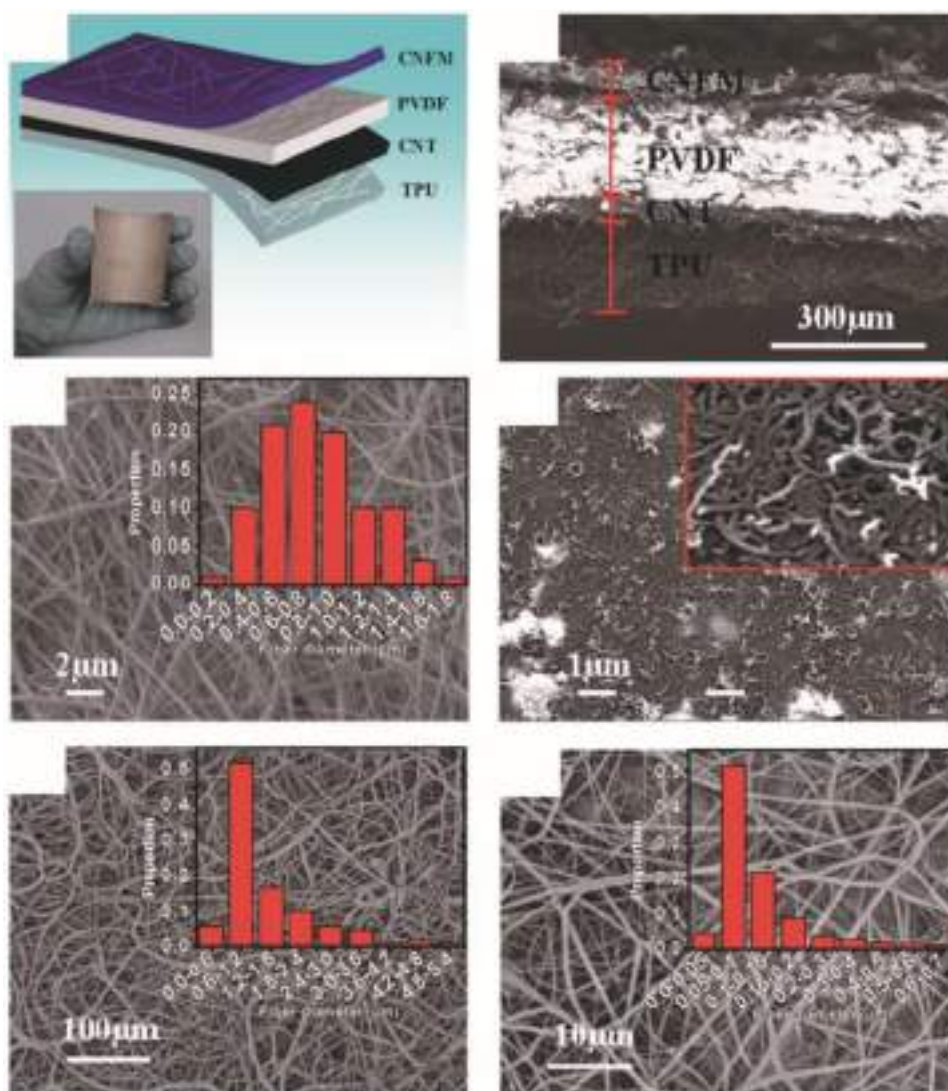


Figure 7. Nanowire ferroelectric polymers based PyNG. Reproduced with permission.^[74] Copyright 2018, The Royal Society of Chemistry.

40% stretchability with slight change. The mechanical deformation of the ES-HNG generated triboelectric and piezoelectric potential with excellent strain sensitivity and pyroelectric potential was formed by temperature change. The hybrid piezoelectric NG (PENG) and TENG generated peak output current of 6 nA at applied 0.3 N force condition and 18 nA at bending condition. The PyNG generated peak output current of 15 nA at small temperature change. They fabricated keyboard cover using ES-HNG to harvest biomechanical energy and to decrease electromagnetic radiation. It successfully harvested 20 μA , charged a 10 μF capacitor, and decreased electromagnetic radiation from 6261 to 0 $\mu\text{W cm}^{-2}$. They also demonstrated self-powered health monitor and wide range electromagnetic radiation protector for pregnant woman. This interesting demonstration of energy harvester-based electromagnetic radiation protecting material suggests future smart functional energy harvesters.

Zheng et al. designed individually/simultaneously harvesting thermal energy and wind energy using hybrid TENG, PENG

and PyNG (Figure 8c).^[79] A PPNG that used polarized PVDF thin film deposited by Cu electrodes was encapsulated by PI tape to prevent water vapor contamination. Fluorinated ethylene propylene (FEP) film was applied to cover the PVDF film for triboelectrification layer. One end of the PPNG flutter was fixed on the side of Cu deposited substrate and the other side of the PPNG was left free. During the contact and separation process between Cu electrode and FEP film by wind, periodic alternative output was generated by TENG, which peak output voltage and current were 350 V and 30 μA , respectively. Temperature change and mechanical deformation of the flutter formed piezoelectric potential and pyroelectric effects induced internal polarization change of PVDF. Peak output voltage of the PENG was 20 V, and peak output voltage and current of PPNG that was enlarged output due to enhanced polarization change was 350 V and 41 μA , respectively. They demonstrated charging a 22 μF capacitor with various combinations of TENG, PENG, and PyNG. TENG and PPNG hybrid generator charged three to five times faster than individual NGs, and it successfully turned

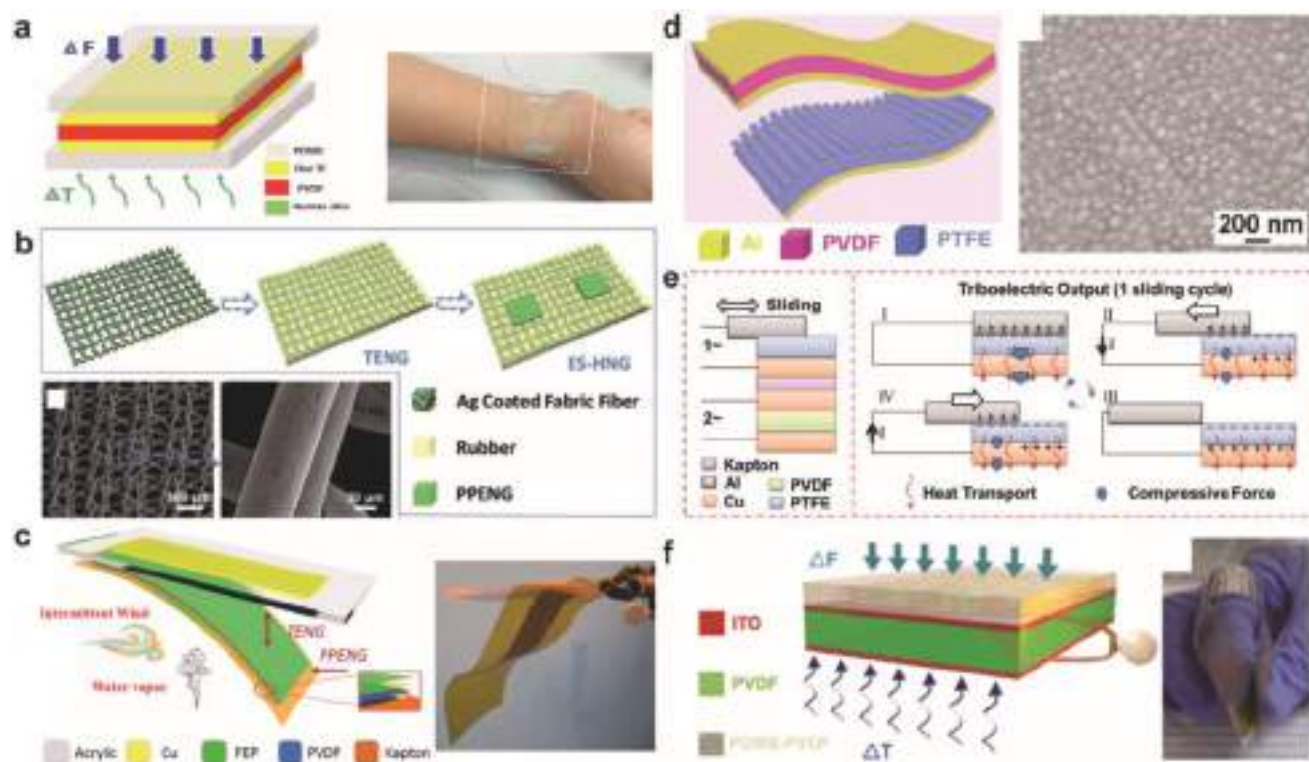


Figure 8. Mechanical and thermal hybrid NGs. a) Schematic and real photo image of hybrid NG. Reproduced with permission.^[75] Copyright 2018, Elsevier Ltd. b) Schematic image of tribo/piezo/pyroelectric hybrid NG. Reproduced with permission.^[76] Copyright 2017, WILEY-VCH Verlag GmbH & Co. KGaA, Weinheim. c) Schematic image of flexible and thin hybrid NG. Reproduced with permission.^[79] Copyright 2018, American Chemical Society. d) Polarized and patterned PVDF film-based hybrid NG. Reproduced with permission.^[80] Copyright 2015, American Chemical Society. e) Schematic working principle of sliding heat induced mechanical/thermal hybrid NG. Reproduced with permission.^[82] Copyright 2015, WILEY-VCH Verlag GmbH & Co. KGaA, Weinheim. f) Schematic illustration of one-structure-based hybrid NG. Reproduced with permission.^[83] Copyright 2016, WILEY-VCH Verlag GmbH & Co. KGaA, Weinheim.

on 24 small white LEDs and turned on 31 green LEDs using human breath.

Zhang et al. demonstrated a flexible PPNG using a polarized PVDF film so as to scavenge both thermal and mechanical energies (Figure 8d).^[80] An inductively coupled plasma-driven reactive ion etching was performed for enhancing a TENG performance to modify surface morphology of the polytetrafluoroethylene (PTFE) film.^[81] In order to harvest mechanical energy based on triboelectrification and electrostatic induction, the Al top and bottom electrodes deposited PVDF film of the PPNG had contact with a surface modified PTFE film to generate large triboelectric charges; peak output voltage and current of the TENG were 8 V and 420 nA, respectively. The PVDF base PyNG was evaluated under 3.2 K s^{-1} temperature change rate; peak output voltage and current of the PyNG were 3.2 V and 100 nA. The PENG generated peak output of 2.3 V and 30 nA when a compressive force was applied. When various energy sources applied to the hybrid NG, output performance of each NG was coupled to each other and successfully turned up a LCD by hand touch. Another practical application of the hybrid NG was self-powered cathodic protection (CP). Electrochemical impedance spectroscopy analysis was performed in order to analyze their electrochemical characteristics. The corrosive property of steel with and without CP showed that the hybrid NG decreased polarization potential and corrosion rate.

Conventional TENGs and PENGs waste thermal energy that is converted from mechanical energy by friction heat, but Zi

et al. reported triboelectric–piezoelectric–pyroelectric hybrid high efficient NG to utilize mechanical energy and friction induced heat energy (Figure 8e).^[82] The mechanical energy of sliding and pressing was harvested by TENG and PENG and friction induced heat energy was converted into electricity by PyNG. The TENG was consisted of Al foil as the sliding part and PTFE film deposited Cu electrode as the static part. The PPNG were consisted of Cu deposited PVDF film and PI film was laminated between TENG and PPNG to prevent electric shortage. When Al foil slide on the hybrid NG, sliding motion induced surface triboelectric charge change and press force induced internal polarization change of PVDF generated current flow through external circuit. Friction induced heat also induced internal polarization change of PVDF by pyroelectric effect and generated current flow. Peak output voltage and current of TENG was 1132 V and 1.45 mA m^{-2} , respectively, and maximum peak power was 146 mW m^{-2} at the matched load of $140 \text{ M}\Omega$. The output voltage and current of PPNG was 3 V and $6 \text{ }\mu\text{A}$, respectively. They successfully demonstrated that it could power up a LED bulb and charge a 41.9 mF capacitor. A self-powered sensor of the temperature and the normal force was also demonstrated using a modified hybrid NG structure. It was able to measure at least $0.09 \text{ }^\circ\text{C}$ change and 0.5 N force.

Wang et al. demonstrated another one structure based tribo-piezo-pyroelectric hybrid NGs using large-scale PVDF (Figure 8f).^[83] PVDF nanowires, PDMS, indium tin oxide (ITO) electrodes were used for transparent, flexible, and hybridized

NG. Ferroelectric β phase of PVDF nanowire fabricated by electro-spinning process having diameters of 200 to 500 nm was confirmed by XRD analysis.^[84,85] The total transparent of the device was exceeding 95% and 30 cm \times 30 cm sized PVDF and PDMS composite film was fabricated for large-scaled NG.^[86] A flexible nylon film was contacted and separated with PVDF-PDMS composite film to make contact electrification and strain in PVDF-PDMS composite. When 15 m s⁻¹ speed of airflow was applied to the device, TENG and PENG part of the device-generated peak current and voltage output of 20 μ A and 0.6 V under 400 k Ω , respectively. The PyNG part of the device generated a peak current and voltage of 120 nA and 120 V, respectively, and maximum output power was 6.05 μ W under a load resistance of 1.5 G Ω . For the application, the hybrid NG successfully turned on two light bulbs and charged a 10 μ F capacitor under various conditions. Therefore, polymer based transparent and flexible hybrid NGs are able to harvest mechanical and thermal energy efficiently for wearable sensor and power source.

In order to enhance the output power of the TENG and PPNG, integration of solar cell and PPNG was introduced by Yang et al. (Figure 9a).^[87] PVDF was used as a PPNG and zinc oxide (ZnO) nanowires grown on flexible polyester and poly(3-hexylthiophene) (P3HT) heterojunction solar cell were used as a solar cell. The bottom PPNG consisted of Ag electrode and PVDF film. The top solar cell consisted of ITO transparent electrode, ZnO nanowire array, P3HT film, and Ag electrode. When temperature change rate was 0.8 K s⁻¹, the PyNG harvested 2.5 V and 2.4 nA, and the pyroelectric coefficient of PVDF was -44 μ C m⁻² K⁻¹, which was larger than ZnO and KNbO₃.^[88,89] When a compress force was applied on the PENG, peak output voltage and current were 0.5 V and 20 nA, respectively. Using the PPNG, they demonstrated the derivation of a LCD by human touch. In order to harvest solar energy, ZnO nanowire-P3HT cell was evaluated under air mass (AM) 1.5 illumination light intensity; open circuit voltage of the solar cell was 0.4 V and short circuit current of solar cell was 31 μ A cm⁻². When the solar cell

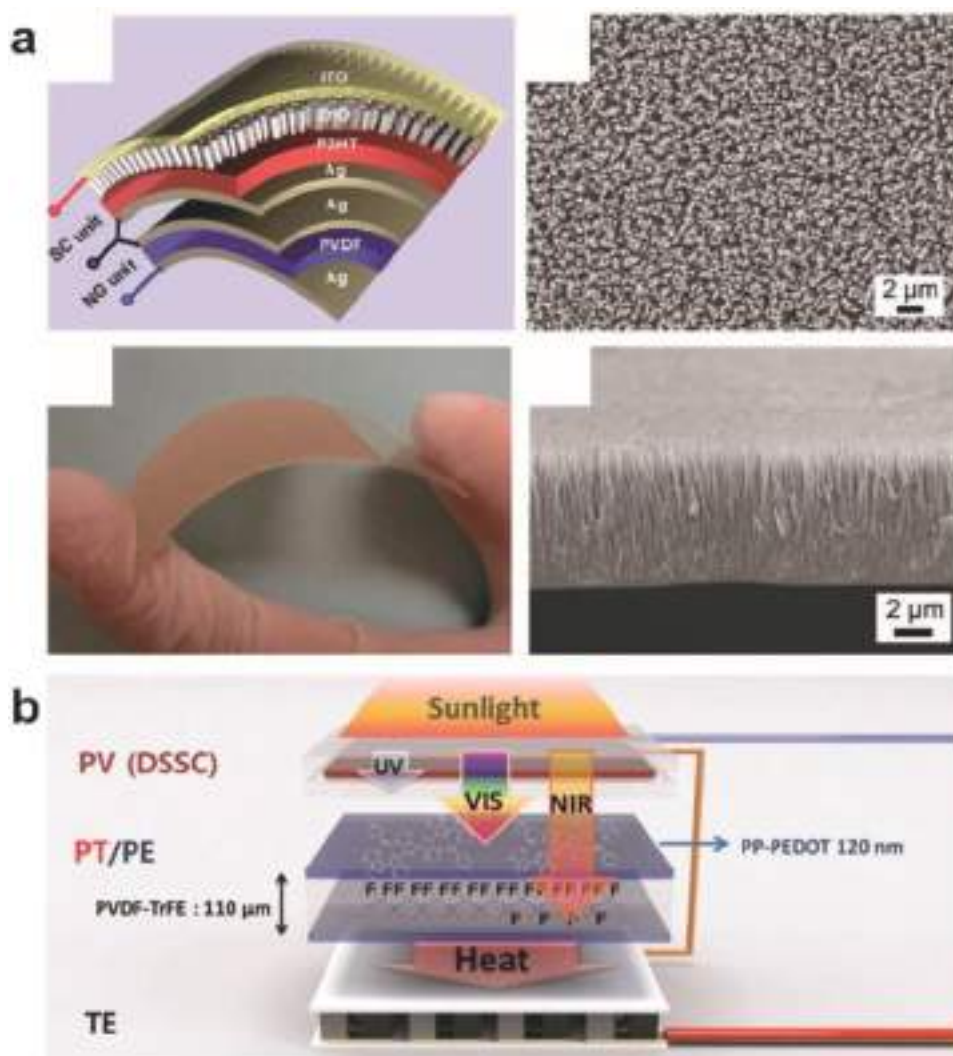


Figure 9. Solar, mechanical and thermal hybrid NGs. a) Schematic image of ZnO nanowires and PVDF-based solar and thermal hybrid NG. Reproduced with permission.^[87] Copyright 2012, American Chemical Society. b) Schematic image of P(VDF-TrFE), DSSC, and thermoelectric hybrid NG. Reproduced with permission.^[90] Copyright 2015, American Chemical Society.

and PyNG were simultaneously operated, both output performances were successfully integrated and enhanced. The PPNG and solar cell hybrid nanogenerator successfully charged a Li-ion battery and charged battery turned on four red LEDs.

Another solar cell, pyroelectric, and thermoelectric hybrid system was introduced by Park et al. for enhancing power performance of polymer based nanogenerator (Figure 9b).^[90] PEDOT film, P(VDF-TrFE) film, titanium dioxide (TiO₂) based dye sensitized solar cell (DSSC) and thermoelectric devices were used as a hybrid nanogenerator. Major challenge of the hybrid nanogenerator was high photothermal (PT) effect, transparency, electrical conductivity, and surface energy matching of the PEDOT film. PEDOT was coated on both side of β phase P(VDF-TrFE) through the solution casting polymerization used as PyNG part.^[91,92] It is abbreviated as PP-PEDOT hereafter. Compare the PT effect of bare PVDF and the PP-PEDOT by near infrared (NIR) irradiation, the PP-PEDOT showed higher PT effect with the greatest temperature change ($\Delta T > 10$ °C). The PyNG generated peak voltage and power under NIR irradiation were 0.2 V and 22 $\mu\text{W m}^{-2}$, respectively. For an efficient heat transfer, a thermal paste was coated on the thermoelectric device; output voltage and current of thermoelectric device were 11 mV and 13.6 mA, respectively, which was five times higher voltage output than previous reports.^[93,94] Due to absorption wavelength of DSSC, from 400 to 1600 nm range of the light was able to transmit DSSC and absorbed by the PP-PEDOT. Thus, the DSSC, the PyNG, and thermoelectric device all efficiently harvested light energy. The energy conversion efficiency of the DSSC under AM 1.5 illumination light intensity was 9.72% and the energy conversion efficiency of the hybrid NG was 11.7% with increasing open circuit voltage. Using the voltage enhanced hybrid NG, they successfully demonstrated that it could charge a 47 μF capacitor and operate a white LED as well as an electrochromic display by light. Therefore, hybridization of energy harvesting systems is able to enhance output performance of NGs, but enhancing pyroelectric coefficient is demanded for higher energy conversion efficiency and simplification of NGs.

4. Ceramic Based Pyroelectric Nanogenerators

4.1. ZnO Based Pyroelectric Nanogenerator

Ceramic based pyroelectric materials such as ZnO, PZT, KNbO₃, 1,4-diazabicyclo[2.2.2]octane perrhenate (dabcoHReO₄), BiFeO₃ (BFO), and BTO have higher pyroelectric coefficient and stronger thermal shocks than the polymer pyroelectric materials that are described above. Thus, ceramic material based PyNGs have been utilized for high-resolution thermal sensor applications. Yang et al. reported ZnO nanowire arrays based pyroelectric nanogenerator (Figure 10a).^[88] ZnO nanowires were grown on the ITO substrate and Ag was deposited on the ZnO as the top electrode in order to make Schottky contact with ZnO. Temperature fluctuation created the anisotropic polarization in ZnO nanowires, which resulted in electron flow through external circuit.^[95] *I*-*V* characteristic of the PyNG confirmed a Schottky contact between ZnO nanowires and Ag. Under 0.5 K s⁻¹ temperature change rate condition, the

PyNG generated peak output voltage and current of 5.8 mV and 108 pA, respectively. Output performance of the PyNG was linearly increasing with increasing the temperature change rate in the device. Pyroelectric coefficient of the ZnO nanowires was 1.2–1.5 nC cm⁻² K⁻¹ that was larger than previous reports due to *c*-axis oriented ZnO structure.^[42,96] COMSOL multiphysics simulation of electrical potential distribution in a single ZnO nanowire was shown from -3.1 to 2.6 V, which was larger than the experimental results due to screening effect of the free charge carriers.^[97,98]

Another wurtzite ZnO nanowire based PT triggered flexible PyNG and self-powered photosensor were reported by Wang et al. (Figure 10b).^[99] Wurtzite crystal structure of ZnO nanowires that used as pyroelectric material was effectively tuned the charge transport across the p-n junction by pyroelectric potential. The variation of the depletion region was caused by built in potential change, which resulted in the expansion of shrinkage of the depletion region. The NIR light triggered PyNG modified p-n junction of Si/ZnO nanowires for self-powered photodetector. Si p-type semiconductor and ZnO n-type semiconductor formed depletion region at the junction interface. With NIR irradiation, the pyroelectric potential was created within ZnO nanowires and induced electron flow through an external circuit. The depletion width was also expanded by change of electric field inside a ZnO nanowire. When NIR irradiation was shut down, a reverse pyroelectric potential occurred in the ZnO nanowire, which resulted in shrinking the depletion width and reverse current flow through an external circuit. Peak current of the PyNG was 2 μA at the NIR light irradiation condition. Under strong NIR irradiation condition, peak current of the PyNG was 1 mA and on/off photocurrent ratio was up to 10⁷.

4.2. PZT Based Pyroelectric Nanogenerator

Yang et al. reported a PZT film based PyNG with a high pyroelectric coefficient and self-powered nanosystems (Figure 11a).^[100] A 175 μm thickness of PZT film was deposited on a 300 nm thick nickel (Ni) and top electrode of Ni was deposited on the PZT film. Peak output voltage and current of the PyNG was 2.8 V and 42 nA, respectively, at temperature change of 0.2 K s⁻¹ condition. Obtained pyroelectric coefficient of PZT film was 80 nC cm⁻² K⁻¹ which was much larger than that of ZnO.^[88,97] At higher temperature change rate condition, the PyNG generated peak voltage of 22 V, peak current of 430 nA, and corresponding maximum peak power of 0.2 mW cm⁻³. The PyNG was able to be continuously driven for longer than 60 s, which was 30 times higher performance than previously reported PENG.^[101] Compared with COMSOL simulation results and experimental result, the PyNG required a lot of enhancement before it could reach the theoretical value. The PyNG was used to charge a Li-ion battery for a practical application. The battery was charged by the PyNG from 650 to 810 mV in 3 h, and total stored capacity was 23 nAh.

PZT micro/nanowire based PyNG was reported to detect the temperature of a fingertip by Yang et al. (Figure 11b).^[102] A PZT micro/nanowire was achieved by pressing of a bulk PZT, and a PZT micro/nanowire was poled by applied voltage of 3.5 kV. Two ends of a PZT microwire were fixed by Ag paste on glass

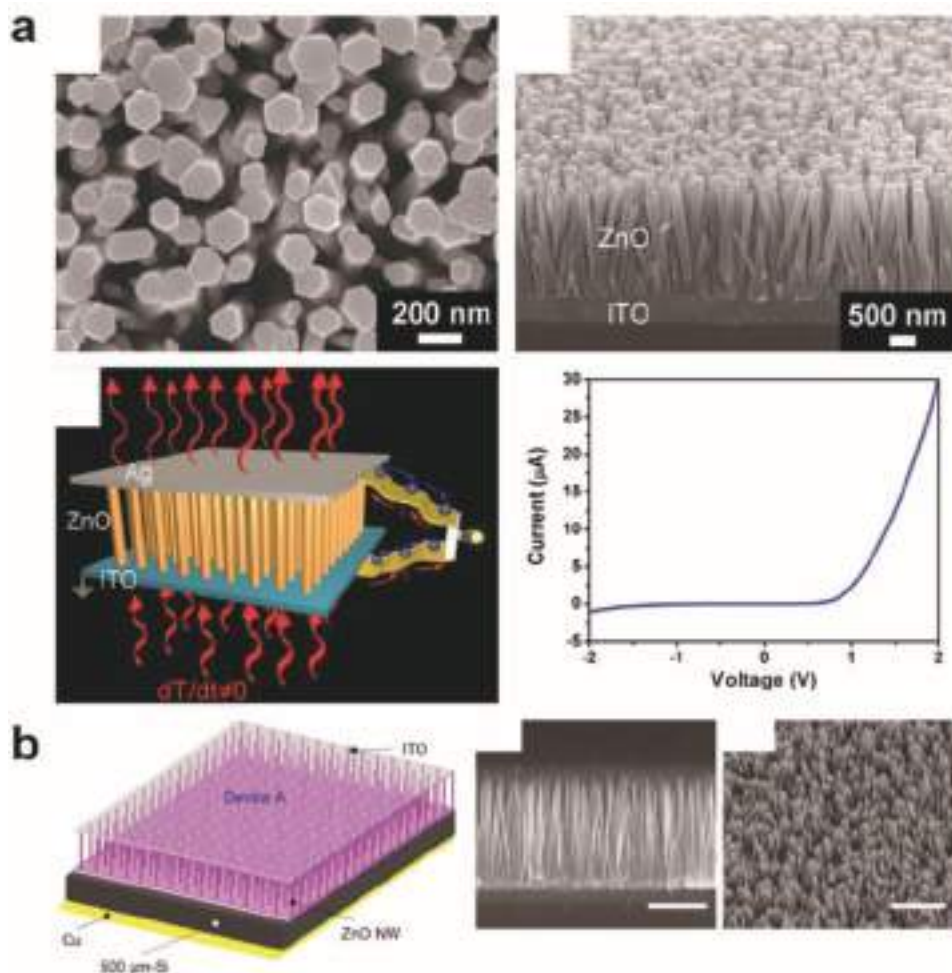


Figure 10. ZnO-based PyNGs. a) SEM and schematic images of the ZnO-based PyNG. Reproduced with permission.^[88] Copyright 2012, American Chemical Society. b) Schematic image of the ZnO-based PyNG and self-powered photodetector. Reproduced with permission.^[99] Copyright 2017, American Chemical Society.

substrate, and PDMS layer was covered on the device to avoid atmosphere, contamination, and corrosive effect. Peak output voltage and current of the PyNG was 60 mV and 0.6 nA under 1.5 K s^{-1} temperature change condition, respectively. In order to utilize the PyNG as a sensor application, the PyNG was attached on the metallic body and contact/separate with heat source. The response time of the PyNG was 0.9 s, and the decay time of temperature response was 3 s. The PyNG was evaluated under different temperatures conditions of heat source. It was able to expect that output voltage increased with an increasing heat source temperature. The linear relationship indicated good performance for temperature sensor and linear change of the output voltage was good to calibrate temperature change rate. They successfully demonstrate detection of a finger touch and moving out and measured the surface temperature of the finger. If temperature of heat source was too high, the output voltage of the PyNG was over 3 V, which was able to drive a LCD using a single PZT micro/nanowire.

Ko et al. reported a flexible PENG and PyNG hybrid energy harvester using PZT film to harvest mechanical and thermal

energies in extreme conditions (Figure 11c).^[103] PZT film was fabricated by spin coated method on a flexible LaNiO_3/Ni -chromium substrate, and platinum electrode was deposited on the PZT film. In order to align the ferroelectric polarization of the PZT film, they applied 20 V for 30 min, and the mechanical property of the PZT film was evaluated by XRD and Raman scattering measurements. The obtained a flexible PZT film's piezoelectric coefficient was 157 pC N^{-1} and pyroelectric coefficient was $50 \text{ nC cm}^{-2} \text{ K}^{-1}$, which was comparable to the reported papers.^[104,105] While the hybrid NG was touched, the temperature change was 1.5 K with the rate of $1. \text{K s}^{-1}$. Peak output voltage and current of the PyNG was 0.05 V and $0.1 \text{ } \mu\text{A cm}^{-2}$, respectively. Peak output voltage and current of the PENG was 0.3 V and $0.3 \text{ } \mu\text{A cm}^{-2}$, respectively under 0.4% strain condition. The hybrid NG generated peak voltage and current of 0.34 V and $0.34 \text{ } \mu\text{A cm}^{-2}$, respectively. Output performance of the wind driven hybrid NG was almost linearly increased with wind velocity and temperature change rate. They demonstrated a highly durable property at harsh environmental conditions at highly humid and strong base conditions. Output performance

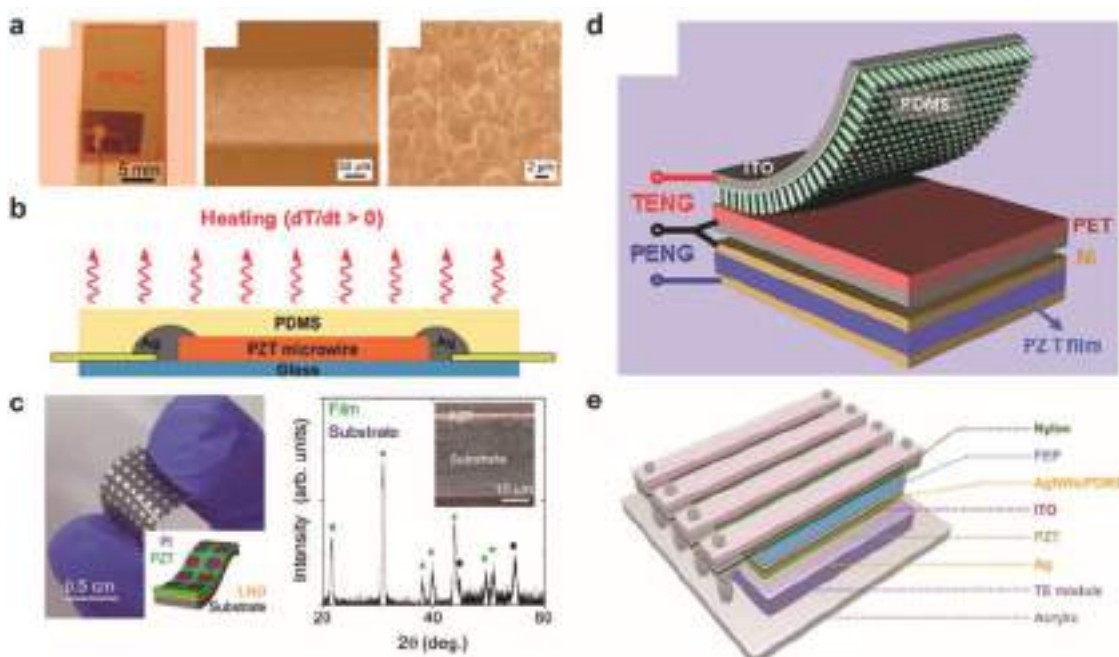


Figure 11. PZT-based PyNGs. a) Photo and SEM image of PZT-based PyNG. Reproduced with permission.^[100] Copyright 2012, American Chemical Society. b) Schematic illustration of single PZT microwire based PyNG. Reproduced with permission.^[102] Copyright 2012, American Chemical Society. c) Real photo and schematic image of PZT-based hybrid PENG and PyNG and XRD analysis of PZT thin film. Reproduced with permission.^[103] Copyright 2016, American Chemical Society. d) Schematic image of the hybrid PDMS nanowire-based TENG and PZT film-based PyNG. Reproduced with permission.^[106] Copyright 2013, American Chemical Society. e) Schematic diagram of one structure-based hybrid NG. Reproduced with permission.^[107] Copyright 2016, WILEY-VCH Verlag GmbH & Co. KGaA, Weinheim.

of the hybrid NG maintained their output performance at RH of 70% and pH of 13. When ultraviolet (UV) was exposed on the hybrid NG, output performance of the PENG was decreased by 24%, but output performance of the PyNG was maintained. Thus, PZT is good candidate for energy harvesters to operate at harsh condition.

Another PZT-based hybrid NG for self-powered electrocatalytic oxidation was reported by Yang et al. (Figure 11d).^[106] Simultaneously/individually mechanical and thermal energy harvesting for a self-powered electrodegradation of methyl orange was fabricated by PZT based PyNG and PDMS based TENG. A flexible PDMS nanowire array was used as triboelectric material and PZT film was used as pyroelectric material. Peak output voltage and current of the TENG was 12 V and 0.2 μ A, respectively, and peak output current of the PyNG was 0.3 μ A. Harvested energy by the hybrid NG was stored in a Li-ion battery from 0.18 to 1 V and then stored energy was used for the electrodegradation of MO. Absorption peak change of MO showed decreased MO concentration, and the color of the MO solution was changed from red to yellow. They also demonstrated MO electrodegradation through direct powering of the hybrid NG.

Zhang et al. demonstrated simultaneously scavenging environmental energy by piezo-tribo-pyro-photoelectric effect coupled NG (Figure 11e).^[107] Integration of a PyNG, solar cell, TENG, and PENG into one device was able to efficient environmental energy harvesting. PZT block was used as active material of piezoelectric, pyroelectric, and photoelectric; polyamide was used as flexible vibrating film for triboelectric

material and applied strain to PZT; Ag, ITO, and Ag nanowire imbedded PDMS film were used as electrodes; thermoelectric module was integrated to convert thermal energy into electric energy. Due to one structure and same output electrodes, simultaneous or individual outputs were integrated. The PyNG generated peak voltage and current of 100 V and 480 nA, respectively. The solar cell generated voltage and current of 60 V and 890 nA with the illumination-induced heat effect, respectively, but the solar cell without the illumination-induced heat effect generated voltage and current of 48 V and 170 nA, respectively. The TENG and PENG hybrid NG generated a peak current of 3.8 μ A under an airflow speed of 15 m s⁻¹, but the voltage was not measurable. When all energy harvesting systems harvest energy, they were able to provide a charge of 71 μ C. For practical application, they charged a 10 μ F capacitor to 5.1 V in 90 s. Therefore, one structure based on various integrated energy harvesting systems realizes maximizing energy scavenging from environment.

4.3. Lead-Free Ceramic Based Pyroelectric Nanogenerator

In order to achieve wearable PyNG applications, the nontoxic property of pyroelectric materials is crucial for biocompatibility. Thus, PZT-based PyNGs have high output performance, but the development of lead-free pyroelectric materials is inevitably required. Yang et al. reported a single crystalline lead-free KNbO₃ nanowire based PyNG (Figure 12).^[89] The KNbO₃ nanowires were synthesized by hydrothermal process. For flexible

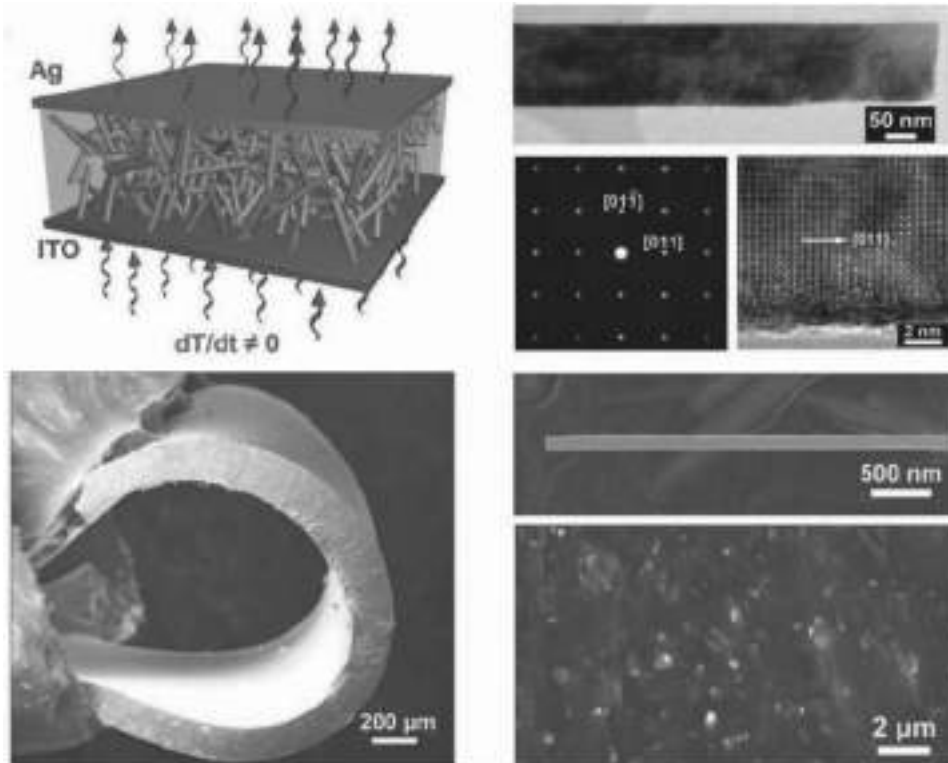


Figure 12. Schematic diagram of the KNbO_3 -based PyNG and TEM, and SEM analysis of KNbO_3 -PDMS composite film. Reproduced with permission.^[89] Copyright 2012, WILEY-VCH Verlag GmbH & Co. KGaA, Weinheim.

property of the PyNG, PDMS and KNbO_3 nanowires were mixed with volume ratio of 7:3. Mixed PDMS was spin coated on ITO substrate and Ag was deposited as a top electrode. A transmission electron microscopy (TEM) measurement and corresponding selected area electron diffraction (SAED) pattern analysis confirmed the phase of the perovskite structure. In the combined SAED patterns and HR-TEM image, the crystal direction of nanowire was along the [011] direction. The mixed nanowires were randomly oriented and dispersed in PDMS without aggregations. Peak output voltage and current of the PyNG were 10 mV and 120 pA under a temperature change rate of 2 K s^{-1} , respectively. Though PDMS decreases the volume efficiency of the PyNG, it realized the flexibility of the PyNG, which was important for practical applications.

Another candidate of the PyNG was nanofiber-based dabcoHReO_4 , which was reported by Isakov et al. (Figure 13).^[108] Uniform dabcoHReO_4 fibers were fabricated by electrospinning process. The crystalline structure of dabcoHReO_4 was examined by XRD, and the most intensive Bragg reflection was (200) followed by (110) in the fibers. Thus, the orientations of the dabcoHReO_4 fibers were all aligned in one direction and had the same polarization. Raman spectroscopy also confirmed a single crystal orientation of dabcoHReO_4 fibers. Piezoresponse force microscopy (PFM) was used to achieve hysteresis loop of piezoresponse and the piezoelectric coefficient was 20 pm V^{-1} . Peak current output performance of the PyNG was 200 pA at temperature change rate of 0.2 K s^{-1} . To evaluate the pyroelectric coefficient, the PyNG was constant heating and cooling, and the corresponding pyroelectric coefficient was $8.5 \mu\text{C m}^{-2} \text{ K}^{-1}$.

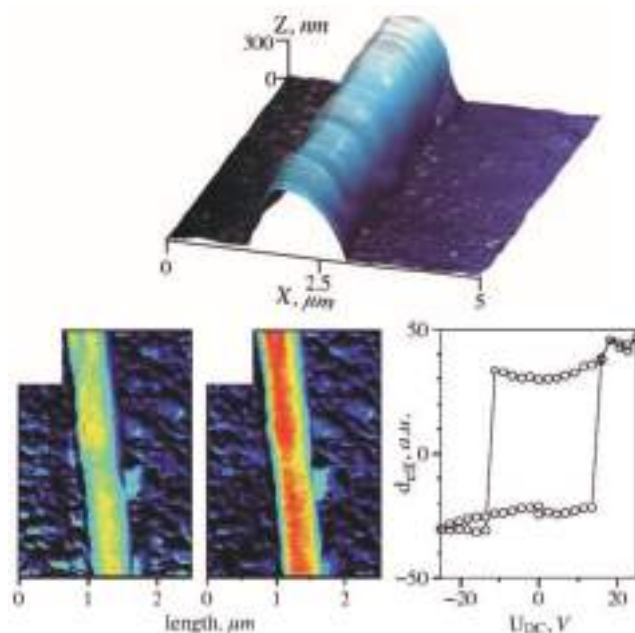


Figure 13. Surface morphology and PFM analysis of the dabcoHReO_4 nanofiber-based PyNG. Reproduced with permission.^[108] Copyright 2014 AIP Publishing LLC.

Although fiber mat dabcoHReO_4 had low pyroelectric constant than bulk dabcoHReO_4 , it was easier to incorporate into wearable electronic applications.

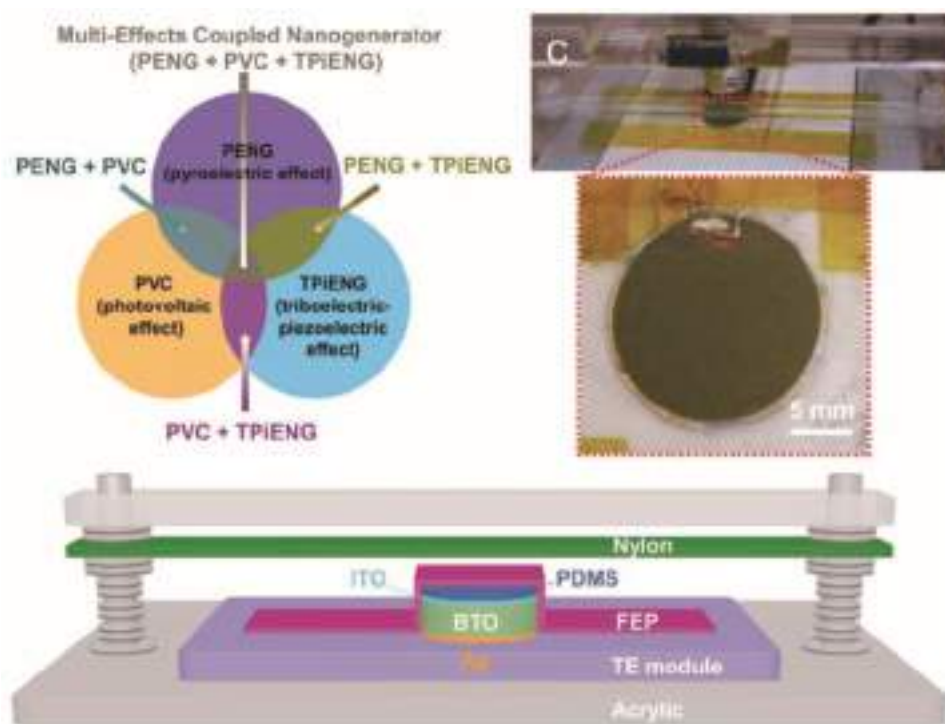


Figure 14. Schematic and real photo images of BTO-based hybrid NG. Reproduced with permission.^[109] Copyright 2017, WILEY-VCH Verlag GmbH & Co. KGaA, Weinheim.

The other candidate of the PyNG was BTO ferroelectric material demonstrated by Ji et al. (Figure 14).^[109] A BTO ceramic disk was fabricated by dry press process for piezoelectric, pyroelectric and photoelectric material. BTO was covered by PDMS as a protective layer and a FEP film was attached on the PDMS as a triboelectric material; a nylon film attached on acrylic was used as counter triboelectric material; commercial thermoelectric module was used for thermal energy harvester. XRD patterns of the BTO confirmed tetragonal phase of BTO which was having ferroelectric property. The PyNG peak output voltage and current were 1.5 V and 15 nA, and the solar cell generated peak current and voltage of 40.5 nA and 0.8 V, and average current and voltage of 10 nA and 0.6 V, respectively. Output current of the TENG and PENG hybrid NG was 3.5 μ A, but voltage was not distinctly detected (<0.1 V).^[83] The calculated pyroelectric coefficient of the hybrid NG was 26 nC cm⁻² K⁻¹. The coupling effect between PyNG and solar cell was evaluated by simultaneous heating/cooling and light irradiation. The enhancement ratio of the output current was 86% by coupling effect. They successfully demonstrated charging a 0.33 μ F capacitor up to 1.1 V in 10 s using the coupled NG.

Qi et al. reported a photovoltaic-pyroelectric coupling effect based self-powered photodetector using BFO ferroelectric material (Figure 15).^[110] BFO powders were synthesis by hydrothermal method, and XRD measurement confirmed perovskite phase of the BFO. The Schottky barrier was formed at the interface of ITO/BFO and BFO/Ag. When the temperature change rate was 0.2 K s⁻¹ under 450 nm light illumination

condition, the ITO/BFO/Ag hybrid NG generated 0.13 V and 8.8 nA, but the photovoltaic current was 2 nA. Due to the differing optimum load resistances of the PyNG and solar cell, the hybrid NG had two optimum load resistances, which were the same as the optimum load resistance of PyNG and solar cell. The responsibility of the hybrid NG was 978% larger than normal solar cell, and the recovery time of the hybrid NG was 0.8 s after 450 nm light irradiation. They successfully demonstrated 3 × 3 photodetectors array for real-time signals mapping on a BFO disk with high resolution. Therefore, lead-free pyroelectric materials are also able to be used in various applications instead of PZT.

5. Other Application of the PyNG

Further development of the PyNGs requires innovative approach to practical applications and enhancement of pyroelectric coefficient. For example, the coupling effect between thermal nanophotonic and pyroelectric (TNPh-pyro) is one of the innovative candidates. Wang et al. utilized thermal nanophotonic effect to enhance pyroelectric output performance and to reflect useless solar irradiation retaining high transparency (Figure 16).^[111] Typically, PyNGs had limited thermal fluctuation,^[112] but TNPh-pyro effect was able to deviate the problem by deliberate channelling of the reflected NIR heat onto PVDF.^[113] The TNPh structure consisted of periodically layered TiO₂ and mesoporous silicon dioxide (SiO₂) films, and topmost layer of mesoporous TiO₂/Cu. PVDF film was an outdoor solar

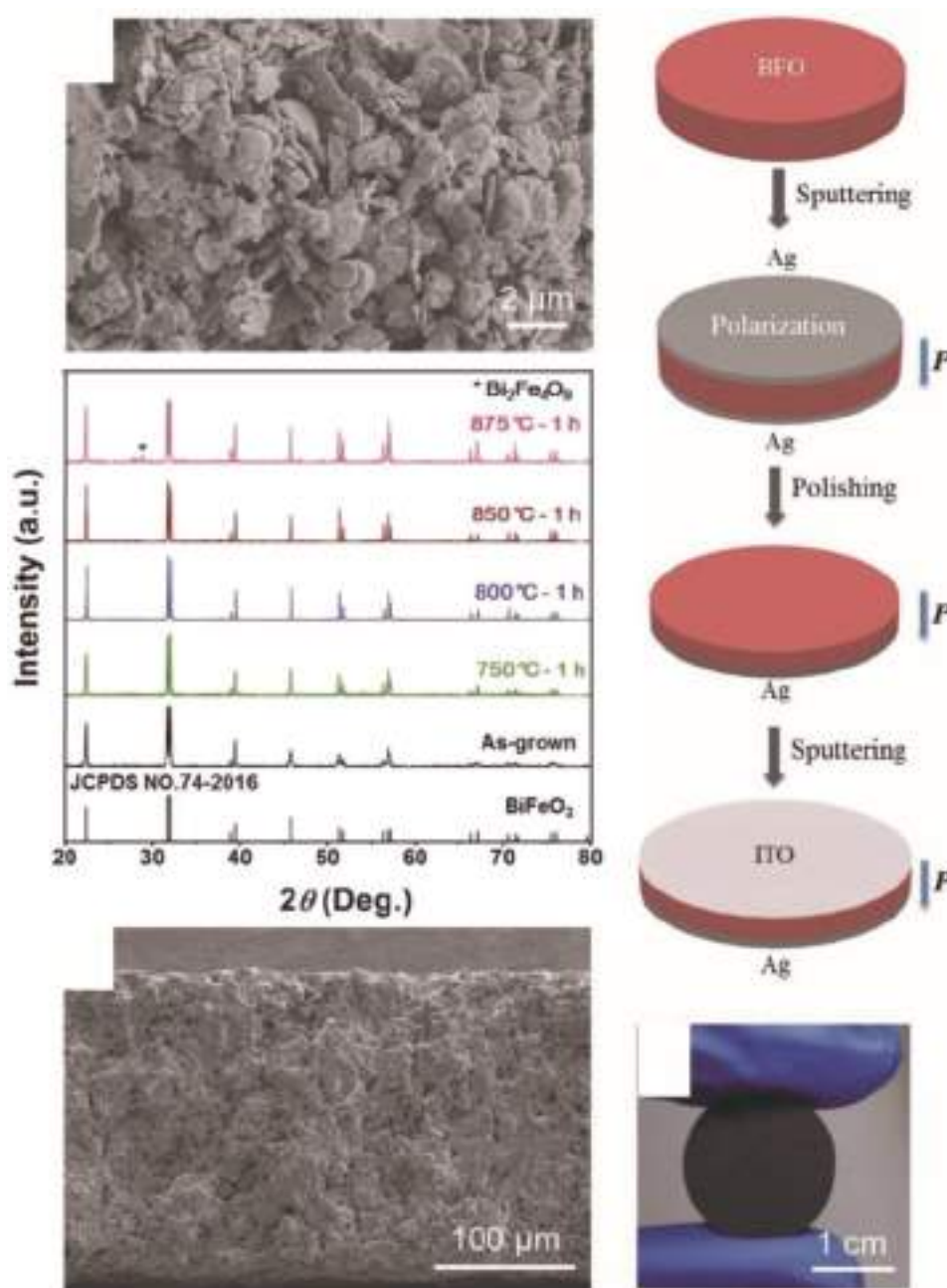


Figure 15. SEM and XRD analysis of BFO and schematic fabrication process of BFO-based PyNG. Reproduced with permission.^[110] Copyright 2017, WILEY-VCH Verlag GmbH & Co. KGaA, Weinheim.

heat harvester and the TNPh layer reflected NIR irradiation, absorbed UV and transmitted visible light for cooling, air purification and lighting.^[114] The crystal structures of TiO_2 and SiO_2 were confirmed by XRD characterization and the NIR reflection characteristic of TNPh-pyro device showed that the NIR transmittance was 35% and that the visible light transmittance was 69.5%, which satisfied the typical transparency requirements of a window. Compare with bare glass and the TNPh-pyro device under 100 mW cm^{-2} solar irradiation, bare glass heated up to $33.1 \text{ }^\circ\text{C}$ and the TNPh-pyro device heated up to $29 \text{ }^\circ\text{C}$, which was able to save up to 45% of energy for the building's

cooling.^[115] In addition, UV irradiation on TiO_2/Cu film decreased ethanol, IPA and formaldehyde, and the TNPh-pyro device generated peak voltage and current of 8.2 V and 23.5 nA, respectively, that was 50% enhanced output performance than pristine PVDF film. They successfully demonstrated that a TNPh-pyro-roofed house had $4.2 \text{ }^\circ\text{C}$ lower internal temperature than glass-roofed house with harvesting peak voltage and current of 32 V and 126 nA, respectively. Another requirement of the improving PyNGs is innovation of pyroelectric material. Although rapid temperature change rate control is able to increase output performance, the most important factor is pyroelectric

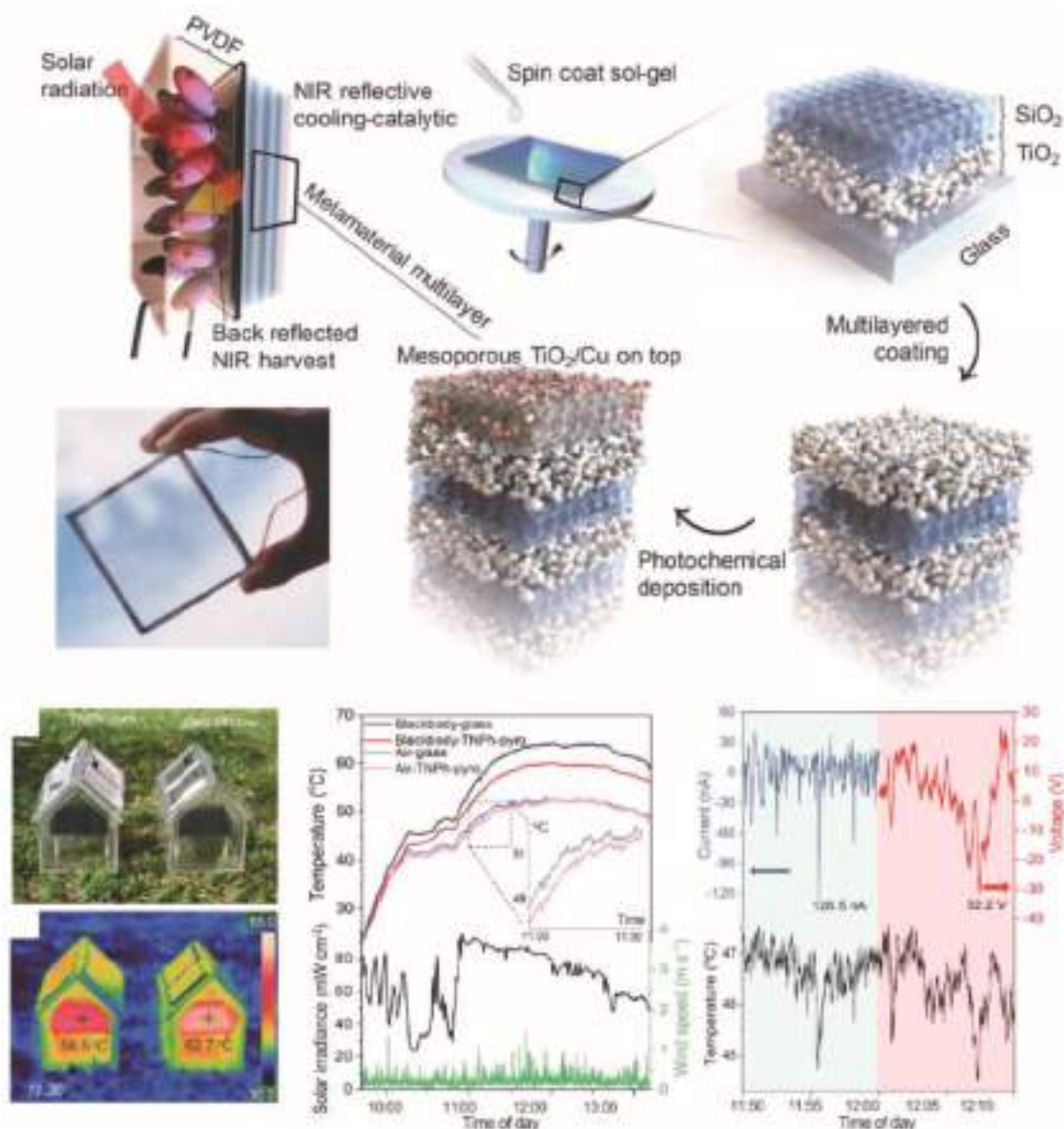


Figure 16. Schematic fabrication process of the thermal nanophotonic and pyroelectric coupled TNPh and practical application of TNPh-pyro device. Reproduced with permission.^[111] Copyright 2017, American Chemical Society.

coefficient, which is unique property of material. Until now, the PyNGs have shown wide discrepancies in theoretical and experimental output performances due to imperfect material structure and property. Thus, heat transfer, internal polarization change, defects, working temperature condition and other physical parameters are necessarily improved.

6. Conclusion

The recent research results of emerging pyroelectric and hybrid nanogenerators are described in this paper. Polymer-based PyNGs are flexible, stretchable and biocompatible, so it is more suitable to use as wearable applications. Ceramic-based PyNGs have higher pyroelectric coefficient, thus its

output power performance is much better than polymer-based PyNGs and more suitable for self-powered IoT systems. **Table 1** shows a summary of materials, pyroelectric coefficient, working condition, output performance, efficiency and flexibility/stretchability of various PyNGs. In order to increase flexibility of PyNGs, micropatterned structure, nanowire structure, and fiber structure are effective approaches. Pyroelectric ceramic nanoparticle/nanowire embedded in flexible polymer is also able to have high flexibility. With the future development of pyroelectric materials, PyNGs may become important new energy harvesting technologies, but there remain the following challenges: Devices should ensure long cycle thermal and sun irradiation stability. If substrate or electrode cannot maintain the mechanical property by thermal and sun light induced damage, the life of system will be limited even

Table 1. A summary of materials, pyroelectric coefficient, working condition, output performance, efficiency, and flexibility/stretchability of various PyNGs.

Ref.	Material	Pyroelectric coefficient [nCcm ⁻² K ⁻¹]	Working condition [ΔT, dT/dt]	Output performance	Efficiency	Flexibility	Stretchability
[47]	PVDF	2.7	35 K, –	190 V, 11 μA	–	Yes	–
[48]	PVDF	3.3	2.8 K, 0.014 K s ⁻¹	60 V, 30 nA	–	Yes	–
[50]	PVDF	2.72	25 K, 23 K s ⁻¹	145 V, 120 nA	–	Yes	–
[51]	PVDF	2.715	>5 K, –	5.7 V, 109 nA	–	Yes	–
[52]	P(VDF-TrFE)	4.39	13 K, –	13.65 V, 2.69 μA	–	Yes	–
[55]	P(VDF-TrFE)	–	18.5 K, 100 K s ⁻¹	2.48 V, 570 nA cm ⁻²	–	Yes	Yes
[60]	Er-PVDF	3.3	24 K, 2 K s ⁻¹	–, 15 nA	–	Yes	–
[69]	PVDF	2.7	12 K, 13 K s ⁻¹	42 V, 2.5 μA	–	Yes	–
[71]	P(VDF-TrFE)	–	–	1.4 V, –	–	Yes	Yes
[74]	PVDF	–	6 K, 10 K s ⁻¹	–, 20 nA	–	Yes	–
[75]	PVDF	–	–	45 V, –	–	Yes	–
[76]	PVDF	–	19 K, –	–, 31 nA	–	Yes	Yes
[79]	PVDF	2.64 ± 0.15	25 K, –	–, 14 μA	–	Yes	–
[80]	PVDF	–	20 K, 3.8 K s ⁻¹	3.2 V, 100 nA	–	Yes	–
[82]	PVDF	3.73	6 K, 0.08 K s ⁻¹	120 V, 60 nA	–	–	–
[83]	PVDF	–	–	120 V, 120 nA	–	Yes	–
[87]	PVDF	4.4	18 K, 0.8 K s ⁻¹	3 V, 30 nA	–	Yes	–
[90]	P(VDF-TrFE)	–	20 K	0.2 V, –	–	–	–
[88]	ZnO	1.2–1.5	30 K, 1.8 K s ⁻¹	18 mV, 0.4 nA	0.05–0.08 Vm ² W ⁻¹	–	–
[99]	ZnO	–	–	–, 2 μA	–	–	–
[100]	PZT	80	45 K, 2.3 K s ⁻¹	22 V, 171 nA cm ⁻²	–	–	–
[102]	PZT	–	37 K, 1.5 K s ⁻¹	60 mV, 0.6 nA	–	–	–
[103]	PZT	50	1.5 K, 1 K s ⁻¹	50 mV, 100 nA	–	Yes	–
[106]	PZT	–	14 K, 0.8 K s ⁻¹	–, 290 nA,	–	–	–
[107]	PZT	–	15 K, –	100 V, 480 nA	–	Yes	–
[89]	KNbO ₃	0.8	39 K, 2 K s ⁻¹	10 mA, 120 pA	–	Yes	–
[108]	dabcoHReO ₄	0.85	6 K, 0.2 K s ⁻¹	–, 200 pA	14.8%	Yes	–
[109]	BTO	22.5–25.9	12 K, 0.85 K s ⁻¹	6 V, 80 nA	–	Yes	–
[110]	BiFeO ₃	–	1.86 K, 0.21 K s ⁻¹	–, 5.5 nA	–	–	–
[111]	PVDF	2.7	19 K, 1.7 K s ⁻¹	8 V, 22 nA	–	Yes	–

pyroelectric material can endure the thermal and sun irradiation induced damage. In addition, extremely high humidity in the atmosphere can react with pyroelectric materials and degrade its performance. Furthermore, spontaneous polarization of pyroelectric materials is depleted at higher temperature condition than Curie temperature. Specialized power management system is necessarily required for high efficient system. Nanoscale power consumed energy management system will significantly increase the energy conversion efficiency. Finally, pyroelectric material innovation, device structure optimization, and device packaging are crucial for high power energy harvesters. A systematic analysis of challenges can be solved by experimental and theoretical approaches, and multidisciplinary development from material science, electronics, and physics will advance output performance of PyNGs in the near future.

The advanced PyNGs will be able to endure practical environmental conditions and actualize new type of IoT power sources and self-powered sensors.

Acknowledgements

This work was supported by the GRRC program of Gyeonggi province (GRRC Sungkyunkwan 2017-B05, Development of acoustic sensor based on piezoelectric nanomaterials) and Korea Electric Power Corporation (Grant number: R18XA02).

Conflict of Interest

The authors declare no conflict of interest.

Keywords

ferroelectric polymers, flexibility, nanogenerators, pyroelectric ceramics, pyroelectric effects

Received: July 2, 2019

Revised: September 14, 2019

Published online: November 4, 2019

- [1] J. Gubbi, R. Buyya, S. Marusic, M. Palaniswami, *Future Gener. Comput. Syst.* **2013**, *29*, 1645.
- [2] L. Atzori, A. Iera, G. Morabito, *Comput. Networks* **2010**, *54*, 2787.
- [3] H. Ning, H. Liu, *Adv. Internet Things* **2012**, *02*, 1.
- [4] B. Guo, D. Zhang, Z. Wang, Z. Yu, X. Zhou, *J. Network Comput. Appl.* **2013**, *36*, 1531.
- [5] J. A. Stankovic, *IEEE Internet Things J.* **2014**, *1*, 3.
- [6] H. Ryu, S.-W. Kim, *Adv. Mater. Lett.* **2018**, *9*, 462.
- [7] R. Hinchet, W. Seung, S.-W. Kim, *ChemSusChem* **2015**, *8*, 2327.
- [8] Z. L. Wang, *ACS Nano* **2013**, *7*, 9533.
- [9] B. H. Robinson, *Sci. Total Environ.* **2009**, *408*, 183.
- [10] X. Wang, G. Gaustad, C. W. Babbitt, C. Bailey, M. J. Ganter, B. J. Landi, *J. Environ. Manage.* **2014**, *135*, 126.
- [11] D. A. Notter, M. Gauch, R. Widmer, P. Wager, A. Stamp, R. Zah, H. J. Althaus, *Environ. Sci. Technol.* **2010**, *44*, 6550.
- [12] H. Ryu, J. H. Lee, U. Khan, S. S. Kwak, R. Hinchet, S.-W. Kim, *Energy Environ. Sci.* **2018**, *11*, 2057.
- [13] I. Lee, K. Lee, *Bus. Horiz.* **2015**, *58*, 431.
- [14] H.-J. Yoon, H. Ryu, S.-W. Kim, *Nano Energy* **2018**, *51*, 270.
- [15] J. H. Lee, J. Y. Park, E. B. Cho, T. Y. Kim, S. A. Han, T. H. Kim, Y. Liu, S. K. Kim, C. J. Roh, H. J. Yoon, H. Ryu, W. Seung, J. S. Lee, J. Lee, S.-W. Kim, *Adv. Mater.* **2017**, *29*, 1606667.
- [16] U. Khan, R. Hinchet, H. Ryu, S.-W. Kim, *APL Mater.* **2017**, *5*, 073803.
- [17] U. Khan, T. H. Kim, H. Ryu, W. Seung, S.-W. Kim, *Adv. Mater.* **2017**, *29*, 1603544.
- [18] J. H. Lee, R. Hinchet, T. Y. Kim, H. Ryu, W. Seung, H. J. Yoon, S.-W. Kim, *Adv. Mater.* **2015**, *27*, 5553.
- [19] U. Khan, T.-H. Kim, K. H. Lee, J.-H. Lee, H.-J. Yoon, R. Bhatia, I. Sameera, W. Seung, H. Ryu, C. Falconi, S.-W. Kim, *Nano Energy* **2015**, *17*, 356.
- [20] J.-H. Lee, H.-J. Yoon, T. Y. Kim, M. K. Gupta, J. H. Lee, W. Seung, H. Ryu, S.-W. Kim, *Adv. Funct. Mater.* **2015**, *25*, 3203.
- [21] S. S. Kwak, S. Lin, J. H. Lee, H. Ryu, T. Y. Kim, H. Zhong, H. Chen, S.-W. Kim, *ACS Nano* **2016**, *10*, 7297.
- [22] H. Ryu, J.-H. Lee, T.-Y. Kim, U. Khan, J. H. Lee, S. S. Kwak, H.-J. Yoon, S.-W. Kim, *Adv. Energy Mater.* **2017**, *7*, 1700289.
- [23] W. Seung, H.-J. Yoon, T. Y. Kim, H. Ryu, J. Kim, J.-H. Lee, J. H. Lee, S. Kim, Y. K. Park, Y. J. Park, S.-W. Kim, *Adv. Energy Mater.* **2017**, *7*, 1600988.
- [24] S. J. Kim, J. H. We, B. J. Cho, *Energy Environ. Sci.* **2014**, *7*, 1959.
- [25] B. Poudel, Q. Hao, Y. Ma, Y. Lan, A. Minnich, B. Yu, X. Yan, D. Wang, A. Muto, D. Vashaee, X. Chen, J. Liu, M. S. Dresselhaus, G. Chen, Z. Ren, *Science* **2008**, *320*, 634.
- [26] L. D. Zhao, S. H. Lo, Y. Zhang, H. Sun, G. Tan, C. Uher, C. Wolverton, V. P. Dravid, M. G. Kanatzidis, *Nature* **2014**, *508*, 373.
- [27] A. J. Minnich, M. S. Dresselhaus, Z. F. Ren, G. Chen, *Energy Environ. Sci.* **2009**, *2*, 466.
- [28] M. Li, A. L. Porter, Z. L. Wang, *Nano Energy* **2017**, *34*, 93.
- [29] Y. Yang, Z. L. Wang, *Nano Energy* **2015**, *14*, 245.
- [30] C. R. Bowen, J. Taylor, E. LeBoulbar, D. Zabek, A. Chauhan, R. Vaish, *Energy Environ. Sci.* **2014**, *7*, 3836.
- [31] V. Nguyen, R. Zhu, R. Yang, *Nano Energy* **2015**, *14*, 49.
- [32] a) H. Wu, Q. Shi, F. Wang, A. V.-Y. Thean, C. Lee, *Small Methods* **2018**, *2*, 1800078; b) A. Ghaffarinejad, J. Y. Hasani, R. Hinchet, Y. Lu, H. Zhang, A. Karami, D. Galayko, S.-W. Kim, P. Basset, *Nano Energy* **2018**, *51*, 173; c) Z. Wang, Z. Ruan, W. S. Ng, H. Li, Z. Tang, Z. Liu, Y. Wang, H. Hu, C. Zhi, *Small Methods* **2018**, *2*, 1800150.
- [33] a) R. Hinchet, U. Khan, C. Falconi, S.-W. Kim, *Mater. Today* **2018**, *21*, 611; b) C. Ma, S. Gao, X. Gao, M. Wu, R. Wang, Y. Wang, Z. Tang, F. Fan, W. Wu, H. Wan, W. Wu, *InfoMat* **2019**, *1*, 116.
- [34] a) R. Hinchet, A. Ghaffarinejad, Y. Lu, J. Y. Hasani, S.-W. Kim, P. Basset, *Nano Energy* **2018**, *47*, 401; b) S. S. Kwak, H. Kim, W. Seung, J. Kim, R. Hinchet, S.-W. Kim, *ACS Nano* **2017**, *11*, 10733.
- [35] R. Hinchet, H.-J. Yoon, H. Ryu, M.-K. Kim, E.-K. Choi, S.-W. Kim, *Science* **2019**, *365*, 491.
- [36] a) S. Xu, B. J. Hansen, Z. L. Wang, *Nat. Commun.* **2010**, *1*, 93; b) X. Fan, X. Liu, W. Hu, C. Zhong, J. Lu, *InfoMat* **2019**, *1*, 130.
- [37] Q. Jing, Y. Xie, G. Zhu, R. P. Han, Z. L. Wang, *Nat. Commun.* **2015**, *6*, 8031.
- [38] Y. Zi, S. Niu, J. Wang, Z. Wen, W. Tang, Z. L. Wang, *Nat. Commun.* **2015**, *6*, 8376.
- [39] J. Wang, S. Li, F. Yi, Y. Zi, J. Lin, X. Wang, Y. Xu, Z. L. Wang, *Nat. Commun.* **2016**, *7*, 12744.
- [40] Y. Zhang, M. Xie, V. Adamaki, H. Khanbareh, C. R. Bowen, *Chem. Soc. Rev.* **2017**, *46*, 7757.
- [41] R. W. Whatmore, *Rep. Prog. Phys.* **1986**, *49*, 1335.
- [42] S. B. Lang, *Phys. Today* **2005**, *58*, 31.
- [43] J. Erhart, *Phys. Educ.* **2013**, *48*, 438.
- [44] S. B. Lang, S. Muensit, *Appl. Phys. A* **2006**, *85*, 125.
- [45] D. Lingam, A. R. Parikh, J. Huang, A. Jain, M. Minary-Jolandan, *Int. J. Smart Nano Mater.* **2013**, *4*, 229.
- [46] a) S. B. Lang, D. K. Das-Gupta, *Handbook of Advanced Electronic and Photonic Materials and Devices*, Academic Press Books, Cambridge, MA, USA **2001**; b) S. Jachalke, E. Mehner, H. Stocker, J. Hanzig, M. Sonntag, T. Weigel, T. Leisegang, D. C. Meyer, *Appl. Phys. Rev.* **2017**, *4*, 021303.
- [47] Q. Leng, L. Chen, H. Guo, J. Liu, G. Liu, C. Hu, Y. Xi, *J. Mater. Chem. A* **2014**, *2*, 11940.
- [48] D. Zabek, J. Taylor, E. L. Boulbar, C. R. Bowen, *Adv. Energy Mater.* **2015**, *5*, 1401891.
- [49] P. C. A. Hammes, P. P. L. Regtien, P. M. Sarro, *Sens. Actuators, A* **1993**, *37–38*, 290.
- [50] F. Gao, W. Li, X. Wang, X. Fang, M. Ma, *Nano Energy* **2016**, *22*, 19.
- [51] M. H. Raouadi, O. Touayar, *Sens. Actuators, A* **2018**, *273*, 42.
- [52] J. Kim, J. H. Lee, H. Ryu, J.-H. Lee, U. Khan, H. Kim, S. S. Kwak, S.-W. Kim, *Adv. Funct. Mater.* **2017**, *27*, 1700702.
- [53] A. P. Indolia, M. S. Gaur, *J. Therm. Anal. Calorim.* **2013**, *113*, 821.
- [54] K.-L. Tung, K.-T. Lu, R.-C. Ruaan, J.-Y. Lai, *Desalination* **2006**, *192*, 380.
- [55] J.-H. Lee, H. Ryu, T.-Y. Kim, S.-S. Kwak, H.-J. Yoon, T.-H. Kim, W. Seung, S.-W. Kim, *Adv. Energy Mater.* **2015**, *5*, 1500704.
- [56] W. K. Jeung, S. M. Choi, Y. J. Kim, *Journal of Electr. Eng. Technol.* **2006**, *1*, 263.
- [57] R. A. Whiter, V. Narayan, S. Kar-Narayan, *Adv. Energy Mater.* **2014**, *4*, 1400519.
- [58] K. Koga, N. Nakano, T. Hattori, H. Ohigashi, *J. Appl. Phys.* **1990**, *67*, 965.
- [59] H. Tada, A. E. Kumpel, R. E. Lathrop, J. B. Slanina, P. Nieva, P. Zavracky, I. N. Miaoulis, P. Y. Wong, *J. Appl. Phys.* **2000**, *87*, 4189.
- [60] S. K. Ghosh, M. Xie, C. R. Bowen, P. R. Davies, D. J. Morgan, D. Mandal, *Sci. Rep.* **2017**, *7*, 16703.
- [61] S. Garain, T. K. Sinha, P. Adhikary, K. Henkel, S. Sen, S. Ram, C. Sinha, D. Schmeisser, D. Mandal, *ACS Appl. Mater. Interfaces* **2015**, *7*, 1298.

- [62] P. Adhikary, S. Garain, S. Ram, D. Mandal, *J. Polym. Sci., Part B: Polym. Phys.* **2016**, *54*, 2335.
- [63] S. K. Ghosh, A. Biswas, S. Sen, C. Das, K. Henkel, D. Schmeisser, D. Mandal, *Nano Energy* **2016**, *30*, 621.
- [64] A. Tamang, S. K. Ghosh, S. Garain, M. M. Alam, J. Haeberle, K. Henkel, D. Schmeisser, D. Mandal, *ACS Appl. Mater. Interfaces* **2015**, *7*, 16143.
- [65] S. O. Grim, L. J. Matienzo, *Inorg. Chem.* **1975**, *14*, 1014.
- [66] H. Seyama, M. Soma, *Clays Clay Miner.* **1986**, *34*, 672.
- [67] Y. J. Kim, C. R. Park, *Inorg. Chem.* **2002**, *41*, 6211.
- [68] T. Sugama, L. E. Kukacka, N. Carciello, N. J. Hocker, *Cem. Concr. Res.* **1989**, *19*, 857.
- [69] H. Xue, Q. Yang, D. Wang, W. Luo, W. Wang, M. Lin, D. Liang, Q. Luo, *Nano Energy* **2017**, *38*, 147.
- [70] F. Mokhtari, M. Latifi, M. Shamshirsaz, *J. Text. Inst.* **2015**, *107*, 1.
- [71] J. H. Lee, K. Y. Lee, M. K. Gupta, T. Y. Kim, D. Y. Lee, J. Oh, C. Ryu, W. J. Yoo, C. Y. Kang, S. J. Yoon, J. B. Yoo, S.-W. Kim, *Adv. Mater.* **2014**, *26*, 765.
- [72] S. Ghosh, I. Calizo, D. Teweldebrhan, E. P. Pokatilov, D. L. Nika, A. A. Balandin, W. Bao, F. Miao, C. N. Lau, *Appl. Phys. Lett.* **2008**, *92*, 151911.
- [73] A. A. Balandin, S. Ghosh, W. Bao, I. Calizo, D. Teweldebrhan, F. Miao, C. N. Lau, *Nano Lett.* **2008**, *8*, 902.
- [74] M.-H. You, X.-X. Wang, X. Yan, J. Zhang, W.-Z. Song, M. Yu, Z.-Y. Fan, S. Ramakrishna, Y.-Z. Long, *J. Mater. Chem. A* **2018**, *6*, 3500.
- [75] J.-G. Sun, T.-N. Yang, C.-Y. Wang, L.-J. Chen, *Nano Energy* **2018**, *48*, 383.
- [76] Q. Zhang, Q. Liang, Z. Zhang, Z. Kang, Q. Liao, Y. Ding, M. Ma, F. Gao, X. Zhao, Y. Zhang, *Adv. Funct. Mater.* **2018**, *28*, 1703801.
- [77] Y. Ding, Z. Zhang, B. Luo, Q. Liao, S. Liu, Y. Liu, Y. Zhang, *Nano Res.* **2017**, *10*, 980.
- [78] S. J. Genuis, *Public Health* **2008**, *122*, 113.
- [79] H. Zheng, Y. Zi, X. He, H. Guo, Y. C. Lai, J. Wang, S. L. Zhang, C. Wu, G. Cheng, Z. L. Wang, *ACS Appl. Mater. Interfaces* **2018**, *10*, 14708.
- [80] H. Zhang, S. Zhang, G. Yao, Z. Huang, Y. Xie, Y. Su, W. Yang, C. Zheng, Y. Lin, *ACS Appl. Mater. Interfaces* **2015**, *7*, 28142.
- [81] S. Wang, L. Lin, Z. L. Wang, *Nano Lett.* **2012**, *12*, 6339.
- [82] Y. Zi, L. Lin, J. Wang, S. Wang, J. Chen, X. Fan, P. K. Yang, F. Yi, Z. L. Wang, *Adv. Mater.* **2015**, *27*, 2340.
- [83] S. Wang, Z. L. Wang, Y. Yang, *Adv. Mater.* **2016**, *28*, 2881.
- [84] E. S. Cozza, O. Monticelli, E. Marsano, P. Cebe, *Polym. Int.* **2013**, *62*, 41.
- [85] S. M. Damaraju, S. Wu, M. Jaffe, T. L. Arinzech, *Biomed. Mater.* **2013**, *8*, 045007.
- [86] S. Tang, P. Zou, H. Xiong, H. Tang, *Carbohydr. Polym.* **2008**, *72*, 521.
- [87] Y. Yang, H. Zhang, G. Zhu, S. Lee, Z. H. Lin, Z. L. Wang, *ACS Nano* **2013**, *7*, 785.
- [88] Y. Yang, W. Guo, K. C. Pradel, G. Zhu, Y. Zhou, Y. Zhang, Y. Hu, L. Lin, Z. L. Wang, *Nano Lett.* **2012**, *12*, 2833.
- [89] Y. Yang, J. H. Jung, B. K. Yun, F. Zhang, K. C. Pradel, W. Guo, Z. L. Wang, *Adv. Mater.* **2012**, *24*, 5357.
- [90] T. Park, J. Na, B. Kim, Y. Kim, H. Shin, E. Kim, *ACS Nano* **2015**, *9*, 11830.
- [91] T. Park, C. Park, B. Kim, H. Shin, E. Kim, *Energy Environ. Sci.* **2013**, *6*, 788.
- [92] T. Park, B. Kim, Y. Kim, E. Kim, *J. Mater. Chem. A* **2014**, *2*, 5462.
- [93] Y. Chen, K. Chen, H. Bai, L. Li, *J. Mater. Chem.* **2012**, *22*, 17800.
- [94] E. Miyako, H. Nagata, R. Funahashi, K. Hirano, T. Hirotsu, *ChemSusChem* **2009**, *2*, 419.
- [95] Y. Hu, Y. Zhang, C. Xu, L. Lin, R. L. Snyder, Z. L. Wang, *Nano Lett.* **2011**, *11*, 2572.
- [96] C. p. Ye, T. Tamagawa, D. L. Polla, *J. Appl. Phys.* **1991**, *70*, 5538.
- [97] Y. Gao, Z. L. Wang, *Nano Lett.* **2009**, *9*, 1103.
- [98] Y. Yang, W. Guo, Y. Zhang, Y. Ding, X. Wang, Z. L. Wang, *Nano Lett.* **2011**, *11*, 4812.
- [99] X. Wang, Y. Dai, R. Liu, X. He, S. Li, Z. L. Wang, *ACS Nano* **2017**, *11*, 8339.
- [100] Y. Yang, S. Wang, Y. Zhang, Z. L. Wang, *Nano Lett.* **2012**, *12*, 6408.
- [101] Y. Hu, C. Xu, Y. Zhang, L. Lin, R. L. Snyder, Z. L. Wang, *Adv. Mater.* **2011**, *23*, 4068.
- [102] Y. Yang, Y. Zhou, J. M. Wu, Z. L. Wang, *ACS Nano* **2012**, *6*, 8456.
- [103] Y. J. Ko, D. Y. Kim, S. S. Won, C. W. Ahn, I. W. Kim, A. I. Kingon, S. H. Kim, J. H. Ko, J. H. Jung, *ACS Appl. Mater. Interfaces* **2016**, *8*, 6504.
- [104] S. Trolier-Mckinstry, P. Muralt, *J. Electroceram.* **2004**, *12*, 7.
- [105] B. Xiao, V. Avrutin, H. Liu, Ü. Özgür, H. Morkoç, C. Lu, *Appl. Phys. Lett.* **2008**, *93*, 052913.
- [106] Y. Yang, H. Zhang, S. Lee, D. Kim, W. Hwang, Z. L. Wang, *Nano Lett.* **2013**, *13*, 803.
- [107] K. Zhang, S. Wang, Y. Yang, *Adv. Energy Mater.* **2017**, *7*, 1601852.
- [108] D. Isakov, E. de Matos Gomes, B. Almeida, A. L. Kholkin, P. Zelenovskiy, M. Neradovskiy, V. Y. Shur, *Appl. Phys. Lett.* **2014**, *104*, 032907.
- [109] Y. Ji, K. Zhang, Y. Yang, *Adv. Sci.* **2018**, *5*, 1700622.
- [110] J. Qi, N. Ma, Y. Yang, *Adv. Mater. Interfaces* **2018**, *5*, 1700622.
- [111] X. Q. Wang, C. F. Tan, K. H. Chan, K. Xu, M. Hong, S.-W. Kim, G. W. Ho, *ACS Nano* **2017**, *11*, 10568.
- [112] G. Ugur, J. Chang, S. Xiang, L. Lin, J. Lu, *Adv. Mater.* **2012**, *24*, 2685.
- [113] X. Shi, H. Jeong, S. J. Oh, M. Ma, K. Zhang, J. Kwon, I. T. Choi, I. Y. Choi, H. K. Kim, J. K. Kim, J. H. Park, *Nat. Commun.* **2016**, *7*, 11943.
- [114] B. Brudieu, A. L. Bris, J. Teisseire, F. Guillemot, G. Dantelle, S. Misra, P. Roca i Cabarrocas, F. Sorin, T. Gacoin, *Adv. Opt. Mater.* **2014**, *2*, 1105.
- [115] T. Hoyt, E. Arens, H. Zhang, *Build. Environ.* **2015**, *88*, 89.